City Research Online

City St George's, University of London

Citation: Coates, L. E. (1982). Diffraction of waves by a vertical circular cylinder : a numerical and experimental study. (Unpublished Doctoral thesis, The City University)

This is the accepted version of the paper.

This version of the publication may differ from the final published version. To cite this item please consult the publisher's version.

Permanent repository link: https://openaccess.city.ac.uk/id/eprint/34839/

Copyright and Reuse: Copyright and Moral Rights remain with the author(s) and/or copyright holders. Copies of full items can be used for personal research or study, educational, or not-for-profit purposes without prior permission or charge, unless otherwise indicated, provided that the authors, title and full bibliographic details are credited, a hyperlink and/or URL is given for the original metadata page and the content is not changed in any way. For full details of reuse please refer to City Research Online policy.

City Research Online: http://openaccess.city.ac.uk/ publications@citystgeorges.ac.uk

Synopsis

The problem of linear wave diffraction by a vertical circular cylinder was studied both numerically and experimentally. The accuracy of the indirect boundary element method was improved by placing the source intensity distribution on a separate fictituous boundary outside the fluid domain. This method was demonstrated for the problem of steady flow past an infinite circular cylinder near a plane boundary, using a linear interpolation of source intensity. Reliable estimates of the force on the cylinder were obtained, provided that the gap between the cylinder and the plane was more than one tenth of the diameter.

The three dimensional problem of wave diffraction by a vertical circular cylinder was solved using a quadratic variation of source intensity. It was possible to use the series form of the Green's function throughout. Good agreement with the exact solution for both the pressure and the total in-line force, was obtained with only twelve elements. This corresponds to fifty-six complex equations.

Experimental measurements of pressure were taken on a vertical circular cylinder in regular waves in the inertia/diffraction regime. The amplitudes of these pressures were consistently higher than the linear theory. The discrepancies did not appear to correlate with wave steepness except at high frequencies. The phase angles were closer to the theoretical predictions. These discrepancies were caused by the effects of finite wave height but a more complete explanation awaits a successful second order theory.

DIFFRACTION OF WAVES BY A VERTICAL CIRCULAR CYLINDER : A NUMERICAL AND EXPERIMENTAL STUDY

BY

L.E. COATES, B.Sc.

Thesis submitted to The City University for the Degree of Doctor of Philosophy in the Department of Civil Engineering

JULY 1982.

To my wife .

ACKNOWLEDGEMENTS

The work presented in this thesis was carried out in the hydraulics and computing laboratories of the Civil Engineering Department, and in the Computer Centre, of The City University, under the supervision of Dr. K. Arumugam. The writer is grateful to Dr. K. Arumugam for his encouragement and advice throughout the period of this work.

The writer gratefully acknowledges the help of Mr. D. Lacey in providing table 4.7.1.

Thanks are extended to [redacted] for manufacturing the pressure transducers, and to [redacted] and his staff for constructing the experimental cylinder.

The writer is indebted to [redacted] for her patience and ultimately her stamina in typing the manuscript.

The writer is thankful for the award of a support grant from the Science Research Council, which made this work possible.

CONTENTS

PAGE NUMBER

Synopsis

Acknowledgements

Contents

List of Figures

List of Tables

CHAPTER 1. INTRODUCTION 1

1.1. Brief Introduction 3

1.2. Scope of the present work

CHAPTER 2. LITERATURE SURVEY

2.1. Forces on small structures in waves 6

2.2. Wave forces on large structures 47

2.3. Numerical analysis of boundless continua 85

CHAPTER 3. POTENTIAL THEORY

3.1. The governing equations of irrotational flow 103

3.2. Uniqueness theorems 108

3.3. Fundamental solutions 113

3.4. Numerical discretisation of a Dirichlet problem 120

3.5. Separation of the source boundary 131

3.6. The Neumann problem of steady flow 135

3.7. The Numerical details 140

3.8. The Numerical results 147

3.9. Linear wave diffraction 153

3.10. The Green's function 161

3.11. The integral equation 164

CHAPTER 4 DIFFRACTION COMPUTER PROGRAM

4.1. Introduction 166

4.2. Separation of the source boundary 167

4.3. The series form of the Green's function 170

4.4. Bessel function evaluation 175

4.5. Numerical formulation 177

4.6. Details of computer program 184

4.7. Numerical results 188

CHAPTER 5 EXPERIMENTAL APPARATUS AND RESULTS

5.1. Wave flume, generator and absorbing beach 197

5.2. Instrumentation for circular cylinder

5.2.1. Cylinder material 201

5.2.2. Cylinder mounting details 202

5.2.3. Displacement transducers 203

5.2.4. Pressure transducers 204

5.2.5. Wave probes 206

5.3. Pressure measurements without cylinder 208

5.4. Pressures on the circular cylinder 213

5.4.1. Pressure transducer calibrations 214

5.4.2. Noise levels 214

5.4.3. Blockage 215

5.5. Presentation of results 216

5.5.1. Wave heights 217

5.5.2. Phase speeds 219

5.5.3. Pressures on the cylinder 220

CHAPTER 6 DISCUSSION OF CHAPTERS 4 AND 5

6.1. The pressure measurements 231

6.2. Program efficiency 237

6.3. Application to arbitrary shapes 240

CHAPTER 7 SUMMARY AND CONCLUSIONS

7.1. Summary 243

7.2. The importance of the present study 245

7.3. Limitations of the present study and recommendations for further work 246

REFERENCES 248

FIGURES 263

TABLES 344

APPENDIX A.1. The pressure on a fixed circular cylinder in water of depth h 368

APPENDIX A.2. Filter amplifier details 377

APPENDIX A.3. Computer program listings 381

APPENDIX A.4. Bessel function notation 395

APPENDIX A.5. Wave radiation and quadratic correction 399

APPENDIX A.6. Equivalent forms of the Green's function 401

List of symbols 410

LIST OF FIGURES

		Page
2.1.1.	Reproduced figure 5 from Morison et al[61] plus remainder function.	263
2.1.2.	C_M vs Um T/D, figure 10 from Keulegan and Carpenter[50]	264
2.1.3.	C_D vs Um T/D, figure 11 " " " "	264
2.1.4.	The effect of time of separation on the instantaneous C_M.	265
2.1.5.	Pressure distribution due to observed vorticity. Figure 10 from Isaacson and Maull[42]	266
3.2.1.	An exterior problem domain	267
3.2.2.	Coordinate system on Σ	"
3.3.1.	The small sphere σ	268
3.3.2.	Portion of curve S	"
3.3.3.	Exclusion of p from S	"
3.3.4.	Exterior and Interior domains	"
3.4.1.	Boundary discretisation	269
3.4.2.	Notation for element i	"
3.4.3.	Boundary conditions	270
3.4.4.	Sixteen element discretisation	"
3.4.5.	Numerical results from program ALB1	271
3.4.6.	Difference between numerical and theoretical results	"
3.4.7.	Source intensity distribution from program ALB1	272
3.5.1.	Boundaries S and Γ	273
3.5.2.	Sixteen element discretisation	"
3.5.3.	Difference between numerical and theoretical results	"
3.5.4.	Source intensity distribution from program ALB2, β = 1.2	274
3.5.5.	'L' shaped domain	275
3.5.6.	Comparitive errors near node II	"
3.6.1.	Horizontal cylinder	276

3.6.2.	Possible method of solution	276
3.6.3.	Method of solution utilising the method of images	"
3.7.1.	The source distribution f	277
3.7.2.	The coordinate systems	"
3.7.3.	The image distance r'	"
3.8.1.	The polygonal source boundary	278
3.8.2.	The test points A, B & C	"
3.8.3.	Ratio of computed value to exact value β=0.9vs.M.	279
3.8.4.	Ratio of computed value to exact value M=16 vs. β	280
3.8.5.	Normalised source intensity distributions for M=16	281
3.8.6.	Ill-conditioning as M increases	"
3.8.7.	Non-dimensional lift force vs. d/2a.	282
3.8.8.	Angular distribution of source intensity for various d/2a values	283
4.2.1.	Two ways in which the numerical solution will round a sharp corner	284
4.3.1.	The roots of $\tan X + h\nu X^{-1} = 0$	"
4.5.1.	Node numbering, natural coordinates and a typical shape function	285
4.5.2.	Gauss quadrature points and weights	"
4.6.1.	Coordinate systems and twenty node discretisation	286
4.6.2.	Computer program BESS flow chart	287
4.6.3.	Areas over which pressure is assumed to be constant	288
4.7.1.	Convergence of normalised force with decreasing $ZK(\beta)$	289
4.7.2.	Computed force expressed as $F/\frac{1}{2}\rho ga^2H$ against ka	290
4.7.3.	Variation of source intensity f with depth	291
4.7.4.	Explanation of reduced accuracy when using higher order integration	292

5.1.1. Wave flume 293

5.1.2. Wave generator 294

5.1.3. Wave steepness kH vs. relative depth d/dc 295

5.2.1. Araldite test specimen "

5.2.2. - 6. Drawings of cylinder apparatus 296

5.2.7. Photograph of cylinder apparatus 301

5.2.8. Linear displacement transducer amplifier 302

5.2.9. Linear transducer calibrations 303

5.2.10. Pressure cell construction 304

5.2.11. Calibration of pressure transducer 1 305

5.2.12. Calibration of pressure transducer 2 306

5.2.13. Calibration of pressure transducer 3 307

5.2.14. Calibration of pressure transducer 4 308

5.3.1. Wave record in the absence of the cylinder 309

5.3.2. Phase speed vs. wave steepness 310

5.3.3. Wave generator idealisation "

5.3.4. Wave heights vs. frequency 311

5.3.5. Pressures in wave vs. frequency "

5.4.1. - 4. Calibrations of wave probes and pressure transducers 312

5.4.5. - 8. Noise levels 316

5.5.1. Wave heights vs frequency 320

5.5.2. Wave heights vs steepness 321

5.5.3. Phase speeds vs wave steepness 322

5.5.4. Phase speeds vs wave steepness for frequency bands 323

5.5.5. Free surface in the presence of the cylinder 324

5.5.6. - 9. Experimental measurements 325

5.5.10. - 14.Pressure amplitudes and phases 329

5.5.15. A wave record 334

5.5.16. - 18.Pressure amplitudes and phases from transducer 2 only 335

5.5.19. A wave record showing harmonic pollution 338

5.5.20 - 21. Pressure amplitudes vs wave steepness 339

5.5.22. Angular pressure variation 341

5.5.23. Averaged pressures in wave compared with cosh ($\frac{1}{2}$kH) factor 342

A.2.1. Typical op. amp configuration 343

A.2.2. Two stage amplifier filter "

LIST OF TABLES

3.5.1. Results along A-b and A'-B' for β=3 344

3.5.2. 'L' Shaped domain - ϕ= 1000x 345

4.7.1. Non-dimensional theoretical force, $\frac{h}{a}$ = 4 346

4.7.2. a - f Numerical results 347

4.7.3. Computed pressures on circular cylinder, 1 351

4.7.4. Computed pressures on circular cylinder, 2. 352

4.7.5. Comparitive computation times. 353

5.3.1. Results without cylinder 354

5.5.1. a - h Experimental results 355

5.5.2. a - b Experimental results 363

6.1.1. Normalised computed pressures at the still water level 365

A.1.1. Exact solution for pressure on cylinder 366

A.2.1. Phase lag and amplitude reduction of 2 stage filter. 367

CHAPTER 1. INTRODUCTION

1.1. Brief Introduction

The design of an offshore structure must be based on the expectation of the worst possible conditions if it is to remain in one place for any length of time. Accurate assessment of the structural responses to such conditions is necessary to avoid prohibitively expensive designs.

For small structures, or large structures composed of small elements the design is based on the equation attributed to Morison, O'Brien, Johnson and Schaaf[61]. The interaction between neighbouring structural elements is usually neglected since each is assumed not to disturb the ambient flow. The total force on a structure is therefore obtained quite simply as the sum of the forces on the individual elements. The only difficulty associated with this approach is in the choice of the inertia and drag coefficients.

For large structures the presence of the structure deforms the ambient flow. Interaction effects between neighbouring large elements of the structure make it impossible to linearly sum the forces on each separate element. However, the fluid problem may be assumed to be irrotational.

Garrison and Chow[25], using the Green's function for this problem have shown how a numerical solution may be obtained which automatically takes account of all interaction effects. The surface of the structure is represented by a number of plane facets at the centre of which is a pulsating source. Hogben and Standing[33] and others, have

developed this approach into á form suitable for commercial use. It appears that these computer packages have had limited use, primarily because of the cost of running a realistic problem. There is therefore, a need for reducing the computation time of these 'facet' methods.

The numerical analysis techniques on which the facet methods are based, are a logical progression from the established techniques used by naval architects and aerodynamicists (e.g. Havelock[29] and Von Karman[48]). They conceive the solution as the superposition of an array of point sources (or vortices, or doublets) and an ambient flow, such that the zero streamline of the resulting flow matches the desired object shape.

A separate (although not radically different) numerical methodology has developed since the 1960's and the advent of fast digital computers. This has become known as the Boundary Integral Equation method or the Boundary Element method. The numerical formulation is based on a version of Green's theorem, in the form of an integral equation. In the method most closely akin to the facet method (known as the indirect method), the sources are conceived as an initially unknown continuous distribution of source intensity over a surface. The integral equation is then discretized by reducing the level of continuity of this source distribution. For steady potential flow problems it has been found that a piecewise quadratic variation can lead to increased accuracy or reduced computation time.

1.2. Scope of the present work

This thesis is concerned with the problem of wave diffraction. Because of the complexity of this problem, many of the techniques used for its numerical solution are studied first in the context of two-dimensional steady flow.

The indirect Boundary Element method is discussed in detail. A steady flow field inside a square boundary, on which Dirichlet conditions are prescribed, is used to demonstrate the typical accuracy obtained using the most common form of this method. The source distribution is assumed to be piecewise linear over the domain boundary. This same problem is then solved using a source distribution on a separate fictitious boundary outside the domain. Thisseparation increases the accuracy of the numerical solution. This improved method is then applied to a problem previously solved numerically by Symm[76], and the results compared. There is a significant increase in accuracy using fewer elements.

The exterior problem of steady flow past a circular cylinder is then considered, firstly when the cylinder is isolated and secondly when it is close to a plane boundary. The numerical formulation is explained in detail. For the first case the numerical results are compared with the exact solution. The position of the source boundary and the number of elements into which it is divided, are varied, to expose some of the limitations of the separate source method. For the second case, the force on the cylinder is of most interest. This force is towards the boundary except when the cylinder is in contact with it. The exact solution for this latter case was given by Jeffreys[45]. It is explained

that this result can not be obtained with a separate source boundary. but, provided the gap between the cylinder and the wall is greater than one tenth of a diameter the force prediction seems reasonable.

The three dimensional problem of linear wave diffraction by a vertical circular cylinder is then considered. This problem has been solved numerically by Garrison and Chow[25], Hogben and Standing[33] and Lebreton and Cormault[52] using the 'facet' method with sources on the cylinder. This study demonstrates how the indirect Boundary Element method may be applied to this problem, using a piecewise quadratic continuous distribution of source intensity on a separate boundary. The details of a computer program are explained. The numerical predictions of pressure and total force are compared with the exact solution, and with previous numerical solutions which used the facet method. It is shown that far fewer elements are required to obtain the same level of accuracy.

The diffraction theory has been compared with the corresponding physical situation. Hogben and Standing[33], Chakrabarti and Tam[15] and Huntington and Thompson[37] have shown that the total force on a vertical circular cylinder is fairly well predicted. There are however small discrepancies which have not been satisfactorily explained. These authors also measured fluid pressure on the cylinder. These measurements which do not agree so well, particularly near the moving free surface, have not been critically discussed.

In this thesis experimental measurements of fluid pressure and phase on a vertical circular cylinder in regular waves are presented. Firstly, the characteristics of the regular waves are measured. In particular the fluid pressure is shown to agree with linear theory to within the level of scatter. It is explained that the second order correction to the pressure does not affect its amplitude, because of the peculiar phase relationships in free waves. The experimental measurements of pressure at two levels on the cylinder are then compared with the exact linear theory. The phase angles agree to within the level of scatter. The amplitudes are consistently larger than the theory, but by an amount which does not appear to depend on the measure of nonlinearity - wave steepness. The errors are apparently of first order. A simple explanation is put forward based on the locally increased wave heights near the cylinder. It is hoped that these measurements will provide data for comparison with a second order analysis, but it is suggested that many more orders may be needed to obtain satisfactory agreement near the front face of the cylinder.

CHAPTER 2 LITERATURE SURVEY

2.1. Forces on small structures in waves.

In response to the need for design procedures, for use in the economic design of offshore structures, a great deal of research into the forces due to waves has been completed. However, the research effort has concentrated on several specific topics often to the detriment of the overall advance. A state of the art survey by Verley[80] in 1975 shows that the field has been segregated into regimes depending on the relative sizes of structure and waves. This has arisen because a general complete solution of the problem has not been discovered. For some special cases certain simplifying assumptions may be made, which lead to useful design rules. The regimes of flow are then the various areas of validity of these assumptions. There are therefore a number of middle ground areas which are not satisfactorily accounted for by any of the regimes.

The waves on the surface of a real sea are multidirectional and contain many different frequency components. The design wave is likely to come from any direction (except possibly for structures close to the shore). The circular cylinder has therefore been used as the main structural element for vertical members, and consequently (on economic grounds) for members in any other direction. Also from a structural view point the circular tube is a strong shape with no areas of stress concentration.

The most fundamental simplifying assumption which has largely been adopted is that of linearity. This enables the trains of waves travelling in different directions to be separated. In addition the Fourier-components of these wave trains may also be treated separately. For irrotational waves-in the absence of a structure - the only non-linearity arises from the free surface boundary condition. For small amplitude waves this non-linear term is small. If it is assumed that the structural response is linear then the responses to each component of the wave field may be treated separately and the effects summed assuming no inter-action. There has therefore been considerable emphasis on the comparatively simple problem of single frequency long-crested waves impinging on circular cylinders.

An important example of the interaction effects which are neglected by this approach is demonstrated by Rainey[70] for the case of dynamics of bouyant structures in cross seas.

If the cylinder diameter is very small in relation to the wave-length, it seems reasonable to assume that conditions are not dissimilar from those in steady flow. Morison et al[61] proposed that the force on a small vertical surface piercing cylinder comprised two parts, one analogous to the steady flow drag force and hence proportional to velocity squared, the second proportional to acceleration, both of these quantities being measured on the axis of the cylinder. To account for the error caused by assuming the presence of the cylinder does not disturb the flow field a coefficient was assigned to each term, the so called drag and inertia coefficients - C_D and C_M.

The Morison equation represents a useful design tool if the values of the coefficients can be found. Keulegan and Carpenter[50] showed that for a given oscillatory flow C_D and C_M could be assumed constant as a first approximation, and that the variation of the coefficients over a number of waves correlated well with a period parameter, which has no physical significance in steady flow.

Wilson and Reid[88] discussing the frustrating amount of scatter in the results up to that time show clearly that C_D and C_M are also a function of Reynolds number. This highlights the problems of scaling up to real structures if both non-dimensional parameters are to be modelled. In particular the high Reynolds numbers in the prototype are difficult to model in the laboratory flume.

To achieve these high Reynolds numbers Sarpkaya[71] has used a U tube device and hence oscillatory flow. His extensive results for both rough and smooth cylinders show clearly the dependence of C_D and C_M on both non dimensional parameters and relative roughness.

The small cylinder regime has then been straitjacketed into the framework of the Morison equation, and it is only recently that this framework has been questioned, Lighthill[54]. It seems clear that, if a dependence on a period parameter is being found, the assumption of quasi-steady flow is being violated.

The problems of real seas have, however been tackled with this framework using linear spectral analysis techniques, by linearising the drag term. Borgman[10] has shown that the spectral density of wave heights and that of structural responses are very similar, which implies that use of a linear model is reasonable. The model breaks down however when the drag component predominates since the structural response must in reality be non-linear. Pierson and Holmes[69] and Nath and Harleman[64] have also used this approach. It is unfortunate that the region where Morison's equation is most likely to be correct (small cylinders) is also when the non-linear drag term is most significant.

In steady flow the in-line force on a cylinder fluctuates about a mean value as a result of the discontinuous nature of separating vorticity. These fluctuations are usually unimportant except when their frequency is close to the natural frequency of the structure. The fluctations in the transverse direction are often larger because the separation takes place at or near the extremes of a transverse diameter. For the case of waves this transverse force has been studied by Isaccson and Maull[42], Chakrabarti et al [16] and Sawargi et al [73]. One conclusion is that it is by no means insignificant, sometimes exceeding the in-line force. It is surprising that no account of the corresponding fluctuations in the in-line direction has been taken, particularly as this would contribute to scatter in C_D values.

The transverse force has often been called a lift force, and a lift coefficient has been introduced in a similar way to steady flow. This has lead to an artifical separation of the causes of the in-line force from the causes of the lift force.

It is far more fruitful, particularly in the case of horizontal cylinders, to consider the instantaneous integral of pressure around the cylinder as giving rise to a resultant force which may be resolved into two components in orthogonal directions. The transverse force is caused by separating eddies just as the in line drag force is.

In steady flow the 'lift' force is usually associated with some asymmetry of shape which is entirely lacking here.

It is clear from the work of Zdravkovich and Namork[90] that the formation of vortices in waves is extremely complicated.

Verley[80] in a useful report setting out the various approaches to the analysis of wave loading summarises the regimes of flow essentially as follows:

$L/D < 1$	Pure reflection
$L/D \leq 5$	Diffraction effects predominate
$H/D < 3$	Inertia increasingly dominant
$H/D = 1.7$	Incipience of drag (and lift)
$H/D > 3$	Drag increasingly dominant

The limit of application of Morison's equation he implies from the above to be $L/D>5$.

There seems no valid reason for supposing that the upper limit of applicability of diffraction theory should be the lower limit for applicability of Morison's equation. It seems far more likely that there is a middle ground where neither approach is applicable.

Use of these simplified rules of applicability must be made with great care. It can be shown that the Keulegan-Carpenter number may be expressed as

$$N_{kc} = \frac{\pi H}{D \tanh kh} \qquad 2.1.1.$$

for small amplitude waves. It is therefore possible to maintain the value of this parameter by increasing H in the same proportion as D in line with the regimes above. For a given wavelength the wave steepness kH will be increasing and leading to increased non-linear effects as shown below , Lighthill[54] . Similar manipulation of H/tanh kh leads to differences in the variation of velocity with depth which must inevitably affect the formation of vorticity. The traditional scatter may simply be an attempt to represent a family of curves by a single line.

A discussion of the results of Sarpkaya, Keulegan and Carpenter and Bidde is included. Bidde[7] uses waves in an experimental investigation of transverse forces on rigid cylinders. It is suggested that the reason for the discrepancies between the results in waves and those in oscillatory flow is due to the different motions of the fluid particles. In waves the particle orbits are elliptical whereas oscillatory flow is rectilinear. There is however a more fundamental difference. It will be seen below Lighthill[54] that forces due to the convective acceleration in waves lead to a second harmonic component of force which is ignored in the traditional Morison approach. It is however not insignificant and could be responsible for the large amount of scatter reported in the values of C_D.

The oscillating flow in a U tube does not possess convective accelerations. That is the particle motions at two different points in the tube are in phase, for incompressible flow. This may be one reason why Sarpkaya's results show very little scatter.

Verley explains that for $8 < N_{kc} < 20$ the timing of eddy separation is likely to lead to considerable variations of C_D and C_M within a wave cycle. He is recognising that the velocity and the drag component of force associated with it may not be in phase because of the finite time taken for an eddy to separate. Since the engineer is usually interested in the maximum force and not its phase his recommended method for calculating C_D for design purposes is to divide the maximum drag force by the maximum velocity squared. This will certainly be conservative but in some cases will lead to gross over-estimation.

Finally a useful set of design calculations is included as an appendix.

Rainey[70] begins with a review of the state of the art in dynamic design of tethered bouyant structures, from which it can be seen that what little mathematical analysis there is relies heavily on the assumption of linearity. For most structures then, tank tests are performed to check for any undesirable effects. These may however be masked by the relatively high damping at model scale. The fundamental assumption in the design of such structures is that they move with the waves. This may be achieved by making sure that the natural frequencies of oscillation are below those in the design wave spectrum.

By considering the equilibrium of a simple tethered sphere in its instantaneous displaced position he arrives at a simple formula for the surge motion.

$$(M+\tfrac{1}{2}\rho.Vol.)\,\ddot{x} + \ell^{-1}\left[(\rho.Vol.-M)g+\tfrac{3}{2}\rho.Vol.\dot{V}\right]x = \tfrac{3}{2}\rho.Vol.\,\dot{H} \qquad 2.1.2.$$

$$\begin{pmatrix}\text{Mass and}\\ \text{added mass}\end{pmatrix}\ddot{x} + \begin{pmatrix}\text{cable}\\ \text{length}\end{pmatrix}^{-1}\begin{pmatrix}\text{Excess bouyancy plus}\\ \text{vertical load on}\\ \text{rigid platform}\end{pmatrix}x = \begin{pmatrix}\text{Horizontal load}\\ \text{on fixed platform}\end{pmatrix}$$

by assuming that vertical motions are small. This equation is arrived at under the assumption of very long waves to avoid the problems associated with the convective terms when the sphere moves. The fluid exciting forces are therefore in the Morison equation regime. This simple model is shown to be the first approximation for many more complicated axisymmetric platform shapes, where in general three such equations arise for the motions of surge, sway and yaw, the latter being homogeneous for such structures.

The inclusion of a velocity dependent damping term is made to account for the effects of viscosity in an apparently arbitrary way. This is subsequently criticised by Sarpkaya who suggests that in the Morison equation regime the correct equations should include a non-linear drag term. Rainey responds by saying that this was a good first approximation.

The equations governing the platform behaviour are then shown to be reducible to a set of Mathieu equations for which instabilities are well known. The presence of instabilities is shown using the symbolism of the analogue computer.

It then appears that the damping is the single most important factor in controlling instabilities which will occur when the wave frequency is twice the natural oscillation frequency.

Subharmonic resonance is then demonstrated to be possible in cross seas if the difference between the major frequency components is close to the natural frequency. This means that although a designer may have been able to keep the natural oscillation frequencies much lower than the expected wave frequencies, in cross seas instabilities can still show up.

The presence of these two types of instability is demonstrated in tank tests and comparison of theoretical and experimental results shows good agreement except for one test result which showed an instability outside the predicted range [Interestingly this was explained by Richardson in the discussion to be due to neglect of the convective terms within a wave. Their inclusion leads to a narrowing of the regions of stability]. Even though the model damping is likely to be greater than in the prototype the oscillations built up to $\pm$ D/2 in surge and $\pm 40^{o}$ in yaw.

Two important conclusions may be drawn from this paper. For dynamic calculations the equation of motion must be written for the structure in its instantaneous displaced position so that the horizontal component of the cable tension (which is substantially due to vertical loads) is included in the horizontal dynamic equation. This component may have been ignored previously since it would normally be expected to aid stability.

The use of superimposed undirectional wave analyses does not predict subharmonic oscillations. For the Mathieu instabilities however, random wave analysis leads to the inescapable conclusion that regular waves are the worst case.

Morison et al[61] studied the forces exerted by waves on surface piercing circular cylinders. They proposed that for small diameter cylinders the force on an infinitessimal element may be expressed as

$$dF = \left[C_M \rho \frac{\pi D^2}{4} \frac{\partial u}{\partial t} \pm C_D \rho \frac{D}{2} u^2 \right] dz \qquad 2.1.3.$$

To avoid complicated sign conventions the velocity squared term has subsequently been expressed in terms of $u|u|$. Using small amplitude wave theory for evaluation of the velocity and acceleration, they discuss the relative magnitudes of the inertia force (the first term) and the drag force. For a cylinder cantilevering from the bed they derive an expression for the total moment about the base. An experimental set up is described from which a continuous time record of bending moment and surface elevation is obtained. The inertia and drag coefficients are then found by identifying the points of zero horizontal velocity and acceleration respectively.

The range of L/D values used for the limited experimental investigation was $24 < L/D < 111$. The lower limit seems much more reasonable and suggests the range $5 < L/D < 24$ is neither diffraction (due to viscosity effects) nor quasi-steady. The results of this investigation are summarised as

$$C_D = 1.626 \pm 0.414$$
$$C_M = 1.508 \pm 0.197 \qquad 2.1.4.$$

There is considerable variation in the C_D results and in view of the preliminary nature of this report it is surprising that the equation was adopted so readily. An example of the comparison of the measured bending moment with the theoretical expression assuming C_D and C_M are constant is reproduced as fig 2.1.1. A second harmonic component is clearly visible even though L/D = 147.

In order to increase the drag component of the force the upper limit of wave steepness is as high as 0.11. It will be shown below that this implies the contribution to the force from the convective acceleration is not negligible and could explain the scatter.

The Morison equation is essentially a split of the total force into two components. The first combines the effects of the added mass and the pressure gradient in the wave, in the absence of the cylinder, and is proportional to the acceleration. The second takes account of any velocity dependent forces which in this case are predominantly form drag since skin friction is extremely small.

The inclusion of just these two terms is valid as a first approximation for the case of very long waves since the flow is quasi-steady. The method has been applied to waves of much shorter length in relation to height with a resulting scatter of coefficients.

Keulegan and Carpenter [50] set out to explain the scatter by correlating C_D and C_M with a period parameter. By integrating the differential equation of momentum throughout the fluid contained between parallel planes equidistant from an infinite cylinder they derive an equation for the force on the cylinder.

By substituting the expressions for the velocity and pressure fields in a fluctuating two dimensional flow they show that for irrotational flow $C_M = 2$. They do not assume that the far field variation of velocity includes any convective terms such as would arise from a truly three dimensional flow.

Section 3 of their paper is the most important. For the restricted case of oscillatory flow they assume that the force per unit length on a cylinder may be expressed as a Fourier-series in terms of the phase angle. Comparison of this expansion with the Morison equation shows that C_M and C_D may each be expressed as a series, the first terms of which are constants.

The non dimensional force is then expressed as Morison's equation plus a remainder function. Analysis of this function enables the variation of C_D and C_M with phase to be calculated.

To examine the form of this remainder function an experimental investigation into the forces experienced by cylinders and plates was conducted. The fluid motion is that of a standing wave in a closed rectangular tank. At the test section, in the middle of the tank and below the surface, the motion is shown to be approximately oscillatory. To be able to investigate the relative magnitudes of vertical and horizontal velocity at the test section a second order wave theory must be used, since to a first approximation the mid-point free surface is a node and hence the vertical velocity is zero.

The authors state that the majority of their results are made with the wave semi-amplitude less than 4% of the half wave length. The results of the experiments are well documented from which it is possible to see that 50% of the cylinder results use a semi-amplitude in excess of this. However, no evidence of non-linear effects in the irrotational component of the force is apparent.

The graphs of C_M and C_D against the period parameter $K = \frac{UmT}{D}$ are reproduced as figures 2.1.2. and 2.1.3. The smooth curve suggested by Keulegan and Carpenter has been replaced by the more realistic family of curves. It appears that above a value of 25 for the period parameter their remains a quite strong dependence on diameter. This may be non-dimensionalized in terms of the parameter $\beta = \frac{D^2}{\nu T}$, called the frequency parameter by Sarpkaya .

C_M is no longer a function of the period parameter but appears approximately to be a constant depending on β. C_D however is a function of both parameters as would be expected.

Theoretical considerations suggest that $C_M = 2$ irrespective of C_D It is difficult to reconcile this fact with the definite reduction of C_M to as low as 0.70 corresponding to peak C_D. However, their method of calculation of C_D and C_M is shown to be equivalent to a weighted average. Any failing in the theoretical representation by Morison's equation inevitably leads to variations of C_M and C_D to accommodate it.

For a cylinder the comparison of measured force with Morison's equation using constant coefficients is given for values of the period parameter of 3.0, 15.6 and 44.7. A value of $C_M = 2$ would not significantly affect the results for K = 3.0 or 44.7, the variations of C_M through a cycle being very slight. For the other case the variation of C_M is shown to be oscillatory, plunging to a value of -2 at the points of maximum drag component.

K = 15.6 is shown to correspond to the formation of a single eddy per half period. This eddy separates from the top of the cylinder in either direction, which means that a substantial 'lift' component will occur.

Detailed examination of their figures 24 and 25 suggests that the most important contributing factor is that the peak drag force is out of phase with and lagging the peak velocity. This is because the eddy contributing to this force takes time to separate and for this particular value of period parameter this separation time is a significant proportion of the quarter period.

The acceleration component falls through zero at peak velocity and is the only available term to accommodate this phase lag. Consequently the instantaneous value of C_M is large and negative. This behaviour may be understood by reference to fig 2.1.4.

It appears then that, if a suitable method of accommodating this phase lag can be incorporated in Morison's equation then C_M may remain constant at 2.

The discussion by Wilson and Reid[88] of a paper by Beckmann and Thibodeaux is often referenced as an illustration of the scatter in the values of C_D and C_M. Their figure 9 showing C_D vs Re is however of little value out of context without the additional values of Keulegan Carpenter number. The main emphasis of the discussion is on the recommendation that designers be more conservative in their choice of C_D, C_M and also the 'lift' coefficient C_L. There is very little substance to this discussion. The only clear indication which appears is that the coefficients necessarily increase due to the proximity of the bed. Some extremely doubtful arguments are used to support this claim based on the assumption that the potential flow solution gives an upper limit to the values of C_L and C_M.

A simple illustration serves to highlight the criticism. If the cylinder (which in this context is a pipe-line) is a small distance above the bed the lift coefficient for the potential flow case is actually quite large and negative as shown below (section 3. 8.). In the case of steady real flow a boundary layer will have formed along the bed which leads to a significantly smaller lift force but of positive sign. However, in the wave case this boundary layer will be extremely thin so that the potential flow result may be substantially correct. Even when the cylinder is resting on the bed, permeability of the soil and/or surface irregularities serve to allow the increased velocity beneath the cylinder. The special case of the uniform cylinder resting tightly on a plane bed is of doubtful practical interest. The implication by the authors that as the bed is approached the lift coefficient increases is refuted.

Sarpkaya[71] has conducted many experiments on forces on cylinders in harmonic flow. This paper summarises much of this work with particular emphasis on the effects of cylinder surface roughness. The results of an extensive investigation, using a 'U' shaped water tunnel, are described.

In a similar way to the experiments of Keulegan and Carpenter the period of oscillation does not significantly differ from 5.5 seconds for all the tests.

The Reynolds numbers in the real sea are much higher than those usually achieved in a laboratory situation, often in excess of 10^7. The high Reynolds numbers achieved in this experiment (up to 1.5×10^6) are therefore remarkable. Although it is stated in the introduction that the range of Keulegan - Carpenter numbers (K) was from 4 to 100, only the results for C_D and C_M for K = 20, 30, 40, 60 and 100 are presented. Examination of his figure 17, where all the results of lift coefficient for relative roughness 1/200 are presented, suggests why. Below K = 20 considerable scatter in the results is apparent. This is the region where only one eddy separates per cycle and scatter is perhaps not surprising. This scatter is likely to show up in the in-line force, but to a lesser extent. In this figure the lift coefficient is seen to reach 3.5 when K = 15, which is almost twice the drag coefficient. This force, and a knowledge of the dominant frequency at which it acts is extremely important in the analysis of vibrations.

Sarpkaya suggests that the Strouhal number controlling the eddy shedding frequency remains approximately constant at 0.22 for rough cylinders when Reynolds number exceeds 2×10^4. This result may not be general because the frequency of operation of the tunnel was constant.

The values of C_D and C_M (calculated in essentially the same way as those of Keulegan and Carpenter) are plotted for each value of K, against Reynolds' number (Re), for different values of relative roughness, together with the results for smooth cylinders.

One striking result is that C_M is considerably below 2 for most of the results. In particular it seems consistently to rise from 1.0 for low Reynolds numbers less than 10^4. The sophisticated analysis method may be masking an effect similar to that previously mentioned in the discussion of Keulegan and Carpenter's paper. The value to which C_M tends with increasing Re is lower for lower K values.

The effect of roughness is to reduce the minimum Re at which separation occurs. The values of C_D up to the minimum are all below the corresponding value for smooth cylinders. After the minimum C_D rises rapidly with inreasing Re to approach a maximum value depending on relative roughness and K, in a similar way to steady flow. It is shown in the subsequent discussion that extrapolation of the data suggests that this maximum value of C_D does not approach the corresponding steady flow result until K = 1000.

This highlights the conclusion that the steady flow results cannot be used for harmonic flows over rough cylinders.

In discussing the applicability to wavy flows, Sarpkaya suggests that his results represent an upper bound. His argument rests on the lack of what he calls 'spanwise coherence' of eddy structure in the wave situation. However, the results reproduced by Miller[59] in the discussion show that Sarpkaya's results are lower than in the regular wave situation.

By spanwise coherence Sarpkaya means that along the cylinder length conditions are the same. In the wave situation the fluid velocity reduces with depth and so for vertical cylinders there is less spanwise coherence. The reduction of velocity with depth is taken into account when Morison's equation is integrated vertically so that this by itself should not lead to a reduction in C_D. However, since C_D varies with Re it should therefore vary with depth, a fact which is often ignored. For smooth cylinders in the drag regime C_D may increase with reducing Reynolds' number. This will lead to a higher average C_D than free surface characteristics would normally dictate. On the other hand, when the free surface velocity is sufficient to cause eddy separation this may trigger early separation lower down the cylinder leading to a higher force than the local Reynolds number would suggest.

It appears then that the apparent lack of spanwise coherence in the theoretical horizontal velocity allows the real fluid room to increase the actual spanwise coherence and hence the force.

This argument leads to the conclusion that the harmonic flow results will be a lower bound to the regular wave results.

The effects of vortex street feedback in real waves may increase or decrease the fluid force depending on the values of Re and K so that in fact no definitive statement may be made (see Zdravkovich and Namork below).

It is often assumed that for Morison's equation to be valid, the cylinder diameter has to be small in comparison with the wavelength. A more accurate definition should include a restriction on wave steepness. In other words, for quasi-steady flow the requirement that - the difference in velocity over a cylinder diameter must be small - is necessary but not sufficient, since this is easily satisfied by an infinitessimally thin cylinder. The spatial gradient of velocity must also be small, and this does not depend on the cylinder at all.

This statement may be understood with reference to the upward buoyancy force acting on a sphere in water. This force depends only on the fluid pressure gradient. The fact that for a small sphere the pressure difference across the sphere is small, is of no particular significance.

In the context of waves this means that the convective accelerations within the flow field may only be ignored if they are insignificant compared with the local acceleration irrespective of the cylinder size.

Lighthill [54] presented a remarkable discussion along these lines to a gathering of structural experts and hydrodynamicists. Although many of the arguments presented may be applied generally, he concentrated on the particular case of a long vertical surface-piercing cylinder in deep water waves. The paper is remarkable not only for its scope but also for its far reaching conclusions.

Lighthill suggests that it is possible to split the fluid flow around a body into an irrotational flow which satisfies the instantaneous boundary conditions and the flow associated with the separated vorticity which satisfies zero boundary conditions. This is because the kinetic energy associated with the irrotational flow component is always a minimum consistent with the instantaneous boundary conditions and the increasing energy (both kinetic and heat) of the wake must therefore balance the work done by the drag force.

The Morison equation may be seen to be a split of the total force into the responses to these two flow components. This suggests that the inertia coefficient (C_M) should maintain its classical value of 2 independent of wake width or separation. Little emphasis is placed on the effects of attached vorticity which must satisfy the no slip condition. This suggests that the effective diameter must be greater than the actual diameter by an amount depending on the thickness of this boundary layer. This effect would lead to a slight increase in C_M over 2 if the actual diameter is used.

Lighthill now concentrates on the irrotational flow response. The components of pressure are defined as hydrostatic ($-\rho gz$), dynamic ($-\frac{1}{2}\rho q^2$) and transient ($-\rho \frac{\partial \phi}{\partial t}$). The usual form of Morison's equation assumes that the structure responds only to the transient pressures and is therefore wholly linear. Any non-linearities must therefore be interpreted as resulting from drag forces only. However, there is a possibility of non-linearities in the irrotational response resulting from significant quadratic (second order) errors caused by the presence of the cylinder.

Quadratic corrections may be found in one of three ways. The linear (first order) wave may be modified by the presence of the structure to include a significant quadratic wave component. The linear response to this component will be of quadratic order i.e. (linearized Bernoulli's equation may be used in a diffraction analysis since the dynamic pressure would lead to a quartic correction). This component of the force he calls Fq.

Another way is to include, from the point of view of the linear waves, any previously ignored quadratic terms. In other words for the calculation of pressures include the dynamic terms in Bernoulli's equation. The corresponding dynamic force he calls F_d.

A quadratic error is also incurred when the linearized free surface boundary condition is applied at the undisturbed water surface.

Including the dynamic terms here would lead to a tertiary error . This force which acts at the water line he calls F_W.

The hydrostatic and transient pressures are equal and opposite at the free surface to satisfy the zero pressure condition. The hydrostatic pressure decays linearly to the still water level whereas the transient pressure decays very slowly (in fact to second order it must be assumed that the transient pressure is constant between $z = 0$ and $z = \eta$ since the linear potential cannot be extrapolated above $z = 0$). The resultant force per unit length of waterline is therefore roughly equal and opposite to the hydrostatic force.

Lighthill shows (using the deep water diffraction theory from Havelock [29]) that the force F_q is small in the Morison equation limit of small kb (b is cylinder radius) but that it increases at least as $(kb)^2$ becoming more important in the diffraction regime. However, the dynamic correction F_d and the water line force F_w (in particular) are shown to be significant in the limit of small kb, increasing in fact with wave steepness ka (a is wave amplitude). An example calculation for a wave of average steepness ($ka = 0.3$) is used to demonstrate that if the method recommended above by Verley is used to calculate C_D, neglect of the non-linear correction would require C_D to double to achieve the positive peak force. However, the negative peak is reduced by the non-linear correction so that a reduction of C_D is required. Since for a fixed value of C_M (say 2) only one value of C_D will give the correct phase position of the peak, it is more likely that both C_M and C_D would be varied to achieve the required maximum at the right phase. This suggests that large variations of these coefficients throughout a cycle will be necessary to fit both peaks if non-linear terms are ignored.

Lighthill contrasts this approach with the use of an incident wave which includes a quadratic correction by virtue of satisfying the non-linear free surface boundary condition but is then assumed incorrectly to give rise only to a linear irrotational response. It appears that in the case of finite amplitude waves Fq may well become more significant in the Morison equation regime.

For demonstrating the calculation of F_d, Lighthill uses the concept of fluid extension. This dynamic force is the integral over the cylinder surface of the dynamic pressures

$$F_d = \int \tfrac{1}{2} \rho q^2 n_x ds \qquad 2.1.5.$$

The components of velocity are calculated separately as a response first to the fluctuating uniform velocity and secondly to the fluctuating extension $(\frac{\partial u}{\partial x})$. In other words these two flow components are the first two terms of an expansion of fluid velocity about the cylinder axis. The response to fluctuating velocity is the well known dipole (or doublet). The response to the fluctuating extension is considered as that due to a quadrupole plus a monopole, the latter potential being given as

$$\phi = \frac{E}{4} (r^2 - 2b^2 \ln r) \qquad 2.1.6.$$

Where E is the instantaneous extension. Clearly r^2 is not a potential function. This term arises from a truncated series of Bessel functions in Havelock's solution. It represents the local behaviour of the potential when kr is small.

It is not emphasized in the paper that the contribution to the dynamic force from cross terms between the vertical velocity and its horizontal gradient is twice as big and opposite to that due to the horizontal extensions. It is perhaps more difficult to give this contribution a physical interpretation.

A simple method for calculating Fq is proposed using the concept of a reciprocal theorem (Green's theorem) explained in an analogy with structural analysis. It is important to emphasize that this method (similar to Haskind's relations for the linear force) gives little information about local forces, but only gives the total force or moment.

To summarize, Lighthill shows that a significant non-linear correction to the irrotational flow response must be included in Morison's equation. The coefficient associated with this term depends on wave steepness and cylinder shape, but not size.

In the diffraction regime an additional non-linear correction becomes increasingly significant (as cylinder diameter increases) caused by the deformation of the wave field, in contrast to the inertia coefficient which is known to reduce.

In other words the presence of the structure places an even greater restriction on the maximum wave steepness required for approximate linearity of irrotational response, than that required for linear waves in its absence.

It will be clear that none of these quadratic corrections arise in purely oscillatory flow without a free surface such as that used by Sarpkaya.

The direct application of Morison's equation to the design of offshore structures is in the form of a design wave approach. The designer chooses a hundred year wave (say) in terms of its height and length. From a knowledge of the depth of water in which the structure will operate values of Reynolds number and Keulegan - Carpenter number can be calculated, and hence from published data (e.g. Hogben et al 35) the values of C_D and C_M can be found.

Faced with the bewildering scatter of published coefficients the designer is forced to choose the highest values to produce a conservative design. For large structures this approach becomes uneconomical. An alternative approach is to calculate using statistical methods the probability of occurrence of a chosen maximum force. A detailed study of the statistical analysis of ocean wave forces is outside the scope of this thesis. However, a critical discussion of four important papers is included since they highlight the basic assumptions behind the methods.

Pierson and Holmes [69] begin by criticising the method of calculating wave force coefficients based on velocities and accelerations implied by a best fit to the water surface. They remark that these methods lead to wide scatter but they do not say why. It appears that they feel the linearization of the drag term in Morison's equation is a major contributing factor.

Using probabilistic techniques they are able to retain the non-linear term, by sampling the fluid force on a pile at equally spaced time intervals over a record time which is long compared to the lowest wave frequency. They propose a two parameter probability distribution which characterises the probability of occurrence of fluid force at a point on the pile.

The two parameters arise from the assumption that the ambient fluid velocity (U) and acceleration ($\dot{U}$) are independent. This leads them to suppose that therefore the corresponding force responses (drag and inertia respectively) are also independent. There are two possible flaws in this argument. The variations of C_D and C_M are often reported as being inversely related, which suggests that they are not independent. The fact that U and $\dot{U}$ may be independent does not necessarily imply that the force responses in the presence of a pile are also. On the other hand, Lighthill [54] has indicated that the inertia coefficient remains unaffected by the drag term but that a significant additional term must be included.

The comparison between the theoretical and measured distributions is constrasted with the normal distribution which is obtained if a linear analysis is pursued. They conclude that the probability of extreme forces is ten times greater than a linear analysis would predict. This conclusion must be based on their measured distribution since their theoretical distribution is not a consistently good fit.

For real waves (unless the amplitude is infinitessimal) the water surface spends longer below mean water level than above it. If equal sample intervals are used then the probability of occurrence of a negative drag force is greatest, although the maximum force is most likely positive (in this context a positive force is in the direction of wave travel). This contributes to a skewness of the probability density function which has maximum effect at the extremes. Simply recognising that the first and third moments are non zero is invalid however since the skewness is caused by the waves themselves being non-linear.

The probability of a force close to zero is obviously high. This means that the curve fit is weighted heavily away from the regions of most interest, the extreme forces. The effects of finite wave height show up clearly here as poor agreement between theoretical and measured distributions. An accurate measurement of the extreme probabilities is severely affected by the record time of twenty minutes. It is difficult to accept their implication that their approach is better than the normal distribution since the differences between them are not significant until a probability level of 2%, at which level the results are based on the number of samples obtained in a twenty-four second period (the sampling interval is not given). In addition these results are more likely to arise from finite amplitude waves.

They indicate that values of C_D and C_M where obtained from the two parameters which achieved the best fit to the measured distribution. No results are presented because they showed no clear correlations.

They felt confident enough however to state that C_D and C_M cannot be assumed constant with depth.

Borgman [10] begins with a useful introduction to the terminology of spectral analysis of random processes. This method, which is based on the Fourier integral transform, has been used extensively in electronics but this application to waves was novel. It is assumed that the variation of a random signal with time may be expressed as the sum of an infinite number of sinusoidal components covering all the frequencies from zero to infinity. Analysis of the signal leads to a function of frequency known as the power spectral density which is often proportional to the energy contained in each frequency component.

The application to wave forces is in the form of a black box approach. The input spectrum is that of the water surface elevation above mean water level (η) and the output spectrum that of the force per unit length (ϕ) on a vertical pile. These two spectra are assumed to be related by a transfer function (of frequency) which characterises the physical process.

This relationship between η and ϕ may be constructed by recognising that the ambient fluid velocity and acceleration are related to η by a wave theory and to ϕ by Morison's equation. The mathematical complications associated with the non-linear drag force are then removed by using the first term of its series representation, an approximation which is in error by about 15%.

Borgman goes on to analyse data from the real sea. From the measured spectral density of $\eta(t)$ the approximate spectral density of force may be calculated but remains a function of the unkown coefficients C_D and C_M. Morison's equation is assumed to be a flexible framework so that C_D and C_M can be found by a least squares fit to the measured force spectrum.

The good agreement is perhaps not so 'surprising' since this procedure allows the coefficients to vary to take up some of the inaccuracy introduced by the linearization of the drag term. The use of Morison's equation in this way will inevitably lead to scatter in the coefficients from different records.

On the strength of the presented results Borgman suggests that the equivalent linearized form of Morison's equation

$$\phi(t) = C_D \tfrac{1}{2} \rho D V(t) \sqrt{\frac{8}{\pi}} v_{rms} + C_M \rho \frac{\pi D^2}{4} \dot{V}(t) \qquad 2.1.7.$$

may in fact be a better representation. There is a possible physical justification for this based on the fact that eddies, once separated, move with the flow. If the flow component normal to the pile is approaching zero, separated vorticity will stay close to, and continue to exert a force on the pile. This may be expected to make the force response more nearly sinusoidal. In addition, the orbital nature of the flow may contribute to increased vorticity compared with the oscillatory flow case. It is clear that equation 2.1.7. still reduces to the accepted steady flow form (except for a multiplicative constant).

This suggestion combined with the additional irrotational flow term may well lead to reduced scatter even for regular waves.

In a second paper Borgman [11] helps to clarify the application of numerical spectral analysis to the simulation of random waves and wave forces. Two similar methods are proposed.

Simulation of $\eta(t)$ by superposition of a finite number of components of different frequency each having a random phase and an amplitude consistent with the energy in the required spectral density. Each component wavelet is assumed to travel at a phase speed given by linear wave theory. All the waves are therefore of small amplitude.

Simulation by digital filtering introduces the idea of the discrete Fourier transform which utilizes the numerical fast Fourier transform available on most computers. Essentially, a digital filter operates on an input sequence of numbers with a kernal (sic) function to produce an output sequence of numbers. The kernal function K(f) is a Fourier series with initially unknown coefficients. The crux of this method lies in the relationship between the input and output spectral densities

$$Syy(f) = |K(f)|^2 Sxx(f) \qquad 2.1.8.$$

If the kernel function can be made equal to the square root of the required sea surface spectral density function then using white noise for the input yields the required spectral density at the output (white noise has a spectral density of one).

Irregular water surfaces simulated using these approaches show marked differences when compared with real sea waves which tend to have more peaked crests and flatter troughs. This occurs as a consequence of the non-linear boundary condition satisfied by all but the smallest waves. The higher frequency components introduced by this condition tend to travel with the same phase speed as the main wave and so invalidate the assumptions of random phase. Although attempts to fit real sea data by introducing skewness may work in the open sea, the presence of a structure causes additional non-linearities which would not be modelled correctly in the force spectrum.

An interesting experiment may be easily set up to investigate the effects of skewness in laboratory generated random waves. From the spectral analysis of $\eta_1(t)$ at one wave probe $\eta_2(t)$ at another probe may be extrapolated. If the distance between the probes and the water depth are chosen so that differences in phase velocity are easily detectable then comparison of the measured phase relationships at the second probe with those predicted, will enable a limiting wave steepness for linearity, to be found.

Nath and Harleman [64] describe an interesting application of the methods proposed by Borgman to the measurement of sea spectra. They show that for certain ratios of wave height to cylinder diameter one or other of the terms in Morison's equation may be safely ignored.

They pursue the case when the drag force is negligible and so the fluid force is linearly related to the water surface elevation. By arranging weights at the top of a vertical surface-piercing cylinder they were able to construct a single degree of freedom transducer which responded to the magnitude of the wave spectrum at its natural frequency, thus acting as a mechanical analogue of the narrow banded filter. The agreement between the spectrum obtained using this mechanical filter and the usual numerical technique is good except, significantly, near the peak energy. It is likely that here the non-linear effects in the irrotational flow plus the gross motions of the resonating vibrator will affect the response. The agreement is all the more surprising when it is realised that C_M was fixed at 2.0 and not calculated to achieve a best fit.

To summarize, it appears that spectral analysis may be a powerful curve fitting technique but the large scatter in the published coefficients makes extrapolation doubtful. It seems likely, however that the main reasons for this scatter are inherent in the use of Morison's equation.

The possible sources of error include

1. Linearizing the non-linear velocity term in Morison's equation.
2. Ignoring the non-linear irrotational flow term.
3. Ignoring the variation of C_D and C_M with depth.
4. Ignoring the variation of C_D and C_M with frequency.
5. Assuming that the structure responds to the instantaneous normal component of velocity i.e. ignoring fluid memory and orbital motions.

6. Assuming that real waves satisfy a linear free surface condition.

7. Assuming that the structure responds independently to each individual component wavelet.

To date most workers have reduced the effects of some of these errors by using narrow banded spectra, small amplitude waves (maximum wave steepness of Borgman's data was approximately 0.03) and allowing C_D and C_M to vary to achieve a best fit. As Borgman suggests, the linear form of the drag term may infact be a better approximation.

The most important assumption is number 6, since this enables the linear superposition of wavelets. Although this may be valid in the open sea often significant forces are caused by interactions in the presence of the structure.

The use of spectral analysis for wave forces has become more widespread since the introduction of the Fast Fourier Transform algorithm by Cooley and Tukey [18]. It is unfortunately all too easy to misuse it. The analysis to date of the transverse or 'lift' forces on small cylinders is an example of just such a misuse.

Isaacson and Maull [42] investigating the transverse forces on a vertical cylinder measured both the resultant force and the pressure distributions around several cross-sections at different depths by assuming that their experimental waves were perfectly periodic.

The pressure distributions are presented in coefficient form by using as a reference pressure the static (sic) pressure within the wave at the same depth. They used two different experimental situations: the rigidly mounted cylinder under the action of regular waves and (to facilitate flow visualisation) a cylinder oscillating in otherwise still water. It is not always clear which results relate to which flow regime. The results from the two cases are only comparable if the depth variation of velocity is small and the waves are small amplitude.

The coefficient of lift force is defined in a similar way to the drag force for steady flow by

$$F_L = C_L \tfrac{1}{2} \rho A U_{max}^2 \qquad 2.1.9.$$

although unlike the drag coefficient the lift coefficient C_L must vary throughout the cycle even as a first approximation. The variation of velocity with depth will affect the separation of vorticity and is characterised by the wave depth parameter kh. The variation of C_L with Keulegan - Carpenter number (KC, defined at the surface) exhibits a maximum at about 10 for all values of kh. They use a depth averaged r.m.s. lift coefficient to compare the results for deep, intermediate and shallow waves. Since this takes account of the depth variation of velocity, the results should be the same for all depths if the transverse force is a response to the local fluctuating velocity. The experimental fact that the intermediate depth results are largest is in agreement with the hypothesis (above) that the reduced spanwise coherence in the ambient flow allows room for more separated vorticity than the local velocity would suggest.

They show that the Fourier components of the lift force occur at multiples of the wave frequency with the strongest being the second harmonic at KC ≃ 10 corresponding to the formation of one eddy per half cycle. The third harmonic peaks at about KC ≃ 20.

To demonstrate that the lift force is closely related to the presence of separated vorticity they show the pressure distributions close to the surface together with the positions of any eddies from the flow visualization. One such result is reproduced as figure 2.1.5a where the broken line represents the potential theory. Figure 2.1.5b shows the variation of pressure derived from this, due to the presence of the eddy only. They do not comment on the surprisingly large positive pressure close to $\theta = 270^{o}$. Two reasons for this large discrepancy are, firstly that their potential theory result is for an oscillating flow without the effects of the free surface (in particular a fluctuating vertical velocity) which may be quite large even if their resultant is small. Secondly they have reduced the potential flow result to mean zero which will obviously not affect the resultant force. However, there is no reason to suppose that the additional pressure distribution due to the single eddy close to $\theta = 150^{o}$ will also be mean zero.

Chakrabarti et al [16] consider both the in-line and the transverse forces on a vertical cylinder although they analyse them separately. The values of C_M and C_D which they obtain by a least squares fit show surprisingly little agreement with the results of Keulegan and Carpenter [50] and Sarpkaya [71] although the integrated theoretical force is within 5% of the measured force.

Although the transverse force traces appear to be irregular, pronounced spikes in the energy spectra occur at multiples of the wave frequency. They show that as KC increases the number of eddies shed per half cycle increases in integer steps. Correspondingly the ratio, lift frequency to wave frequency is always an integer. They therefore propose that the lift force expression should be in the form of a Fourier series for which they calculate the first five coefficients. Their results are in general agreement with Isaacson and Maull [42]. The largest component is the second harmonic for KC between 6 and 16, corresponding to one eddy shed per half cycle.

Their measured forces confirm the importance of the transverse force in this range since for KC about 15 the resultant force is as much as 60% more than the in-line force. They conclude by proposing that the resultant force be considered as the vector sum of Morison's equation and their Fourier series representation of the transverse force.

Although the Fourier analysis of the transverse force will usually yield the phase angles of the components, the above two papers make no mention of them.

Sawaragi et al [73] investigated the transverse forces on a vertical cylinder using synchronized photographic and tape recording techniques to try to accurately relate eddy formation to transverse force.

They define a surface tracer KC (which is closely related to the usual definition but is more easily estimated from the photographic record) and classify eddy formation into six categories according to the ultimate distribution of shed eddies in a half cycle, each category being a specific range of KC.

Using these techniques they are able to closely relate the asymmetry of the vortices to the occurrence of a transverse force, showing how their categorization defines the frequency at which it occurs.

They present a comparison between the phase of occurrence of the maximum in-line force and the maximum transverse force. The considerable scatter makes it difficult to draw any useful conclusions. In any case it is the in line drag force which should correlate with the transverse force since both are derived from the eddy structure.

They calculate the frequency components of the transverse force in the same way as Chakrabarti et al [16] and obtain similar results. They draw the surprising conclusion that, because the frequency ratio in waves increases in discrete steps whereas for undirectional steady flow it varies continuously, the mechanism of vortex shedding is qualitatively different for the two cases.

Their results again confirm that design based solely on Morison's equation is likely to seriously underestimate total forces. In this context it is worth remarking that the usual statistical analysis of irregular ocean wave forces pays little attention to the direction of the maximum force for uni-directional spectra. The effect of transverse forces is therefore to some extent included in the calculated Morison coefficients. However, for multi-directional wave spectra the effects of transverse forces will be ignored since the force response will be assumed to be in the wave component direction.

There seems to be considerable agreement between the experimental findings of these researchers.

It is clear that the variation of transverse force with time is usually irregular within a single wave cycle but shows remarkable consistency from wave to wave. This means that for periodic waves the transverse force is periodic at the wave frequency. However irregular the variation within a wave this periodicity dictates that only harmonics of the wave frequency may be used to represent the force.

This is not to say however, that the dominant frequency of vortex shedding must be a multiple of the wave frequency. The mechanism of vortex shedding is unlikely to differ very much for steady or unsteady flow. The similarity between the two cases can be brought out by an analysis based on the concept of time of separation.

The time it takes an eddy to separate and hence exert a force is related to the local velocity and a dimension representative of the distance the vorticity must travel to separate by

$$T_s \propto \frac{\text{Dimension defining separation}}{\text{Velocity at which vorticity travels}} \qquad 2.1.10.$$

For a cylinder this dimension is related to the diameter and the velocity of travel to the fluctuating velocity in the wave. The frequency of vortex shedding within a single wave is therefore related to the inverse of T_s and hence (for a given cylinder) directly to the fluctuating velocity. If only one eddy separates per half cycle then the maximum velocity in the wave may be used to characterize T_s. As more eddies are shed the frequency will reduce with the reducing velocity.

The frequency of vortex shedding within each half cycle is therefore expected to be a continuous function of KC.

It is generally accepted that the drag component of wave force given in Morison's equation depends largely on the shed vorticity since skin friction effects are small. It is remarkable therefore that no one has related the discrete formation of eddies to the variation of this drag component. Most researchers have preferred to manipulate the coefficients C_D and C_M to best fit the measured in-line force. One possible difficulty is the fact that this force is not solely due to drag but includes the irrotational flow response.

If it is accepted that $C_M = 2$ and non-linear irrotational effects if significant are equally determinate then the drag force may be isolated and analysed with reference to the shed vorticity. This may help to explain the anomalously low values of C_M close to the region of maximum lift force. It may also answer the question raised by Borgman of whether the linearized form of the drag term is more accurate.

As if to underline the complicated nature of vortex formation in unsteady flow Zdravkovich and Namork [90] show a previously unobserved phenomenon for apparently the same situation. They show that the persistence of vorticity is such that when a separated vortex is swept back (as the ambient flow reverses) onto the cylinder on the same side as it was formed, it does not mix with the increasing vorticity of opposite sign. Instead a vortex pair is formed which persists for a considerable time. This suggests (contrary to the usual expectations) that vortex feedback may in certain circumstances increase the lift and drag forces.

The physical explanation of this phenomenon appears to be that the local velocity near the separation zone is increased by the presence of the previously separated eddy. The increase contributes to increased vorticity of opposite sign because of the no slip condition on the cylinder boundary. The low pressure near the eddy contributes to the greater adverse pressure gradient required for separation.

Zdravkovich and Namork observed that this behaviour usually led to a vortex doublet in the wave trough.

This is because the wave height to water depth ratio is quite high for their experiment so that the crest has more vortex generating power and hence the separated eddy lasts longer. This is probably why the researchers working in greater water depths have not observed this.

2.2. Wave Forces on Large Structures

As the size of the structural elements comprising an offshore structure increases in relation to the incident wavelength the effects of separated vorticity become less significant. This is particularly so for shapes that do not possess sharp edges, such as the commonly used circular cylinder. There is therefore a significant range for such shapes, called the inertia regime where Morison's equation with $C_M = 2$ and $C_D = 0$ may be applied. The equivalent regime for shapes such as rectangular prisms may not exist since the form drag component will reduce much more slowly. Keulegan and Carpenter[50] presented results for the case of flat plates which showed that C_D in fact increases rapidly with increasing plate size.

As the structure increases in size still further its effect on the incident wave pattern is no longer negligible. Characterising the flow response in terms of the acceleration on the axis of the structure becomes less physically reasonable. Morison's equation has still been used but C_M is no longer 2 even though the flow may be considered as irrotational. Chakrabarti[13] however, presented a semi-analytical approach to the forces on submerged objects in the inertia/diffraction regime. The effects of the free surface and the presence of the object were small for the cases considered.

For small amplitude waves the free surface boundary condition may be linearised. For large structures the fluid problem therefore reduces to that of finding a velocity potential satisfying Laplace's equation and the boundary conditions which are now all linear.

Traditionally a distinction has been made between the two different ways in which an incident wave train may be modified. The continual modification of the waves caused by variations in bed topography is termed refraction, whereas the wave scattering effect of arbitrarily shaped obstructions is termed diffraction. Both of these terms are borrowed from the partly analogous problem of the propagation of electromagnetic waves, hence the often used term 'monochromatic' water waves when referring to single frequency waves.

When the variation of bed topography is gradual, and all other lateral boundaries to the flow may be assumed to be vertical, the variation of the potential with depth may be separated out leading to a wave equation in the plan dimensions, Berkhoff[4]. For the particular case of constant depth the wave equation reduces to a Helmholtz equation and further separation of variables in a number of co-ordinate systems is then possible depending on the shape of the cylindrical obstruction. For a circular cylinder the solution may be found as an expansion in cylindrical harmonics. Havelock[29] quotes the result for the special case of infinite depth and periodic single-frequency waves. The periodicity allows a further variable separation by introducing the complex potential. In addition, linearity allows the effects of the incident wave and the scattered wave to be treated separately. This analytical solution was extended by McCamy and Fuchs[58] to the case of constant finite depth. The importance of their result is that it is a particular case of both the diffraction and refraction problems.

If a rigid structure is able to move under the action of the waves then additional forces will be induced by virtue of its motion. These motions may be considered as a linear combination of the six degrees of freedom. The added mass forces are those in phase with the structure accelerations and the damping forces are those in phase with the structure velocities.

The analysis of such motions has long been the concern of Naval Architects. However, it has often been possible for them to consider a ship as a slender body and thereby reduce the complexity of the problem. The so called strip theory arises from the assumption that forces on cross-sections of a ship may be integrated along its length to obtain total forces without consideration of interaction effects. In the case of offshore structures Morison's equation for force per unit length is an example of just such a strip theory.

In a survey of the state of the art of structural dynamics of fixed and floating platforms Eatock-Taylor[20] points out that much of the work has actually been of a quasi-static nature considering the structure as a rigid body. The flexing of the structure in the dynamic sense has received very little attention, and even when it has the wave frequency has been so far removed from that of the first mode of the structure that dynamic amplification has been negligible.

The importance of the small amplitude motions of the structure whether fixed or floating is demonstrated by Newman[65] in a presentation of Haskind's relations. This approach which leads to a single total force for each mode of oscillation may be likened to an application of the principle of virtual work, similar to that

utilised by Lighthill[54] for the calculation of the forces due to the quadratic potential.

However, for all but the simplest shapes the radiated potentials (due to the motions) are no easier to find than the corresponding scattered potential.

It has long been known that any irrotational flow may be represented by a distribution of sources around the boundary, (Lamb(51)). It is only comparatively recently that this fact has been utilised in the case of waves to enable the numerical solution of problems with more complicated boundaries. Much of this work stems from the derivation by John[47] of a series form of the integral expression presented by Wehausen and Laitone[84] for a pulsating source in three dimensions, and the development of fast computers. Because these expressions already satisfy the boundary conditions on the free surface and at constant depth, the distribution of sources may be limited to the boundary of the submerged object.

Lebreton and Cormault[52] applied the facet approach using the pulsating source solution to the problem of surface-piercing and non-surface-piercing cylinders. They were particularly interested in the interaction between adjacent cylinders. They found that if the cylinders were about 5 diameters apart the forces each experienced could not be derived from simple superposition of results for single cylinders.

Garrison and Chow[25] presented the basis of the general numerical approach for bodies of arbitrary shape. They evaluate the coefficients necessary both for finding the unknown source distribution and for calculating the resulting potential function in parallel. The forces and moments acting on the structure are then derived from the linearised Bernoulli equation. They overcome the problems associated with the singular kernel of the integral form of the pulsating source in the same way as Monacella[60].

Their numerical discretization consists of dividing the immersed surface of the object into many plane facets and assuming that a single unknown value of source strength is associated with each one. They make a number of simplifying assumptions which although consistent in the limit of small facet size do require a large number of facets for an accurate solution.

This method is the basis for a number of computer packages for the analysis of wave forces on large structures, for example Hogben and Standing[34].

The extension of this approach to the case of floating bodies is extremely simple being merely a slight modification of the boundary conditions. Faltinsen and Michelsen[22] consider this problem for large floating bodies and in addition show how the second order horizontal drift force may be evaluated.

The true dynamic problem of a flexing cylindrical cantilever has been solved by Eatock-Taylor and Waite[21] for the first two flexural modes.

After considerable application of this approach to real design problems it has become clear that it can be an extremely costly method in terms of computer time. One reason for this is the complexity of the fundamental (pulsating source) solution or Green's function. In either form it involves computations of Bessel functions for coefficients contributing to the fully populated matrix prior to solution. Invariably the time taken to calculate these coefficients far outweighs that required for solution of the equations.

Bai and Yeung [1] present a method, which has received little attention, which aims to reduce some of these problems by using a simpler fundamental solution and distributing sources over all boundaries to the flow. Although the number of equations is increased the reduction in overall computation time may be significant.

Another problem in the application of this method has been put on a theoretical footing for the particular case of a circular cylinder by Murphy [63]. This is the existence of certain irregular frequencies for which a solution is not possible by this method.

Ursell [77] has shown for the case of acoustic wave scattering (analogous to long water waves) that the fundamental solution may always be modified by the addition of a regular wave function to avoid this problem. An alternative is to distribute sources over an external ficititous boundary. Van Oortmerssen [67] and Boreel [9] have used this approach for the general water wave problem but little critical study of the problems of uniqueness has been made.

Much research has therefore been directed towards ways of modifying the approach to make it more economical. Black[8] and later Fenton[23] considered diffraction by objects with a vertical axis of symmetry. This method relies for its economy on the fact that only the first two terms in a Fourier expansion in polar co-ordinates will contribute to a net force. Discretization of the immersed object need only take place along an arbitrarily shaped generating curve.

Isaacson[40] and Harms[27] have considered the case of vertical cylinders of arbitrary cross-section. Isaacson starts from the three dimensional case and integrates the fundamental source along a vertical line to find the expression for a line source. Harms starts with the Helmholtz equation in the plan dimensions and utilises the known fundamental solution directly. Both approaches lead to the same numerical formulation and necessitate the discretization of the cylinder cross-section only. This approach is particularly appropriate for studying interactions between many cylinders.

Unlike the results from an experimental investigation in the Morison equation regime, the diffraction theory should agree exactly with experimental measurements on large structures provided the waves are of small amplitude. Measurements of total force on small cylinders in the diffraction regime have confirmed that $C_M = 2$. However, very few results are available for large cylinders.

Chakrabarti and Tam[15] considered the forces and pressures on a large surface piercing cylinder in long crested waves. Although the total forces are shown to agree well with the theoretical curve from McCamy and Fuchs the measured pressures are not so good particularly near the free surface.

Hogben and Standing[33] measured the forces and pressures on a square cylinder finding that vortex separation from the corners severely effects the measurement of pressure.

In addition, they found that second harmonic pressure fluctuations due to the finite wave height were significant but concluded that they were unlikely to affect the measured forces. They also showed numerically that superposition of diffraction forces for elements of a structure may be sufficiently accurate in certain circumstances.

Garrison et al[26] extended this idea to consider a gravity platform by using a diffraction analysis for the large base and the resulting velocity field for a Morison equation analysis of the legs. They found it necessary to include the velocity squared terms in calculation of the vertical force on the base even though the waves satisfied a linearized boundary condition at the surface.

Huntington and Thompson[37] used the powerful technique of linear spectral analysis to analyse measured forces on a large surface piercing cylinder in multi-directional seas in addition to long crested waves. In agreement with the experimental results of Hogben and Standing[33] the inline force and moment seem to be consistently over-estimated by the theory.

These and other experimental findings have highlighted the importance of non-linear effects caused by the free surface being in reality finite amplitude, particularly in the region where wave enhancement is caused by the presence of the structure.

Initially, this non-linearity was allowed for in the incident wave using a higher order Stokes representation without reference to the increased non-linearity in the presence of the structure. Chakrabarti and Naftzger[14] considered bottom seated structures in an approximate manner using Stokes 5th order waves and the full Bernoulli equation for pressure.

A more consistent approach of extending the first approximation for the potential to a second order has been shown by Isaacson[39] to lead to an inconsistency in the boundary conditions on the structure and the free surface if they meet at a place where the local curvature is cylindrical. Discussions by Venkatanarasaiah[79] and Garrison[24] merely serve to confirm the problem. There is therefore a need for accurate experimental investigation of the non-linear effects on large cylinders.

The Froude-Krylov force is due to that part of the pressure resulting from the ambient flow acting on the object boundary in its absence. It is therefore usually simple to calculate by integration of the known incident wave potential. The pressures corresponding to the flow scattering of the object require a solution of the governing equations in the presence of the object which is not so readily achieved.

Using first order wave theory Ckakrabarti[13] evaluated the expressions for the Frounde-Krylov force on a number of objects of symmetry which have associated co-ordinate systems which yield useful separation of variables. The additional force due to the presence of the object is then assumed to be proportional to the Froude-Krylov force so that the total may be represented by multiplying the latter by an initially unknown coefficient.

Wave scattering is assumed to be small since the objects are close to the bed and one order smaller than the wavelength. Wave scattering is certainly not linearly related to the Froude-Krylov force, being frequency dependent.

The values of the coefficients are then found by a best fit to the published data in the inertia regime. This yields an expression for the force which is compared graphically with the experimental data from which it was derived. Only one set of data was used for each object so that the superficially good agreement is not surprising. For the horizontal circular cylinder the agreement is however remarkably good even though the coefficient, which for this shape is equivalent to the inertia coefficient in Morison's equation, takes a value 2.1. The position of this cylinder relative to the bed is unclear but since the depth to diameter ratio is 3, then blockage effects must be significant and are unlikely to be linear. The high value of the vertical force coefficient for the rectangular block (6.0) is extremely doubtful because of the effects of separation, as the comparitively large scatter confirms. A high value implies that the major part of the force results from the presence of the object. The assumption of simple porportionality to the Froude-Krylov force is in this case a gross over simplification. The vertical force will depend on complicated interactions between vortex shedding from the sharp edges, and the eddy size to object length and fluid particle trajectories. As suggested above, the inertia regime will probably never exist in this case. It would have been useful if estimates of precision were given for the coefficients. It would then be possible to see if the accuracy of the mathematical evaluations was warranted or whether a straight forward Morison equation inertia term would have sufficed.

Certainly none of the objects was too large to invalidate this approach. In fact, it is probably possible to calculate the exact results using Haskind's relations.

Considering the case of waves on water of infinite depth Havelock[29] shows that if all bounding surfaces are vertical, the governing equation reduces to a Helmholtz equation for the scattered potential, for which the solution is a series of Hankel functions. One of the special boundary surfaces for which a solution is shown is that of a vertical circular cylinder. The velocity potential is constructed from a Bessel function expansion of the incident wave and an expansion in outgoing circular waves the coefficients of which are chosen to satisfy the kinematic condition on the cylinder. Wave amplitude ratios for positions at 45^{o} intervals around the cylinder are quoted from which it can be seen that as the wavelength approaches the radius of the cylinder the amplitude ratio on the front face approaches 2. The results for a parabolic cylinder are shown to lead to the surprising result that the amplitude ratio is constant along the boundary for a given wave. As a result a possible simple expression for run up at the bow of a ship is proposed.

Subsequently, calculations of pressures, to second order, on a plane wall are performed. It is clear from these that the arbitrary function of time in Bernoulli's equation is generally non- zero to second order but reduces to zero to first order, rather than being absorbed into the potential as usually stated. Clearly a fluctuating pressure without a spatial gradient can generate no net forces on completely submerged objects, nevertheless it contributes to a second harmonic term which obviously does not decay with depth in the usual way and is probably responsible for the problems encountered by Hogben and Standing[33].

Following rigorous calculations, Havelock shows that the results for pressure on a plane wall may be more simply derived from the reversal of momentum flux by total reflection.

Analysis of the additional force on a circular cylinder to second order is shown to lead to an infinite series of cross terms between Bessel functions of adjacent orders (see also Lighthill[54]). For short waves the limiting behaviour of the series is shown to be the same as assuming complete reflection from the front half of the cylinder only, using the previously derived expression for a plane. He concludes that since his results nowhere exceeds this limit (coming close at $\lambda/D = \pi$) that it may be an upper bound even for longer waves. Without an efficient computing machine he is only able to calculate five values. It is quite possible in view of their irregular nature that intermediate results do exceed this limit.

MacCamy and Fuchs[58] extended rather simply the results of Havelock for a fixed circular cylinder in deep water to the general case of finite depth. Since in this case the vertical variation is still separable, the only difference is in the introduction of a hyperbolic cosine function to satisfy the kinematic condition on the bed. The pressure from the linearised Bernoulli equation and hence, the total force per unit length are then simply derived. A consistent expression for total moment is then calculated by integration to still water level.

They continually work in terms of the force per unit length but it must be remembered that the only body for which their results are valid is the vertical circular cylinder. For small diameters their results reduce to the Morison equation expression with $C_M = 2$ when drag force is negligible.

They then embark on a somewhat circular argument which seems wrong in principle but rather fortuitously arrives at the correct answer. Havelock had shown that for short waves the cylinder acts as a perfectly reflecting plane (locally), so that the total result may be derived by assuming that the hydrodynamic pressure on the structure is twice that in the ambient flow. MacCamy and Fuchs attempt to use this approach for long waves. They double the ambient pressure and then integrate it around the cylinder arriving at the correct result, fortuitously, because in this case the added mass force is equal to the Froude-Krylov force. This is unlikely to be a general result, as they conclude. It seems wrong to assume that for large wavelengths the effect of the cylinder is a perfect reflector, particularly as in the limit the cylinder does not radiate any wave energy. Consideration of, for example, the thin flat plate (for which the Froude-Krylov force is zero) would seem to confirm this.

In a review of the state of the art of the dynamics of offshore structures Eatock-Taylor[20] attempts to group all the methods of analysis within a unified framework. This makes it easier to demonstrate that the vast majority of so-called dynamic analyses have been in fact quasi-static. The true dynamic amplification terms are clearly identifiable and distinct from the quasi-static loads which include the effects of rigid body motions. He points to the increasing importance of true dynamic analyses as structures are placed in deeper and deeper water (120m +) since the increased structural element lengths imply a lowering of the lowest fundamental frequencies towards those of typical ocean waves.

It appears that the only non-linearities associated with wave-structure interaction which have been studied are those arising from the drag term in Morison's equation. The unified framework relies on the linearity implied by small structural displacements. Finally, the importance of modelling the structure-foundation interaction is stressed since it contributes to a further lowering of the overall fundamental frequency. It seems that a great deal of work is required on true dynamic flexural problems.

Newman[65] presents a version of Haskind's relations, which have received little attention since they were originally presented in Russian. The approach may be summarized as follows. What are sought are the exciting forces on a submerged body which may be considered as comprising the Froude-Krylov component (due to the incident wave only) which is easily calculable and the force due to the scattered potential, which is initially unknown. If it is accepted that the effects of the locally generated scattered and radiated potentials die out at infinite depth then Green's second identity may be used to relate these potentials in a way which may be interpreted as a statement of the principle of virtual work.

'The forces due to wave scattering acting through the displacements due to body motion are equal to the forces due to body motions acting through the displacements due to wave scattering'.

This, when used in combination with the kinematic condition on the body gives an expression for six total exciting forces in terms of the six virtual rigid body motions.

It is important to recognise that being a statement of virtual work its application is not restricted to bodies where the rigid body motions are physically meaningful. Therefore Lighthill[54] has applied this approach to the case of second order forces on a vertical circular cylinder rigidly connected to the sea bed.

To reconcile this virtual work statement with Green's second identity, since it is actually a statement of rates of work, for forces and displacements read potentials and velocities respectively.

Thus the six exciting forces may be expressed wholly in terms of radiated potentials and the incident wave potential. Newman makes a final simplification by a further application of Green's theorem to the region between the body and an external cylinder in the far field. This enables the final result to be evaluated in terms only of the far field behaviour which is often considerably simpler to derive than the near field.

Although at present, Haskind's relations have only been used for total exciting forces, it seems possible that they may be just as widely applicable as in the corresponding structural engineering case.

In a remarkable two part paper John[47] tackles the various problems of uniqueness associated with floating bodies. The second part is of direct relevance, in which he derives a series form of the Green's function. Assuming that the motion is simple harmonic, he defines a 'wave function' as a complex function which satisfies Laplace's equation and all the linearized boundary conditions outside a bounded region but with unprescribed behaviour at infinity.

He then shows that any wave function may be uniquely decomposed into an everywhere regular wave and a wave satisfying the Sommerfeld radiation condition. These two waves may be intuitively identified with the incident (primary) and the scattered waves respectively. He further shows that the regular wave may be expanded in terms of Bessel functions of the first kind and that the scattered wave may be expanded outside a circular region in terms of Hankel functions. The first term of this latter expansion consists of outgoing finite amplitude waves at infinity and is called the secondary wave. The other terms in the series called local waves satisfy the radiation condition trivially by dying out at infinity. Radiated energy is therefore carried out to infinity only by the secondary wave.

Because of his use of cylindrical harmonics John only attempts to prove uniqueness for a limited class of bodies of convex shape which break the free surface.

As a consequence of the uniqueness theorem, 'there is only one wave function which satisfies the radiation condition and that is the Green's function', the derivation of the simple singular wave function leads to a Green's function which automatically satisfies the radiation condition. This is in contrast to the derivation by Wehausen and Laitone [84] of the pulsating source solution (Green's function) where they do not introduce the complex plane and are therefore forced to ensure that their solution satisfies the radiation condition separately.

Lebreton and Cormault[52] use the pulsating source in an application of the so called facet method. They present John's theory in a form which yields the added mass and linear damping coefficients. Working in terms of transfer functions relating the free surface elevation to the force on cylindrical piles they show how the function is modified by the

presence of another pile. This presence can lead to considerable constructive or destructive interference depending on the ratio of separation distance to wave length. This was particularly so for the orientation of piles where one sheltered the other (enhancement of up to 24%). They also considered vertical circular cylinders truncated below the free surface concluding that the inertia coefficient approaches one as the height of the pile reduces for quite a wide range of ratios of wavelength to diameter. Very little detail of their numerical procedures is shown which makes it very difficult to draw any firm conclusions, particularly in view of the singular behaviour at the pile top.

Garrison and Chow[25] present the details of a numerical application of the pulsating source to the problems of hydrodynamic forces on submerged objects. They show how the total potential, which is assumed to be time harmonic, may be split into the incident and scattered potentials which are complex. The scattered potential is expressed in terms of an initially unknown distribution of pulsating sources on the surface of the object. An integral equation for the unknown source strengths at the centroids of a discrete number of plane facets is formed by satisfying the kinematic boundary condition on the object.

Once the source strengths have been found the total potential and hence all the other variables of interest may be found by back-substitution.

They discuss a number of problems associated with the detailed numerical application of the theory. The integrand of the fundamental solution is singular within the domain of integration at a point corresponding to the real root of the dispersion relation.

This is a simple singularity however, which may be subtracted out using the scheme proposed by Monacella[60]. Another problem is associated with the singular nature of the pulsating source. The effect of this on the integral equation has been accounted for by the limiting process which leads to the diagonal terms. During the back-substitution the source strength is assumed to be distributed uniformly on each facet and the local behaviour calculated as if the object was in an infinite fluid in all directions. Since the behaviour of R^{-1} dominates the local behaviour this will be correct in the limit of small facet size.

They validate their program using the result for a heaving sphere of Havelock and the MacCamy and Fuchs solution for a vertical circular cylinder. The reported accuracies are subsequently improved still further by the correction in their closure, which therefore suggests that perhaps too many facets were used. Finally, the results of an experimental investigation on a submerged oil tank are shown to agree very well with the corresponding numerical results. They do mention the importance of the velocity squared terms in the case of steep waves.

In Studying the far field pressures due to oscillation of a slender ship in waves Monacella[60] encountered the problem of the singular integrand in the Green's function. He evaluates this in what appears to be a fairly standard way by subtracting the simple singularity to leave an integrand which is well behaved throughout the domain. It is however, indeterminate numerically without resorting to a limiting procedure at the singular point. The three eighths rule is therefore used to avoid the singular point. There are two points of additional interest in this paper.

Although his solution is only valid in the far field it appears that he could have made use of Haskind's relations to at least evaluate the exciting forces on the ship. He formulates his potential problem in terms of what might be called the direct form of Green's theorem relating potentials and potential gradients directly without the use of fictitious sources.

Hogben and Standing[33] have had considerable experience of using a program based on the method of Garrison and Chow and present some results of its application to truncated circular and square cylinders. In discussing their results they deliberately avoid the use of the diffraction coefficient since it is artificially affected by the zeroes in the Froude-Krylov force, preferring to quote both the total and the Froude-Krylov forces so that the additional effects of diffraction are clearly visible. They also present some interesting photographs of the behaviour of the flow around a square cylinder placed with one face normal to the waves. The inevitable separation at the rear edges leads to some interesting focusing effects which yield quite large discrepancies between theoretical surface profiles and those estimated from the photographs.

They compare their numerical results for the circular surface-piercing cylinder with those of MacCamy and Fuchs. These comparisons are made more interesting by the fact that they have not used too many facets. Even with 96 facets at wavelength/diameter ratio of about 1, when the facets are evenly distributed the results are quite poor. When they are concentrated near the surface, in this short wave case, the results improve 100% but are still not as close as the long wave results.

This is presumably because the piece-wise constant variation of source strength cannot accurately model the rapid exponential variation required. They also recommend that no less than 8 facets per wavelength be used for the same reason. For these short waves the ratio of circumference to wavelength is 3 so that with 24 facets per level only 4 vertically is obviously insufficient.

Clustering of the facets in one region although often improving accuracy may lead to unbalanced equations and numerical problems.

They then show how economies may be made by recognising regions where diffraction forces are likely to be insignificant e.g. more than $3\lambda/4$ below the surface, and objects whose size is too small for diffraction effects to be significant. They suggest that in certain configurations interference effects are quite small so that the total forces may be calculated from summation of elemental forces.

In a series of appendices they summarise Garrison and Chow's approach in detail leaving no doubt over the numerical procedures involved. Several time saving checks have been included in their formulation to curtail infinite series and tailor integration schemes to the expected variation of the integrands.

They were able, in the final appendix and in the subsequent discussion to present perhaps the most interesting results. They showed that the experimental results for horizontal force and moment on a truncated circular cylinder were less than their numerical results, with the error a significant proportion of the diffraction force. The experimental values of vertical force showed a 50% reduction in the diffraction force. This discrepancy was not explained.

It could be a complicated interaction between local energy loss in separated vorticity and the resulting wave height reduction. In the discussion they mention that the phenomenum of second harmonic pressure fluctuations with no spatial gradient was detected within their cylinder due to the local standing waves outside.

Faltinsen and Michelsen[22] use the plane facet method to evaluate the exciting forces and the added mass and damping coefficients for a floating box by splitting the total potential into that due to the incident wave plus a scattered potential from the stationary body and the radiated potentials from motion in the six degrees of freedom. They are then able to solve the full dynamic problem for motion of the box in these six directions. This indirect approach is necessary because the fictitious source strengths must first be found before the potentials may be evaluated.

It appears that in such problems, direct use of the Green's theorem relation between the potentials and their normal gradients may enable a more direct evaluation of the exciting forces.

In waves of finite height there is a net mass transport of fluid in the direction of propagation. This can lead to gross displacements of a floating body, since, a restoring force is absent in the horizontal plane. They show how these drift forces may be calculated to second order and present graphically their results for two boxes of equal plan area but different drafts.

In particular, they illustrate the reduction in the drift forces when the motion of the body is taken into account, except when dynamic amplification occurs. They also contrast their three dimensional results with a finite strip program which generally gives poor results but underestimates the yaw added mass in particular. It is important to realise that even though the body may be freely floating the dynamic analysis relies on the linearity implied by small displacements from the mean position.

Following on from the review paper above[20], Eatock-Taylor and Waite[21] show how the true dynamic problem of a flexible body whether fixed or floating may be split into the structural dynamics in vacuo and the fluid boundary value problem. This split again relying on linearity. The modal analysis is therefore based on the mode shapes of the structure vibrating in vacuo. This corresponds to keeping the fluid added mass and damping forces on the forcing function side of the dynamic equations.

They make use of Green's theorem to remove the necessity for evaluating the diffracted potential(Newman[65]) but do not see the possibility of using it for solving the numerical problem. Instead they use the facet method in its usual form. For the particular cases of a vertical circular cylinder and a vertical frustum of a cone they show how the first couple of flexural modes may be calculated. The cross coupling between these modes caused by the presence of the fluid is seen to be significant.

In a remarkable dual-theme paper Bai and Yeung[1] present a comparison of the modified variational finite element method and the fundamental singularity distribution.

The variational method is modified by virtue of the fact that the domain is split into an outer region (truncated at a suitable radiation condition boundary) in which the solution is expanded in cylindrical harmonics (for 3-D) and an inner region in which the advantages of the F.E.M. discretization are utilized. The inner region therefore allows for the change from a region in which the horizontal and vertical dimensions are separable, to the region dominated by the arbitrarily shaped body and bed boundary conditions.

They then present a novel alternative to the traditional facet approach (referred to by them as the Green's function approach) using only the fundamental point source solution for an infinite fluid. This function is much simpler than the constant depth Green's function in particular being purely real. Because it does not satisfy any of the boundary conditions, application of Green's theorem to the domain results in an integral equation for the potential over the whole boundary. Since solution of the discretized equation yields the potential on the boundary, their approach may be interpreted as a direct boundary element method. The only complex terms in the equations arise from the necessary radiation condition at the outer boundary.

They attempt a comparison of the computer time necessary for a solution using several different numerical approaches which appears to show that this new fundamental singularity approach is three times as expensive as the Green's function method. They conclude by suggesting that a modification using eigenfunction expansions in an outer region along the lines of the variational approach might yield similar savings.

It is surprising, in view of the possibility of coping with variable bed topography, that this approach has received little attention. Certainly no one who discussed the paper seemed to appreciate the direct nature of the equations. It is not made clear in the paper that the comparison is based on the time taken for solution of the equations. In the usual facet method there is considerable extra computation involved in order to evaluate the fluid pressures on the body. The important point is made however, that the extension to higher order solutions via a numerical perturbation scheme is made much simpler by a knowledge of the potential on the free-surface.

One minor advantage of the fundamental singularity method is that there is no possibility of encountering the so called 'fictitious frequencies' which affect the short wave solutions of the Green's function method. Murphy[63] shows that the potential representation in terms of a wave source distribution on the surface of a circular cylinder fails whenever the incident wavelength and the cylinder diameter are related by

$$J_n \left(\frac{2\pi a}{\lambda} \right) = 0 \qquad 2.2.1.$$

The lowest root of this equation is however when

$$\frac{2a}{\lambda} = 0.77 \qquad 2.2.2$$

So that for most practical cases this is not a problem. It can however pollute a spectral analysis, which would normally extend to such frequencies. Murphy shows that these roots arise from the existence of non-trivial solutions to the associated homogeneous form of the integral equation.

Ursell[77] has shown for the exterior acoustic wave problem (the governing Helmholtz equation arises from any diffraction problem in which the vertical variable is separable and also in the long wave approximation) that it is possible to redefine the fundamental solution in such a way that the source representation never fails.

He first shows that - in the usual method - the exterior Neumann problem will not possess a solution whenever the wave number corresponds to one of the eigenvalues of the interior Dirichlet problem, and vice versa. The kinematic boundary condition for the exterior diffraction problem makes it a Neumann problem and it can be seen from e.g. Lamb §191[51], that the interior Dirichlet problem for a circular cylinder has eigenvalues at

$$J_n(ka) = 0$$

confirming Murphy's result.

To understand the way in which Ursell removes this problem it is important to appreciate the distinction between the physical problem and its mathematical realisation. Once found, the mathematical solution consists of two parts. The unique exterior solution corresponding to the real physical problem (in this case) and an interior solution to the interior problem as defined. These two mathematical solutions exist together and influence each other. The presence of a free surface in unsteady flow enables non-trivial solutions of the Helmholtz equation for completely homogeneous boundary conditions (eigenfunctions).

In the Green's function method these interior solutions correspond to forced oscillations in a closed tank, and failure of the method, to forcing standing waves at a natural frequency.

To remove the difficulty Ursell therefore redefines the mathematical interior problem by introducing an additional ficititous boundary on which a Newton (dissipative) condition is to be satisfied in the form

$$(\frac{\partial}{\partial n} + K)\phi = 0 \qquad 2.2.3$$

This has the effect of disallowing any non-trivial solutions of the homogeneous interior problems. Ursell shows that a Green's function may be found which satisfies this additional condition in the form

$$G = G_0 + \Gamma \qquad 2.2.4$$

where Γ is an analytic wave function everywhere except at the centre of the interior, and G_0 is the usual Greens function.

An alternative approach is used by van Oortmerssen[67] in which it is assumed that the exterior problem may be analytically continued across the physical boundary into the interior. The singularity distribution may therefore be placed on a fictitious boundary inside the real boundary. This reduces the problem to solution of an integral equation of the first kind for which the only homogeneous solution is trivial.

The important difference between this approach and that of Ursell is that it places a further restriction on the class of problems which may be solved since singular behaviour between the real boundary and the fictitious one can not be accommodated.

Van Oortmerssen uses this method to study the mooring forces on large ships. As a test problem, he compares the results of the numerical analysis with experimental measurements of total force on a square cylinder on top of a pyramid. The agreement is not good and is clearly not due to experimental scatter, since the experimental results appear to lie on a curve distinctly different from the numerical results. The sharp corners on the real boundary of this object make it necessary to accommodate the possible singular behaviour to obtain a unique solution. Hogben and Standing[33] also showed that the presence of vortices separated from the corners in the real problem leads to large discrepancies in the free surface behaviour. These may be masked to a certain extent by a comparison based only on total force.

The motives for separating the singularity distribution from the real boundary are 1) the increased numerical accuracy, 2) the avoidance of the singular behaviour and hence the necessity of using the integral form of the fundamental solution and 3) the consequent reduction in computer time.

Using the same numerical and physical model as Van Oortmerssen, but with the pyramid completely immersed Boreel[9] concentrates on experimental measurements of pressure at six points on the plane.

By rotating the model he was able to do a complete pressure traverse. The agreement between experimental and numerical pressures is only good sufficiently far removed from the effects of the moving free surface. The water depth was 0.9m whereas the highest pressure tapping on the body was 0.4m below the surface. Even so the measured pressures are significantly higher than the numerical results, increasingly so as the frequency (and hence probably the wave steepness) increases. Unfortunately, there are at least two possible reasons for this. One is that complete neglect of the inevitable singularities at the sharp edges of the body renders the numerical solution particularly suspect close to these edges. The other is that the experimental wave heights will never be infinitessimally small.

No critical discussion of the pressure results was attempted, which was a shame, becausethey are quite remarkable by their consistency. Detailed inspection of the 'scatter' in the experimental results shows that it is in fact largely due to systematic error, because the pattern of scatter is the same for each pressure tapping. This maybe attributed directly to the effects of different finite wave heights. The width of the tank is not given but it is always possible that interference effects (blockage) between the real structure and its infinite series of images in the side walls can lead to increased (or decreased) wave heights close to the structure in the same way as reported by Lebreton and Cormault[52] and Isaacson[40]. The major cause of scatter is more likely to be finite wave steepness (a parameter given no consideration in a linear theory). This may be concluded from comparisons of the results for total force when the waves approach either normal to a face or at 45^{o} to each face. The pattern of scatter in both cases is identical, although the blockage effects would be expected to be significantly different.

This emphasises the importance of reporting wave height (or steepness) results so that non-linear effects may be identified, particularly as the major contribution to the force arises from the region close to the surface.

A much greater economy may be achieved by reducing the dimensions of the problem still further.

By using a fundamental solution which is a Fourier expansion in cylindrical co-ordinates Black[8] shows that vertical axisymmetric problems may be solved as a series of Fourier component problems. Fortunately, because of the symmetry only the first two terms are needed for evaluation of the total force which significantly reduces the necessary computation, unless pressures are required. He suggests that his fundamental solution is non-singular whilst at the same time, satisfying a Poisson equation, calling it a source and allowing for its singular behaviour on the real boundary when formulating the integral equation.

This integral equation is expressed in direct form but approximated by a piecewise constant distribution along the boundary. It is applied to the two classical problems of the floating sphere and the vertical circular cylinder, exhibiting excellent agreement. Black mentions that this good agreement is obtained using only eight unknowns, chiefly because of numerical convergence difficulties associated with the apparently singular behaviour of the Green's function. This would place a severe restriction on the geometrical complexity which this method could accommodate. Even so, the results for a truncated circular cylinder are remarkably good, even without allowance for the likely singular behaviour at the top edge.

The importance of his results is the great saving in computer time - 60 times less than the method of Garrison & Chow[25].

Fenton[23] using essentially the same approach only in indirect form, shows the singular nature of Black's Green's function and explains the consequent problems of numerical convergence. By making use of an important relation for the Bessel functions (Graf's addition theorem) he is able to express John's Green's function as a Fourier expansion in cylindrical polar co-ordinates. For the singular Bessel functions (Y_0 and K_0) this is achieved by splitting the domain in two so that the singular behaviour of each individual function is never encountered. This led Black to suppose that the singular behaviour of the total function had also disappeared. Fenton shows however, that it is only hidden in the infinite series which are at least logarithmically singular. It is to be expected that redefinition of the co-ordinate system cannot remove the singular behaviour.

Having established the nature of the singularity Fenton shows how it may be subtracted from the Green's function and its contribution evaluated in closed form leading to much quicker convergence of the series expressions close to the singular point. This leads to a further saving in computer time which Fenton estimates to be 800 times less than for a three dimensional body.

One further way of reducing the dimensions of the problem is to separate out the vertical dimension. This may be achieved in those cases where the immersed body is motionless and its boundaries are all vertical, i.e. for vertical surface piercing cylinders. Then the unknown potential satisfies a Helmholtz equation in the plan dimensions for which the fundamental solution is a Hankel function.

Attempting to show that this solution may be obtained from the three dimensional Green's function, Isaacson[40] shows that integration of a source distribution along a vertical line yields the Hankel function provided that the vertical variation of all quantities is as

$$\cosh k(y + d)/\cosh kd \qquad 2.2.5.$$

He does not make it at all clear that this assumption is only valid as a consequence of the separation of the potential into that due to the incident wave (which varies as 2.2.5.) and that due to the scattered wave which must therefore vary as 2.2.5. on the body to satisfy the kinematic condition there.

A more rigorous analysis along the lines suggested by Havelock[28] for the case of forced waves needs only the assumption that a source representation for the scattered potential exists for the vertical variation of source strength to be as 2.2.5. for diffraction by vertical bodies. It becomes clear when following this analysis that the radiated potential due to sway or surge cannot be similarly solved without including the local waves (terms which vary as $\cos k_n(y + d)$.

Isaacson goes on to show how the resulting line integral equation may be numerically solved using a piecewise constant source distribution. This formulation was verified against the MacCamy & Fuchs solution for a circular cylinder. The comparison showed that an accurate evaluation of total force was easily obtained to within 1% using only 8 equations.

The run up on the front of the cylinder was however 50% in error. The artificial numerical symmetries of this particular problem make it a less severe test of a numerical method. Not only should a comparison of total force be made but also the potential on the body.

Harms[27], using a virtually identical numerical formulation to that of Isaacson, shows in some detail how the integral equation may be solved. He then concentrates on showing that the influence of body shape extends over quite a small region close to the body. The far field behaviour is however only a function of body width and orientation. A simple way of evaluating far field effects is therefore obtained by a superposition of two diffracted wave trains emanating from the extremes of the body. This represents a considerable economy for such problems as coastal protection in the lea of offshore breakwaters.

An experimental investigation of the diffracted wave pattern encountered severe difficulties in generating long crested waves, the wave amplitude varying typically by 50% along the crests. Nevertheless, measured wave heights in the lea of the breakwater were significantly higher than the theory suggested. He concludes that the increasing discrepancy with distance from the body could be attributed to the effects of finite wave steepness. In view of the three dimensional nature of the incident wave train any firm conclusions are difficult to justify. Finally, the mathematical model is applied to a problem for which no verification is attempted to show the type of geometries which can be accommodated. Since no mention of singular behaviour was made the two sharp cusps on the boundary of the chosen cylinder render the numerical results highly suspect.

It is well known that finite height deep water waves are unstable to small perturbations , which vary slowly enough (Benjamin and Feir[3]. The wide piston type generator used here is unlikely to be able to escape this problem, particularly as the wave depth parameter kd used in these experiments was well above the maximum value for stability of 1.363 (Whitham[86]), being 2.45.

An experimental study of the forces and pressures on a large vertical circular cylinder in waves was conducted by Chakrabarti and Tam[15]. They present without correction the theoretical derivation of the diffraction force from MacCamy and Fuchs[58], making the same mistaken use of the Hankel function of the second kind, in combination with a negative imaginary time constant. However, they obtained the correct result for total force and moment. They showed that the results may be discussed in terms of a diffraction coefficient C_h or a C_M coefficient defined in a similar way to the inertia coefficient in Morison's equation. The diffraction coefficient C_h is defined as the ratio of total force to Froude-Krylov force. It has not gained widespread popularity because of its artificial variation with increasing wave number. Although the two coefficients approach the same long wave limit of 2 as the wave number reduces, the diffraction coefficient approaches infinity whenever the Froude-Krylov force is zero, this behaviour being different for different shaped objects.

The experimental measurements of pressure are made using differential pressure transducers for increased sensitivity, by flooding the interior of the cylinder from below. Unless correct allowance is made for the oscillations of the internal free surface, the experimental accuracy is severely affected. To establish that non-linear effects were negligible they plotted maximum force against wave-height for two fixed frequencies. Using a least squares fit through three data points

they apparently seem convinced of the linearity of their results. In such a situation the fit should be heavily weighted to pass through the origin. When this is done, on their graph, there is clear evidence of increasing non-linearity with increasing wave height.

The pressure results are inconclusive and are certainly not critically discussed. Some quite large discrepancies are evident in both vertical and horizontal distributions. The agreement between measured and theoretical force is good for all the quoted results but it is clear that the results have been selected.

It was mentioned above that in a similar experimental situation Hogben and Standing[33] observed genuine second harmonic components in the pressure field which extend to the bed without decay (Longuet-Higgins[55]). Chakrabarti and Tam do not appear to have taken account of these effects. In a later review paper Hogben and Standing[34] mention them again, as well as concluding that not much good experimental data exists for short waves. If investigations are being extended to the second order then a clear understanding of these fluctuating pressures in the presence of standing wave energy is necessary.

Garrison et al[26] analysed the problem of a typical gravity platform with a large base and smaller vertical surface piercing columns using the method suggested by Hogben and Standing[33]. A diffraction analysis of the base alone was used to calculate the modified velocity field on the centrelines of the columns. The force on the columns was then estimated using Morison's equation with $C_D = 1$ and $C_M = 2$. Because the columns are still large compared with the wavelength the drag component makes a negligible contribution to the total force and may even have more accurately been neglected, since the Keulegan-Carpenter number was about 2. The use of $C_M = 2$ for each individual

column was justified on the basis of a steady flow result which showed negligible interference for the spacing of between 4 and 6 cylinder radii. The interference effects caused by wave diffraction are certainly not negligible in this case, and could easily account for the increased experimental results compared with the theory. The results of Lebreton and Cormault[52] show, for a spacing of 10 cylinder radii, that the interference effects at $ka \doteqdot 0.15$ (which is the value appropriate to this case) are of the order of 10%. Nevertheless, the comparison of the predicted results with those of an experimental study at 120th scale shows remarkable agreement, and confirms the assumption of negligible inter-action between columns and base.

Huntington and Thompson[37] used random waves to test the transfer functions derived from linear theory for pressures, forces and moments on a vertical circular cylinder in the inertia/diffraction regime. In general, the agreement between experimental pressures and theoretical predictions is excellent. Close to the free surface however the discrepancies increase so that the total force and moment results are over-estimated by about 20% at the peak spectral frequency. Although this is in agreement with the regular wave results of Hogben and Standing no explanation is attempted, it being fortunate that the error is conservative. In order to identify any non-linear effects of wave height each spectrum was used with significant wave heights in the ration of 1 : 2 : 3. What is remarkable is that all the results for total force fall on the same curve consistently below the theoretical curve, with no evidence of non-linearity. The error is evidently of first order.

An attempt to allow for the effect of non-linear waves was presented by Chakrabarti and Naftzger[14] for the special case of bottom seated structures. For these it is assumed that the scattering effect of the structure does not extend to the free surface so that it is only the incident wave which satisfies the correct non-linear boundary condition taking the form of a Stokes fifth order wave. However, it seems likely that the scattering of the first order component will be modified at least to second order by the free surface, and so on through the orders. This suggests that the results become increasingly doubtful to higher orders and fifth order results (being typically 10,000 times smaller than first order) must be extremely inaccurate.

A more consistent approach is to extend the complete boundary value problem to second order by letting the total potential satisfy the correct non-linear boundary condition. Isaacson[39] showed that for objects which pierce the still water surface at least locally as a circular arc, the boundary conditions on the free surface and the body are inconsistent where they intersect; to second order. Subsequent discussions of this paper only served to confirm the existence of an inconsistency. However, subsequent papers, notably Hunt and Baddour[36] have suggested that although certain derivatives of the second order potential may not exist at this point a solution may still be obtained. It is worth remembering that Lighthill[54] obtained an expression for the second order correction to the total force without difficulty and without having to evaluate the second order potential.

At the time of writing,the problem is by no means resolved. It seems appropriate here to point out some facts which have been consistently neglected by the various authors.

Havelock[29] showed for waves incident on a plane vertical wall, that the arbitrary function of time in Bernoulli's equation is non-zero to second order, to satisfy the free surface boundary conditions. Longuet-Higgins[55] generalised this result to show that in the presence of standing waves, a second harmonic pressure fluctuation occurs, throughout the fluid, in proportion to the square of their amplitude. A non-oscillatory term in this function can also occur if the boundary conditions are satisfied at still water level which implies a distinction between mean and still water level which is often misinterpreted (e.g. Wiegel[87], pp. 29 - 31). Whitham[85] has shown clearly how these two phenomena are inextricably linked with the consequences of placing the origin of coordinates in the mean water level. Phillips[68] and Longuet-Higgins and Ursell[57] show in slightly different ways how the correct second order pressures may be derived from a balance of vertical momentum using first order results.

Without exception the researchers in the field of second order wave forces on vertical cylinders have assumed that the arbitrary function of time in Bernoulli's equation may be absorbed into the definition of the velocity potential. This is perfectly acceptable, provided that subsequent analysis does not preclude the inclusion of arbitrariness in the solution. For example, the widespread use of complex variables, forces the potential to be periodic or constant.

A better procedure would be to consider the periodic solution as a particular solution to which must be added, for generality, a function of time to satisfy the boundary conditions. So far, this step has probably been ignored because (fortuitously), for first order problems (and second order free waves) this function is in fact zero.

It is clear from the solution of MacCamy and Fuchs[58], that standing wave energy does occur around the cylinder, increasing with the frequency of the incident waves as the cylinder becomes more and more efficient as a reflector of waves. Since the waves are steepened in front of and flattened behind the cylinder, a resultant force exists by implication, even though to second order there is no spatial gradient. However, Cooper and Longuet-Higgins[19] demonstrated clearly for an infinitely long partially immersed vertical barrier that the so called second order contribution to the total force was more than twice the first order contribution.

2.3. Numerical analysis of boundless continua

Following the introduction of the weighted residual method for transforming the differential field equations into integral form, the finite element method (FEM) has developed rapidly into a powerful numerical tool for analysing continuum problems. Problems including material and geometric non linearities, inhomogeneity and time dependence may all be solved with varying degrees of complexity (Zienkiewicz[91]). Complicated boundary geometries may be easily accommodated, using higher order interpolation polynomials.

However, the FEM can prove inefficient and costly for solving those problems for which the region of interest is concentrated in one part of the domain. This is because the whole domain must be discretised reasonably uniformly to obtain reliable results. If one or more of the boundaries is so far away as to be mathematically at infinity, the domain must be artificially truncated and convergence of a norm of the solution examined as the fictitious boundary is moved outwards. This becomes particularly costly for three-dimensional problems.

The boundary value problem corresponding to the physical problem of wave forces on structures in the oceans is characterised by the fact that the solution must satisfy boundary conditions at infinity. A more economical approach to the numerical solution of these problems is to partition the domain into a near field in which the effects of non-linearity, inhomogeneity and/or geometric complexity are contained, and a far field in which the field equations take on a particularly simple form.

Working within the framework of the existing F.E. methodology Bettess[5] proposed a special 'infinite' element which relies on an assumed form of the far field behaviour of the solution and is used to model the effect of the infinite domain on the near field finite element discretisation. This special element possesses many of the advantages of normal elements and in particular, does not affect the symmetric, banded nature of the simultaneous equations.

For the three-dimensional problem of wave refraction by a parabolic shoal Berkhoff[4] showed how the field equation could be reduced to a wave equation in the plan dimensions. He then split the domain (the horizontal plane at still water level) into the region over the shoal, which he discretised using finite elements, and the far field in which the depth could be assumed constant, so that the field equation reduced still further to a Helmholtz equation. Using a singular distribution of Hankel functions on the fictitious boundary between the two regions to model the far field behaviour, he was able to obtain the strengths of these wave sources by satisfying straightforward juncture conditions.

Another method of allowing for the far field behaviour was used by Chen & Mei[17] for the problem of wave forces on large floating harbours. The fictitious boundary is deliberately chosen as a circular cylinder so that the far field solution may be expanded as a Fourier series of cylindrical harmonics which being singular only at the cylinder axis cannot suffer from the problem of fictitious frequencies. The coefficients of this series become additional unknown parameters.

Using the same finite element formulation as Berkhoff, Bettess and Zienkiewicz[6] demonstrated how their novel 'infinite elements' could be used to model the far field behaviour of the scattered waves from an inner region in which refraction was modelled using finite elements. The method used by Berkhoff for the far field can in fact be used to solve the whole problem provided refraction effects are negligible. In these cases, the singularity distribution is placed on the physical boundary and discretised to enable numerical satisfaction of the boundary conditions. Before discretisation, the boundary conditions yield integral equations of Fredholm type for the source intensity function. In the past, mathematicians have been able to prove existence and uniqueness theorems (with limited success) by assuming the intensity to be piecewise constant and examining the limiting behaviour of the solutions of the resulting matrix system as the number of equations increases (Jeffreys & Jeffreys[46] p.167). That this same system of equations could be used in finite terms as a basis for the approximate solution of potential problems was demonstrated by Jaswon[43] and Symm[76], although, at the time, the FEM proved more popular. They showed that the reduction in the dimensions of the problem lead to a smaller system of equations, which were in general fully populated. Any linear problem for which a complete set of independent fundamental solutions is available is amenable to this approach. Oliveira[66] solved the problem of elastostatics using distributions of point loads on auxiliary boundaries external to the domain. Banerjee[2] used the same formulation for the problem of a plate embedded in a semi-infinite elastic half-space but distributed the surface stresses on the plate itself.

This technique was not totally new Naval architects (e.g. Havelock[29]) used a source distribution on the axis of a thin ship to solve the problem of wave forces. An analogous procedure became extensively used for thin aerofoils. Von Karman[48] used distributions of sources and doublets on the axis of revolution of simplified airship hulls to obtain pressure coefficients. Subsequently, aerodynamicists (Hess[31]) have tended to place the sources and point vortices on the actual body surface for maximum numerical stability. The main difference between these well tried methods and the Boundary Element methods (BEM) as reviewed by Brebbia and Walker[12] for example, is that the latter are couched in a form which can benefit from the knowledge gained in the application of FEM.

The established methods required the evaluation of a fictitious source distribution before any useful quantities could be evaluated. They are in that sense called 'indirect' methods. A more recent approach is that of discretisation of the integral relation between the essential and natural boundary conditions. For potential flow, this is derived from Green's second identity and for elastostatics from Betti's theorem. For a well posed potential problem, either the potential or its normal derivative is known (or some additional relation between them is prescribed) at every point on the boundary. If Green's identity is discretised by assuming the potential and its normal derivative to be piecewise constant on the boundary, then substitution of the prescribed boundary values yields a system of matrix equations for the unknown values directly. Formulations based on the use of such reciprocal formulae are therefore known as direct methods.

Because of their increased accuracy and ease of use, these direct methods have been gaining wide acceptance. Whichever method is used however, if values of potential or its gradients within the domain are required, they must be obtained by additional numerical application of Green's theorem once the boundary values are known.

Much of the research on wave forces on immersed objects has followed in the footsteps of established methods used by Naval architects. The thin ship theory has therefore lead to the singularity distributions of Garrison & Chow[25], Hogben and Standing[33], Eatock-Taylor & Waite[31] and others. With the notable exception of Bai & Yeung[1] they all use a piecewise constant distribution of source strength in an indirect formulation, thus necessitating considerable additional computation before the hydrodynamic pressures can be calculated.

Watson[83] for the case of elastostatics and Hess[30] in aerodynamics have shown two different approaches to the inclusion of higher order terms in the approximation for the direct and indirect formulations respectively. Both report significantly increased accuracy which allows a trade-off in the number of unknowns.

It is now becoming increasingly recognised that the FEM and the BEM may be most usefully employed in combination, primarily because of the (current) difficulty of solving non-linear problems using BEM and infinite domains using FEM. Zienkiewicz, Kelly and Bettess[92] have shown how the coupling may be accomplished without sacrificing the symmetry of the FE formulation. Shaw[74] has discussed how the use of a boundary integral equation as a natural boundary condition enables an extended variational principle to be obtained for the F.E. domain.

Walker[81] has shown how the problem of fluid-structure interaction may be modelled, using a more mechanical coupling of nodal compatibility conditions between the FE idealisation of the structure and the BE idealisation of the fluid.

Bettess[5] showed how a special element could be formulated for problems for which the domain extends to infinity. The usual Lagrange interpolation functions were multiplied by an exponential decay to account for the expected decay of the solution towards infinity. Since in most problems, the actual decay rate is initially unknown, an arbitrary decay length L was introduced. As an example of how this element performs in the one-dimensional case, he solved an ordinary differential equation for which the infinite behaviour was known to be as the inverse of the distance. The behaviour of the numerical solution was shown to depend significantly on the choice of decay length, with the decay being obviously too rapid to model the correct behaviour.

The degree of arbitrariness in the choice of L could have been reduced by minimizing the functional with respect to L as well as the other unknowns, although, this would have lead to a system of non-linear equations.

Because of the rapid decay of the interpolation functions, the far field behaviour could only be modelled at the expense of the nearfield and vice-versa. The best near field behaviour was shown to occur with a decay length of 2 for this particular problem.

The two dimensional problem of zero Reynolds number flow past a circular cylinder was then solved using a decay length of 2. The agreement of the numerical solution with the analytical solution is remarkably good. However, in this case, the behaviour is also R^{-1}, and no results are shown for other decay lengths. In the conclusion Bettess admits that this element does not give a true indication of the far field behaviour of the solution. It is at best a small improvement on simple truncation of the finite element domain, and should only be used as the last row of elements in a finite element analysis of an exterior problem. In most realistic problems where an analytical solution is not available, parametric variation of decay length will not give any indication of what is a reasonable choice unless minimization of an energy norm is achieved.

Although diffraction may be solved by a source method, and refraction may be estimated by following wave rays, the combined problem has always proved difficult (see e.g. Ippen[38]). Even in the absence of diffraction, the ray method fails in places where wave focussing causes a caustic to form. For combined diffraction-refraction Berkhoff[4] derived a general wave equation, on the assumption of a small wave steepness and small bed slope, by expanding the potential as a power series in terms of these two parameters. Although it is more general than the shallow water approximation (because it includes the effects of dispersion), it nevertheless relies on depth being small in comparison with the wavelengths of both the bed undulations and the fluid free surface. Identifying an outer region in which the depth may be assumed constant, for which the source distribution method is satisfactory, and an inner region in which a finite element formulation may be used, he concentrates on the details of the method by which these two solutions may be matched at the interface.

The finite element formulation is based on the functional corresponding to the above wave equation. It is therefore straightforward to include in such a functional an integral over the interface of the normal potential gradient as the natural boundary condition. In turn, this may be expressed in terms of the unknown source distribution for the outer domain to satisfy continuity of flux. Minimization of this functional can only yield enough equations for the values of the potential at the FEM nodes. Satisfaction of continuity of the potential at each boundary point yields just enough equations for finding the source strengths. The matrix equations are partitioned and solved in a way which makes maximum use of the banded nature of the FE terms.

It is clear, that use of a 'direct' numerical relation between the potential and its gradient on the interface would remove the need for indirect calculation of the fictitious source strengths.

With particular regard for economical engineering application, he shows how the calculations of refraction over a parabolic shoal by ray methods may be continued across the caustic using the ray results as a boundary conditions for the numerical model.

An excellent example of coupling far field and near field behaviour is demonstrated by Chen and Mei[17] for the case of long wave impinging on a large floating power station. Using a pseudo-variational representation they show with commendable clarity how the contribution from the outer region may be included as a constraint condition on the interface only. They use linear triangular finite elements inside the near field which contains all the floating bodies. By deliberately choosing a circular interface, the outer solution may be constructed from a Fourier series of Hankel functions singular only at the centre, combined with the known incident wave. The unknown coefficients of this series are combined with the unknown values of the potential at the nodes of the

FE mesh in a linear system of equations. The bandwidth of these equations is considerably increased by the constraint condition connecting all the interface nodes. They show an efficient partitioning of the equations that can lead to savings if Gauss elimination is used.

They demonstrate the excellent accuracy achievable with this approach for both the simple vertical circular cylinder and a semi-circular breakwater protecting an infinite straight coast for which they derive a new analytical solution. Finally, they analyse the floating harbour. They are unable (in a two-dimensional model) to model the sloping sides, but for the wavelengths they are using, the effect of breaking would be negligible, so the boundaries would act as perfect vertical reflectors. For bodies with sharp edges they show how the ideas used for far field behaviour may be used to enable matching of an inner singular series solution, satisfying the correct behaviour near the edge, with the FE mesh. This approach has been used in crack propagation problems in solid mechanics. It is of doubtful value in this case, since, in the physical situation the flow will almost certainly separate at such an edge. The effect of separation on such large structures is likely to be so small that they might just as well round off any edges in the mathematical model.

Using the same theoretical formulation as Berkhoff for wave refraction by gradual depth variation, Bettess and Zienkiewicz[6], solve a number of problems in which the fluid domain extends to infinity. Instead of a distribution of wave sources, they model the outer region using infinite elements for the scattered waves. The interpolation function in the infinite direction in these special elements was assumed to be the product of a Lagrange polynomial, an exponential decay term and a complex exponential term to represent the wavy nature of the potential.

The arbitrary decay length was chosen to give approximately the same decay rate as the first term in the series solution, when available. The actual decay of this term for large R is as $(R^{-\frac{1}{2}})$ but they do not indicate where they chose the best fit. It is clear from the results presented, that the numerical solution is increasingly inaccurate as the infinite elements are approached. In many cases the incident wavelength is so long that the scattered part of the solution is likely to be quite small so that they do not constitute a severe numerical test. The main disadvantage of this method of coping with infinite domains is the necessity of numerical integration over infinite elements. In practice, the element is truncated at a large distance but this computation still involves 32 sample points per element. The considerable advantage of this approach is that the values of potential on the interface between near and far field are no longer interconnected. The bandwidth of the overall matrix is therefore not increased.

A similar effect can be achieved using zoned boundary elements. In this case numerical integration along an infinite line might be necessary, but the correct far field behaviour would be included automatically. Watson[83] has used this for elastostatics, where the far field behaviour is monotonic decreasing. In waves the oscillatory nature of the far field behaviour makes numerical integration more difficult.

One of the first expositions of the boundary integral technique was made by Jaswon[43] and Symm [76] in a two part paper. This coincided with the rapid emergence of powerful digital computers whose absence had previously limited the methods of solution of integral equations.

In the first part Jaswon summarises the theoretical background to the equations of Fredholm type, suggesting that numerical solutions should be possible for both the indirect method and the direct method which he refers to as Green's boundary formula. He concentrates on the more difficult two-dimensional problem (because of logarithmic behaviour at infinity). In the second part, Symm shows how these integral equations may be approximately solved. He assumes for the indirect case, that the fictitious source distribution is piecewise constant along an inscribed polygonal approximation to the boundary. For evaluation of the resulting integrals, he uses Simpson's three point rule except when the boundary point and integration point are on the same element (i.e. terms contributing to the diagonal coefficients) when an exact integration is possible. A detailed investigation of the error bounds is performed on the Dirichlet problem of a notched circular cylinder. The maximum error which always occurs on the boundary is typically 4%.

Not long after the previous papers Oliveira[66] solved the problem of elastostatics using the Kelvin solution for a concentrated load in an infinite medium. He preferred not to present the theory in the form of integral equations but rather as a linear superposition of independent solutions. This is one of the few papers in which the fictitious force distribution is placed on an auxiliary boundary outside the real boundary. He is well aware of the limitations this places on his solution, but does not seem to be wholly motivated in this choice by a desire for increased accuracy. In fact, in all the examples cited, the auxiliary boundary and the real boundary are extremely close together. He seems only to be concerned to avoid the logarithmic singular behaviour of the Kelvin solution for small argument.

Another simple example of the application of the indirect formulation is shown by Bannerjee[2] for the problem of a plate embedded in an elastic half-space. By using the fundamental solution of Mindlin instead of Kelvin, the zero stress condition on the surface is automatically satisfied, thus removing the necessity of discretising the whole surface. The numerical agreement with the Boussinesq solution for a circular disc was shown to be better than 5%.

One of the earliest applications of the indirect boundary element method, as distinct from superposition of a small number of solutions was made by Von Karman[48]. He solved the problem of flow past airship hulls, by taking account of axisymmetry and so using Stokes' stream function. He considered the general problem of flow at any angle by splitting it into the flow along the axis and the orthogonal component. The perturbation of the former he represented by an initially unknown distribution of (piecewise constant) source strength along the axis and the latter similarly by a dipole (or doublet) distribution. The source strengths were then found which made the zero stream line pass through as many points of the actual body profile as there were unknown values. Once the flow is simulated, the pressure coefficients may be found. For the particular airship considered the results of this calculation were compared with measurements from an actual flight and the agreement shown to be excellent.

In an introductory review paper Brebbia and Walker[12] use the weighted residual formalism to show how the governing field equation of a boundary value problem may be couched in integral form. By successive integration by parts, they show how the finite element equations may be related to the direct boundary element method and then in turn to the indirect method. They then show that many of the techniques of finite elements may be usefully employed in boundary elements.

In particular, in the direct method the variation of the potential and its normal derivative on the boundary may be approximated by high order interpolation or shape functions, and curvilinear co-ordinates using these same functions may be used to specify the boundary shape.

A number of examples of the application of boundary elements are reproduced. In view of their statement that 'boundary' methods are generally more accurate than 'domain' methods it is interesting to examine this accuracy. Typical accuracy is shown to be about 4%. The plane strain problem of an anchor plate embedded in a crack in an infinite medium is particularly interesting. The distribution of tensile stress along a line through the crack side is plotted. Although, this stress will remain bounded up to the edge, the results stop mysteriously short. This is almost certainly because of the breakdown of the results as the boundary discretisation is approached. It was just such a problem which first suggested to the writer the use of an auxiliary boundary, since it is the boundary results which are usually of most interest.

Finally, for the problem of wave diffraction governed by the Helmholtz equation, they derive the boundary integral relation for wave height (say) from the direct BEM statement. The theoretical results of this section are extremely doubtful. One rather obvious solution of the Helmholtz equation is the plane progressive wave. It clearly (c.f. John[47]) does not satisfy the radiation condition at infinity. Any general statement of Green's second identity for this problem should, at least initially, include a boundary at infinity. This is primarily the reason for traditionally separating out the incident wave in such problems, and they have therefore derived a relation for the scattered wave only. Having assumed that the observation point is within the

inner region, they then use the asymptotic formulae for the Hankel functions as if it is a long way outside this region eventually producing the radiation condition. They have obtained this fortuitously because of the symmetry of the Hankel functions. The statement -

> " As a test to determine the adequacy of the radiation condition in representing a train of plane harmonic waves, the case with no solid cylinder was first studied"

makes it all the more surprising that the quoted numerical results for the cylinder run-up are closer to the analytical solution than those of Chen and Mei[17] who used a better approximation. In short, all that they have done is apply the radiation condition on the boundary of the finite element domain.

Watson[83] shows for three-dimensional elastostatics how the same shape functions used in two-dimensional finite elements may be used to interpolate over curvilinear surface boundary elements. It is frequently stated that an advantage of the BEM is that it can handle infinite domains easily. This sweeping generalisation is only true if the boundary surfaces of the domain are finite. Watson is interested in solving for the state of stress around the intersection of underground tunnels. Mathematically, the tunnel surfaces extend to infinity away from the intersection. Using an infinite surface element, he shows how a non-linear mapping of the infinite domain onto the range for which Gauss quadrature formulae are available, may be justified. This approach does not require any assumptions to be made about the far field behaviour save that it decreases away from the intersection.

Hess, co-author of one of the most well known papers on the numerical calculation of potential flow problems in the field of aerodynamics[32] showed in this later paper[30] how the accuracy of the formulation could be significantly improved by the use of higher order representations of both the boundary geometry and the source strength distribution. Working in a two-dimensional coordinate system based on the tangent to the mid point of an element, he supposes both the element shape and the source strength to be expandable as power series in the tangential coordinate. The velocity at a general point caused by the presence of this element can then be found by integration term by term. The result is a power series in the element length which reduces for small elements to the simple constant source, straight elements. The next term in the series includes a contribution from the linear term in the source strength plus a term from the curvature (second power) of the geometry. The usual reason for extending to higher order interpolation is to enable the curved geometry to be more accurately represented. Hess has shown that a mathematically consistent improvement may be made by including the boundary curvature without having to assume a parabolic variation of source strength. His examples bear this out. The increase in accuracy obtained by using a linear variation of source strength was always of the same order as that improvement when curvature was added (without increasing the number of unknowns). Whereas the addition of parabolic source terms showed negligible improvements. All his examples where for cases of uniform flow perturbed by the presence of an object. For the more rapidly varying boundary conditions of water waves the additional complexity may be justified.

Zienkiewicz, Kelly and Bettess[92] discussed the problems of linking the indirect or direct boundary integral procedures to those of finite elements. They concentrate on the need for establishing symmetrical equations, which they achieve by using an energy principle for the BE domain. For the indirect method the principle must include as an additionalconstraint the satisfaction of the Dirichlet conditions, whereas for the direct method the satisfaction is guaranteed by the coupling of the inner and outer potentials. If the interpolation functions are the same on both sides of the interface, the coupling is continuous along the interface. They make no mention of the possiblities of reducing the bandwidth of the BEM region by zoning.

They redefine the finite element methodology in a sufficiently general form to enable them to show that the boundary element formulation may be viewed as a subset of it. To do this, they have to drop the requirement of locally based shape functions which is essential for the economic use of FEM. They then compare the two methods. The major failing of the BEM to date has been its inability to model non-linear field equations.

Although the FEM can cope with nonlinear equations,ultimately it leads to a set of nonlinear simultaneous equations which have to be solved by iteration. For economic reasons,weak nonlinearity is often assumed so that the initial 'stiffness' matrix may be retained throughout the calculation.

It is possible that the BEM may be applied to the linearized field equations and again the solution obtained by iteration. After the first iteration however, this will almost certainly involve numerical integration over the whole domain even though the unknowns will still be concentrated on the boundaries. This additional computation may only yield savings for three - dimensional problems.

In most realistic exterior wave problems, the only interest in the outer domain is in how it affects and controls the behaviour of the inner local solution. The use of an indirect formulation for the outer solution means that in order to incorporate its interface values the fictitious source strengths (or similar parameters) must be included as additional unknowns in the overall matrix system. Application of Green's theorem to the outer region (a direct method) yields a relation between the potential and its gradient all around the boundary which may be incorporated into a variational principle for the inner region without introducing any new unknown variables. This is the procedure sketched by Shaw[74] for the long water wave case. It should be equally possible to include this boundary integral relation in a weighted residual sense, which extends the possibilities for the inner field equation.

Most of the results of diffraction analyses yield the forces exerted by the waves on the rigid structure. The structural analyst then uses these forces to calculate the displacements of the structure. The implied displacement of the fluid boundaries and hence modification of the fluid forcing is seldom taken into account. Eatock-Taylor[20] has shown how for small displacements these problems may be correctly uncoupled. Walker[81] shows a procedure for solving the coupled motion of a closed tank containing fluid with a free surface. He does not emphasise the fact that motions are again assumed to be small, about the mean position of the tank. He represents the structure as thin shell finite elements and the fluid as boundary elements. The coupling is achieved 'mechanically' by deriving a force displacement relationship for the fluid boundary (by averaging the hydrodynamic pressure over each element) and satisfying equilibrium and compatibility with the structure.

The problem is still nevertheless linear. The nonlinear problem of finite displacements has not yet been solved. This problem could still have been solved using the modal analysis of Eatock-Taylor but with greater complexity. Because Walker does not have to restrict the analysis to the first few modes of structure vibration his results are in that sense more accurate.

CHAPTER 3 POTENTIAL THEORY

3.1. The governing equations of irrotational flow

The motion of an incompressible fluid may be characterized by the velocity vector u_i. The flux of this vector through any closed surface Γ, within the fluid , is

$$\int_{\Gamma} n_i \; u_i \; d\Gamma \qquad 3.1.1.$$

Where n_i are the components of the outward normal vector, and the index is repeated to imply summation. The flux is then the volume of fluid crossing Γ in unit time.

For constant density, the conservation of mass of the fluid requires that the flux be zero across every surface Γ wholly within the fluid. If Ω is the region within Γ then, from Green's lemma

$$\int_{\Gamma} n_i \; u_i \; d\Gamma = \int_{\Omega} \frac{\partial u_i}{\partial x_i} \; d\Omega = 0 \qquad 3.1.2.$$

By letting Γ tend uniformly to zero at a point P it may be shown[46] that at point P

$$\frac{\partial u_i}{\partial x_i} \equiv \text{div } \underline{u} = 0 \qquad 3.1.3.$$

Where the repeated index is used to imply summation, and div is the divergence operator.

Clearly for incompressible flow of a fluid this result must hold at every point of the fluid. A vector which has zero divergence everywhere in a region is called a solenoidal vector.

The circulation of u_i is the integral of velocity along a circuit Γ within the flow

$$\int_{\Gamma} u_i \, dx_i \qquad 3.1.4.$$

If the circulation is zero along all circuits within a region then u_i is called an irrotational vector within that region. If A is now a two-sided surface bounded by Γ, from Stokes' theorem

$$\int_{\Gamma} \underline{u} \cdot \underline{dx} = \int_{A} \underline{n}. \text{ curl } \underline{u} \; dA = 0 \qquad 3.1.5.$$

As before letting Γ tend to zero whilst all the time A is the smallest surface bounded by Γ, for an irrotational flow

$$\text{curl } \underline{u} = 0 \qquad 3.1.6.$$

If u_i is irrotational the line integral of velocity between any two points A and B is single valued, irrespective of the path taken, since any two such paths form a circuit for which the total is zero. A velocity potential ϕ may then be defined by usually

$$\phi_B - \phi_A = \int_A^B u_i dx_i \qquad 3.1.7.$$

Consider now a point P (x_i) and a point Q$(x_i + \delta x_i)$ a small distance away. Since the δx_i are small, the small change in ϕ is

$$\delta\phi = \frac{\partial \phi}{\partial x_i} \delta x_i = \int_P^Q u_i \, dx_i \qquad 3.1.8.$$

As the δx_i approach zero the integral approaches $u_i \delta x_i$. Since the δx_i are arbitrary any two may be assumed to be zero from which the result follows

$$u_i = \frac{\partial \phi}{\partial x_i} \qquad 3.1.9.$$

An irrotational vector may then be expressed as the gradient of a scalar potential. If in addition, the velocity vector is solenoidal then the potential satisfies Laplace's equation,

$$\frac{\partial^2 \phi}{\partial x_i \partial x_i} = 0 \qquad 3.1.10$$

The equations of motion of an ideal fluid may be found by an application of Newton's second law, to be

$$\frac{\partial u_j}{\partial t} + u_i \frac{\partial}{\partial x_i} u_j = X_j - \frac{1}{\rho} \frac{\partial P}{\partial x_j}, \; i \; j = 1,2,3 \qquad 3.1.11.$$

Where a summation on i is implied and P is the fluid pressure and ρ the constant density. For the particular case of irrotational flow

$$u_j = \frac{\partial \phi}{\partial x_j} \qquad 3.1.12.$$

and

$$\frac{\partial u_i}{\partial x_j} = \frac{\partial u_j}{\partial x_i} \qquad 3.1.13.$$

whence

$$\frac{\partial}{\partial x_j}\left(\frac{\partial \phi}{\partial t}\right) + u_i \frac{\partial u_i}{\partial x_j} = X_j - \frac{\partial}{\partial x_j}\left(\frac{P}{\rho}\right) \qquad 3.1.14.$$

If the body forces are due to a potential (such as gravity) Ω then

$$\frac{\partial}{\partial x_j}\left\{\frac{\partial \phi}{\partial t} + \frac{u_i u_i}{2} + \Omega + \frac{P}{\rho}\right\} = 0 \qquad 3.1.15.$$

These equations may now be integrated to yield the generalized Bernoulli equation

$$\frac{\partial \phi}{\partial t} + \frac{u_i u_i}{2} + \Omega + \frac{P}{\rho} = F(t) \qquad 3.1.16.$$

A velocity potential may be found which satisfies the kinematic conditions. However, for the corresponding flow to be dynamically possible then equation 3.1.16. must be satisfied everywhere within the fluid. In most applications the potential is redefined to include the arbitrary function F(t).

If, on the boundaries of a flow, the effects of viscosity are negligible the boundary condition is that of free slip. The kinematic boundary condition for moving impermeable boundaries is therefore:

$$n_i \frac{\partial \phi}{\partial x_i} = V_n \qquad 3.1.17.$$

A free surface boundary must be treated separately. The origin of co-ordinates is at mean water level, with y positive upwards. The velocity components u, v, w correspond to the x, y, z directions respectively.

The body force potential due to gravity is then $\Omega = gy$. The elevation of the free surface above mean water level may be considered as a function of x, z and t,

$$\eta = \eta\ (x, z, t) \qquad 3.1.18.$$

The kinematic condition is that the velocity of the free surface must be that of a particle of fluid on the surface

$$\frac{\partial \eta}{\partial t} + u\frac{\partial \eta}{\partial x} + w\frac{\partial \eta}{\partial z} = v \quad \text{on } y = \eta \qquad 3.1.19.$$

The position of the free surface is not usually known a priori so that an additional condition is required. If in particular it is assumed that the pressure on the surface is constant, then without loss of generality it may be zero. The dynamic condition then becomes

$$\frac{\partial \phi}{\partial t} + \tfrac{1}{2}(u^2 + v^2 + w^2) + g\eta = 0 \quad \text{on } y = \eta \qquad 3.1.20.$$

By considering each condition as a Taylor series expansion about $y = 0$ it can be shown[51] that a consistent first approximation reduces these two conditions to

$$\frac{\partial \eta}{\partial t} = v = \frac{\partial \phi}{\partial y} \quad \text{on } y = 0 \qquad 3.1.21.$$

and

$$\frac{\partial \phi}{\partial t} + g\eta = 0 \quad \text{on } y = 0 \qquad 3.1.22.$$

Combining to remove the initially unkown η leads to the free surface boundary condition

$$\frac{\partial^2 \phi}{\partial t^2} + g \frac{\partial \phi}{\partial y} = 0 \quad \text{on } y = 0 \qquad 3.1.23.$$

The first order approximation represented by the satisfaction of the free surface conditions at $y = 0$ becomes more accurate as η reduces so that for infinitessimal waves it approaches the exact solution.

3.2. Uniqueness theorems

Potential theory is concerned with the problem of finding ϕ subject to boundary conditions sufficient to make its existence unique.

The following sections are concerned with those aspects of potential theory which are necessary for setting up a framework for numerical evaluation of ϕ using the technique of Boundary Elements.

Consider now Laplace's equation governing the variation of a potential ϕ

$$\frac{\partial^2 \phi}{\partial x_i \partial x_i} = \nabla^2 \phi = 0 \qquad 3.2.1.$$

If two solutions exist ϕ_1 and ϕ_2 each satisfying arbitrary boundary conditions a third function ϕ_3 may be defined as

$$\phi_3 = \phi_1 + \phi_2 \qquad 3.2.2.$$

$$\text{Since } \nabla^2 \phi_3 = \nabla^2 (\phi_1 + \phi_2) = \nabla^2 \phi_1 + \nabla^2 \phi_2 = 0 \qquad 3.2.3.$$

then ϕ_3 is also a solution of Laplace's equation. In short Laplace's equation is linear. Clearly the above result may be generalized to include any number of solutions.

Consider now an arbitrary domain Ω boundary Γ on which the gradient of a potential ϕ is prescribed

$$\frac{\partial \phi}{\partial n} = \bar{q} \qquad 3.2.4.$$

this is the interior Neumann problem.

Green's theorem may be written in the form

$$\int_\Omega \phi \, \nabla^2 \psi \, d\Omega + \int_\Omega \text{grad } \phi . \text{ grad } \psi \, d\Omega = \int_\Gamma \phi \, \frac{\partial \psi}{\partial n} \, d\Gamma \qquad 3.2.5.$$

If $\phi = \psi$ is a solution of $\nabla^2 \phi = 0$ this reduces to

$$\int_\Omega (\text{grad } \phi)^2 \, d\Omega = \int_\Gamma \phi \, \frac{\partial \phi}{\partial n} \, d\Gamma \qquad 3.2.6.$$

the object being to show that the interior Neumann problem possesses a unique solution.

Consider then that two solutions exist ϕ_1 and ϕ_2, both satisfying Laplace's equation and the conditions $\frac{\partial \phi}{\partial n} = \bar{q}$ on Γ

Then $\phi_3 = \phi_1 - \phi_2$ is also a solution but satisfying

$$\frac{\partial \phi}{\partial n} = 0 \text{ on } \Gamma \qquad 3.2.7.$$

Therefore, from equation 3.2.6.

$$\int_{\Omega} (\text{grad } \phi_3)^2 \, d\Omega = 0 \qquad 3.2.8.$$

Since the integrand is non-negative it must be zero, that is

$$\text{grad } \phi_3 = 0$$

or

$$\phi_3 = C \qquad 3.2.9.$$

where C is an unknown constant.

It follows that the two solutions ϕ_1 and ϕ_2 are unique except for an additive constant. The physical interpretation of this is that the datum from which ϕ is measured may be shifted by an arbitrary amount without affecting the gradient of ϕ.

If however, in addition, ϕ is prescribed anywhere on Γ then the solution will be unique absolutely.

For if $\phi = \bar{\phi}$ in a neighbourhood of a point i on ε, and $\frac{\partial \phi}{\partial n} = \bar{q}$ on $\Gamma - \varepsilon$; then considering two solutions which satisfy Laplace's equation and the above boundary conditions ϕ_1 and ϕ_2, then $\phi_3 = \phi_1 - \phi_2$ is also a solution but satisfying zero boundary conditions.

$$\int_{\Omega} (\text{grad } \phi_3)^2 \, d\Omega = \int_{\varepsilon} \phi_3 \frac{\partial \phi_3}{\partial n} \, d\Gamma + \int_{\Gamma-\varepsilon} \phi_3 \frac{\partial \phi_3}{\partial n} \, d\Gamma = 0 \qquad 3.2.10.$$

Again $\phi_3 = C$. However on ε, $\phi_3 = 0$ and since ϕ_3 is continuous and constant it must be zero everywhere. Therefore $\phi_1 = \phi_2$ and the solution is unique.

It is also necessary to prove uniqueness for the exterior Neumann problem, in which ϕ exists in aregion Ω exterior to a boundary Γ (see figure 3.2.1).

Green's theorem is applied to the region Ω between the boundary Γ and a large sphere Σ completely enclosing Γ, whence

$$\int_{\Omega} \phi \, \nabla^2 \phi \, d\Omega + \int_{\Omega} (\text{grad } \phi)^2 \, d\Omega = \int_{\Gamma} \phi \frac{\partial \phi}{\partial n} \, d\Gamma + \int_{\Sigma} \phi \frac{\partial \phi}{\partial \nu} \, d\Sigma \qquad 3.2.11.$$

If ϕ satisfies $\nabla^2 \phi = 0$ then

$$\int_{\Omega} (\text{grad } \phi)^2 \, d\Omega = \int_{\Gamma} \phi \frac{\partial \phi}{\partial n} \, d\Gamma + \int_{\Sigma} \phi \frac{\partial \phi}{\partial \nu} \, d\Sigma \qquad 3.2.12.$$

The behaviour of ϕ and $\frac{\partial \phi}{\partial \nu}$ must clearly be restricted at large distances if the contribution from the integral over Σ is to vanish as Σ approaches infinity.

If the radius of Σ is R then the integral of a function f over Σ is given by (see figure 3.2.2.).

$$\int_{\Sigma} f d\Sigma = \int_{\theta=-\frac{\pi}{2}}^{\frac{\pi}{2}} \int_{\lambda=0}^{2\pi} f\, R \sin\theta\, d\lambda R d\theta$$

$$= \iint f \sin\theta\, R^2\, d\lambda d\theta \qquad 3.2.13.$$

For this to vanish as $R \to \infty$ the integral must behave as $O(R^{-1})$. Since $|\sin\theta| < 1$, f must be at least $O(R^{-3})$. for large R.

Hypothesizing, again, that two solutions exist whose difference satisfies zero boundary conditions on Γ then

$$\int_{\Omega} (\text{grad}\ \phi_3)^2\, d\Omega = \int_{\Sigma} \phi_3 \frac{\partial \phi_3}{\partial R}\, d\Sigma \qquad 3.2.14.$$

Provided then that ϕ_1 and ϕ_2 tend to 0 for large R and that their derivatives behave as $O(R^{-2})$ for large R, then ϕ_1 and ϕ_2 behave as $O(R^{-1})$ and the integral behaves as $O(R^{-1})$ for large R. In this case the Neumann problem possesses a unique solution.

The corresponding result for two dimensions is that if

$$I = \int_{\Sigma} f\, d\Sigma = \int_{0}^{2\pi} fR d\theta \qquad 3.2.15.$$

then f must be at least $O(R^{-2})$ for the integral to be bounded for large R.

3.3 Fundamental Solutions

The results necessary for the derivation of the Indirect Boundary Element method will now be derived.

The three dimensional case will be presented in detail with the results for two dimensions quoted without derivation.

If r is the distance from the origin to the point $P(x_1, x_2, x_3)$ then

$$r^2 = x_i\, x_i \qquad 3.3.1.$$

and $$2r \frac{\partial r}{\partial x_j} = 2x_j$$

$$\frac{\partial r}{\partial x_j} = \frac{x_j}{r} \quad \text{no sum on } j \qquad 3.3.2.$$

If $\phi^*(r)$ is a fundamental solution of Laplace's equation then

$$\frac{\partial^2 \phi^*}{\partial x_i \partial x_i} = 0$$

$$= \frac{\partial}{\partial x_i}\left(\frac{d\phi^*}{dr}\frac{\partial r}{\partial x_i}\right) = \frac{\partial}{\partial x_i}\left(\frac{1}{r}\frac{d\phi^*}{dr}x_i\right)$$

$$= x_i \frac{d}{dr}\left(\frac{1}{r}\frac{d\phi^*}{dr}\right)\frac{x_i}{r} + \frac{1}{r}\frac{d\phi^*}{dr}.\ N$$

Where N is the number of dimensions

$$= \frac{x_i\, x_i}{r}\left(\frac{1}{r}\frac{d^2\phi^*}{dr^2}\right) - \frac{1}{r^2}\frac{d\phi^*}{dr} + \frac{N}{r}\frac{d\phi^*}{dr}$$

$$= \frac{d^2\phi^*}{dr^2} + \frac{1}{r}\frac{d\phi^*}{dr}(N-1) \qquad 3.3.3.$$

For three dimensions

$$\phi^* = \frac{1}{r} \qquad 3.3.4.$$

Whence $$\frac{\partial^2 \phi^*}{\partial x_i \partial x_i} = \frac{2}{r^3} + \frac{1}{r} \cdot -\frac{1}{r^2} \quad (3\text{-}1) = 0$$

For two dimensions $\phi^* = \ln r$ 3.3.5.

whence $$\frac{\partial^2 \phi^*}{\partial x_i \partial x_i} = \frac{-1}{r^2} + \frac{1}{r} \cdot \frac{1}{r} \quad (2\text{-}1) = 0$$

Therefore $\phi^* = \frac{1}{r}$ is a solution of $\nabla^2 \phi = 0$ everywhere except at $r = 0$.

The physical significance of ϕ^* is that it is the potential due to a point sink at the origin. Consider a small sphere of radius a, centred at the origin, whose surface is σ (see figure 3.3.1.). The radial velocity V_r at any point on σ is then

$$\frac{\partial \phi}{\partial r} = \frac{-1}{a^2}$$

The total flux of ϕ across σ is

$$\int \frac{-1}{a^2} \, d\sigma = -4\pi \qquad 3.3.6.$$

Since the surface of the sphere is $4\pi a^2$.

Green's theorem may be written

$$\int_\Omega \phi \, \nabla^2 \frac{1}{r} d\Omega + \int_\Omega \text{grad}\phi \cdot \text{grad} \frac{1}{r} d\Omega = \int_\Gamma \phi \, \frac{\partial}{\partial n} \frac{1}{r} \, d\Gamma \qquad 3.3.7.$$

If $\phi = C$ this reduces to

$$\int_\Omega \nabla^2 \frac{1}{r} \, d\Omega = \int_\Gamma \frac{\partial}{\partial n} \frac{1}{r} \, d\Gamma \qquad 3.3.8.$$

(This is actually Green's lemma, or the Divergence theorem).

Evidently, the above result for a sphere may be generalized to any surface containing the origin, since it may always be surrounded by a sphere and equation 3.3.8. applied to the region between the two surfaces.

Applying Green's lemma to the domain ω within σ gives

$$\int_{\omega} \nabla^2 \frac{1}{r} \, d\omega = -4\pi \qquad 3.3.9.$$

a result which holds for all a as a tends to zero.

This behaviour is most easily represented by recourse to the theory of generalized functions. As a tends to zero the radial velocity tends to infinity but in such a way that the flux across σ remains finite and equal to -4π. The Dirac delta function may be conceived in the same way so that in the limit

$$\delta(r) = 0 \quad r \neq 0$$
$$\delta(r) = \infty \quad r = 0$$

and $$\int_{\Omega} \delta(r)\, \phi(\Omega)\, d\Omega = \phi\Big|_{r=0} \qquad 3.3.10.$$

Formally then $\phi^* = \frac{1}{r}$ satisfies the Poisson equation

$$\nabla^2 \phi^* = -4\pi\delta(r) \qquad 3.3.11.$$

where $\delta(r)$ is the Dirac delta function centred at the origin.

Integrating equation 3.3.11 over Ω recovers equation 3.3.9.

In a similar fashion it may be shown that $\phi^* = \ln r$ satisfies

$$\nabla^2 \phi^* = 2\pi \, \delta(r) \qquad 3.3.12.$$

where ϕ^* represents the potential due to a line source. The foregoing results may evidently be generalised by a shift of the origin of co-ordinates.

Consider now the solution of Laplace's equation generated by the addition of a number M of fundamental solutions ϕ_i^* centred at points q_i (ξ_i, η_i, ζ_i) of strengths f_i. The potential at a point $P(x_j)$ is

$$\phi(p) = f_i \, \phi_i^*(p,q) \qquad 3.3.13.$$

Provided then that the points q_i may be enclosed by a finite surface, $\phi(p)$ behaves as $\phi^*(p)$ for large distances. Clearly for the three dimensional case no problems of uniqueness will arise since $\phi^*(p)$ is $O(R^{-1})$ for large R. To avoid unnecessary notational difficulties the two dimensional case will be pursued on the understanding that many of the results will generalize to three dimensions by replacing 2π with -4π, and $\ln r$ with $\frac{1}{r}$.

Application of Green's lemma to this potential within a domain Ω enclosing all the points q_i gives

$$\int_\Omega \nabla^2 \phi(p) d\Omega = \int_\Gamma \frac{\partial}{\partial n} \phi(p) d\Gamma = 2\pi \sum_{i=1}^{M} f_i \int \delta(p-q_i) d\Omega$$

Whence

$$\int_\Gamma \frac{\partial \phi(p)}{\partial n} \, d\Gamma = 2\pi \sum_{i=1}^{M} f_i \qquad 3.3.14.$$

The points q_i may be arranged uniformly around a closed curve S. For sufficiently large M the small distance dq may be defined as shown in figure 3.3.2. If the source strength associated with q_i is assumed to be constant over the small distance dq, then as $M \to \infty$ the sum may be interpreted as an integral over S. In other words the potential

$$\phi(p) = \int_S \phi^*(p,q)\, f(q)\, dq \qquad 3.3.15.$$

may be generated by the continuous distribution of source strength f(q) on S. Evidently $\phi(p)$ does not satisfy Laplace's equation on S. The corresponding expression for the normal derivative of $\phi(p)$ must be derived with care because of the singularity when p and q coincide. Consider the boundary S to be split into two parts, the smaller part σ being a semi-circular curve radius a centred at p (see figure 3.3.3.). The correct expression is obtained by letting a tend to zero.

For a point p on the boundary S

$$\phi(p) = \int_{S-\sigma} \ln r\, f(q)\, dq + \int_\sigma \ln r\, f(q)\, d\sigma \qquad 3.3.16.$$

where r is the distance from q to p. The normal derivative of ϕ at p directed into the domain is

$$\frac{\partial \phi(p)}{\partial n} = \lim_{a \to 0} \left\{ \int_{S-\sigma} \frac{\partial}{\partial n} \ln r\, f(q)\, dq + \int_\sigma \frac{\partial}{\partial n} \ln r\, f(q)\, d\sigma \right\} \qquad 3.3.17.$$

The first term on the R.H.S. is well behaved. For the second term

$$\frac{\partial}{\partial n} = \frac{\partial}{\partial r}_{r=a} \quad \text{and} \quad d\sigma = a\, d\theta$$

$$\lim_{a\to o} \int_\sigma \frac{\partial}{\partial n} \ln r \; f(q)\, d\sigma = \lim_{a\to o} \int_\alpha^{\alpha+\pi} \frac{1}{a} \; f(q)\, a\, d\theta \Rightarrow \pi f(p)$$

Therefore

$$\frac{\partial \phi(p)}{\partial n} = \int_S \frac{\partial}{\partial n} \ln r \, f(q)\, dq + \pi f(p) \qquad 3.3.18.$$

accounts for the singular behaviour of the integral. If P is not on S then the second term does not arise. Clearly there will be a similar expression for the exterior domain.

Using the notation n_i for the normal directed into the interior and n_e for the normal directed into the exterior from S then (see Figure 3.3.4)

$$\frac{\partial}{\partial n_i} \phi(p) = \int_S \frac{\partial}{\partial n_i} \ln r \; f(q)\, dq + \pi f(p) \qquad 3.3.19.$$

$$\frac{\partial}{\partial n_e} \phi(p) = \int_S \frac{\partial}{\partial n_e} \ln r \; f(q)\, dq + \pi f(p) \qquad 3.3.20.$$

Because ln r is uniformly continuous on crossing S then addition of the above equations gives

$$\frac{\partial \phi(p)}{\partial n_i} + \frac{\partial \phi(p)}{\partial n_e} = 2\pi f(p) \qquad 3.3.21.$$

by virtue of n_i and n_e being in opposite directions. There is, then, a step change in potential gradient on crossing S corresponding to the inflow $f(p)$.

Integrating equation 3.3.21. over S gives

$$\int_S \frac{\partial \phi(p)}{\partial n_i} \, dS + \int_S \frac{\partial \phi(p)}{\partial n_e} \, dS = 2\pi \int_S f(p) \, dS \qquad 3.3.22.$$

If there are no sources in the interior domain Ω_i then, by Green's lemma, remembering that n_i is an inward normal

$$\int_{\Omega_i} \nabla^2 \phi(p) d\Omega_i = - \int_S \frac{\partial \phi(p)}{\partial n_i} dS = 0 \qquad 3.3.23.$$

Equation 3.3.22. becomes

$$\int_S \frac{\partial \phi(p)}{\partial n_e} dS = 2\pi \int_S f(p) \, dS \qquad 3.3.24.$$

Consider now the domain exterior to S but bounded by another boundary Σ containing S. Application of Green's lemma to the region between Σ and S leads to

$$\int_\Sigma \frac{\partial \phi(p)}{\partial n} \, d\Sigma = \int_S \frac{\partial \phi(p)}{\partial n_e} \, dS = 2\pi \int_S f(p) \, dS \qquad 3.3.25.$$

provded that no sources exist between Σ and S. Here n denotes the normal directed outwards to infinity from Σ.

3.4. Numerical discretisation of a Dirichlet problem

The potential generated by a distribution of source strength f(q) on a closed curve S may be used as the basis of a method for solving interior boundary value problems subject only to Dirichlet conditions, in the form

$$\int_S \ln r \, f(q) \, dS = \bar{\phi}(p) \qquad p \text{ on } S \qquad 3.4.1.$$

where the bar indicates that the values of ϕ are known on S for a Dirichlet condition. This equation represents an infinite set of equations for the unknown source strength f(q). This is an integral equation of the first kind.

For numerical computation it is necessary to reduce the infinite degrees of freedom of f(q) to a finite number M. The early approaches to this were made by approximating the curve S by a finite number of straight segments subsequently called elements. On each element the source strength f(q) was assumed to be constant.[43] Subsequently, many of the approaches to discretization used in the Finite Element method have been utilized.[83] These involve the use of higher order interpolation functions, often called shape functions because they may be used to descibe the geometry of the elements of the boundary. The motive for the use of higher order interpolation is that the same accuracy may be achieved with fewer elements and fewer unknowns. A considerable advantage is gained in the case of Finite Elements as a consequence of the localized nature of these shape functions.

The effect of each element is only felt by its neighbours so that the matrix of coefficients involved in the simultaneous equations is sparse and banded. There is a reduction in computer storage requirements, as compared with that of a traditional Rayleigh-Ritz approach using global interpolation. In the case of the Boundary Element Method, no such advantage may ever be gained. The fundamental solutions are continuous throughout the domain of interest and can only have zero effect at infinity. Consequently every point on the boundary comes under the influence of the source strength at every other, so that the matrix is fully populated. The only advantage gained is that the integral over each element only involves the source strengths within it, leading to a reduction in computation time.

The use of global interpolation functions may then be possible and desirable. The use of complete Lagrange polynomials may be possible, although difficulties are envisaged in consistently achieving continuity on a closed boundary curve.

For closed curves the possiblity of expanding f(q) as a Fourier series seems the most attractive of these global approaches.

Black[8] and Fenton[23] have used Fourier expansions of the potential and source strength functions, restricting their analyses to axisymmetric problems. Their approaches lead to a reduction in the number of equations, but for each term of the expansion a separate problem must be solved. Fortunately in their case only the first two terms lead to results of significance.

What is envisaged here is the possibility of reducing the number of unknowns by recognising that in many non-symmetrical cases the first few terms of a complete Fourier series may still be used to adequately represent f(q). This may be most easily accomplished in two dimensional problems. To attempt to satisfy the boundary conditions at as many points as may be required, a least squares procedure could then be adopted. The number of equations would therefore still be governed by the number of terms in the expansion for f(q).

In some cases the function ϕ or its derivatives may be expected to vary quite rapidly, for example, near regions of small radius of curvature on the boundary. The simplest solution to this problem is to replace this portion of the boundary with a more suitable radius of curvature and investigate convergence by varying this radius.

For cases where singular behaviour is expected, such as at re-entrant corners, two alternative approaches have been adopted. Liggett[53] has used special interpolation functions in the elements close to the singularity. He assumes that the singular behaviour close to the corner is not influenced by the shape of the rest of the boundary. For example, if the behaviour is of the form

$$\phi \sim r^{\nu} \text{ for } r \to 0 \; ; \; \nu < 1$$

where r is measured from the corner and ν is a known function of the angle at the corner, the interpolation functions can be chosen to behave similarly

$$1 - \xi^{\nu} \text{ and } \xi^{\nu}$$

where the natural co-ordinate ξ is measured from the corner.

The fundamental assumption of this approach makes it necessary for any special elements used to be very small and close to the corner. The interpolation functions used are incomplete polynomials and cannot accommodate any other variation, except perhaps a constant.

The method proposed by Jaswon and Symm[44] does not suffer from this shortcoming. They assume that the singular behaviour exists in addition to an otherwise regular behaviour. They redefine the potential

$$\phi = \psi + m\gamma \qquad 3.4.2.$$

Where γ is the singular function of strength m and ψ is a regular function which satisfies modified boundary conditions involving m. The strength of the singularity becomes an additional unknown which is found by satisfying a compatibility condition at the elements adjacent to the singular point.

In order to accommodate as many of these approaches as possible the approximation for f(q) may be written

$$f'(q) = N_i \quad \alpha_i \qquad 3.4.3.$$

where the N_i are a set of known independent functions and the α_i are a set of unknown parameters.

The particular case when $\alpha_i = f_i$ and the N_i are localized linear interpolation functions will now be examined (see Figure 3.4.1).

Substituting the approximation for f(q) into equation 3.4.1. gives

$$\int_S \ln r \, N_i \, dq \, f_i = \bar{\phi}(p) \; p \text{ on } S \qquad 3.4.4.$$

Since the f_i are no longer functions of position. The Dirichlet boundary condition may be satisfied at M points p_j on S.

A set of linear algebraic equations for f_i results

$$\int_S \ln r \, N_i \, dS. \, f_i = \bar{\phi}(p_j) \qquad 3.4.5.$$

or

$$[A] \{f\} = \{\bar{\phi}\} \qquad 3.4.6.$$

Replacing r with (p_j, q) to indicate the distance from point q to point p_j a typical term of [A] is then

$$a_{ji} = \int_S \ln (p_j, q) \, N_i \, dq \qquad 3.4.7.$$

Provided the functions N_i are sufficiently continuous across element boundaries then this may be evaluated as the sum of the contributions from each element

$$a_{ji} = \sum_{k=1}^{NE} \int_{E_k} \ln (p_j, q) \, N_i \, dq \qquad 3.4.8.$$

where NE is the number of elements and E_k is element k.

Because the function N_i is only non-zero in elements E_{i-1} and E_i then this reduces to two terms

$$a_{ji} = \int_{E_{i-1}} \ln (p_j, q) \, N_i \, dq + \int_{E_i} \ln (p_j, q) N_i dq \qquad 3.4.9.$$

This is the only reduction in computation gained by the use of localized functions.

The points p_j may be chosen to be at the nodes i.e. the inter-element junctions. In general the integrals may be evaluated numerically provided that p_j is not within the element along which integration is taking place. For this case the singular point associated with the fundamental solution ln r is within the path of integration and the improper integral must be evaluated by a limiting process. Alternatively numerical integration formulae are available which automatically take account of the logarithmic behaviour.

In the particular case of piecewise constant variation of f(q), all the integrals may be evaluated exactly.[44] However, in general, the complexity of these closed form evaluations should be carefully considered. Since every part of the source distribution on S gives rise to a component of the potential $\bar{\phi}\ (p_j)$ at each point p_j the matrix [A] represents $2\ M^2$ integral evaluations. Any saving in each one of these is then extremely significant. In view of the fact that for the constant and linear case the boundary is approximated by an inscribed polygon, the extra complexity seems unjustifiable. In the examples which follow the integrations were evaluated using Simpson's rule for three points.

If the point p_j is at i then the following integrals must be evaluated for the contributions from element i.

$$I_1 = \int_{E_i} \ln (p_j,q)\ N_i\ dq \qquad 3.4.10.$$

$$I_2 = \int_{E_i} \ln (p_j,q)\ N_{i+1}\ dq \qquad 3.4.11.$$

A local co-ordinate system is defined by

$$q = \ell\xi \qquad 3.4.12.$$

where ℓ is the length of the element (see Figure 3.4.2.)

Therefore

$$N_i = 1 - \xi \qquad 3.4.13.$$

$$dq = \ell d\xi \qquad 3.4.14.$$

The integral is evaluated as a limit thus

$$I_1 = \lim_{\alpha\to 0} \int_\alpha^1 \ln(p_j,q)\,(1-\xi)\ell\,d\xi \qquad 3.4.15.$$

For this case since the singular point is at i then

$$(p_j,q) = r = \ell\xi \qquad 3.4.16.$$

$$I_1 = \lim_{\alpha\to 0} \int_\alpha^1 \ell\,(1-\xi)\ln\ell\xi\; d\xi \qquad 3.4.17.$$

Integrating by parts leads to

$$I_1 = \lim_{\alpha\to 0}\left\{\ell\,(\xi - \frac{\xi^2}{2})\ln\ell\xi\Big|_\alpha^1 - \ell\int_\alpha^1 (\xi-\frac{\xi^2}{2})\,\frac{1}{\xi}\,d\xi\right\}$$

$$= \lim_{\alpha\to 0}\left\{\frac{\ell}{2}\ln\ell - \ell\alpha(1-\frac{\alpha}{2})\ln\ell\alpha - \ell\left[\xi - \frac{\xi^2}{4}\right]_\alpha^1\right\}$$

$$= \frac{\ell}{2}(\ln\ell - \frac{3}{2}) + \lim_{\alpha\to 0}\left\{\ell\,\frac{\alpha^2}{2}\ln\ell\alpha - \ell\alpha\ln\ell\alpha - \ell\alpha(1-\frac{\alpha}{4})\right\} \qquad 3.4.18.$$

From L'Hospitals rule

$$\lim_{\alpha \to 0} \alpha \ln \ell\alpha = \lim_{\alpha \to 0} \frac{\ln \ell\alpha}{\frac{1}{\alpha}} = \lim_{\alpha \to 0} \frac{\frac{1}{\alpha}}{-\frac{1}{\alpha^2}} = 0 \qquad 3.4.19.$$

$$\therefore \quad I_1 = \frac{\ell}{2} \left(\ln \ell - \frac{3}{2}\right) \qquad 3.4.20.$$

Similary

$$I_2 = \frac{\ell}{2} \left(\ln \ell - \tfrac{1}{2}\right) \qquad 3.4.21.$$

Once the f_i values have been found the value of $\phi(P)$ at any point of the domain can be calculated by backsubstitution into equation 3.4.1. in the form

$$\phi(p) = \int_S \ln r \, N_i \, dS \, f_i \; ; p \text{ in } \Omega \qquad 3.4.22.$$

Flow velocities at p represented by the gradients of ϕ may also be found, for example

$$\frac{\partial \phi(p)}{\partial x} = \int_S \frac{\partial}{\partial x} \ln r \, N_i \, ds \, f_i \qquad 3.4.23.$$

The integrals are in this case evaluated numerically. If the point p is close to the boundary then the accuracy may be poor for two reasons. Firstly, the boundary is being approximated by an inscribed polygon and this has greater effect closer to the boundary. Secondly, the integral over the element nearest to p involves an integrand which may be of much higher order than that assumed for the integration formula.

For numerical purposes, logarithmic behaviour is weakly singular and so, increasing the order of integration may suffice except when p is very close to the boundary. Hence the exact integrals may be used. This conclusion will not generalize to three dimensions.

A third non-rigorous argument is suggested by the previous statement that ϕ (p) does not satisfy Laplace's equation on S. Numerically the effect of this may extend into the domain.

The unknown values of source strength f_i must be found, by solving a set of simultaneous equations, before equations 3.4.22. and 3.4.23. can be evaluated. The source distribution f'(q) is fictitious and usually has no physical significance in any particular problem. Because of this the formulation outlined above is often called the Indirect Boundary Element Method.

A simple example of the implementation of the two dimensional formulation outlined above is the problem shown in figure 3.4.3. for which the exact solution is clearly

$$\phi = (100 - x)\ (100 + y)\ /200$$

A typical discretization is shown in figure 3.4.4.

A computer program based on the above formulation was written (see ALB 1 in Listings) to calculate the matrix of coefficients [A] and to solve for the f_i values using Gauss elimination

The results were examined along the lines A - B and A' - B'. The latter being chosen so as not to meet the boundary near a point at which the integrand is evaluated for use in Simpson's rule.

Figures 3.4.5. and 3.4.6. show a comparison of the exact solution with the numerical results and an exaggerated plot of the error, for discretizations involving 8, 16 and 32 equal elements. The accuracy of the solution is seen to deteriorate as the boundary is approached. The results are clearly converging as the number of elements is increased.

Often the results of most interest are on the boundary and even if a closed form evaluation of the integrals was used the piecewise linear approximation f'(q) on S, where it is clearly going to vary continuously, will lead to inaccurate results on or close to the boundary.

Figure 3.4.7. also shows the variation of f'(q)

3.5. Separation of the source boundary

The potential generated by a distribution of source strength f(q) on the boundary S in figure 3.5.1. is

$$\phi(p) = \int_S \ln r.\ f(q)\ dq \qquad 3.5.1.$$

where now p is in the extended domain $\Omega_I + \Gamma + \Omega_M$. Equation 3.5.1. may be used as the basis of a Dirichlet formulation as before

$$\int_S \ln r.f(q)\ dq = \bar{\phi}(p),\ p \text{ on } \Gamma \qquad 3.5.2.$$

except that now the point p is on the real boundary Γ, and the fictitious source distribution is on the fictitious boundary S. This is the approach originally adopted by Oliveira[66] for the case of elastostatics.

It is assumed that $\phi(p)$, which satisfies $\phi(p) = \bar{\phi}(p)$ on Γ, also satisfies

$$\nabla^2\phi(p) = 0 \quad \text{in } \Omega_I + \Gamma + \Omega_M \qquad 3.5.3.$$

If however, the particular shape of Γ is such that singular behaviour occurs on Γ at a point $V(\xi_i)$, then $\phi(p)$ actually satisfies a Poisson equation of some form

$$\nabla^2\phi(p) + \alpha.\delta(x_i - \xi_i) = 0 \qquad 3.5.4.$$

where ξ_i are the coordinates of the singular point.

It has been demonstrated that equation 3.5.1. generates a potential which satisfies Laplace's equation everywhere except on S. It is clearly incapable of simulating singular behaviour on Γ or in Ω_M.

This reduces the application of this method to the particular cases where either singular behaviour is clearly not going to occur, or the form of the singularity is known and it may be removed with suitable modification of the boundary conditions, as described in section 3.4.

Since p and q are never coincident, numerical integration may be used throughout. To illustrate the improvement in accuracy obtainable using this approach, the problem previously solved with Γ and S coincident, is solved with Γ and S as shown in figure 3.5.2., using program ALB2. There appears to be no reason why S should be geometrically similar. Indeed it may be better if it is not since there is a possibility of it being a 'Γ contour' (Jaswon and Symm[44]). Equally good results have been obtained using a regular polygon for S.

Numerical results were obtained for the two cases when a representative dimension on S was 1.2 and 3 times that on Γ. The results were again examined along the lines A - B and A' - B'. The errors in the first case are plotted in figure 3.5.3, to the same exaggerated scale as in figure 3.4.6. In the second case, the errors were so small that the results are shown in table 3.5.1.

The results on the boundary are no longer so inaccurate. In a physical situation this means that the pressures may be derived with some confidence. The overall accuracy of the results improves as the source boundary S is moved away from Γ.

In this particular case the increase in accuracy may seem surprising. It is a consequence of the behaviour of the source strength at the corners of the domain when Γ and S are coincident. Although the potential is regular over all Γ, the variation of source strength required to model the behaviour at the corners is singular. This is explained by Symm[76], to be a consequence of the exterior solution corresponding to the given boundary conditions on Γ. The use of equal length linear elements will make it difficult for the source intensity f'(q) to model this behaviour accurately. The accuracy of the overall solution may not be improved significantly by concentrating elements near the corners, because the equations for f_i become ill-conditioned.

The slightest separation of Γ and S however removes the singular behaviour and consequently the accuracy improves. The change in the source distribution for the β=1.2 case is shown in figure 3.5.4, which may be compared with figure 3.4.7.

This may be illustrated convincingly by solving the problem of the L shaped domain shown in figure 3.5.5.

Symm[76] has solved this problem subject to the boundary conditions ϕ = 1000 x on Γ. The accuracy of his solution at the corners was poor even though he used a total of 64 elements.

Clearly, the solution is ϕ = 1000x everywhere and is therefore regular throughout $\Omega_I + \Gamma + \Omega_M$. The results near the corners for the discretisation shown, with the S boundary 1.2 times and 3 times the Γ boundary, are presented in table 3.5.2. Figure 3.5.6. compares the errors in these results with those given by Symm, in the region of the corner at node 11. There is a significant improvement with fewer elements.

The indirect B.E.M. with separate Γ and S boundaries was used below for the problems of waves in finite depth water. Because of the possibility of difficulties associated with singular behaviour on the real boundary Γ, the problems in the next section were tested to check the limits of the validity of the approach. For simplicity the test problems are restricted to two dimensional behaviour.

3.6. The Neumann problem of steady flow

It will be found below that the particular formulation of the B.E. method applicable to diffraction theory involves a Neumann boundary value problem.

A particular problem which serves to illustrate several of the features of the B.E. method when applied to a Neumann problem is that of flow past an infinite circular cylinder parallel to an impermeable plane boundary and positioned normal to an otherwise uniform stream parallel with the boundary.

The solution of this problem for the particular case when the cylinder is resting on the boundary may be found analytically for irrotational incompressible flow. This problem was solved by Jeffreys[45]. He utilized a conformal transformation which transforms the plane boundary into another but inverted plane and the cylinder into a parallel plane boundary. Successive application of the method of images to satisfy the kinematic boundary condition on each plane leads to a series which is recognised as an expansion of the hyperbolic cotangent.

The complex potential is then given by

$$\omega = \phi + i\psi = \pi a U \cosh\left(\frac{\pi a}{z}\right) \qquad 3.6.1.$$

Where $z = x+iy$, a is the cylinder radius and U the stream velocity. ω is therefore the solution for a uniform stream travelling in the positive x direction, perturbed by a cylinder.

It can be shown that the real and imaginary parts of ω may be separated thus:-

$$\omega = \phi + i\psi = \pi aU\ (\sinh X + i \sin Y)/(\cosh X - \cos Y) \quad 3.6.2.$$

where

$$X = \frac{2\pi ax}{x^2+y^2} \quad \text{and} \quad Y = \frac{2\pi ay}{x^2+y^2}$$

whence

$$\phi = \frac{\pi\ aU \sinh X}{\cosh X - \cos Y} \quad 3.6.3.$$

Using the Bernoulli equation for steady flow the pressure on the cylinder could be found and hence, the lift force. The result is derived more simply by considering the conservation of momentum in a vertical direction, since the integral is then along the x axis.

The component of the lift force, due to the deformation of the streamlines causing a high velocity and low pressure at the top of the cylinder and a high stagnation pressure at the base, is then found to be

$$F_L = \pi\rho\ aU^2 \left[\frac{1}{3} + \left(\frac{\pi}{3}\right)^2\right] = 1.430\ \pi\rho aU^2 \quad 3.6.4.$$

Once the cylinder lifts off this component of the lift force diminishes rapidly and becomes negative.

The details of the solution of this problem by the indirect B.E. method are now presented. The boundary value problem consists of finding the potential ϕ_T which satisfies Laplace's equation

$$\nabla^2\phi_T = 0 \quad \text{in 2 dimensions} \quad 3.6.5.$$

and the homogeneous Neumann boundary conditions

$$\left(\frac{\partial \phi_T}{\partial y}\right)_{y=0} = 0 \qquad 3.6.6.$$

and $$\frac{\partial \phi_T}{\partial n} = 0 \quad \text{on } x^2 + (y-d)^2 = a^2 \qquad 3.6.7.$$

where n is the normal direction into the domain from the boundary of the cylinder, and is therefore directed radially outwards (see fig. 3.6.1.).

In addition at large distances from the cylinder

$$\phi_T \Rightarrow Ux \qquad 3.6.8.$$

where the suffix T stands for total. This behaviour at infinity is extremely inconvenient since it means that contributions from the usual large external boundary are no longer negligible. However, recognising that Laplace's equation is linear the total potential may be considered to be made up of two parts

$$\phi_T = \phi_u + \phi \qquad 3.6.9.$$

where $\phi_u = Ux$ 3.6.10.

and ϕ is the perturbation of this stream caused by the presence of the cylinder which is expected to have zero effect at infinity.

The boundary conditions of the original problem will all be affected by this change of variable. The boundary conditions at infinity are satisfied by ϕ_u, therefore ϕ must satisfy zero boundary conditions here. The boundary condition on the x axis is still homogeneous since the uniform stream satisfies a zero boundary condition here.

On the cylinder.

$$\frac{\partial \phi_T}{\partial n} = \frac{\partial \phi_u}{\partial n} + \frac{\partial \phi}{\partial n}$$

Whence

$$\frac{\partial \phi}{\partial n} = \frac{-\partial \phi_u}{\partial n} \qquad 3.6.11.$$

is the new boundary condition for ϕ. Using the notation of figure 3.6.2.

$$\frac{\partial \phi_u}{\partial n} = \frac{\partial \phi_u}{\partial x} \cdot \frac{\partial x}{\partial n}$$

$$= U \cos\theta$$

Therefore $$\frac{\partial \phi}{\partial n} = - U \cos \theta \qquad 3.6.12.$$

At this stage it is possible to solve the Neumann problem by arranging for a continuous distribution of source strength for example, along the broken lines in figure 3.6.2. The boundary condition on the x axis would have to be satisfied over most of its length to obtain an accurate solution. This respresents a prohibitively large set of equations.

If the method of images is utilized it will be seen that the problem of flow between two such cylinders is identical. The problem is then solved by using as a fundamental solution, a point source and its image in the x axis (see figure 3.6.3.) .

Any combination of such fundamental solutions will clearly satisfy the Neumann condition on the x axis. In general this approach may be used for a large family of bounding surfaces provided that all possible image sources are considered.

The following section shows in some detail the formulation for this particular problem.

3.7. The numerical details

The fundamental solution of Laplace's equation in two dimensions has been shown to be that of a unit line source

$$\phi^* = \ln r \qquad 3.7.1.$$

Referring to figure 3.7.1. a continuous distribution of line sources of strength f (q) on closed curve S generates the potential at a point P exterior to S

$$\phi (p) = \int_S f(q) \ln r \, dq \qquad 3.7.2.$$

The gradient of ϕ along the inward normal at p is then, in general, from equation 3.3.18.

$$\frac{\partial \phi(p)}{\partial n} = \int f(q) \frac{\partial}{\partial n} (\ln r) \, dq + \pi f(p) \qquad 3.7.3.$$

In this particular case however, q and p can never coincide so

$$\frac{\partial \phi(p)}{\partial n} = \int_S f(q) \frac{\partial}{\partial n} (\ln r) \, dq \text{ , p on } \Gamma \qquad 3.7.4.$$

Equation 3.7.4. may then be used as the basis of a Neumann formulation in a similar way to the Dirichlet problem already demonstrated. The source distribution is given finite degrees of freedom by the approximation.

$$f'(q) = N_i f_i \qquad i = 1, M \qquad 3.7.5.$$

yielding the set of equations for the f_i

$$\int N_i \frac{\partial}{\partial n} (\ln r) \, dq \, f_i = \frac{\partial \phi(p)}{\partial n} \qquad 3.7.6.$$

or in matrix form

$$\left[A\right] \quad \{f\} \quad = \{\phi'\} \qquad 3.7.7.$$

Where $\{f\}$ is the vector of M unknown source strengths and $\{\phi'\}$ is the vector of known gradients of the perturbation potential where

$$\phi' \ (p) \ = \ \frac{\partial \phi(p)}{\partial n} \qquad 3.7.8.$$

A typical term of matrix $[A]$ is

$$a_{ji} \ = \int_S N_i \ \frac{\partial}{\partial n} \ (\ln r_j) \ dq \qquad 3.7.9.$$

Where r_j is the distance from one of the points p_j on Γ at which $\phi' \ (p_j)$ is known. A small benefit is now derived from the choice of localised interpolation functions N_i, in that the coefficient a_{ji} may be evaluated as the sum of the integrals over each element, most of which are zero

$$a_{ji} \ = \sum_{k=1}^{NE} \int_{\Gamma_k} Ni \ \frac{\partial}{\partial n} \ (\ln r_j) \ dq \qquad 3.7.10.$$

Where NE is the number of elements into which S has been divided, which in the linear interpolation case is equal to the number of unknowns M. If q_i is taken to represent the ith point on S then element k is between q_k and q_{k+1}. Therefore a typical coefficient becomes simply

$$a_{ji} = \int_{q_{i-1}}^{q_i} N_i \frac{\partial}{\partial n} \ln(r_j) \, dq + \int_{q_i}^{q_{i+1}} N_i \frac{\partial}{\partial n} \ln(r_j) \, dq \qquad 3.7.11.$$

It is this step in the case of the F.E. method which leads to the banded nature of the matrix of coefficients.

In this case however, the point p_j is not necessarily between q_{i-1} and q_{i+1}.

In order to show how these coefficients are evaluated it is simpler to work in terms of a typical element. Consider the element of S between q_i and q_{i+1}, where the indices increase in a clockwise direction since we are considering an exterior problem. Within this element the source distribution is interpolated linearly between f_i and f_{i+1} that is,

$$f'(q) = N_i f_i + N_{i+1} \cdot f_{i+1} \qquad 3.7.12.$$

where now no summation is implied. A local coordinate system is defined, ξ, such that

$$\xi = 0 \text{ at } q_i$$

$$\xi = 1 \text{ at } q_{i+1} \qquad 3.7.13.$$

The distance from a general point ξ on the element to the point p_j is given by

$$r^2 = (x_\xi - x_j)^2 + (y_\xi - y_j)^2 \qquad 3.7.14.$$

At the point p_j the normal direction n will in general be known for a particular problem so that the set of angles α_j shown in figure 3.7.2. will be given. If the tangential direction is defined in the clockwise positive sense for an exterior problem then

$$\frac{\partial \phi^*_j}{\partial n} = \frac{\partial \phi^*}{\partial r}\left(\frac{\partial r}{\partial x_j}\cdot\frac{\partial x_j}{\partial n} + \frac{\partial r}{\partial y_j}\cdot\frac{\partial y_j}{\partial n}\right)$$

and

$$\frac{\partial \phi^*_j}{\partial s} = \frac{\partial \phi^*}{\partial r}\left(\frac{\partial r}{\partial x_j}\cdot\frac{\partial x_j}{\partial s} + \frac{\partial r}{\partial y_j}\cdot\frac{\partial y_j}{\partial s}\right) \qquad 3.\,7.15.$$

are the normal and tangential gradients of the fundamental solution ϕ^*_j at P_j. From equation 3.7.14.

$$\frac{\partial r}{\partial x_j} = -\frac{(x_\xi - x_j)}{r} \quad \text{and} \quad \frac{\partial r}{\partial y_j} = -\frac{(y_\xi - y_j)}{r} \qquad 3.\,7.16.$$

and also from figure 3.7.2.

$$\frac{\partial x_j}{\partial n} = -\frac{\partial y_j}{\partial s} = \cos\alpha_j$$

and

$$\frac{\partial y_j}{\partial n} = \frac{\partial x_j}{\partial s} = \sin\alpha_j \qquad 3.\,7.17.$$

For two dimensions $\phi^*_j = \ln r$

Hence

$$\frac{\partial \phi^*_j}{\partial r} = \frac{1}{r} \qquad 3.\,7.18.$$

So that finally

$$\frac{\partial \phi^*_j}{\partial n} = \frac{\partial \ln r}{\partial n} = \frac{-1}{r^2}\left[(x_\xi - x_j)\cos\alpha_j + (y_\xi - y_j)\sin\alpha_j\right]$$

$$\frac{\partial \phi^*_j}{\partial s} = \frac{\partial \ln r}{\partial s} = \frac{-1}{r^2}\left[(x_\xi - x_j)\sin\alpha_j - (y_\xi - y_j)\cos\alpha_j\right] \qquad 3.\,7.19.$$

The contribution to equation j from this element is then

$$I = \int_{q_i}^{q_{i+1}} f(q) \frac{\partial \ln r}{\partial n} \, dq$$

$$= \int_0^1 N_i \frac{\partial}{\partial n} \ln r \, d\xi . f_i + \int_0^1 N_{i+1} \frac{\partial \ln r}{\partial n} \, d\xi . f_{i+1} \qquad 3.7.20.$$

Although it may be possible to evaluate the integrals in closed form, in general when a higher order approximation is used for f'(q) this will not be the case. As mentioned above it may prove prohibitively expensive in terms of computer time to use the closed form anyway.

In the program based on this formulation, Simpson's rule for 3 points was found to be sufficiently accurate.

The potential generated by a continuous distribution of line sources is of the form

$$\phi(p) = \int f(q) \ln(r) \, dq \qquad 3.7.21.$$

Where r is the distance from p to q . Interpreting p and q as vectors indicating the position of points p and q then

$$\phi(\underline{p}) = \int f(q) \ln|p-q| \, dq \qquad 3.7.22.$$

The behaviour of this potential for large p may be derived by expanding this expression in terms of p using the series expansion of ln (1 - x) to obtain

$$\phi(p) \sim \ln|p| \int f(q) dq - |p|^{-2} \int (p.q) f(q) dq + O(|p|^{-2}) \qquad 3.7.23$$

The potential generated by equation 3.7.21. behaves logarithmically at large distances, its derivatives will be $O(|p|^{-1})$ and so the formulation may not lead to a unique solution, in view of equation 3.2.15.

If the formulation includes satisfaction of the additional condition

$$\int f(q)\, dq = 0 \qquad 3.7.24.$$

then a unique solution is obtainable.

It was shown above that for two dimensions

$$\int \frac{\partial \phi(p)}{\partial n} d\Sigma = 2\pi \int f(q)\, dq \qquad 3.7.25.$$

Where n is directed outwards to infinity from the large boundary Σ.

If equation 3.7.24 is satisfied then

$$\int \frac{\partial \phi(p)}{\partial n} d\Sigma = 0 \qquad 3.7.26.$$

and $\phi(p) \to C$ for large distances, where C is an unknown constant.

In order to provide the additional unknown required to enable equation 3.7.24. to be satisfied the datum from which ϕ is measured may be shifted by this unknown amount C. The discretized form of equation 3.7.24. is then

$$\int_S N_i\, dq\, f_i = 0 \qquad 3.7.27.$$

Recalling also however that for any boundary surrounding S and in particular for Γ

$$\int_{\Gamma} \frac{\partial \phi(p)}{\partial n_e} \, d\Gamma = 2\pi \int_{S} f(q) \, dq \qquad 3.7.28.$$

On Γ however, for the general perturbation problem

$$\frac{\partial \phi}{\partial n_e} = - \frac{\partial \phi_u}{\partial n_e} \qquad 3.7.29.$$

and by the divergence theorem, since ϕ_u is a known solution of Laplace's equation everywhere then

$$\int \frac{\partial \phi_u}{\partial n_e} \, d\Gamma = 0 \qquad 3.7.30.$$

Therefore the side condition on f(q) is always satisfied automatically for the perturbation problem.

A computer program {see listings B C Y L} was written for the particular Neumann problem of flow past a cylinder near a plane boundary by using the previous formulation but with a fundamental solution which satisfied the Neumann condition on the plane automatically, that is

$$\phi^* = \ln (rr') \qquad 3.7.31.$$

where the sense of r and r' is shown in figure 3.7.3. The formulation is not significantly changed by this form of fundamental solution.

3.8. The numerical results

As a first check on the validity of the method and to enable estimates of convergence to be obtained the image source distribution was omitted and the classical problem of flow past a cylinder was tested.

The well known exact solution for this problem is generated by superposing a doublet and a free stream. The perturbation potential sought is therefore that of a doublet. A doublet, like a source has singular behaviour near its centre and so care must be taken to exclude the centre of the cylinder from the domain. This is always achieved if the source distribution boundary S is a regular M sided polygon concentric with Γ as shown in figure 3.8.1. The radius of the boundary Γ is that of the circular cylinder, a. The radius of the source boundary S can be defined as βa.

The convergence of the exact solution was examined by varying β and M.

Three indicators of convergence of results were chosen as indicated in figure 3.8.2, the potential at points A and B and the tangential velocity at point C. These are obtained, once the f_i values have been found, by back-substitution in to equation 3.7.21. above.

The particular numerical problem solved was that of a uniform stream of velocity U = 10 and a cylinder of radius a = 1 for which the exact values are $\phi_A = 25$, $\phi_B = 20$ and $V_C = 2U = 20$. For $\beta = 0.9$ the convergence to the exact results is seen, from figure 3.8.3. to be slow as M is increased. For values of M greater than 16, however, the results appear to be always within 1.5% of the exact results. The presence of the source discretization quite close to the real boundary is the cause of this poor accuracy. Figure 3.8.4. shows the convergence for a fixed value of M = 16 as β is varied. It is clear that as the source boundary is moved further and further away from Γ the results become more and more accurate. Figure 3.8.5. shows the variation of normalised source strength for the cases when β is 0.2 and 0.1. The results for $\beta > 0.2$ lie on the same curve as those of $\beta = 0.2$. Somewhere between β is 0.2 and 0.1 numerical ill-conditioning occurs leading to instabilities in the source strength. This ill-conditioning is caused by the diagonal term losing its dominance in the row of coefficients because all the distances involved are now very similar.

It is perhaps surprising that the results of interest do not appear to be affected by this ill conditioning even when β=0.01. It is felt however, that this behaviour is peculiar to this problem because of inherent symmetries in the results. In general, it would be unwise to use such a small value of β.

A similar problem occurs for fixed β as M is increased. In this casethis is the numerical analogue of the difficulties involved in finding solutions to integral equations involving non-singular kernels [44]

If the kernel is singular; such as in the Dirichlet problem shown above, then the diagonal coefficients are always dominant. In the method used here, as the number of elements is increased the diagonal dominance is always reduced locally (See figure 3.8.6) since the contributions from adjacent elements become closer together. The only remedy is to increase β. Examination of the results suggests the optimum values for this particular problem are M = 16, β = 0.4.

The next set of results are presented for the case of flow past a circular cylinder near a plane boundary, by including the image source distribution. Figure 3.8.7. shows the variation of lift force on the cylinder with its distance above the plane. This distance is expressed in the non-dimensional form d/2a. The negative sign indicates that the force is acting to pull the cylinder towards the boundary.

The lift force has been evaluated by making use of the dynamic boundary condition on the cylinder in the form

$$p_j = \frac{-\rho}{2} \left(\frac{\partial \phi_u}{\partial s} + \frac{\partial \phi}{\partial s} \right)^2 \quad \text{at a point } j \text{ on } \Gamma \qquad 3.8.1.$$

Where p_j is that part of the pressure due to the deformation of the streamlines. The bouyancy force is not considered here.

Now
$$\frac{\partial \phi_u}{\partial} = U \sin\alpha_j \qquad 3.8.2.$$

and
$$\frac{\partial \phi_j}{\partial} = \int_S N_i \frac{\partial}{\partial} \ln r_j \; dq.f_i \qquad 3.8.3.$$

by backsubstitution. The lift force may then be evaluated by Simpson's rule in the form

$$Fy = \frac{-2\pi a}{3m} \sum_{j=1}^{m} \{3 + (-1)^j\} p_j \sin \frac{2\pi}{m}(j-1) \qquad 3.8.4.$$

where m must be even. The results presented here were calculated with m = M for simplicity, but in general m could be much greater than M.

It might be expected that as d/2a → ½ the lift force should approach the analytical result

$$\frac{FL}{\pi\rho a U^2} = 1.430 \qquad 3.8.5.$$

However, the potential function associated with this solution is

$$\phi = \frac{\pi a U \sinh X}{\cosh X - \cos Y} \qquad 3.8.6.$$

Where $X = \frac{2\pi a x}{x^2+y^2}$; $Y = \frac{2\pi a y}{x^2+y^2}$

For y = 0

$$\phi = \frac{\pi a U \sin h \frac{2\pi a}{x}}{\cosh \frac{2\pi a}{x} - 1}$$

Therefore

$$\lim_{x \to 0^-} \phi_{y=0} = -\pi a U \qquad 3.8.7.$$

and

$$\lim_{x \to 0^+} \phi_{y=0} = \pi a U \qquad 3.8.8.$$

The step change in ϕ as x crosses the origin implies infinite velocity at this point. This singular behaviour is within the domain of interest and so the source distribution on S cannot model this behaviour. If the sources are distributed on Γ then the singular behaviour may be achieved but as shown previously the accuracy will be limited unless a large number of unknowns is used.

The variation of source strength around S is shown in figure 3.8.8. from which it can be seen that as $\frac{d}{2a}$ reduces towards 0.5 the source distribution at $\theta = \frac{3\pi}{2}$ is approaching infinity.

If a doublet is used at this point instead of the source, which may be assumed known and equal to zero, the number of equations is still the same. The accuracy should then improve.

In this case however a more consistent approach would be to remove the singularity from the origin by assuming that the perturbation potential is made up of two parts, one due to a singular point of suitable form at the origin and the second an unknown but everywhere harmonic function which can now be generated by the source distribution on S without difficulty. See section 3.4. above.

The results over which doubt is cast as a consequence of this problem are those in figure 3.8.7. for which $\frac{d}{2a}$ is less than 0.6. Unfortunately no exact solution of this problem exists in order to verify the results.

To summarise, it has been shown that a problem involving behaviour at large distances, of the form of a known harmonic function, may be solved by considering the total potential to comprise this function plus a perturbation potential.

For exterior problems, not involving singular behaviour, the Neumann formulation involving a source boundary everywhere exterior to the real boundary, from the point of view of the domain, has been shown to give accurate results.

The method of images may be employed fruitfully to satisfy an otherwise troublesome boundary condition.

3.9. Linear wave diffraction

The foregoing methods of analysis will now be applied to the case of wave diffraction by large objects. The physical assumptions necessary for the forces on structures in waves to be closely approximated by diffraction theory are mentioned in chapter 2. The following sections concentrate on the mathematical and numerical aspects.

The analysis will be restricted to the case of waves in an infinite sea of finite constant depth. If the motion is irrotational and incompressible then a velocity potential exists which satisfies

$$\nabla^2 \Phi = 0 \qquad 3.9.1.$$

where

$$\Phi = \Phi(x,y,z,t)$$

with y positive upwards from an origin in the mean water level. On the bed the normal velocity is zero

$$\frac{\partial \Phi}{\partial y} = 0 \text{ on } y = -h \qquad 3.9.2.$$

and on the structure

$$\frac{\partial \Phi}{\partial n} = \underline{V} \cdot \underline{n} \qquad 3.9.3.$$

where V is the velocity of the surface of the structure. For small amplitude waves the linearized boundary conditions on the free surface may be used. In any case, the results of this analysis will act as the first approximation from which the non-linear approximations may be derived.

Therefore $$\eta = -\frac{1}{g}\frac{\partial \Phi}{\partial t} \quad \text{on } y = 0 \qquad 3.9.4.$$

and $$\frac{\partial \eta}{\partial t} = \frac{\partial \Phi}{\partial y} \quad \text{on } y = 0 \qquad 3.9.5.$$

these results combine - as shown above - to give the boundary condition for Φ

$$\frac{\partial^2 \Phi}{\partial t^2} + g\frac{\partial \Phi}{\partial y} = 0 \text{ on } y = 0 \qquad 3.9.6.$$

In a manner analogous to that used previously for the perturbation problem, it is supposed that the potential is made up of that due to the incident waves, which without loss of generality may be assumed to be travelling in the positive x direction, and that due to the presence of the structure. This latter - scattered potential being composed of that due to the diffraction of the waves by the stationary structure and that radiated from the motion of the structure.

$$\Phi = \Phi_w + \Phi_s \qquad 3.9.7.$$

This separation relies heavily on linearity of the problem.. For a linear system, the components of the wave at different frequencies may be analysed separately, and their effects summed using Fourier's theorem.

Therefore, consider the case when the potential is time harmonic of radian frequency σ so that

$$\Phi = \phi_1 \cos \sigma t + \phi_2 \sin \sigma t \qquad 3.9.8.$$

The subsequent analysis may be simplified by assuming that

$$\Phi = Re\left\{\phi(x, y, z)\, e^{-i\sigma t}\right\} \qquad 3.9.9.$$

where $\phi = \phi_1 + i\phi_2$

Throughout the subsequent analysis real parts of the complex expressions are taken to recover the physical quantities. It is clear that ϕ will still be governed by Laplace's equation and the kinematic conditions on the solid boundaries remain unchanged. The free surface condition reduces to

$$\frac{\partial \phi}{\partial y} - \frac{\sigma^2}{g}\phi = 0 \quad \text{on } y = 0 \qquad 3.9.10.$$

It has been shown by John[47] that sufficient conditions for the unique prescription of the problem must include that Φ_s satisfies a radiation condition of the type of the Sommerfeld condition at infinity

$$\lim_{R \to \infty} R^{\frac{1}{2}} \left(\frac{\partial \phi_s}{\partial R} - \frac{\sigma^2}{g}\phi_s\right) = 0 \qquad 3.9.11.$$

which is equivalent to the statement that the scattered potential must behave as an outgoing wave at infinity. This is analogous to the requirement that the perturbation potential should tend to zero at infinity, used above.

In principle then, the potential generated by

$$\phi_s = \int_S f(q)\, \frac{1}{R}\, dq \qquad 3.9.12.$$

where now f is complex, could be utilised to solve the Neumann problem. The opportunity to satisfy the condition at y = -h should not be missed, so that

$$\phi_s = \int f(q)\, G\, dq \qquad 3.9.13.$$

where $G = \frac{1}{R} + \frac{1}{R'}$

could be used.

The free surface boundary condition is not so readily handled, neither is the radiation condition. The numerical procedure would then have to consist of satisfying the remaining conditions at a finite number of points. Although this would represent a large number of equations, this approach should not be dismissed out of hand. Watson[83] has shown how the infinite element approach used successfully in finite element work [Bettess[5]] may be adopted to cope with just such an infinite boundary as the free surface here. The reduction in complexity of the fundamental solution at the expense of an increased number of equations is worthy of consideration.

However, a fundamental solution, or Green's function does exist which satisfies all the boundary conditions in the absence of an immersed object and is equivalent to waves issuing from a point (a, b, c) radially outwards - the so called pulsating source solution. Wehausen and Laitone[84] derive the following integral form

$$G(x,y,z,a,b,c) = \frac{1}{R} + \frac{1}{R'} + PV \int_0^\infty \frac{2(k+\nu)e^{-kh}\cosh k(b+h)\cosh k(y+h)Jo(kr)dk}{k\sinh kh - \nu\cosh kh}$$

$$+ \frac{2\pi i(m_o+\nu)e^{-m_o h}\sinh m_o h \cosh m_o(b+h)\cosh m_o(y+h)Jo(m_o r)}{\nu h + \sinh^2 m_o h} \qquad 3.9.14.$$

where $R^2 = (x-a)^2+(y-b)^2+(z-c)^2$

$$(R')^2 = (x-a)^2+(y+2h+b)^2+(z-c)^2$$

$$r^2 = (x-a)^2+(z-c)^2$$

and $\nu = \frac{\sigma^2}{g} = m_o \tanh m_o h$

where $m_o = \frac{2\pi}{\lambda}$ the radian wave number.

Jo(x) is the Bessel function of the first kind of zero order.

The integral must be evaluated as a Cauchy principal value because of the singular point in the path of the integral at

$$k \tanh k.h = \nu \qquad 3.9.15.$$

The imaginary part arises in their derivation from satisfaction of the radiation condition. In the derivation of John[47], it arises from the use of the integration path in the complex plane.

It is instructive to show how the Bessel functions arise in this context although for the complete derivation of the above, reference should be made to Wehausen and Laitone[84]

The distance R' is from the image of the point (a,b,c) in the bed so that the bed kinematic condition is satisfied. The rest of the Green's function involves terms in cosh k(y+h) which will contribute nothing to the gradient of the potential at the bed.

Also G possesses radial symmetry. For cylindrical polar co-ordinates Laplace's equation becomes

$$\frac{\partial^2\phi}{\partial y^2} + \frac{\partial^2\phi}{\partial r^2} + \frac{1}{r}\cdot\frac{\partial\phi}{\partial r} + \frac{1}{r^2}\cdot\frac{\partial^2\phi}{\partial\theta^2} = 0 \qquad 3.9.16.$$

If ϕ possesses radial symmetry i.e. $\phi = \phi(r,y)$ then this reduces to

$$\frac{\partial^2\phi}{\partial y^2} + \frac{\partial^2\phi}{\partial r^2} + \frac{1}{r}\frac{\partial\phi}{\partial r} = 0 \qquad 3.9.17.$$

Assume now that $\phi = Y(y).\ R(r)$, then

$$R\frac{d^2Y}{dy^2} + Y\frac{d^2R}{dr^2} + \frac{Y}{r}\cdot\frac{dR}{dr} = 0 \qquad 3.9.18.$$

From which

$$\frac{d^2Y}{dy^2} - \alpha^2 Y = 0 \qquad 3.9.19.$$

$$\frac{d^2R}{dr^2} + \frac{1}{r}\frac{dR}{dr} + \alpha^2 R = 0$$

The first equation has the solutions

$$Y = e^{\pm \alpha y} \qquad 3.9.20.$$

and the second equation is a particular form of Bessel's equation which has a solution, for finite values at r = o of

$$R = Jo(\alpha r) \qquad 3.9.21.$$

clearly $\phi = \cosh \alpha(y+h)\ Jo(\alpha r)$ 3.9.22.

may be constructed as a possible solution which satisfies the finite depth condition. In addition, the free surface boundary condition must be satisfied.

Since

$$\frac{\partial \phi}{\partial y} = \alpha \sinh \alpha(y+h) Jo(\alpha r) \qquad 3.9.23.$$

then $\alpha \sinh \alpha h\ Jo\ (\alpha r) - \frac{\sigma^2}{g} \cosh \alpha h\ Jo\ (\alpha r) = 0$ on $y = 0$ 3.9.24.

whence $\alpha \tanh \alpha h = \frac{\sigma^2}{g} = \nu$ 3.9.25.

the dispersion relationship. It may be seen then that the Bessel functions arise from the choice of coordinate system.

The restriction to radial symmetry is unnecessary however, since for any variation of ϕ by Fourier's theorem

If $\phi = \phi(y,r).\theta(\theta)$

$$= \phi(y,r) \sum_{s=0}^{\infty} a_s \cos s\theta + b_s \sin s\theta \qquad 3.9.26.$$

where s must be integral if the domain is the exterior of a closed cylinder

The case of s = 0 has already been examined but considering a typical term involving cos $s\theta$

If $\phi = \phi(y,r) \cos s\theta$ 3.9.27.

The governing equation becomes

$$\frac{\partial^2\phi}{\partial y^2} + \frac{\partial^2\phi}{\partial r^2} + \frac{1}{r}\frac{\partial\phi}{\partial r} - \frac{s^2}{r^2}\phi = 0 \qquad 3.9.28.$$

Now assume $\phi = Y(y).R(r)$ 3.9.29.

from which $Y = e^{\pm \alpha y}$ 3.9.30.

and R satisfies

$$\frac{d^2R}{dr^2} + \frac{1}{r}\frac{dR}{dr} + (\alpha^2 - \frac{s^2}{r^2})R = 0 \qquad 3.9.31.$$

which is the more general form of Bessel's equation with the solution for finite values at r = 0

$$R = J_s(\alpha r) . \qquad 3.9.32.$$

Series involving Bessel functions are therefore to be expected in many problems of diffraction where the use of cylindrical polar co-ordinates is justified. See for example McCamy and Fuchs[58], Lebreton and Cormault[52] and Lamb[51]. As a final illustration of the expansion of a function in cylindrical harmonics, the expression

used by many authors (notably McCamy and Fuchs[58]) for the potential of a wave travelling in the positive x direction will be derived.

In the case of simple harmonic waves the complex potential may be written in cartesian co-ordinates as

$$\phi_w = \frac{-gH}{2\sigma} \frac{\cosh k(y+h)}{\cosh k.h} e^{ikx} \qquad 3.9.33.$$

Or in cylindrical polar co-ordinates simply

$$\phi_w = \frac{-gH}{2\sigma} \frac{\cosh k(y+h)}{\cosh kh} e^{ikr.\cos\theta} . \qquad 3.9.34.$$

The Bessel functions of integral order may be defined [Sneddon[75] Jeffreys and Jeffreys[46]] as the coefficient of t^n in the expansion of $\exp\left\{\frac{x}{2}(t - \frac{1}{t})\right\}$, in which context they are often known as Bessel coefficients.

The expression for the complex potential is shown in appendix A.1. to be expandable in Bessel coefficients

$$\phi_w = \frac{-gH}{2\sigma} \frac{\cosh k(y+h)}{\cosh kh} \left[Jo(kr)+2 \cdot \sum_{n=1}^{\infty} i^n Jn(kr)\cos n\theta\right] \qquad 3.9.35.$$

3.10. The Green's function

For most numerical work using the Green's function the infinite integral is inconvenient. Monacella[60] has shown a numerical scheme for evaluating the integral by removing the singularity and then evaluating the infinite integral as an infinite series of integrals which is truncated in accordance with a convergence criterion. Each integral term of this series is evaluated numerically using the $\frac{3}{8}$ rule. Most numerical work has relied heavily, to date, on the equivalent series form of G derived by John[47].

The derivation relies on the use of an identity relating the fundamental solution R^{-1} to the Bessel function of the first kind of zero order. In general

$$\frac{1}{(a^2+b^2)^{\frac{1}{2}}} = \int_0^\infty e^{-b\mu} Jo(\mu a)\, d\mu \qquad 3.10.1.$$

which is valid for positive b. (Watson[82] and appendix A.6).

Consider now the following form of the fundamental solution

$$G = \frac{1}{R} + \frac{1}{R'} + \int_0^\infty \frac{2(\mu+\nu)e^{-\mu h}\cosh\mu(b+h)\cosh\mu(y+h)\, Jo(\mu r)}{\mu\sinh\mu h - \nu\cosh\mu h}\, d\mu \qquad 3.10.2.$$

where it is recognised that the contribution from the positive real root of the denominator is avoided by letting the path of integration follow a small semi-circle in the complex plane below the root. Making use of relation 3.10.1. the two singular functions may be taken under the integral sign to give

$$G = \int_0^\infty \frac{2\cosh\mu(b+h)(\mu\cosh\mu y + \nu\sinh\mu y)\, Jo(\mu r)\, d\mu}{\mu \sinh\mu h - \nu\cosh \mu h} \qquad 3.10.3.$$

The integrand may be expanded as an infinite series of terms by the method of partial fractions, whereby there is one term associated with each of the roots of the denominator. The real roots of $\mu\tanh\mu h - \nu = 0$ are equal and opposite, since if

$\mu = -t$, $-t \tanh(-th) - \nu = t.\tan h(th) - \nu = 0$

The imaginary roots of

$$\mu\tanh\mu h - \nu = 0$$

are found by putting $\mu =$ is from which

is $\tanh(ish) - \nu = isi \tan(sh) - \nu = 0$

therefore $s \tan sh + \nu = 0$

and again $-s \tan -sh + \nu = s \tan sh + \nu = 0$

All the roots may then be expressed as

$$\mu = \pm m_k ; \; k = 0, 1, 2 \ldots\ldots , \qquad 3.10.4.$$

where m_o is the real positive root.

The following expansion for the integrand results

$$4J_o(\mu r) \sum_{k=0}^{\infty} \frac{\mu}{\mu^2 - m_k^2} \cdot \frac{m_k^2 - \nu^2}{h(m_k^2 - \nu^2) + \nu} \cosh m_k(y+h) \cosh m_k(b+h) \qquad 3.10.5.$$

where the terms involving corresponding positive and negative roots have been combined. By substituting this series in place of the integrand above and integrating term by term John arrives finally at the following series form of G

$$G = 2\pi i \sum_{k=0}^{\infty} \frac{m_k^2 - \nu^2}{h(m_k^2 - \nu^2) + \nu} \cosh m_k(y+h) \cosh m_k(b+h)\, H_o^{(1)}(m_k r) \qquad 3.10.6.$$

where $H_o^{(1)}(x)$ is the Hankel function of the first kind and zero order.

The Hankel function is related to $J_n(x)$ and $Y_n(x)$ by

$$H_n^{(1)}(x) = J_n(x) + i\, Y_n(x) \qquad 3.10.7.$$

where $Y_n(x)$ is Weber's Bessel function of the second kind. John calls this $N_n(x)$. The modified Bessel function of the second kind $K_n(x)$ is related to the Hankel function by [Jeffreys and Jeffreys [46]]

$$K_n(x) = \frac{\pi i}{2} e^{\frac{n\pi i}{2}} \cdot H_n^{(1)}(x.e^{\frac{\pi i}{2}}) \qquad 3.10.8.$$

for n = 0

$$K_o(x) = \frac{\pi i}{2} H_0(ix) \qquad 3.10.9.$$

The Green's function may be written

$$G = 2\pi i \frac{m_o^2 - \nu^2}{h(m_o^2 - \nu^2) + \nu} \cosh m_o(y+h) \cosh m_o(b+h) \left[J_o(m_o r) + i Y_o(m_o r) \right]$$

$$+ 2\pi i \sum_{k=1}^{\infty} \frac{m_k^2 - \nu^2}{h(m_k^2 - \nu^2) + \nu} \cosh m_k(y+h) \cosh m_k(b+h) H_o^{(1)}(m_k r) \qquad 3.10.10.$$

by separating the contributions from real roots and imaginary roots. Noting that m_k are the imaginary positive roots, replace m_k with im_k where now m_k is real to obtain

$$G = 2\pi i \frac{m_o^2 - \nu^2}{h(m_o^2 - \nu^2) + \nu} \cosh m_o(y+h) \cosh m_o(b+h) \left[J_o(m_o r) + i Y_o(m_o r) \right]$$

$$+ 4 \sum_{k=1}^{\infty} \frac{m_k^2 + \nu^2}{h(m_k^2 + \nu^2) - \nu} \cos m_k(y+h) \cdot \cos m_k(b+h) K_o(m_k r) \qquad 3.10.11.$$

This is the form quoted by Wehausen and Laitone[84], and Isaacson[40], where the m_k are now the real positive roots of

$$m_k \tan m_k h + \nu = 0 \qquad 3.10.12.$$

3.11. The integral equation

The scattered potential generated by constructing a distribution of pulsating sources over a surface S.

$$\phi_s(x, y, z) = \int_S f(a, b, c).\ G(x, y, z; a, b, c)dS \qquad 3.11.1.$$

will satisfy all the boundary conditions of the wave problem except those on the boundary of the immersed structure. Since G is singular like R^{-1} as $R \to 0$ then

$$\frac{\partial \phi_s}{\partial n}(x, y, z) = \int_S f(a, b, c)\ \frac{\partial G}{\partial n}\ dS - 2\pi f(x, y, z). \qquad 3.11.2.$$

as before.

On the surface of the structure the kinematic boundary condition is

$$\frac{\partial \phi}{\partial n} = V_n = \frac{\partial \phi_s}{\partial n} + \frac{\partial \phi_w}{\partial n} \qquad 3.11.3.$$

Where V_n is the velocity of the boundary along an inward normal direction with respect to the fluid domain.

Because the problem is linear the traditional procedure has been to assume that the scattered potential is made up of that due to the presence of the stationary object under the influence of the incident wave, plus that due to the motion of the object in otherwise still water. The latter is called the radiated potential and the former will continue to be referred to as the scattered potential to avoid confusion when referencing other work. The boundary condition then becomes

$$V_n = \frac{\partial \phi_s}{\partial n} + \frac{\partial \phi_w}{\partial n} + \frac{\partial \phi_R}{\partial n} \qquad 3.11.4.$$

Separating according to the definitions above

$$\frac{\partial \phi_R}{\partial n} = V_n \qquad 3.11.5.$$

and $$\frac{\partial \phi_s}{\partial n} = \frac{-\partial \phi_w}{\partial n} \qquad 3.11.6.$$

are the boundary conditions for the two parts of the unknown potential. The scattered potential may be found as the solution of the Neumann problem

$$\int f \cdot \frac{\partial G}{\partial n} dS - 2\pi f(x, y, z) = -\frac{\partial \phi_w}{\partial n}(x, y, z) \qquad 3.11.7.$$

Once the source distribution f is known, the scattered potential may be calculated at any point by backsubstitution as before. With ϕ_s and hence ϕ known at any point, other results of interest may be derived. In particular, the fluid hydrodynamic pressure may be found from the linearised Bernoulli equation

$$\begin{aligned} p &= -\rho \frac{\partial \Phi}{\partial t} \\ &= Re\left\{ -\rho\phi \cdot -i\sigma e^{-i\sigma t} \right\} \\ &= Re\left\{ j\rho\sigma\phi e^{-i\sigma t} \right\} \end{aligned} \qquad 3.11.8.$$

The forces and moments on an immersed object may be found by integration of these pressures. Garrison et al[26] have used the resulting potential to define velocities and accelerations along the axis of a thin object for subsequent application of Morison's equation. Monacella[60] calculated pressures on the bed caused by the presence of an object.

CHAPTER 4 DIFFRACTION COMPUTER PROGRAM

4.1. Introduction

The theoretical formulation on which this chapter is based is applicable to quite general boundary geometries. However, for the purposes of testing the use of quadratic variation of source intensity, as well as facilitating program debugging the vertical circular cylinder has many advantages.

With very little input data the whole of the coordinate geometry may be automatically generated, so avoiding the problems of checking large quantities of input data. This in turn makes it possible to conduct parametric studies.

Numerical integration is also more easily accomplished, since the mapping of a cylindrical element onto the Gaussian quadrature range is achieved directly, using cylindrical polar coordinates.

The most important advantage is the availability of an exact solution which relies on exactly the same mathematical assumptions as the numerical method.

Once the numerical method has been verified, the program may be extended to accommodate other boundary shapes by using the established techniques of the Finite Element Method.

4.2. Separation of the source boundary

In chapter 3 it was shown how separating the boundary on which the kinematic condition is prescribed, from the fictitious boundary on which the source distribution is placed can lead to increased accuracy. In the context of wave diffraction this has been done (Boreel[9], van Oortmerssen[67] and others) primarily to avoid the so called 'irregular frequencies'.

For a given geometry and boundary condition there are always two distinct solutions, the usual one of interest in wave diffraction is exterior to the boundary. But the solution in the closed interior is always available if required. If the interior region possesses a free surface then there may be certain wave frequencies which correspond to standing wave modes or eigenvalue solutions. In such cases the matrix to be inverted will inevitably be singular and so neither solution can be obtained.

One way of deliberately avoiding this problem proposed by Ursell[77], is discussed in chapter 2. Murphy[63] gives the particular values of incident wave frequency at which this problem may occur for a circular cylinder. In general, for the lowest possible frequency, the standing wave length must be of the order of twice the longest length of the geometry or ka must be at least 1.5. In reality, this corresponds to very large structures.

Physical reasoning suggests perhaps the most obvious technique for avoiding this problem. If the kinematic condition of zero flow across that portion of the still water contained in the interior, is additionally prescribed, then all wave motion in the interior is prevented at the expense of a few more equations.

Mathematically, the possibility of non-trivial eigenvalues corresponds directly to the 'diagonal term' which makes the integral equation one of the second kind. Defining a separate source boundary removes this term and so eigenvalue solutions are not possible. The integral equation is now of the first kind and is unfortunately no longer so well conditioned.

For a stationary immersed object in waves the integral equation (3.11.7) becomes

$$\int f \frac{\partial G}{\partial n} \, dS = \frac{-\partial \phi_w}{\partial n}(x, y, z) \qquad 4.2.1.$$

where the point (x,y,z) is on the physical boundary P, and the complex source distribution f is on the fictitious boundary S.

This integral equation is the basis of the numerical formulation used here. It is difficult to prove uniqueness for integral equations of the first kind, but it is possible to put forward physically reasonable arguments for particular boundary shapes. It seems likely that a wide class of problems must be excluded. In particular, structures with sharp edges cannot be expected to yield the correct results unless some singular behaviour is allowed at these edges.

In many cases in which diffraction forces predominate, the corners may be artifically rounded. It is likely that the nearest singular behaviour will occur at the local centre of curvature of these corners. Provided that the fictitious source boundary is always closer to the physical boundary than the local radius of curvature, then reasonable results may be obtained.

Boreel[9] applied the constant source 'facet' method to a structure with many sharp edges. He provides no information about the relative positions of his source boundary and his physical boundary, but he mentions that 176 facets were used. Since the kinematic condition is only satisfied at the centre of each facet, the numerical model assumes that sharp corners have a radius of curvature of about half the width of the nearest facet as shown in figure 4.2.1. This may explain some of the discrepancies between his numerical predictions and the experimental results.

The vertical circular cylinder used here is a very special case. As the analytical solution (Appendix A.1) shows, the only singular behaviour required is at the cylinder axis. The source distribution may be placed almost anywhere and accurate results should be obtained, provided always that the cylinder axis is inside the source boundary.

In chapter 3, it was shown that two forms of the Green's function are available. Garrison and Chow[25] recommended that the series form could be used as long as the argument of the Bessel functions exceeds 0.1, since then it converges reasonably quickly. The effects of diffraction do not become important until ka is at least 0.3. If the source distribution is arranged on a co-axial cylinder of radius r_s, then to satisfy this criterion, r_s must be less than two thirds of the cylinder radius a. This restriction may be progressively relaxed as ka increases.

4.3. The series form of the Green's function

The form of the various terms in equation 4.2.1. may now be examined in detail.

For a wave travelling in the positive x direction, the potential is given by equation 3.9.33 as

$$\phi_w = \frac{-gH}{2\sigma} \frac{\cosh m_o(y+h)}{\cosh m_o h} e^{im_o x} \qquad 4.3.1.$$

The normal velocity across the cylinder due to this wave is given by

$$\frac{\partial \phi_w}{\partial n} = \frac{\partial \phi_w}{\partial x} n_x + \frac{\partial \phi_w}{\partial y} n_y \qquad 4.3.2.$$

where n_x and n_y are the direction cosines along the outward normal from the body.

Therefore

$$\frac{\partial \phi_w}{\partial n} = -A \left\{ \frac{\sinh m_o(y+h)}{\cosh m_o h} n_y + i \frac{\cosh m_o(y+h)}{\cosh m_o h} n_x \right\} e^{im_o x} \qquad 4.3.3.$$

where $A = \dfrac{gHm_o}{2\sigma}$

Garrison and Chow[25] leave the constant A out of their analysis for dimensional reasons. This merely leads to a compensating change in the fictitious source intensity function.

The series form of the Green's function is

$$G = 2\pi i(m_o^2 - \nu^2)\ \frac{\cosh m_o(y+h)\cosh m_o(b+h)}{h(m_o - \nu^2)+\nu}\left[J_o(m_o r) + iY_o(m_o r)\right]$$
$$+ 4\sum_{k=1}^{\infty} \frac{m_k^2 + \nu^2}{h(m_k^2+\nu^2)-\nu} \cos m_k(y+h).\cos m_k(b+h)\ K_o(m_k r) \qquad 4.3.4.$$

where $r = \left[(x-a)^2 + (z-c)^2\right]^{\frac{1}{2}}$ is the projection of the distance between the source point (a, b, c) and the point (x, y, z), on the horizontal plane.

The normal velocity across the cylinder due to this source is given by

$$\frac{\partial G}{\partial n} = \frac{\partial G}{\partial x}.n_x + \frac{\partial G}{\partial y}.n_y + \frac{\partial G}{\partial z}.n_z \qquad 4.3.5.$$

where in general the direction cosines are given as input data. For the circular cylinder these are automatically generated within the computer program.

Once the source distribution has been found the scattered potential maybe obtained by back substitution into

$$\phi_s = \int fG\,dS \qquad 4.3.6.$$

Because of the similarities between G and $\frac{\partial G}{\partial n}$, they are calculated in parallel in the computer program. The real and imaginary parts are tested separately, indexed by 1 and 2 respectively. Performing the straightforward differentiations and then simplifying by use of the recurrence relations for the Bessel functions yields the following results. Where possible the same symbols are used as in the program.

$$G_1 = AC \cosh m_o(y+h)\, Y_o(m_o r) + \sum_{k=1}^{\infty} C \cos m_k(y+h)\, K_o(m_k r) \qquad 4.3.7.$$

$$G_2 = -AC \cosh m_o(y+h)\, J_o(m_o r) \qquad 4.3.8.$$

$$\frac{\partial G_1}{\partial x} = D(x-a)\, Y_1(m_o r) - \sum_{k=1}^{\infty} C\, m_k \left(\frac{x-a}{r}\right) \cos m_k(y+h)\, K_1(m_k r) \qquad 4.3.9.$$

$$\frac{\partial G_2}{\partial x} = -D(x-a)\, J_1(m_o r) \qquad 4.3.10.$$

$$\frac{\partial G_1}{\partial y} = E.Y_o(m_o r) - \sum_{k=1}^{\infty} C.m_k.\sin m_k(y+h)\, K_o(m_k r) \qquad 4.3.11.$$

$$\frac{\partial G_2}{\partial y} = -E.J_o(m_o r) \qquad 4.3.12.$$

$$\frac{\partial G_1}{\partial z} = D.(z-c)\, Y_1(m_o r) - \sum_{k=1}^{\infty} C\, m_k \left(\frac{z-c}{r}\right).\cos m_k(y+h).K_1(m_k r) \qquad 4.3.13.$$

$$\frac{\partial G_2}{\partial z} = -D\,(z-c).\, J_1(m_o r) \qquad 4.3.14.$$

where $D = -AC \dfrac{m_o}{r}.\cosh m_o(y+h)$

$E = AC.\, m_o.\, \sinh m_o(y+h)$

$$AC = \frac{2\pi(\nu^2 - m_o^2)}{h(m_o^2 - \nu^2) + \nu} .\cosh m_o(b+h)$$

$$C = \frac{4(m_k^2 + \nu^2)}{h(m_k^2 + \nu^2) - \nu} .\cos m_k(b+h)$$

Here the real positive root m_o is identical to the wave number k used elsewhere. The notation used here is that of Wehausen and Laitone[84].

If the input data for a particular problem includes the incident wavelength rather than the period then m_o is fixed, and from it may be calculated the frequency

$$\sigma^2 = g m_o \tanh m_o h = \nu g \qquad 4.3.15.$$

The real positive roots of

$$m_k \tan m_k h + \nu = 0 \qquad 4.3.16.$$

must still be found. The roots are most easily identified by defining a new set of non-dimensional roots.

$$X_k = m_k h \qquad 4.3.17.$$

and rearranging equation 4.3.16. into the form

$$\tan X_k + \frac{h\nu}{X_k} = 0 \qquad 4.3.18.$$

The positions of the roots of this equation on the X axis are shown in figure 4.3.1.

Tne Newton-Raphson method was applied to find the roots X_k, using as the initial guess for each one, the previous root plus π. The initial guess for the first root X_1 is a minor difficulty, since it is always greater than $\frac{1}{2}\pi$ but by an initially unknown amount. If the initial guess is greater than X, then there is no guarantee that the iterative procedure will converge to the correct root.

Of the many possibilities the one chosen here was to define the 'residual' function as

$$\psi(X) = \tan X + \frac{h\nu}{X} \qquad 4.3.19.$$

Examination of figure 4.3.1. shows that the Newton-Raphson procedure will converge to X_1 provided that the initial guess is in the range $\frac{1}{2}\pi < X^0_1 < X_1$. The continued fraction

$$X = \pi + \frac{1}{\frac{2}{\frac{1}{2}\pi} + \frac{1}{\frac{2}{\frac{1}{2}\pi} + \frac{1}{2}}} \qquad \ldots\ldots 4.3.20.$$

will eventually be in this range. This fraction is repeatedly substituted into equation 4.3.19. until the function ψ becomes negative. The value of X when this happens is then used as the initial guess for the following Newton-Raphson algorithm

$$\psi^r = \tan X^r_k + \frac{h\nu}{X^r_k} \qquad 4.3.21.$$

$$\left(\frac{\partial\psi}{\partial X}\right)^r_k = \sec^2 X^r_k - \frac{h\nu}{(X^r_k)^2} \qquad 4.3.22.$$

$$\Delta X^r_k = -\psi^r / \left(\frac{\partial\psi}{\partial X}\right)^r_k \qquad 4.3.23.$$

$$X^{r+1}_k = X^r_k + \Delta X^r_k \qquad 4.3.24.$$

Because of the method of choosing the initial guesses (X^0_k) the correction in equation 4.3.23. is always positive. When the correction is found to be in the range

$$0 < \Delta X^r_k < \text{ALIM}$$

the iteration is stopped. The required root is then obtained from equation 4.3.17.

4.4. Bessel function evaluation

To evaluate equations 4.3.7. to 4.3.14. the Bessel functions J_0, J_1, Y_0, Y_1, K_0 and K_1 are required. On many mainframe computers mathematical packages are available for calculating these functions. It is unfortunately all too easy to obtain answers from a package with no knowledge of the governing theoretical assumptions. Hence, all the Bessel functions used in the diffraction computer program were calculated by a separate FORTRAN function segment called BESS. This is listed in appendix A.3.

The call statement is made by using the word BESS as a function with three arguments, for example

```
A = BESS (K, N, X)
```

where K is an integer in the range 2 to 5, used to indicate the kind of function.

For $I_N(X)$, K = 2 ; $J_N(X)$, K = 3 ; $K_N(X)$, K = 4 and $Y_N(X)$, K = 5. N is the positive order of the function and X is its argument. The function segment is more general than required by this application since N can have any positive integral value.

The change between the power series expansion for small X and the asymptotic expansion for large X is made at X = 9. This corresponds to the point at which both series require roughly the same number of terms for convergence to a given accuracy.

The convergence criterion for small argument is quite straightforward. For large argument an asymptotic series always diverges having first (unless X is too small) attained a minimum. It may be shown (e.g. Jeffreys and Jeffreys[46]) that the error in the sum of an asymptotic series is less than the first term neglected. Accurate assessment of the sum requires that the smallest term be found and the sum stopped one term before it.

In the case of the Bessel functions each term in the series is calculated from the previous one by multiplying it by a term dependent factor. The minimum is therefore, most easily established by testing for this factor exceeding unity.

For quite large arguments, this check alone would give unnecessarily high accuracy. In these cases, the series is truncated prematurely by the same convergence check as for small arguments.

There are several forms of notation in the literature when referring to Bessel functions. The definitions used in this function segment are explained in appendix A.4. This function segment has been thoroughly tested against the extensive tables in Watson's[82] treatise.

4.5. Numerical Formulation

The numerical solution of equation 4.2.1. is achieved by restricting the source distribution to a finite number of degrees of freedom. The fictitious cylinder on which the source distribution is placed is split into a number of elements and the variation of source intensity is assumed to be defined in terms of the values at the nodes of each element.

The bi-quadratic variation used here is illustrated in figure 4.5.1. Each element has 9 nodes.

Because of the banded nature of Finite Element equations, the equation corresponding to the middle node of a 9 node element, only involves contributions from the nodes in that particular element. The number of equations in the overall system may therefore be reduced by the technique of nodal condensation, whereby the 9 equations corresponding to this element are reduced to 8 by eliminating the middle unknown. The 8 node isoparametric element is often used instead to avoid this complication.

In the Boundary Element technique used here, the matrices are fully populated because every point on the prescribed boundary feels the effect of every point on the source distribution. The 9 node element was used in this case, because it simplifies the automatic generation of nodal coordinates.

The source intensity within an element may be expressed as

$$f(x, y, z) = N_i(x, y, z).\ f_i \qquad 4.5.1.$$

where the repeated index is used to imply summation up to nine, and the source intensities at the nodes (f_i) are complex. The interpolation or shape functions (N_i) are most easily defined in a natural coordinate system (ξ, η) as shown in figure 4.5.1. The bi-quadratic variation is obtained as the product of a quadratic Lagrange interpolation function in each coordinate direction as

$$\phi_{IJ} = L_{I\eta} \cdot L_{J\xi}; I, J = 1, 2, 3 \qquad 4.5.2.$$

where $L_{1\xi} = \xi(\xi - 1)/2$

$L_{2\xi} = 1 - \xi^2$

$L_{3\xi} = \xi(\xi + 1)/2$

and similarly for the η direction. This coordinate system also corresponds to that in which the Gaussian quadrature formula is defined. The functions ϕ_{IJ} and N_i are related through

$$N_i = \phi_{IJ} \qquad 4.5.3.$$

where

$$i = 3(I - 1) + J$$

If the real and imaginary parts of all complex quantities are identified by the subscripts 1 and 2 respectively then the integral equation 4.2.1. becomes

$$\int (f_1 + if_2)\left(\frac{\partial G_1}{\partial n} + i\,\frac{\partial G_2}{\partial n}\right) ds = -\frac{\partial \phi_{w1}}{\partial n} - i\,\frac{\partial \phi_{w2}}{\partial n} \qquad 4.5.4.$$

Equating real and imaginary parts yields the pair of coupled integral equations

$$\int f_1 \frac{\partial G_1}{\partial n} - f_2 \frac{\partial G_2}{\partial n} \, dS = -\frac{\partial \phi_{w1}}{\partial n} \qquad 4.5.5.$$

$$\int f_1 \frac{\partial G_2}{\partial n} + f_2 \frac{\partial G_1}{\partial n} \, dS = -\frac{\partial \phi_{w2}}{\partial n} \qquad 4.5.6.$$

These may now be discretised by substituting for the source intensity functions from equation 4.5.1. In matrix form they become

$$\left[\begin{array}{c|c} \int N_i \frac{\partial G_1}{\partial n} \, dS & -\int N_i \frac{\partial G_2}{\partial n} \, dS \\ \hline \int N_i \frac{\partial G_2}{\partial n} \, dS & \int N_i \frac{\partial G_1}{\partial n} \, dS \end{array}\right] \cdot \left\{\begin{array}{c} f_{1i} \\ f_{2i} \end{array}\right\} = \left\{\begin{array}{c} -\frac{\partial \phi_{w1}}{\partial n} \\ -\frac{\partial \phi_{w2}}{\partial n} \end{array}\right\}, \qquad 4.5.7.$$

This equation system is of the form

$$\left[\begin{array}{c|c} A & -B \\ \hline B & A \end{array}\right] \cdot \left\{\begin{array}{c} f_1 \\ f_2 \end{array}\right\} = \left\{\begin{array}{c} W_1 \\ W_2 \end{array}\right\} \qquad 4.5.8.$$

Therefore, only submatrices [A] and [B] need be stored. Hogben and Standing[33] showed how advantage may be taken of the form of these equations to avoid inverting the large matrix. This involves solving for the real (or imaginary) parts first from half of the equations and then backsubstituting to obtain the imaginary (or real) parts from the other half. Four distinct possibilities exist depending on which submatrix is inverted and which set of unknowns is eliminated. One such possibility is

$$f_2 = [A]^{-1}\{W_2 - [B]\ f_1\} \qquad 4.5.9.$$

and hence

$$f_1 = \left[[A] + [B].[A]^{-1}.[B]\right]^{-1}\left\{W_1 + [B].[A]^{-1}\ W_2\right\} \qquad 4.5.10.$$

If one of the submatrices is found (or known) to be singular then this one need never be inverted. Each inversion only involves a matrix of the size of each submatrix. Since the number of operations required to invert a N x N matrix is roughly proportional to N^2, then this procedure may be expected to halve the computation time.

Because matrices [A] and [B] are fully populated, the use of a direct inversion technique may not be the most efficient. Fenton[23] showed that, for integral equations of the second kind, the diagonal dominance of the overall matrix makes an iterative method such as Gauss-Siedel converge rapidly. This method is also more suitable for use with disk backing store. The elements of the overall matrix are not changed, but simply read repeatedly from the disk. This means that sequential file storage could be used. On most computers this is a more efficient way of accessing and storing data.

The integral equation used here is of the first kind. The more refined the element mesh, the less dominant are the diagonal terms. Attempts were made to use Gauss-Siedel iteration but convergence was extremely slow. A linear convergence accelerator was also included but in many cases this did not improve the situation.

The computer program,as shown in the listing,uses a Gaussian elimination technique applied directly to equation 4.5.7. Although it is recognised that this application is not the most efficient, the computer time devoted to solving the equation system is an insignificant part of the total.

Once the source intensities at the nodes have been found, the scattered potential is calculated from the discretized form of equation 4.3.6.

$$\begin{Bmatrix} \phi_{S1} \\ \phi_{S2} \end{Bmatrix} = \left[\begin{array}{c|c} \int N_i G_1 \, dS & -\int N_i G_2 \, dS \\ \hline \int N_i G_2 \, dS & \int N_i G_1 \, dS \end{array}\right] \begin{Bmatrix} f_{1i} \\ f_{2i} \end{Bmatrix} \qquad 4.5.11.$$

which is of the form

$$\begin{Bmatrix} \phi_{S1} \\ \phi_{S2} \end{Bmatrix} = \left[\begin{array}{c|c} C & -D \\ \hline D & C \end{array}\right] \begin{Bmatrix} f_1 \\ f_2 \end{Bmatrix} \qquad 4.5.12.$$

In general the argument of the Green's function is (x, y, z; a, b, c) where (a, b, c) are the cartesian coordinates of the integration point on the source boundary, and (x, y, z) is any point outside the physical boundary. In this case, the L.H.S. vector contains only two values. The equations would be used in this form if, for example, the wave height at some point on the fluid surface (y = 0) were being calculated.

Although this calculation could be appended to the existing program the most important quantities of interest are the pressures on the cylinder and the total force and moment. These may be calculated once the scattered potential is known at the nodal points on the physical cylinder. This is not the only possibility, but it is certainly the simplest since the coordinates of these points are also required for the calculation of the source intensities. In this context the L.H.S. of equation 4.5.11 will be the same size as the vector on the R.H.S.

Because of the lack of diagonal dominance and the possibilities of round off error with a direct elimination technique, most of the variables were stored in double precision. Matrices [A] [B] [C] and [D] therefore represent a considerable storage problem. For most cases, the computer resident memory was insufficient. These matrices were therefore stored in disk backing store, as random access files.

A typical integral over an element on the source boundary is of the form

$$I = \int_e N_i \cdot \frac{\partial G_m}{\partial n} \, dS \, f_{li} \qquad 4.5.13.$$

where m and l can be either 1 or 2. For the nine nodes used here this may be expanded as

$$I = \int_e N_1 \cdot \frac{\partial G_m}{\partial n} \, dS \cdot f_{l1} + \ldots + \int_e N_9 \frac{\partial G_m}{\partial n} \, dS \, f_{l9} \qquad 4.5.14.$$

The complexity of each integrand makes it impossible to attempt an exact integration. Each integral may be evaluated using Gaussian quadrature. To do this, the variables of integration must be more clearly defined. In general the integral would have to be transformed onto the (ξ, η) plane by numerically evaluating the Jacobian of the transformation. In the particular case of a circular cylinder the transformation is made especially simple by the use of cylindrical polar coordinates. If α is half the angle swept by the element, Δ is half its vertical dimension and r_s is the radius of the source cylinder, then each term may be transformed thus

$$\int_e N_i \frac{\partial G_m}{\partial n} dS = \int_{-\Delta}^{\Delta} \int_{-\alpha}^{\alpha} N_i \frac{\partial G_m}{\partial n} r_s \, d\theta dy$$

$$= r_s \Delta\alpha \sum_{k=1}^{9} W_k \left(N_i \frac{\partial G_m}{\partial n}\right)_k \qquad 4.5.15$$

where $(\ )_k$ means the value of the function in parentheses at sample point k, and W_k is the Gaussian weighting factor. Figure 4.5.2. shows the positions of the sample points and weights for the 3 x 3 quadrature used here. The nine point quadrature scheme was chosen primarily because it corresponded with the use of nine nodal points and not because the integrand was known to require it. The form of the Green's function makes it difficult to estimate the order of the equivalent polynomial. Nevertheless the distance between the points (a, b, c) and (x, y, z) is always large enough to justify the use of a polynomial based method. In application where this distance is small, the singular behaviour of the fundamental solution must be taken into account.

4.6. Details of computer program

The main segment of the computer program is listed in appendix A.3. The following is a short explanation of how it is constructed. The variable names in the program are also listed in appendix A.3 Every attempt has been made to use names which correspond with the symbols used in the text. Alternatively, the name has been chosen as a mnemonic.

The two coordinate systems utilized are defined in figure 4.6.1. together with an example of the node numbering system. The origin of both is in the still water level with the y axis directed positive upwards. The waves are assumed to be travelling in the positive x direction in water of constant depth.
The structure geometry consists of two co-axial circular cylinders, the outer one corresponding to the physical boundary has a radius PRAD. The inner one on which the fictitious source distribution is placed has a radius SRAD which is generated by the input factor ZK.

Each cylinder is equally divided into the same number of surface elements specified by the number in the horizontal plane (NIH) and in the vertical plane (NIV). The total number of elements is therefore.

$$NE = NIV * NIH \qquad 4.6.1.$$

In the present formulation the boundary conditions are only satisfied at the nodal points, so that the elements on the physical cylinder are not used directly. It is conceivable that the boundary conditions could be satisfied in a weighted residual sense, in which case, these elements would take on a greater significance.

The nodes of these elements take on a different role depending on which cylinder is involved. On the source cylinder they correspond to the finite number of values of source intensity. On the physical cylinder the node numbering system is identical but each point corresponds to one complex equation satisfying the kinematic condition. The total number of nodes is

$$N = 2 * NIH * (1 + 2 * NIV) \qquad 4.6.2.$$

because of the mid-side nodes.

The node numbering system on the outer cylinder starts at the point

$$(x, y, z) = (PRAD, 0, 0) \qquad 4.6.3.$$

and completes one rotation in the horizontal plane before jumping down to the next horizontal level.

In generating meshes for Finite Element programs, the node numbering sequence is extremely important in defining the bandwidth of the overall matrix. Strictly speaking, the numbering sequence does not matter for the fully populated Boundary Element matrices. However, the presence of Bessel functions in the Green's function implies that, on average, the smaller the argument the larger the value. By ensuring that the two sequences have the same number on each radial line the matrix diagonal coefficients are made as large as possible, on average.

The generation of the coordinates on this regular mesh is achieved through the use of the two increments ALPHA in the rotational sense and DEL in the vertical direction.

A general element on the source cylinder has a local numbering system from 1 to 9 as shown in figure 4.5.1. This is related to the global numbering system through the vector NNS. This vector is then used to define the positions in each equation where the contributions from each integral must be accumulated. The coordinates of the corner nodes of these elements are never calculated. The coordinates of the middle nodes are

$$(r, \theta, y) = (SRAD, GAMA, YMID) \qquad 4.6.4.$$

From these the coordinates of the Gaussian sampling points are calculated using the non-dimensional factor GAUSS (in this case $\sqrt{0.6}$) and the two increments.

The majority of the program is involved with the calculation of the matrix elements and their storage. The three pairs of large nested loops which go to make up this section are explained in the form of a simplified flow chart in figure 4.6.2. Each pair of loops corresponds to the vertical and angular coordinate directions. The core store required is significantly reduced by generating the coordinates only when required.

To minimise the time involved in transferring data to disk the coefficients are stored in vectors corresponding to the real and imaginary parts of matrices [A], [B], [C] and [D]. By making the outermost pair of loops correspond to each boundary condition on

the physical cylinder, each equation can be accumulated in a ROW vector before transfer. These ROW vectors are then overwritten by the next equation. The data transfer to disk is via channel number 3.

The contribution from a typical element was shown in equation 4.5.14. to comprise nine separate integrals each of which is numerically integrated by sampling at nine points. Because, for a given sample, the same Green's function contribution occurs in each integral, it is more efficient to calculate all nine integrals in parallel, one sample point at a time, rather than completing each separate integral before proceeding to the next.

That is, equation 4.5.15 is evaluated as

$$I = \int_e N_i \frac{\partial G_m}{\partial n} dS \quad f_{li} = \sum_{k=1}^{9} W_k \left[\sum_{i=1}^{9} (N_i \frac{\partial G_m}{\partial n})_k \quad f_{li} \right] \qquad 4.6.5.$$

rather than

$$I = \sum_{i=1}^{9} f_{li} \left[\sum_{k=1}^{9} (N_i \frac{\partial G_m}{\partial n})_k \quad W_k \right] \qquad 4.6.6.$$

Once all the contributions from the elements on the source boundary have been accumulated for each node on the physical boundary the disk backing store is re-arranged in the form of equation 4.5.8. The complete system of equations is then solved for the source strengths, using a standard Gaussian elimination technique, augmented by the need to read in two ROWS at a time from disk.

The scattered potential ϕ_s is then combined with the incident wave potential at each node. The pressure may then be evaluated from equation 3.11.8. as

$$p_1 + ip_2 = \rho i\sigma \, (\phi_w + \phi_s)$$

$$= \rho\omega \left[\phi_{w2} + \phi_{s2} - i\,(\phi_{w1} + \phi_{s1})\right] \qquad 4.6.7.$$

This enables the real and imaginary parts of the total force to be calculated separately and then combined to obtain the maximum. Figure 4.6.3. shows how the total force was calculated by assuming the pressure at a node to act at a constant value over its area of influence.

4.7. Numerical details

The aim of using a bi-quadratic variation of source strength was to enable accurate numerical results to be obtained with a smaller number of equations. This should lead to significant savings in computation time, over the traditional facet method.

A further advantage of this choice is the ability to accurately model curved boundary geometries. In this particular application, to the circular cylinder, the curved boundaries are exactly modelled as circular arcs. In general applications, a transformation from curvilinear coordinates to plane cartesian cooridnates would fit a circular arc with a portion of a parabola. In other words, if this program was modified to accommodate general boundary geometries, and then applied to the circular cylinder, the results would be slightly different from those obtained here.

Most of the comparisons between numerical and theoretical results will be based on the non-dimensionalised total in-line force. It is often suggested (e.g. Isaacson[40]) that this is not a particularly severe test of the numerical method since the only contribution to the in-line force is from the first cosine term in the infinite series. For this reason some numerical pressures are also compared with the theoretical results calculated using appendix A.1.

The exact expression for the total force may be found by integration of this pressure. Chakrabarti and Tam[15] give the result

$$\frac{F}{\frac{1}{2}\rho g a^2 H} = \frac{4A(ka)}{(ka)^2} \cdot \tanh\left(ka.\frac{h}{a}\right) \cdot \cos(\sigma t - \alpha) \qquad 4.7.1.$$

where $$\alpha = \tan^{-1}\left[\frac{J_1'(ka)}{Y_1'(ka)}\right]$$

and $$A(ka) = \left[J_1'(ka)^2 + Y_1'(ka)^2\right]^{-\frac{1}{2}}$$

This force is a function of both ka and $\frac{h}{a}$. For fixed ka, the ratio $\frac{h}{a}$ appears only as a simple multiplying factor. All the numerical results were obtained for a depth of four times the cylinder radius. Table 4.7.1. shows the exact results for the range $0 < ka < 4.00$, and $\frac{h}{a} = 4.0$. Any other results may therefore be obtained by multiplying by tanh(kh)/tanh (4ka).

Tables 4.7.2a to 4.7.2f show the numerical results obtained from the computer program. These are in the form of an incomplete parametric study. The four parameters are, the position of the source cylinder defined by ZK (see appendix A.3), the wavelength parameter ka which is a measure of the amount of diffraction, the number of elements and the accuracy limit for convergence of the infinite series (ALIM).

The parameter ALIM would normally remain fixed to ensure convergence to the required number of significant figures. However, in this case, the amount of computation time required is related almost directly to this parameter. To obtain results for the 16 element cases, the convergence criterion had to be relaxed.

As the number of elements is increased, all other things being equal the results should converge to the exact solution. Because of the restrictions of computer time, the effect of this parameter is not so obvious.

As shown in chapter 3 the accuracy of the numerical results improves as the source boundary is moved away from the physical boundary. Figure 4.7.1. shows how the results for fixed ka converge as ZK is reduced towards zero. For a larger number of elements, this convergence is towards a more accurate value for these particular values of ka. However, there is a surprising jump in some of the 4 element results between the values of 0.5 and 0.6, which must be attributable to the larger value of ALIM in this case.

This effect is highlighted in figure 4.7.2. The results on the upper graph are obviously not affected by the accuracy limit. On the lower graph it is clear that the accuracy limit is not sufficently strict. When the number of elements is increased from 4 to 16 the forces become completely unreliable in a restricted range approximately $0.2 < ka < 1.0$.

From the equations 4.3.7. to 4.3.14. it will be seen that there are three distinct infinite series involved in the calculation of the Green's function and its derivatvies. These are

$$S_1 = \sum_{k=1}^{\infty} C m_k \cos m_k(y+h) \cdot K_1(m_k r) \qquad 4.7.2.$$

$$S_2 = \sum_{k=1}^{\infty} -C m_k \sin m_k(y+h)\ K_0(m_k r) \qquad 4.7.3.$$

$$S_3 = \sum_{k=1}^{\infty} C \cos m_k(y+h)\ K_0(m_k r) \qquad 4.7.4.$$

where the factor

$$C = \frac{4(m_k^2+\nu^2)}{h(m_k^2+\nu^2)-\nu} \cos m_k(b+h) \qquad 4.7.5.$$

has the dimensions of $(\text{Length})^{-1}$. In the program from which these numerical results were obtained it was (incorrectly) assumed that convergence of series S_1 would be slower than the other two because of the presence of $K_1(m_k r)$. In fact series S_1 and S_2 have different dimensions from S_3.

Detailed examination of the results confirmed that the erratic behaviour of the force is caused by the fact that series S_3 has not converged sufficiently when the accuracy check is satisfied. The source intensities were identical (to the four significant figures printed) at corresponding points in the 4 and 16 element cases. The pressures, which rely directly on series S_3, were significantly different.

The convergence criterion was poorly chosen in a misguided attempt to reduce computation time by having one conditional branch instead of three. A much better way of checking convergence is to compare the series term being added with the total, since this is based on the number of significant figures and is not affected by dimensions.

Despite this problem it is clear from the upper graph in figure 4.7.2. that quite remarkable agreement between theoretical and numerical results is obtained with a very coarse discretization.

As ka increases beyond 2 the arguments of the Bessel functions cover an increasingly wide range. The effect of the series terms involving $K_0(x)$ and $K_1(x)$ becomes insignificant. The integrals which are being numerically integrated therefore have more rapidly varying integrands and may therefore require not only a higher order integration scheme but also higher order interpolation functions for the source distribution.

For the constant source 'facet' method it has been generally agreed that at least ten facets must span one wavelength to obtain reasonable accuracy. The more significant discrepancies at these ka values are to be expected since even with 16 elements, each element spans about half of one wavelength. Hogben and Standing[33] explain that,

to obtain reasonable accuracy at these short wave lengths they had to concentrate their facets close to the surface using angular increments of $11\frac{1}{4}^{o}$ and 15^{o}. This is because of the rapid decay of the cosh $m_o(y+h)$ terms for these waves.

The variation of source intensity with depth is shown in figure 4.7.3. for the 16 element case at ka = π. It appears that the quite reasonable agreement shown in figure 4.7.2. for this case has been obtained by effectively only using the top row of four elements.

Tables 4.7.3. and 4.7.4. show a comparison between the numerical and theoretical pressures for two cases, one using 4 elements (20 nodes) and one using 12 elements (56 nodes). The average percentage errors between the two are also compared with the error in the total force. With 4 elements the errors are about the same. In the 12 elements case the pressures appear to show better agreement than the total force would suggest. This must be because of the crude method of integration of the pressures.

The direction cosines and the pressures are available at the nodes of an element mesh which is already defined on the physical boundary. The same interpolation functions which were defining the source distribution may be used as the basis for an improved numerical integration of the pressures.

The contribution to the in-line force from a typical element is given by

$$F_{xe} = -R\int_{-\Delta}^{\Delta}\int_{-\alpha}^{\alpha} P\cos\theta \, d\theta dy \qquad 4.7.6.$$

If it is assumed that the variation of the integrand is biquadratic then

$$P\cos\theta = N_i (P\cos\theta)_i \qquad 4.7.7.$$

the force is therefore transformed to

$$F_{xe} = -\sum_{i=1}^{9} R\alpha\Delta\,(P\cos\theta)_i \int_{-1}^{1}\int_{-1}^{1} N_i \, d\xi d\eta \qquad 4.7.8.$$

Because the N_i are already factorised this reduces simply to the integration scheme

$$F_{xe} = -\frac{R\alpha\Delta}{9}\sum_{I=1}^{3}\sum_{J=1}^{3}(4-3|I-2|)(4-3|J-2|)(P\cos\theta)_{3I+J-3} \qquad 4.7.9.$$

in a form suited to computation.

When this is applied to the pressures in table 4.7.1. the total force evaluated is approximately one third of the correct value. If the scheme is rotated through 90^0 then a value four times larger is obtained. Figure 4.7.4. demonstrates clearly why this should be. This is an example of the possible benefits of 'reduced integration' which is often used in Finite Element work. This integration scheme should become much more accurate as the number of elements is increased. To obtain consistently accurate results the pressure will have to be evaluated, either at more points or at different (Gauss) points.

In view of these difficulties the merits of the approach used in this thesis will be discussed on the basis of the reasonable agreement with pressure.

There is no doubt that, for such a coarse discretization, this agreement has been obtained because of the strong symmetry of the problem. If the physical boundary was irregular, it would be unreasonable to expect accurate results. Whatever order of interpolation is used for the source discretization, the boundary conditions are satisfied at a finite number of points. The resulting potential function will actually satisfy the kinematic condition on a boundary curve which fits smoothly through these points.

Nevertheless, the number of equations required to obtain less than 1% error is somewhat less than the 96 used by Hogben and Standing[33] and the 120 used by Garrison and Chow [25].

The aim of any refinement to the traditional constant source facet method, is to reduce computation time and/or storage. Since storage relates directly to the number of equations then clearly a saving has been made.

Comparisons of computation time are usually difficult to make because they depend on so many factors. However, in this case, the differences between the two approaches may be isolated. Table 4.7.5. shows the numbers controlling the size of the computer program for the three element meshes used here. In the facet method, the number of times that the Green's function is evaluated is proportional to the square of the number of facets, and there is one equation per facet. In this quadratic source method the Green's function is evaluated at every Gauss point of which their are nine on each element. The number of

evaluations is therefore related to the number of nodes multiplied by nine times the number of elements.

For the same number of equations then the facet method is about twice as fast, but the quadratic source method is more accurate.

In an attempt to reduce computation time the numerical integration was reduced to a four point Gauss scheme. However, the accuracy deteriorated dramatically.

Figure 4.7.1. shows that provided a reasonable number of elements is used, (56 in this case) the accuracy is not particularly sensitive to the position of the source boundary. The optimum value for ZK should be about 0.5. The smaller number of equations involved should make this method particularly suitable for studies of interaction between objects. If these objects are smooth (as most offshore structures are) and not too close then no problems should arise. For closely spaced objects, care must be taken to make the source boundary contain the likely position of any images of one object in its neighbour.

Chapter 5 Experimental Apparatus and Results

5.1. Wave flume, generator and absorbing beach.

The experiments were conducted in a glass sided wave flume approximately 16 metres long, 750 millimetres wide with a typical water depth of 500 millimetres. This is shown diagramatically in figure 5.1.1.

The wave generator was of the plunging wedge type. The driving mechanism is illustrated in figure 5.1.2. Previous tests had shown the optimum wedge angle to be about 30^{o}. The mean depth of immersion of the wedge could be varied, but with difficulty, and for these experiments it was fixed so that in its mean position the bottom of the wedge was 19.8 centimetres above the bed. The vertical amplitude of oscillation could be fixed at any value between zero and 12 centimetres and the oscillation frequency was limited by the wave characteristics rather than by the driving mechanism.

The gap underneath the wedge allows a possible back flow which generates waves behind the wedge. In an attempt to damp these down, a board was placed on the rear free surface and its motion restricted by frictional resistance with four vertical bars. This loss of energy contributes to a reduction in the efficiency of this type of generator For higher frequencies the effect of the back flow may be less significant because of the rapid decay of the particle orbits with depth.

There are two advantages of this type of generator. Firstly, there is a possibility of studying the combined effects of waves and

current. Secondly, if the rotational speed of the motor is constant the vertical oscillation has no higher harmonic content. This is in contrast to most piston and paddle type generators which use a rotating crank and connecting arm where the harmonic content is related to the crank : connecting arm ratio. Each harmonic will generate a corresponding free wave which will pollute the main wave shape.

At the other end of the flume the majority of the energy in the waves must be converted into heat and/or a uniform back flow. One way of achieving this is by increasing the steepness of the waves until they break thus dissipating most of their energy. This may be achieved with negligible reflection by gradually reducing the water depth to zero.

The effect of this on the wave steepness may be derived by assuming that the waves behave locally as if the depth is constant. If energy dissipation due to friction with the bed is neglected, then the energy flux is conserved

$$EU = ECn = EC\tfrac{1}{2}\left(1 + \frac{2kd}{\sinh 2kd}\right) = \text{constant} \qquad 5.1.1.$$

Consequently, if there is no accumulation of energy within a fixed control volume the period must also be constant. The dispersion relation relates the behaviour at any depth to that at the constant depth section of the flume d_c,

$$C/C_c = \frac{\lambda}{\lambda_c} = \frac{\tanh kd}{\tanh k_c d_c} \qquad 5.1.2.$$

The ratio of wave steepnesses is therefore given by

$$\frac{kH}{k_c H_c} = \sqrt{\frac{n_c}{n}\left(\frac{\tanh k_c d_c}{\tanh kd}\right)^3} \qquad 5.1.3.$$

This ratio is plotted in figure 5.1.3. against the depth ratio ($^{d}/dc$) for a range of incident wave lengths (λ_c/d_c). This shows that for short waves the steepness initially reduces and only st arts to increase dramatically when the waves 'feel' the bed which is much later than might be expected, because of the reduction in wave length given by equation 5.1.2. The longer waves being already in shallow water get steeper as soon as the depth reduces.

Because of the short wave behaviour many beach designs use a curved profile to reduce the depth to less than half, as quickly as possible. The length scale of the beach must be at least as long as the wave length for the bed slope to be negligible. If it is not, the beach will act as an efficient reflector. This fact combined with the much lower initial steepness of the longer waves (because of the generator characteristics) makes it very difficult to destroy long waves by breaking. Because the velocity variation with depth is almost uniform for long waves, beach designs based on frictional dissipation with the bed are liable to be more successful.

The beach used in these experiments was a straight slope at about 9^{o} up to still water level and then a flat section in a region where the flume widened. The sloping section forced the waves to break and then the flat section dissipated much of the energy of the resulting flow by friction by spreading it over as large an area as possible. This design was successful for waves up to 2 metres long.

However, well the beach is designed some of the wave energy will be reflected back. Typical reflection coefficients obtained in practice are less than 5% which is fortunately small enough for second powers and higher to be negligible (Ursell, Dean and Yu[78]). The wave motion in the middle of the flume may therefore be assumed to be the linear superposition of an incident wave.

$$\eta_I = \alpha \cos(kx - \sigma t) + \alpha\varepsilon\cos(kx - \sigma t - \delta) + O(\varepsilon^2) \quad 5.1.4.$$

and a reflected wave

$$\eta_R = \alpha\varepsilon\cos(kx + \sigma t + \delta) + O(\varepsilon^2) \quad 5.1.5.$$

The importance of the second term in the incident wave, due to the assumed perfect reflection at the generator, is often not recognised, on the incorrect assumption that it is of higher order (Keating and Webber[49]). Simple manipulation of the trig. functions shows that the reflection coefficient is

$$\varepsilon_r = \frac{a_{max} - a_{min}}{a_{max} + a_{min}} \quad 5.1.6.$$

and the primary wave amplitude

$$\alpha = \frac{a_{max} + a_{min}}{2(1+\varepsilon\cos\delta)} \quad 5.1.7.$$

For most practical purposes the denominator of this expression may be assumed to be 2, but not when attempting to verify the small amplitude generator theory. The maximum (a_{max}) and minimum (a_{min}) amplitudes of the wave envelope occur at points one quarter of the incident wavelength apart and are easily detected visually (when present) by following a wave crest as it travels down the flume.

By varying the wave generator amplitude and frequency the intermediate range of waves was found for which problems of reflection, first

harmonic generation (for long waves), in-line or transverse instability and breaking (for short waves) were negligible.

5.2. Instrumentation for circular cylinder

5.2.1. Cylinder material

The circular cylinder on which the measurements were taken was made of green araldite sprayed on to a wooden former and then turned down to a thickness of 1.4 mm. The original intention was for this cylinder to flex under the action of the waves so that measurements of displacement could be compared with the predictions of a mathematical model, including the coupling effect.

Because of the method of manufacture the manufacturer's figures for elastic modulus and density were unlikely to apply. A simple pair of tests was devised for measuring them.

A small sample was sawn from the cylinder and accurately measured as follows:-

Mean diameter	D = 100.70	$\pm$ .08 mm.
Thickness	t = 1.41	$\pm$ .01 mm
Width	b = 19.60	$\pm$ .01 mm
Mass	P = 10.51	$\pm$0.02 gms.

From these the density was calculated as

$$\rho_A = \frac{P}{b\pi Dt} = 1202 \pm 9 \text{ kg.m}^{-3} \qquad 5.2.1.$$

To estimate the elastic modulus this same sample was suspended as shown in figure 5.2.1. on a knife edge support. A series of accurately measured weights were suspended from the lower knife edge hanger. The displacement of the lower edge of the cylinder was measured using a travelling microscope and the following results obtained

Load gms	50.072	95.481	140.565	163.265	185.845	185.845
Displ.mm	0.61	1.23	1.75	2.09	2.40	2.29

The last result was taken from zero load to enable an estimate of the creep for which araldite is notorious. The linear behaviour is clear from the figure from which the slope is 80.0 gms. mm^{-1}. It may be shown that for linear elastic behaviour in this situation the elastic modulus is given by

$$E = \frac{P}{\delta} \cdot \left(\frac{D}{t}\right)^3 \cdot \frac{1}{b} \cdot \frac{3(\pi^2-8)}{8\pi} = 3260 \pm 80 \text{ N.mm}^{-2} \quad 5.2.2.$$

The crucial measurement of thickness (t) was made as accurately as the variability of the material would allow.

5.2.2. Cylinder mounting details

Copies of the five drawings from which the cylinder mounting was constructed are included as figures 5.2.2. to 5.2.6.

The cylinder was glued rigidly to an araldite base using araldite adhesive. The internal aluminium frame served a dual purpose.

Firstly, it enabled the cylinder to be positioned anywhere in the flume by jacking down from the top against the base. The six holes in the base were only used for convenience in preliminary tests. Secondly, once this framework was under compression it acted as a rigid support on which the displacement transducers could be mounted inside the cylinder.

The great strength of the circular cross-section in overall bending meant that the primary mode of displacement was likely to be an ovalling of the cross-section. For this reason the displacement transducers were arranged in a cross at two levels 226 and 476mm above the base. In between these points at 130 and 370mm above the bottom of the flume, pressure tappings were arranged at 45^{o} intervals. The ease with which the cylinder could be rotated meant that measurements could be taken at any angle. The P.V.C. tubing connected permanently to these tapping points was carefully arranged so as not to foul the displacement transducers. The aluminium framework could be withdrawn to allow calibration of the displacement transducers. Figure 5.2.7. shows the completed assembly.

5.2.3. Displacement transducers

The displacement transducers used were of the linear (1kO) potentiometer type. The resistance element is a conducting plastic so that the resolution is infinite. The linearity is better than 1% over the 12 mm displacement range. This does assume that no significant loading is placed on the output by any additional electronics. Because the input resistance of the analogue tape-recorder was not particularly high an 8 channel amplifier was constructed primarily as a buffer between the transducers and the recording equipment. This was based

on a simple 741 operational amplifier configured as a variable gain non-inverting differential amplifier. The circuit for this is shown on figure 5.2.8. An immediate advantage of the differential amplifier was the ability to null balance the output from each transducer when the cylinder was stationary whatever its initial position.

In order to measure the cylinder displacement at four points on the same level, the transducers had an additional perspex element fixed on the sensing end (see figure 5.2.6.). Unfortunately, the transducer was rotationally weak and the additional lever arm provided by this element accentuated the problem. Each transducer was fitted with a low-stiffness return spring to maintain contact with the cylinder without restraining its motion significantly.

The calibrations of all eight transducers are shown in Figure 5.2.9. together with their respective calibration constants. The calibrations were performed by clamping a micrometer on the aluminium frame to which the transducers were attached. As expected, each transducer shows excellent linearity and sensitivity, typically 1 cm. division on the U.V. recorder represents 60μm. The small amount of hysteresis is caused by rotation of the extension head on the transducer. If this problem could be removed these transducers are capable of extremely precise measurement.

5.2.4. Pressure transducers

The measurement of water pressure was made using four pressure transducers manufactured by the technicians in the Hydrodynamics Laboratory of the Civil Engineering Department at The City University. The details are shown in figure 5.2.10. The sensor is a brass diaphragm 3

thousandths of an inch (76μm) thick on the rear of which is glued a circular strain gauge. As they were not differential transducers it was felt that the diaphragm had to be able to withstand the 500 mm head of water which it might experience if placed level with the base of the flume. Attempts to make the device more sensitive by using thinner diaphragms led to problems of drift of the electrical signal due apparently to temperature.

It was the original intention to fix the transducers inside the cylinder so every attempt was made to keep them small. Since, eventually, they were placed outside the cylinder larger diaphragms could have been used. One advantage of the lack of sensitivity was the linearity associated with minute displacements of the diaphrams.

Figures 5.2.11 to 5.2.14 demonstrate this linearity over a much wider pressure range than was actually used. Although attempts had been made to prestrain the diaphragms and strain gauges to enable zero pressures to be accurately measured, the transducers were always operated under a positive mean static head of about 100 mm of water.

The connection between the pressure tappings on the cylinder and the transducers was made with about 1.5 metres of clear P.V.C. tubing with an internal diameter of approximately 2.5 millimetres. Although this tubing may have flexed significantly under the hydrostatic pressure component, the small superimposed dynamic pressure fluctuations caused very little additional flexure. The speed at which pressure fluctuations travelled along the tubing could not have been very much below the speed of sound in water, 1400 $m.s^{-1}$. To cause a phase lag of 1% of the typical wave periods the speed of travel would have to have been reduced by a factor of ten. No problemsof phase lag were encountered from this source.

Because of the low sensitivity of these devices it was necessary to construct additional amplifiers to boost the signal from the strain gauge amplifiers. At each stage, an attempt was made to filter out some of the inevitable noise by including a 10 nano-farad capacitor in the negative feedback loop of each op-amp, such that the cut-off frequency was at approximately 16 Hz. Although a lower cut-off would have removed much more of the 50Hz and other more random noise, it was found to lead to unacceptably large phase shifts in the main signal. Appendix (A.2.) shows the design and characteristics of these simple active filters.

Also associated with these high D.C. gains (typically 10^6 x) is the inevitable drift caused by contact resistances in potentiometers for example. It was therefore important to be able to check the calibration of the transducers quickly, while still connected to the cylinder tapping points. This was achieved by mounting all four transducers on a moveable frame. Movement of the transducers upwards was equivalent to the still water level moving downwards. Care was taken to bleed all air bubbles from the connecting tubing. The transducers were filled with water by forcing it in through a hypo-dermic until all the air was expelled before connecting the tubing.

5.2.5. Wave probes

The measurement of water surface elevation was made using a purpose built amplifier based on the well known design from the Hydraulic Research Station. The probes were twin stainless steel conductors enabling an audio-frequency alternating current to be passed through the water. The output from the amplifier is proportional to the immersed length of the conductors since this governs the resistance between them. These devices are extremely reliable, do not suffer from

drift, are easy to calibrate and are linear over a wide range of wave heights.

5.2.6. U.V. Recorder and analogue tape recorder

Because of the high noise levels on the pressure signals, and the erratic drift, it would have been very difficult to use digital techniques to obtain reliable information. The intermediate process of tape recording magnified the noise level to such an extent that the signal-to-noise ratio was always less than 1. Because of this the signals were stored on ultra-violet light sensitive paper using a 12 channel U.V. recorder. The pre-amplifiers of the tape recorder were still used as a low output resistance buffer to drive the galvonometers. Details of the data reduction technique from the U.V. paper are given with the results.

The galvonometers used with the pressure transducers were type A100, those with the displacement transducers were B160. Both types are manufactured by S.E. labs (E.M.I).

5.3. Pressure measurements without cylinder

For a single frequency progressive wave travelling in the positive x direction the dynamic pressure at depth h above the bed is given by

$$P/\rho g = \frac{\cosh kh}{\cosh kd}\eta = \frac{\cosh kh}{\cosh kd}\frac{H}{2}\sin(kx-\sigma t) \quad 5.3.1.$$

This pressure is therefore in phase with the surface elevation and is proportional to the wave height. This theory is only valid for small wave steepness and relatively large depths. In view of the finite height of experimental waves it was necessary to check this simple theory by measuring the pressure in the side wall of the wave flume. The linear diffraction theory for a vertical cylinder assumes a coshine variation with depth for the potential and pressure and if this is to be tested experimentally, it is important to know if it is valid in the absence of the cylinder.

A pressure tapping point was fixed in the side wall of the flume 399 mm above the bed in water of depth 523 mm. Two wave probes were fixed 1.86 m apart and the one in line with the pressure tapping calibrated. The calibration constant was 18.5 mm of water per centimetre division on the U.V. recorder. The calibration of the pressure transducer was performed as accurately as possible but it seems likely that the calibration constant of 22.2 mm of water per centimetre, could be 5% in error over 80 mm of water. The connection between the transducer and the tapping point was made with the same length of P.V.C. tubing as would ultimately be used with the cylinder.

Figure 5.3.1. is an example of a typical wave record. The pressure signal contains an unusually high amount of mains (50 Hz) noise and also some 100Hz noise from an unknown rectifying device. This noise was polluting even the main earth lines at about 50 mV between earth and a separate ground connection to the water main. The signal to noise ratio is seen to be close to unity. However, the regularity of the noise made it possible to draw a smooth curve through the signal from which the maximum and minimum pressures could be measured. The results were then averaged over several wave cycles.

The results from the 14 waves used are summarised in table 5.3.1. The variable parameters were the generator frequency and amplitude.

From the record the following quantities could be measured,

T - the wave period

T_t - the time taken by a wave crest to travel 1.86 metres

H - the trough to crest wave height

A_2 - the amplitude of the pressure fluctuation.

From T, the non-dimensional frequency parameter $\frac{\sigma^2 d}{g}$ was calculated From the dispersion relation

$$k_1 d \tanh k_1 d = \frac{\sigma^2 d}{g} \qquad 5.3.2.$$

the equivalent parameter $k_1 d$ was calculated and from this the theoretical wavelength and celerity correct to second order

$$\lambda_1 = 2\pi/k_1 \text{ and } C_1 = \lambda_1/T \qquad 5.3.3$$

The wavelength and celerity were also calculated from

$$C_2 = 1.86/T_t \text{ and } \lambda_2 = C_2 T \qquad 5.3.4.$$

Since C_1 was calculated from only the measured period (to better than 0.01 seconds) and the still water depth (to better than 0.5%) the difference between C_2 and C_1 should be a third order quantity in the wave steepness k_2H. Wiegel[87] shows that the third order correction increases with wave steepness. Figure 5.3.2. shows the ratio C_2/C_1 against wave steepness, from which it is clear that although the steeper waves are definitely travelling faster, some of the less steep waves are travelling slower than theory would predict. Similar trends are exhibited in the experimental results quoted by Wiegel[87], although there, as here, the scatter in the results is certainly as great as the discrepancy between theory and measurement.

As well as measuring the pressure, the relationship between the wave generator parameters and the resulting wave height was required in the absence of the cylinder.

The linear wave generator theory (Havelock[28], Ursell, Dean and Yu[78]) predicts that for a given generator executing small amplitude oscillations, there is a one to one relationship between the frequency of oscillation and the wave height/generator stroke ratio. This two dimensional theory is only directly applicable to generators whose mean position is vertical since this enables the spatial co-ordinates to be separated. An accurate result for the plunging wedge could be obtained numerically using the boundary element technique. A simple approximate expression can be obtained by assuming the wedge acts as a piston generator extending from the surface down to its mean position above the bed, which in this case was 19.8 centimetres as shown in figure 5.3.3.

Straightforward application of the theory gives

$$\frac{H}{S} = \tan(\alpha)\ \sinh(kd)\ \frac{\int_{-b}^{o} \cosh k\,(y+d)\ dy}{\int_{-d}^{o} \cosh^2 k(y+d)\,dy} \qquad 5.3.5.$$

$$= \tan(\alpha).\ 4.\ \sinh kd\ \frac{[\sinh kd - \sinh (kd - kb)]}{[\sinh 2kd + 2kd\ ]} \qquad 5.3.6.$$

where α is the wedge angle and b is the depth to the bottom of the wedge. This expression will be a good approximation provided the horizontal dimensions of the wedge are small compared with the wave length or

$$b \tan\alpha < \lambda/_5 \text{ (say)} . \qquad 5.3.7.$$

Most of the waves used satisfied this condition.

Equation 5.3.5. assumes that no flow takes place under the wedge.

Figure 5.3.4. shows the ratio H/S plotted against $\sigma^2 d/g$. There seems to be no clear dependence on wave steepness even though some of the waves were clearly quite steep. The limiting steepness for breaking of periodic waves is usually given as

$$kH = 0.887 \tanh kd . \qquad 5.3.8.$$

From table 5.3.1. it may be seen that several of the waves were close to half this value. The reason for the surprising lack of non-linearity in figure 5.3.4. is because the second order correction to the wave shape travels in phase with the main crest and being half the wave length does not affect the trough to crest height until it is some 30% of the first order term. The energy in the wave depends, to second order, on the wave height so that the linearised generator theory actually predicts the wave height correct to second order.

Also shown on this graph is the approximate relationship (equation 5.3.6). It is clear that the back flow is reducing the efficiency of the wedge by about 18% (or 30% based on energy).

The efficiency of the generating device becomes important when trying to generate low frequency (long) waves. Because of the form of the generator characteristics, for a given stroke (S), lower frequencies generate significantly lower wave heights. In practice, this means that the generator amplitude must be increased to provide waves of useable height and herein lies a problem. The large displacements of the generator contribute to a significant nonlinear forcing term at twice the generator frequency. This does not give rise to a Stokes type second order correction to the primary wave because the waves are not steep. Instead, it generates a significant 'free' wave travelling at its own phase speed. A numerical example clearly illustrates what happens.

If the period of the primary wave is 2 seconds in water 0.5 metres deep then its length is 4.1 metres and its phase speed 2.0 $m.s^{-1}$. The free wave with twice this frequency has a wavelength of 1.5 metres and travels at 1.5 $m.s^{-1}$.

Although its length is less than half that of the primary wave, the secondary wave (because of the reduced effects of dispersion for such long waves) travels almost as fast. This now provides a simple explanation for the reduced phase speeds of certain of the less steep waves in figure 5.3.2. The usual method of estimating phase speed is to compare the time histories of water surface elevation at two points a known distance apart . What is actually measured is the velocity of travel of the wave envelope. Because of the presence of the slower

moving secondary wave this velocity will not be the same as the correct value. Whether it is higher or lower will depend on the relative positions of the wave probes and the generator.

The comparison between the measured pressure and the theoretical pressure in table 5.3.1. shows a remarkable agreement. All the results are within 3mm of water of the prediction, the overall r.m.s. error being 1 mm. There is no clear correlation between the errors and wave steepness or frequency. In view of the high noise level and the estimated precision of the calibration there is nothing to suggest that the theory is inadequate.

It is important to recognise that this agreement has been obtained in the absence of the cylinder. Many of the comments regarding the self cancelling effect of the second order corrections to the wave height apply equally in this case. Because the theory does not predict a wave height but simply includes it as a linear multiplier then the coshine variation with depth is stretched to fit the given wave shape.

Figure 5.3.5. shows the scatter in the pressure results to the same scale as they will be shown below in the presence of the cylinder. There was no detectable phase lag.

5.4. Pressures on the circular cylinder.

The circular cylinder was fixed in the wave flume about 6 metres from the wave generator. It was found that the displacements of the cylinder under wave action were so small that most of the movement of the displacement transducers was taken up in rotation because of the

extension pieces. It was unfortunately not possible to obtain reliable results from these transducers.

5.4.1. Pressure transducer calibrations

The measurments of pressure were far more successful. The cylinder was exposed to a total of 93 different waves. Each was given a number which has been included in all the tables to facilitate cross-referencing. Each wave record 'stored' on U.V. paper included (over about four periods) the information from two wave probes and four pressure transducers. The measurement were taken on four separate occasions. Figures 5.4.1. to 5.4.4. show the corresponding calibration lines and the record numbers to which they apply. An indication of the drift of the calibration constants is given on figure 5.4.1. by the recalibration at record number 12. The change in calibration from figure to figure is not a result of drift, but corresponds to the quite distinct amplifier configuration on each occasion.

One wave probe was placed alongside the cylinder in line with its axis and the other typically 1.8 metres in front of the cylinder on the flume centreline.

5.4.2. Noise levels.

The wave probe signals did not suffer from noise or drift. There was always considerable noise on all four pressure transducer signals, however the character of the noise changed on each of the four occasions. Therefore, a typical piece of wave record has been faithfully reproduced from each occasion as figures 5.4.5. to 5.4.8. to illustrate the noise levels. Unlike the previous tests in the

absence of the cylinder this noise appeared to be random, which made it slightly more difficult to draw a smooth curve through it.

Each transducer signal drifted by varying amounts. The slow rate at which this occurred made it easy to remove its effects from the data. Unfortunately, it does mean that no information about steady mean pressures could be obtained. The only information which could justifiably be extracted was the maximum and minimum pressures and their phase in relation to the wave on the axis of the cylinder.

5.4.3. Blockage

The cylinder diameter was 100.8 mm whereas the width of the flume was 750 mm. The blockage of the flow by the cylinder presents a number of problems which can only be quantified approximately.

For the high frequency, short waves the cylinder becomes capable of greater wave radiation and this will be reflected by the sides of the flume. This situation is equivalent to the diffraction of waves by a row of cylinders at 750 mm centres which in this case is approximately 15 times the cylinder radius (a). For two such cylinders 10a apart the computations of Lebreton and Cormault[52] and Isaacson[40] suggest the effect on the maximum force for $ka < 0.5$ is less than 2½% and 2% respectively due to the interaction between the cylinders. A row of cylinders may be expected to double this figure. As the spacing increases the amount of scattered wave energy incident on the adjacent cylinder may be expected to fall off as the inverse square of their separation because of the reducing angle of incidence and the reducing wave amplitude. This suggests that for $ka = 0.5$ the blockage effect increases the forces by less than 2%. Most of the waves were lower

frequency than this and since the interaction falls off rapidly with increasing wave length,blockage by diffraction may be expected to affect most of the results by less than 1%.

For the lower frequency, longer waves the flow past the cylinder is approaching quasi-steady uniform flow. The presence of the cylinder in such a flow may be assumed to increase the ambient flow in inverse proportion to the reduction in area. In this case, the ambient velocity may be increased by 15%. It may be shown that, at the still water level, the ratio of the two components of pressure in Bernoulli's equation due to the flow velocity and the rate of change of the potential is

$$\frac{\frac{1}{2}\rho q^2}{\rho \frac{\partial \phi}{\partial t}} = \frac{kH}{4} \coth kd \qquad 5.4.1.$$

For a typical wave kH = 0.24 and kd = 1.3, which gives a figure of 7%. The effect of this mode of blockage on the total pressure is therefore about 1%.

A possible problem associated with the size of the cylinder is the reflection from the generator of the scattered waves from the cylinder. Because of the small amount of scattered wave radiation and the 6 metres between the cylinder and the generator this was not expected to be a problem.

5.5. Presentation of Results

All the results, both measured directly (indicated by an asterisk) and subsequently calculated are presented in tables 5.5.1. and 5.5.2. Much of this information has also been presented graphically

as will be discussed below. In these tables the following suffices are used

1 - refers to the wave probe alongside the cylinder

2 - refers to the wave probe in front of the cylinder.

T - refers to quantities calculated only from the wave period at probe 2, and water depth, and thus represents the theoretical results.

C - refers to quantitites calculated from the measured time of travel of the wave crest.

It will be seen that nearly all of the waves fall into 6 broad groupings on the basis of frequency. Although this arose by accident it fortunately allows results to be plotted against wave steepness for fixed frequency.

5.5.1. Wave heights

Measurements of the wave height were obtained at both wave probe positions although the probe at the cylinder is more likely to suffer from the effects of diffraction by the object. These two heights, together with the generator stroke are shown in table 5.5.2. In most cases, the wave height at the cylinder was higher. However, because of the possibility of reflection of the scattered wave by the generator, a partial standing wave system will be set up which may affect the wave probe in front of the cylinder depending on its position in the system. Accordingly, both results are plotted against the frequency parameter in figure 5.5.1. Superimposed on this graph is the curve from the measured results in the absence of the cylinder, which appears to define the mean line through the considerable scatter.

Figure 5.5.2. shows 80 of these results grouped into four frequency bands and plotted against wave steepness. The scatter does not appear to correlate with wave steepness. Because the mean position of the wedge remained at 198 mm above the bed, changing the water depth necessarily changes the generator characteristic. For this reason the results corresponding to different water depths are represented by different symbols.

The lower the water depth the less efficient the generator will become, and so the lower will be H/S. This is borne out by results. The water depth in the tests without the cylinder was 523 mm. All the results with the cylinder in place should be lower than the curve on figure 5.5.1. The results in figure 5.5.2. are in approximately the correct relative positions but as the frequency increases, they shift higher than they should. This is consistent with the presence of standing wave energy due to increasing diffraction.

There is still further evidence of this standing wave behaviour. For a fixed frequency and distance between wave probes the position of the standing wave envelope should not depend on wave height (for small steepness). This suggests that the difference between the measurements at each wave probe should be largely the same. This is indeed the case. In particular, for a water depth of 503 mm the results in band 3 exhibit much less scatter. The mean frequency for this band corresponds to a wavelength of 1.66 metres. Since the wavelength of the standing wave envelope in this case will be about 0.83 metres, the distance between the wave probes is close to a multiple of this length and so the two measured heights are much closer.

It should also be clear from this, that the correct value of H/S is not necessarily in between the values from the two probes, although the larger the discrepancy, the more likely it is to be.

5.5.2. Phase Speeds.

The wave celerity was again estimated from the time of travel of a wave crest between probes 1 and 2 (distance L metres in table 5.5.2). The results are plotted in figure 5.5.3. as the ratio of the calculated celerity C_c to the second order value C_T, against wave steepness. Over 90% of the results are within 4% of unity. The third order correction over this range of wave steepness is much less than the scatter. In an attempt to explain the scatter, the results are separated into the same frequency bands as were the wave heights, and replotted on figure 5.5.4. The only definite conclusion that can be drawn from this figure is that the low frequency, low steepness waves exhibit the most scatter. Whilst the arguments put forward in section 5.3 are still appropriate, this trend is also consistent with the greater difficulty of estimating the position of the wave crests for the longer waves. In view of the lack of correlation of the scatter with any particular parameter, it appears that random experimental errors are its most likely cause. Also shown on this figure are the third order corrections, based on the mean frequency parameter of each band, taken from Wiegel[87].

5.5.3. Pressures on the cylinder

The measured pressures on the circular cylinder are shown in table 5.5.1. Four pressure transducers were used at one time, all at the same depth and 90^{o} apart around the cylinder surface. Sixteen pressure tappings were available, eight at 130mm and eight at 370 mm above the bed, at 45^{o} intervals. For simplicity, the angular position of each pressure tapping has been assigned a number N as shown in figure 5.5.10. where the pressure tapping number 1 ($\theta = 180^{o}$) faces directly into the waves and is therefore referred to as the front of the cylinder. The symbols U and L are used to refer to the upper and lower pressure tappings respectively.

To condense the presentation of the results all the pressures have been normalised with respect to the pressure in the incident wave at the same depth. This has the effect of removing the dependence on the depth by assuming it to be a coshine variation. This enables all the results for a given angular position to be plotted on the same graph.

The results derived from the upper and lower pressure tappings have been kept separate for two reasons. Firstly, the smaller pressure fluctuations and hence, lower signal to noise ratio suggested that increased scatter should be expected in the lower results. This would give a false impression if all the results were together. Secondly, the lower results should have a different spectral composition because the decay terms of higher harmonics become increasingly rapid. Normalisation on the basis of the first order depth variation ignores this. Due to the presence of standing wave energy at the front of the cylinder, the non-decaying pressure fluctuation was expected to occur . This would lead to a proportionately higher 1st harmonic content at lower depths.

The analytical solution for the pressure on a circular cylinder in water waves of arbitrary depth is usually attributed to MacCamy and Fuchs[25]. The only difference between their solution and many similar wave solutions for a circular cylinder (e.g. acoustics and electromagnetics in Morse and Feshbach[62], deep water waves in Havelock[29]) is in the coshine variation with depth. Several mistakes occured in their paper, which have led to some confusion in the literature. This is mainly as a consequence of the initially arbitrary choice of either $e^{i\sigma t}$ or $e^{-i\sigma t}$ for the harmonic time. Once a choice is made this then fixes the form of the radiation condition, which in turn depends on whether the positive or negative gradient of the potential is used to define velocity. Sarpkaya and Isaccson[72] use both forms of harmonic time in different contexts but persist with the same radiation condition. Chakrabarti and Tam[15] give an expression for the pressure which cannot be derived from their theory. It is in any case incorrect, since they misuse the Jacobi symbol in such a way that the second term in their series expression is half what it ought to be. Had they used this expression the pressures would have been about 40% too small. The correct derivation of the potential and hence the pressure is therefore included in appendix A.1. The results of this calculation have been verified against those given by Havelock[29] and those of Wiener given by Wiegel[87] for ka = 0.5.

The disagreement between the phase results of Wiener and those given in the appendix is merely a difference of definition. Wiener has defined the phase angle relative to the incident wave at the same position, wherease the figures used in this thesis are all relative to the wave at the axis of the cylinder. This was simply because the wave probe was fixed in line with this axis. For position 1, for example, the phase must be in advance of the wave probe by at least

the time it takes a wave to travel the distance of the cylinder radius a. This gives a phase angle of

$$\alpha = \frac{\sigma a}{C} = ka \qquad 5.5.1.$$

Figure 5.5.5. shows the theoretical variation of wave height along a radial line through position 1 in front of the cylinder for ka = 0.3, as a fraction of the incident wave height over the range in which the wave probe was situated. The wave height measured by the probe could therefore be as much as 6% out depending on its position in relation to the wave system. In practice this curve will be modified slightly by the multiple reflections between the cylinder, the wave generator and the side walls. Once steady state is achieved, a curve of this form will still emerge.

The effect of this partial standing wave on the measured wave heights has already been discussed. It does, however, have an important bearing on the comparison between measured and theoretical pressures on the cylinder.

In order to normalise the pressures, they are divided by the amplitude in the incident wave

$$\frac{H}{2} \frac{\cosh k\,(y+d)}{\cosh kd} \qquad 5.5.2.$$

which requires a choice to be made for the value of the wave height in the experiment. It is tempting in view of the reduced scatter to use the incident wave in the absence of the cylinder. However, the incident wave to which the cylinder is responding clearly has an increased amplitude because of the reflection from the generator.

Since the diffracted wave amplitude reduces with distance from the cylinder, the wave probe in front of the cylinder (at least 1.6 metres away) is likely to be closer to the correct height than the probe along side the cylinder (about 0.15 metres away). Rather than rely on this probability the results were normalised with respect to both measured wave heights, it being remembered that it is, in general, coincidental if both measurements are the same and not at all indicative of increased accuracy.

Figures 5.5.6. to 5.5.9. show how the measurements of pressure amplitude and phase were made from the wave records. The amplitude in this case is half the difference between the maximum and minimum pressures and therefore is not necessarily the amplitude of the fundamental frequency component. The presence of a first harmonic (at twice the wave frequency) in the pressure signal will always increase this measured amplitude unless it happens to be a multiple of 90^{o} out of phase with the fundamental, as it is in the absence of the cylinder.

The phases of the peak pressures relative to the wave were always averaged over an integral number of cycles. Therefore, the presence of a first harmonic will not affect the phase if it is a multiple of 45^{o} out of phase with the fundamental. The phase measurements are therefore less affected by the presence of higher harmonics.

Figures 5.5.10. to 5.5.14. illustrate graphically the theoretical and experimental results for amplitude and phase. Because of symmetry the measurements at positions 2, 3 and 4 have been combined with those at 8, 7 and 6 respectively.

The phase results although exhibiting some scatter, generally show excellent agreement with the theoretical curves. Because measurement of phase requires an estimate of the position of a turning point, rather than its value, it is in a sense one order more difficult to estimate, particularly in view of the noise levels. The probable reason for the good agreement is that the phase angles do not depend on the measured wave height. Any fluctuations in the wave height which made for difficult measurement of amplitude, had less effect on the phases. This also means that the phases do not depend on the calibration constants of the transducers.

It appears from these results that the theoretical predictions for phase are correct. This is in contrast to the results reported by Boreel[9] where in general, the phase showed poor agreement even when the measured pressure amplitudes agreed with their numerical predictions.

The amplitude measurements in all five figures seem consistently higher than the theoretical predictions. There is however, considerable scatter.

Some of this scatter was actually present in the traces as an experimental fact, even apart from the noise. At least one wave record (see figure 5.5.15.) showed a remarkably consistent periodic behaviour, at approximately half the wave frequency, at the pressure tapping at position 3. This is close to the likely position of separation and may indicate an asymmetry in the flow which is usually observed at much larger values of the Keulegan and Carpenter number.

The largest values in this experiment were about 3 which is well into inertia dominance.

The normalised pressures will also include the scatter in the wave heights already shown on the generator characteristic, figure 5.5.1.

It was not particularly difficult over four or more cycles to estimate the maximum and minimum pressures in a wave quite precisely. However, it was quite difficult to calibrate the pressure transducers because of the high noise level, particularly for transducer No.3. Since the measured pressures are ultimately only as accurate as the calibration this is a severe limitation. This source of error should be random and in view of the twenty independent calibrations it is unlikely to have led to a consistent increase.

Transducer number 2 was twice as sensitive as the rest and therefore required less amplification. In turn, the lower noise level led to a more reliable calibration constant (see figures 5.4.1. to 5.4.4.) To see if this transducer gave results which were consistently closer to the theory they are replotted as figures 5.5.16. to 5.5.18. The consistent discrepancy is still clearly apparent, particularly for position 5 (fig 5.5.18).

Figure 5.5.19 shows a copy of record number 19d, which is quite a high frequency wave, for which measurements of pressure were taken at the lower pressure tappings. On the front of the cylinder (position 1) there is clear evidence of a large first harmonic component which has clearly contributed to the large amplitude labelled in figure 5.5.10. For this frequency the depth factor cosh kh/cosh kd = 0.132. The amplitude of the first harmonic pressure fluctuation in the incident

progressive wave should be less than 1% of the first order value at this depth. The much larger component suggested by record 19d (and similarly by 21c, 21d and others) seems to confirm the presence of a first harmonic pressure fluctuation which does not decay with depth in the usual way. Longuet-Higgins[55] analysis suggests that the size of this pressure fluctuation, in the presence of the standing wave energy near the front of the cylinder, should be

$$\frac{p}{\rho g} = \frac{H}{2}\left(\frac{\alpha}{4}\, kH\right) \cos 2\sigma t \qquad 5.5.3.$$

whereas the first order pressure in the wave at this depth is approximately

$$\frac{p}{\rho g} = \frac{H}{2} \times 0.132. \cos(\sigma t + \phi) \qquad 5.5.4.$$

Here, α is the reflection coefficient at the front of the cylinder which from figure 5.5.10. may be estimated, in this case to be 0.14. Substitution into 5.5.3. shows that this second order term may be some 10% of the first order, which explains some of the 60% increase over linear theory in this case.

If the presence of higher harmonics in the pressure fluctuations is the main cause of the discrepancy between the linear theory and the measured values then the disagreement should increase with wave steepness. Figures 5.5.20 and 5.5.21 show the results in the four middle frequency bands (some 85% of the total) plotted against wave steepness. There is little clear evidence to support this explanation except perhaps in the higher frequency band 5. Certainly, there is no evidence that the results are approaching the predictions at zero steepness.

This comparison is unfortunately complicated by the apparent positive correlation between wave steepness and frequency (see for example figure 5.5.4.). This is obviously coincidental, since the two parameters are independent. For the high frequency waves the lower limit of wave steepness was governed by the difficulty of detecting any pressure fluctuation at all, because of their rapid decay with depth. For the lower frequency waves the upper limit of wave steepness was fixed by the maximum wave generator stroke of 240 millimetres.

Since it has been suggested that the effects of blockage are too small to have caused the observed discrepancies (which are typically 20%) the only possible conclusion is that the linear theory is somehow invalid.

Perhaps the clearest trend in the results is the steadily increasing pressure a mplitude at the rear of the cylinder, in figures 5.5.14 and 5.5.18. Here the linear theory predicts very little change in the amplitude ratio over this range of ka before it steadily reduces due to the sheltering effect of the cylinder as ka increases. For some of the waves, there was clear visual evidence on the surface of a focussing of the wave energy arriving from both sides of the cylinder. This focussing was reported by Hogben and Standing[33] for the more obviously separated flow around a square cylinder.

Figure 5.5.22. shows the variation of pressure amplitude around the cylinder, both on cartesian axes and as a polar diagram, for the results in frequency band 4. The results have been averaged to remove the scatter. Because these amplitudes are actually out of phase this figure is only for qualitative comparison. Nevertheless, because

the measured phases are in agreement with the theory, this figure gives some idea of why the total force is usually much less affected by the errors in the pressure.

The main difficulty in applying linear wave theory in the presence of a cylinder is that the rise and fall of the water surface dominates the measurement of pressure whereas the theory assumes that this vertical motion is negligibly small, such that the free surface boundary condition may be applied without correction at the still water level. This shift of the boundary condition is a feature of all the subsequent non-linear corrections. Obviously, the pressure between the trough of a wave and the still water level is zero, and non-zero between the crest and the still water level. The theory maps this behaviour onto the still water level.

Lighthill[54] shows how a consistent correction to the total wave force may be derived but this still assumes infinitessimal wave height. This is why he recommends it be applied at the waterline rather than at $\eta/3$. This problem was in fact the primary reason for conducting the preliminary experiments on the free waves. It was expected that just below the wave troughs the proximity of the free surface would modify the pressures. It has already been shown how these waves appear fortuitously to escape this problem. It appears (as Lighthill suggested) that the situation is radically different once the cylinder deforms the flow.

Bearing in mind that the free surface boundary condition may be satisfied to first order either on the moving free surface or on the still water level, the following heuristic analysis suggests itself.

The pressure at a point y in the fluid is given by

$$\frac{p}{\rho g} = \frac{H}{2} \frac{\cosh k(y+d)}{\cosh kd} \sin\sigma t \qquad 5.5.5$$

As a wave trough passes above this point it is actually at a depth $y + \frac{H}{2}$ below the free surface. Conversely when a crest passes it is apparently in deeper water at a depth $y - \frac{H}{2}$ (y is positive upwards). The actual pressure at this fixed point y may therefore be

$$\frac{p}{\rho g} = \frac{H}{2} \cosh k\frac{(y+d-\frac{H}{2}\sin\sigma t)}{\cosh kd} . \sin\sigma t \qquad 5.5.6.$$

The amplitude of this pressure fluctuation is therefore

$$\left(\frac{p}{\rho g}\right) \text{amp.} = \tfrac{1}{2}\left[\left(\frac{p}{\rho g}\right)_{max} - \left(\frac{p}{\rho g}\right)_{min}\right] = \frac{H}{2} \frac{\cosh k}{\cosh kd} (y+d) . \cosh \frac{kH}{2} \qquad 5.5.7.$$

Expansion of the cosh $\frac{kH}{2}$ term shows that this correction is in fact third order in the wave steepness, but unlike the Stokes correction it does not decay rapidly with depth.

The measured pressures in a wave are replotted in figure 5.5.23. against wave steepness. The agreement between the five point moving average curve and the cosh $\frac{kH}{2}$ factor is quite good. For waves of steepness kH = 0.5 this factor predicts a 3% increase over linear theory. On the front of an object this steepness can double for high frequency standing waves and the factor then becomes 1.13 because of the rapid increase of the coshine function.

The derivation of this correction factor has been included only in an attempt to show how the rise and fall of the free surface may have

a significant effect on the pressures beneath it. It would not stand up to rigorous scrutiny. There is promise of a numerical solution to the problem using a three dimensional equivalent of the approach of Longuet-Higgins and Cokelet[56]. By solving the irrotational flow problem at the instantaneous position of the free surface, there is no need to involve the still water level. It is only the free surface condition which makes the problem nonlinear.

CHAPTER 6. DISCUSSION OF CHAPTERS 4 AND 5

6.1. The pressure measurements

The mathematical solutions of Havelock[29] and MacCamy and Fuchs[58], and the numerical calculations based on the indirect formulation of Garrison and Chow[25] make the same fundamental assumptions about the fluid flow. In particular it is assumed that the vertical displacement of the free surface is small enough for a Taylor series expansion of the free surface boundary condition about its mean position, to be truncated after the first term.

The linearised boundary condition at the free surface of a simple harmonic motion is of the form

$$\frac{\partial \phi}{\partial y} + \nu\phi = 0 \quad \text{on } y = \eta \qquad 6.1.1.$$

The importance of the second order terms left out when this is satisfied at $y = 0$ is therefore given by the size of $\nu\eta$ relative to unity. This may be estimated from first order theory for progressive waves to be less than $(kH \tanh kd)/2$, which for deep waves is limited by incipient breaking to be less than 0.89. This is clearly not small. The comparative success of the linearized analysis for progressive waves up to half breaking height has been shown in chapter 5 to be due to the self cancelling effect of the second order corrections. Indeed, covergence of the Stokesian perturbation expansion has only been proved for progressive waves, by Levi-Civita.

For waves diffracted by structures, the comparison between theory and experiment has been made on problems for which the effect of the free surface is small, either by considering completely immersed objects (see Chapter 2, Chakrabarti[13]) or by using structures which span the whole water depth so that the free surface effect is an insignificant part of the total response.

The two forms of this response which have been measured are the total forces and the fluid pressures. Chakrabarti and Tam[15] and Huntington and Thompson[37] have measured both, on a vertical circular cylinder. Hogben and Standing measured both on a circular cylinder and a square cylinder. Boreel[9] and Van Oortmerssen[67] used a square cylinder on a pyramid. This list is not exhaustive but all of these objects extended from the bottom through the free surface.

The measurements of total force on these objects generally showed fair agreement with the theoretical or numerical predictions over most of the frequency range. Indeed, Chakrabarti and Tam[15] quote a correction for the free surface effect, but comment that it was insignificant in most cases.

Some researchers used several wave steepnesses at fixed frequency to enable the effects of non-linearity to be identified. For example, Huntington and Thompson[37] note that all their results lie on the same curve showing that the results were linear in wave steepness. However, this curve was below the linear theoretical prediction.

Although many measurements of pressure have been taken, they have not been critically discussed. Consistently the pressure results do not agree with the theory, particularly close to the free surface. Boreel[9] shows that, as the effects of diffraction increase the pressures become larger than the theory predicts, for measurements close to the free surface. He also shows the runup at the front of his object to be 50% greater than the theory for ka= 0.87, which is consistent with the pressure observations. Although he gives no information about wave heights his experimental total force is consistently higher than his numerical predictions. For a circular cylinder the experimental total force is usually lower than predicted.

There are very few reliable results available for objects which are larger than half the incident wave length ($ka > 1.5$), which is true diffraction. This is because of the practical difficulties of wave generation. The reflection from the front face of the object increases with frequency.

The local wave elevation may double but the total forces are reduced because the effect of the waves is beginning to cancel around the object.

Because of this, and the fact that the pressure variation in such waves falls off rapidly with depth, the wave heights have to be increased to obtain measureable forces. This necessarily increases the steepness of the incident wave (and often its free harmonic content) which then becomes increasingly unstable and three-dimensional (Benjamin and Fier[3], Whitham[86] and Yuen and Lake[89]) and also very near to breaking.

The doubling of the wave height at the front of the object is caused by standing waves which may exceed the limiting steepness for progressive waves by up to 50% before breaking. In these situations, the expansion parameter $\nu\eta$ may approach unity. The contribution from the terms neglected in the expansion may actually exceed the linearised term retained.

Until recently, most offshore structures for which the design was governed by diffraction forces, had extended from the sea bed through the free surface. As oil exploration goes into deeper water, different types of structures are being designed, such as tethered buoyant platforms. Most of the wave action on such structures is in the region close to the free surface. It now becomes important to understand the discrepancies in the pressures.

Much current research is directed towards extending the linearized theory to second order. The above discussion suggests that quite large increases may be found in some cases. The expansion may not even converge for high frequency steep waves. The controversy surrounding Isaacson's assertion, that the second order theory was inconsistent, has been discussed in Chapter 2.

If the perturbation expansion does not converge then an alternative must be sought. One way of achieving this, is to place a source distribution on the moving free surface as well as on the body. The use of a separate source boundary will only be possible if proper account is taken of the logarithmic singularity at the junction of the two boundary conditions. The only difficulty envisaged in this analysis is the construction of a non-linear radiation condition.

The experimental measurements of pressure presented in Chapter 5 are some 20% higher than the linear theory. The definition of pressure amplitude and phase used in these results may include contributions from second and higher order terms. Since the differences between experiment and theory do not depend on steepness, rather on frequency, it appears that there is quite a large first order error. Huntington and Thompson[37] would have to come to the same conclusion on the basis of their results.

The lower limit of wave steepness was governed by the signal to noise ratio on the pressure signals. The higher limit was fixed by the generator characteristics. It is possible that the range of values does not go low enough to reach true small amplitude theory. If this is true it is in remarkable contrast to the measurements in the free progressive waves and would seem to confirm Lighthill's conclusions (see Chapter 2).

The measured phases of these pressures generally showed good agreement with linear theory. Appendix A.2. describes how these signals were amplified and filtered. It seems likely that these phases were lagging the actual values by an amount which, although within the level of scatter, was significant. This phase lag would increase with wave frequency. There appears to be evidence of this behaviour in figures 5.5.10. and 5.5.14. Because the characteristics of these filters were not accurately known, the results have not been corrected. The amplitude reduction of these filters was definitely not the cause of the increased pressures.

It is perhaps surprising that such large discrepencies do not affect the total force to the same extent. It was suggested with reference to figure 5.5.22., that the increase in pressure amplitude was about the same all the way round the cylinder so that the net effect was reduced. However, as was stressed, the pressures are not in the same phase with each other.

From Appendix A.1. the expression for the pressure on the cylinder is of the form

$$p = \frac{\rho g H}{\pi ka} \frac{\cosh k(y+d)}{\cosh kd} \mathrm{Re} \sum_{n=o}^{\infty} \frac{\varepsilon_n . \cos n\theta . i^n e^{-i\sigma t}}{(J_n'^2 + Y_n'^2)} (Jn' - iY_n') \quad 6.1.2.$$

The in line force may be obtained by integrating this expression as

$$F = -\int_{-d}^{o} \int_{o}^{2\pi} p.a. \cos\theta \, d\theta . dy \quad 6.1.3.$$

The orthogonality of the cosine terms makes the only non-zero term from the series, that for n = 1. Whence

$$F = \frac{\rho g H}{\pi k \cosh kd} . 2\mathrm{Re} \frac{e^{-i\sigma t}(Y_1' + iJ_1')}{(J_1'^2 + Y_1'^2)} \int_{-d}^{o} \cosh k(y+d) dy \int_{o}^{2\pi} \cos^2\theta d\theta \quad 6.1.4.$$

which reduces to

$$F = \frac{2\rho g H}{k^2} \frac{\tanh kd}{(J_1'^2 + Y_1'^2)} \cos\left(\sigma t - \tan^{-1} \frac{J_1'}{Y_1'}\right) \quad 6.1.5.$$

For small ka (less than 0.5) the first two terms of the series in equation 6.1.2. dominate. The pressure may therefore be expressed as

$$p = \frac{\rho g H}{\pi k a} \cdot \frac{\cosh k(y+d)}{\cosh kd} \left[\frac{\cos(\sigma t + \tan^{-1} \frac{Y_o'}{J_o'})}{(J_o'^2 + Y_o'^2)^{\frac{1}{2}}} + \frac{2\cos\theta\cos(\sigma t - \tan^{-1} \frac{J_1'}{Y_1'})}{(J_1'^2 + Y_1'^2)^{\frac{1}{2}}} + \ldots\ldots \right] \quad 6.1.6.$$

The first term corresponds to the rise and fall of the free surface whereas the second term which corresponds to its slope gives rise to theforce. It seems possible that the effects of finite wave height could contribute to an increased amplitude of the first term without significantly affecting the second.

6.2. Program efficiency

In chapter 4 the efficiency of the diffraction program based on quadratic variation of source strength was compared with the constant source facet method, using as a basis for comparison the number of Green's function evaluations. This gives the relative efficiencies of the two approaches, all other things being equal.

An absolute saving in computation time may only be obtained by making the existing program at least as efficient as a typical facet method program. A major contribution to this time is the evaluation of the Bessel functions.

Several possibilities exist for improvement. The most obvious one is to replace the subroutine with a reference to a machine coded package. Further improvements may then be obtained by storing values in a look-up table as they are calculated. For many typical geometries, repeated calculations may then be avoided if the results are already available. In the special case of the circular cylinder this would reduce the number of references to the package to three for each Bessel function.

As computer storage capabilities increase it is becoming feasible to store the completed evaluations for all arguments in 'tabular' form. Linear or quadratic interpolation may then be used to quickly obtain any value.

A similar saving may be obtained in the evaluation of the imaginary roots of the dispersion relation. At present, these are duplicated at each Green's function evaluation because it is not known a priori how many will be required. This duplication may be avoided by storing the roots in a 'vector' and maintaining a parallel vector of flags which are set once a root is calculated.

The use of the continued fraction for obtaining the initial guesses is not the most direct way. It is clear from figure 4.3.1 that

$$\chi_k^0 = k\pi - \tan^{-1}\left[\frac{2h\nu}{\pi(2k-1)}\right] \qquad 6.2.1.$$

provides an initial guess on the required side of the root.

In more general terms, the indirect method used here is by definition inefficient. It requires the intermediate computation of a distribution of source strength, which is not of any physical significance, before the values of interest may be obtained. Few researchers in this field have seen the advantages of using the direct boundary element method, based on Green's theorem, although Haskind's relations based on the same theorem have been in use for some time. Monacella[60] commenced his semi-analytical approach to ship motions using a direct boundary integral statement. Bai and Yeung[1] used a direct numerical discretisation which appears to have gone largely unnoticed.

The direct B.E.M. (see chapter 2. section 3) yields a numerical boundary relation between the normal velocity (q) of the fluid and its potential (ϕ) in the matrix form

$$[H]\{\phi\} = [G]\{q\} \qquad 6.2.2.$$

For wave diffraction by a fixed obstacle the vector $\{q\}$ is known in terms of the incident wave. The matrices $[H]$ and $[G]$ involve similar integrals to those in the indirect method. For simple harmonic waves the use of complex notation means that the fluid pressure may be directly related to ϕ (equation 4.6.7). The equations therefore reduce to

$$[H]\{p\} = i\rho\sigma[G]\{q\} \qquad 6.2.3.$$

The unknown pressures are now given directly once matrix $[H]$ is inverted. Equation 6.2.3. is in a form which lends itself to the solution of fluid-structure interaction problems. Walker[81] solved the coupled problem of a thin walled container of fluid by using a complex notation to relate the normal velocity of the container to its normal displacement. This is a small displacement analysis since it neglects the time variation of the normal direction necessary for an admissible displaced shape.

There is no possibility in this method of defining an auxiliary boundary in an attempt to improve accuracy. However, the accuracy of this approach is generally better than the traditional indirect method. The integral form of the Green's function will have to be used for arguments close to zero.

The homogeneous form of equation 6.2.2. may be expressed as

$$\pi \phi(p) - \int \phi(q) \frac{\partial G}{\partial n}(p,q) \, dq = 0 \qquad 6.2.4.$$

which has solutions at exactly the same values of ka as equation 3.117. Therefore the problem of fictitious frequencies still exists for the direct method.

6.3. Application to arbitrary shapes

The excellent agreement obtained with a small number of elements, in the numerical calculations in chapter 4, was obviously due in some part to the considerable symmetry which the vertical circular cylinder possesses in the plan dimensions. The way that this symmetry influences the results, must be understood if estimates of the behaviour for other less regular shapes are to be made.

The numerical solution makes use of the pulsating point source solution. The fact that the total force only requires the use of the first cosine term of the analytical solution would seem to be of no direct relevance. The only information that the numerical formulation has about the shape of the cylinder is its position and normal direction at the finite number of points chosen for satisfaction of the boundary conditions. It seems reasonable to suppose that the final solution will attempt to fit the smoothest surface through these points, which in this particular case, is very close to the actual shape.

In general, the points on the physical boundary should be so chosen that the smoothest curve through them coincides with the required shape. For bodies with sharp edges, the normal direction must be be specified at either side of the edge, by introducing additional nodes. This must accompany proper allowance for singular behaviour.

The other numerical advantage peculiar to the circular cylinder is that singular behaviour is only necessary at its axis. One way of investigating the effect this has on the numerical results, is to change the position of the axis of the fictitious cylinder.

The difficulty of properly testing a diffraction program is that there are very few analytical solutions available which do not possess either singular behaviour at some point on the boundary or many axes of symmetry, whereas many realistic structures have neither.

In the absence of such solutions, validation is often based on experimental results which apparently satisfy the same assumptions.

The previous arguments associated with containing any possible singular behaviour suggest that the fictitious boundary should be placed fairly close to the physical boundary.

For the circular cylinder Table 6.1.1. shows the pressures from three cases for which a 56 node discretisation was used, for values of ZK of 0.1, 0.5 and 0.9. The values given are the normalised amplitudes at the still water level for a value of ka = 0.571. The exact solution is also shown.

It might be concluded, on the basis of the experimental evidence in chapter 5, that the most accurate estimate would be obtained with ZK = 0.9 or even higher. It is clear, that this result would be the furthest from the exact solution. Figure 4.7.1. shows that this indeterminancy reduces as the number of elements is increased.

To apply the separate source diffraction program therefore requires a parametric study based on the position of the source boundary as well as the number of elements. Because of the cost of running diffraction programs not even the latter is done in practice.

CHAPTER 7 SUMMARY AND CONCLUSIONS

7.1. Summary

The problem of linear wave diffraction by a vertical circular cylinder in arbitrary but constant water depth was solved numerically using the indirect boundary element method. Many of the numerical procedures used, were first discussed in the context of the simpler case of steady flow without a free surface, in two dimensions.

It was demonstrated that greatly increased accuracy may be obtained by defining a separate fictitious boundary on which the source distribution is placed. Both interior and exterior problems were solved using a piecewise linear interpolation for the source intensity. The numerical formulation for the particular problem of steady flow past a circular cylinder near a plane boundary was shown in detail. The limitations of the separate source boundary approach are highlighted by this example, since the analytical result for the case of the cylinder resting on the boundary cannot be modelled without additional allowance for the singular behaviour at the point of contact. The three computer programs written for these steady flow cases are included in appendix A.3.

The separate source boundary technique was then applied to the wave diffraction problem using the series form of the corresponding Green's function. In this case, quadratic interpolation of source intensity was used. The computer program, listed in appendix A.3. was tested against the analytical solution for the circular cylinder. It was demonstrated that the accuracy of the numerical solution increases as the source boundary is moved away from the physical boundary.

Although the majority of the comparisons was based on the total in-line force, the pressures were also shown to be predicted equally well. Within the limits of computer time it was shown that the force converges rapidly as the number of elements is increased. Nevertheless, very few elements are needed to obtain reasonable agreement with the theoretical force.

Experimental measurements of pressure due to regular waves on a vertical circular cylinder in the inertia/diffraction regime were also presented.

The pressure amplitude in the waves in the absence of the cylinder was shown to agree with the linear theory to within the level of scatter. The measured pressure amplitude on the cylinder was about 20% higher than the theoretical prediction whereas the phase measurements were scattered closely about the theoretical line. The discrepancy in the amplitudes only appeared to correlate with wave steepness for very high frequencies. A large first harmonic pressure component at points on the lower half of the cylinder was observed.

It is shown that the numerical predictions of pressure on the cylinder may increase as the fictitious source boundary is moved towards the physical boundary. It is possible that experimental and numerical pressures may agree if a coarse discretisation is used. This agreement should always be tested by refining the discretisation until convergence is obtained in the numerical procedure.

7.2. The importance of the present study.

Some linear diffraction programs separate the source boundary and the physical boundary to avoid the problem of the 'fictitious frequencies', particularly when spectral techniques are used. This study shows that this separation must be made with care to make sure that an accurate solution is obtained. At least one incorrect application of this approach has been published.

Most diffraction programs are based on the point source 'facet' method. This study demonstrates how the concept of a continuous distribution of source intensity may be used to introduce higher order interpolation. This does not result in significant savings in computation time.

Most comparisons of experimental measurements and theoretical or numerical predictions have been based on total forces. The good overall agreement often masks quite significant local discrepancies. The measured pressures in this study show such discrepancies near the free surface to be quite large. This may be extremely important for structures which do not extend to great depths. These results will prove useful for comparison with a non-linear solution.

7.3. Limitations of the present study and recommendations for further work

The present study has been limited to the vertical circular cylinder. This is not a severe limitation since many offshore structures are nearly circular or composed of elements of circular cross-section. Any structures which possess sharp corners will exhibit flow separation at least locally.

The reduction in the number of elements required for accurate numerical solution, does not necessarily lead to reduced computation time. Because of the quadratic interpolation and the size of each element in relation to a wave length, it appears that at least nine point Gaussian quadrature is required. One definite advantage of higher order interpolation is that the rapid decay of source intensity with depth is accurately represented without having to concentrate elements near the free surface.

In general, few benefits appear to be obtained from separation of the source intensity boundary from what must be a smooth physical boundary. However, existing facet methods cannot model singular behaviour at corners either, unless the facet mesh is extremely fine. The uncertainty in the choice of boundary position and the lack of diagonal dominance in the matrix of coefficients make it very difficult to apply this method without a parametric study. Unlike the case when the sources are on the physical boundary, there is no guarantee that convergence (if obtained) will be to the correct solution. In this context the studies of convergence for the cylinder in steady flow are important, since they showed (without being limited by computer time) that increasing the number of elements may actually reduce accuracy. This behaviour must also occur in wave diffraction.

The experimental results seem to point to a first order error in the linear diffraction theory near to the moving free surface. These results will be useful for comparison with the non-linear theories, which are currently being derived. There is however, still room for improvement in the normalisation of these results. The considerable scatter may be reduced by scanning the wave envelope in front of, and behind, the cylinder to enable a more precise determination of the incident wave height. This may in turn show that many of the high frequency waves are in fact unstable. A theoretical development based on Stokes perturbation expansion will not predict this real phenomenum.

A numerical method which should predict the correct behaviour (including instability, and other less well understood phenomena such as wave set down) is one in which the free surface boundary conditions are actually numerically satisfied at the moving free surface. Such a method will remain valid until the free surface actually breaks.

A more sophisticated method of data analysis is required to separate the Fourier components of the pressure signals. This would make it much easier to find the dependence on wave steepness.

References

1. Bai, K.J. and Yeung, R., "Numerical solutions of Free-surface Flow Problems", 10th Symposium in Naval Hydrodynamics, Office of Naval Research, 1974.

2. Banerjee, P.K., "Foundations within a Finite Elastic Layer: Application of the Integral Equation Method". Civil Engineering and Public Works Review, Nov. 1971, pp. 1197-1202.

3. Benjamin, T.B. and Feir, J.E., "The Disintegration of Wavetrains on Deep Water, Part 1. Theory," Journal of Fluid Mechanics, Vol. 27, 1967, pp 417-430.

4. Berkhoff, J.C.M., "Linear Wave Propagation Problems and the Finite Element Method", Finite Elements in Fluids, Vol 1, Eds R.H. Gallagher et al., Wiley, London, 1975 pp 251-264.

5. Bettess, P., "Infinite Elements", International Journal for Numerical Methods in Engineering, Vol 11, 1977, pp 53-64.

6. Bettess, P. and Zienkiewicz, O.C., "Diffraction and Refraction of Surface Waves using Finite and Infinite Elements," International Journal for Numerical Methods in Engineering, Vol. 11, 1977, pp 1271-1290.

7. Bidde, D.D., "Laboratory Study of Lift Forces on Circular Piles". Proc. ASCE, Vol 93, WW2, May 1967, pp 129-156.

8. Black, J.L., "Wave Forces on Vertical Axisymmetric Bodies," Journal of Fluid Mechanics, Vol. 67, May 1975, pp 369-376.

9. Boreel, L.J., "Wave Action on Large Offshore Structures," Proceedings of the Institute of Civil Engineers Conference on Offshore Structures,London, 1974.

10. Borgman, L.E., "Spectral analysis of Ocean Wave Forces on Piling". Proceedings ASCE, Vol 93, WW2, May 1967, pp 129-156.

11. Borgman, L.E., "Ocean Wave Simulation for Engineering Design", Proceedings ASCE, Vol 95, WW4, Nov 1969, pp 557-583.

12. Brebbia, C.A. and Walker, S., "Introduction to Boundary Element Methods," in Recent Advances in Boundary Element Methods, proceedings of the International Conference, Southampton, 1978, publ. Pentech Press, pp 1-44.

13. Chakrabarti, S.K. "Wave Forces on Submerged Objects of Symmetry", Journal of the Waterways Harbours and Coastal Engineering Division, A.S.C.E, Vol. 99, No. WW2, May, 1973, pp. 147 - 164

14. Chakrabarti, S.K. and Naftzger, R.A., "Non-Linear Wave Forces on Halfcylinder and Hemisphere" Journal of the Waterways Harbours and Coastal Engineering Division, ASCE, Vol. 100, No. WW3, Aug. 1974, pp 189 - 204.

15. Chakrabarti, S.K. and Tam, W.A. "Gross and Local Wave Loads on a Large Vertical Cylinder - Theory and Experiment, "Proceedings of the fifth off-shore Technology Conference, Paper No. OTC 1818, Vol.I, Houston Texas, Apr-May 1973. pp 203 - 221.

16. Chakrabarti, S.K.,Wolbert, A.L. and Tam, W.A., "Wave Forces on Vertical Circular Cylinders", Proc. ASCE, Vol 102, WW2, May 1976, pp 203-221.

17. Chen, H.S. and Mei, C.C., "Oscillations and Wave Forces in a Man-Made Harbour in the Open Sea," 10th Symposium in Naval Hydrodynamics, Office of Naval Research, 1974.

18. Cooley, J.W. and Tukey, J.W., (An Algorithm for the Machine Calculation of Complex Fourier Series'. Journal of Mathematics of Computations, April 1965, pp 297-301.

19. Cooper, R.I.B. and Longuet-Higgins, M.S., "An Experimental Study of the Pressure Variations in Standing Water Waves," Proceedings of the Royal Society of London, A206, 1951, pp 424-435.

20. Eatock-Taylor, R. "Structural Dynamics of Fixed and Floating Platforms in Waves", Proceedings of the International Symposium on the Dynamics of Marine Vehicles and Structures in Waves, University College London, publ I. Mech Eng., Apr 1974.

21. Eatock-Taylor, R and Waite, J.B., "The Dynamics of Offshore Structures Evaluated by Boundary Integral Techniques," International Journal for Numerical Methods in Engineering, Vol.13, 1978, pp 73-92.

22. Faltinsen, O.M. and Michelsen, F.C., "Motions of Large Structures in Waves at Zero Froude Number, "Proceedings of the International Symposium on the Dynamics of Marine Vehicles and Structures in Waves, University College London, published by Institute of Mechanical Engineers, April 1974.

23. Fenton, J.D., "Wave Forces on Vertical Bodies of Revolution," Journal of Fluid Mechanics, Vol.85 Mar 1978, pp 241-255.

24. Garrison, C.J., discussion of "Nonlinear Wave Forces on Large Offshore Structures", by M.de St.Q. Isaacson, Journal of the Waterway, Port, Coastal and Ocean Division, ASCE, Vol.104,No. WW1, Feb 1978, pp 93-94.

25. Garrison, C.J. and Chow, P.Y., "Wave Forces on Submerged Bodies, "Journal of the Waterways, Harbours and Coastal Engineering Division, ASCE, Vol.98, No. WW3, Aug., 1972,pp. 375-392.

26. Garrison, C.J., Tørum, A., Iversen, C., Leivseth, S. and Ebbesmeyer, C.C., "Wave Forces on Large Volume Structures - A Comparison Between Theory and Model Tests," Proceedings of the Sixth Offshore Technology Conference, Paper No. OTC 2137, Houston Texas, May 1974, pp 1061-1070.

27. Harms, V.W., "Diffraction of Water Waves by Isolated Structures," Journal of the Waterway, Port, Coastal and Ocean Division ASCE,Vol. 105, No. WW2, May 1979, pp 131-147.

28. Havelock, T.H., "Forced Surface-Waves on Water," Philosophical Magazine of the Royal Society of London, Vol.8, No.51, Oct 1929, pp 569-576.

29. Havelock, T.H., "The Pressure of Water Waves on a Fixed Obstacle", Proceedings of the Royal Society of London, series A, Vol. 175, 1940, pp 409-421.

30. Hess, J.L. "Higher Order Numerical Solution of the Integral Equation for the Two-dimensional Neumann Problems," Computer Methods in Applied Mechanics and Engineering, Vol.2, 1973, pp 1-15.

31. Hess, J.L., "Review of Integral-Equation Techniques for Solving Potential-Flow Problems with Emphasis on the Surface-Source Method," Computer Methods in Applied Mechanics and Engineering, Vol.5, 1975, pp 145-196.

32. Hess, J.L. and Smith, A.M.O. "Calculation of non-lifting potential flow about arbitrary three-dimensional bodies," Report No E.S. 40622, 1962 (Douglas Aircraft Division, Long Beach, California). Also in abbreviated form in Journal of Ship Research, Vol. 8, 1964.

33. Hogben, N., and Standing, R.G., "Wave Loads on Large Bodies," Proceedings of the International Symposium on the Dynamics of Marine Vehicles and Structures in Waves, University College London, published by Institute of Mechanical Engineers, April 1974.

34. Hogben, N.,and Standing, R.G., "Experience in Computing Wave Loads on Large Bodies," Proceedings of the Offshore Technology Conference, Paper No. OTC 2189, Vol II, Houston, Texas, May 1975, pp.413-431.

35. Hogben, N., Miller, B.L., Searle, J.W. and Ward, G. "Estimation of Fluid Loading on Offshore Structures', NMI Report No. R11, 1977.

36. Hunt, J.N. and Baddour, R.E., "Second-Order Standing Waves Bounded by Circular Cylinders," Journal of the Waterway Port Coastal and Ocean Division, ASCE, Vol. 106, No WW4, Nov. 1980, pp 122-127.

37. Huntington, S.W. and Thompson, D.M., "Forces on a Large Vertical Cylinder in Mutli-Directional Waves," Proceedings of the Eigth Offshore Technology Conference, Paper No. OTC 2539, Vol. II, Houston Texas, May 1976, pp 169-183.

38. Ippen, A.T. Estuary and Coastline Hydrodynamics, McGraw-Hill, 1966.

39. Isaacson, M. de St. Q., "Nonlinear Wave Forces on Large Offshore Structures," Journal of the Waterway, Port, Coastal and Ocean Division, ASCE, Vol.103, No. WW1, Feb. 1977, pp 166-170.

40. Isaacson, M. de St.Q., "Vertical Cylinders of Arbitrary Section in Waves," Journal of the Waterway, Port, Coastal and Ocean Division, ASCE Vol. 104, No. WW4, Aug. 1978, pp 309-324.

41. Isaacson, M. de St.Q., "Closure of Nonlinear Wave Forces on Large Offshore Structures," Journal of the Waterway, Port, Coastal and Ocean Division, ASCE Vol. 104, No. WW4, November 1978, pp 457-459.

42. Isaacson, M. de St. Q. and Maull, D.J. "Transverse Forces on Vertical Cylinders in Waves", Proc. ASCE, Vol 102, WW1, Feb 1976, pp 49-60.

43. Jaswon, M.A., "Integral Equation Methods in Potential Theory;I", Proceedings of the Royal Society of London, Series A. Vol 275, 1966. pp 23-32.

44. Jaswon, M.A. and Symm. G.T., Integral Equation Methods in Potential Theory and Elastostatics, Academic Press, London, 1977.

45. Jeffreys, H., "On The Transport of Sediments by Streams", Proceedings of the Cambridge Philosophical Society, Vol. 25, 1929. part III, pp 272-6.

46. Jeffreys, H. and Jeffreys, B., Methods of Mathematical Physics, 3rd Edn., Cambridge University press, 1972.

47. John, F., "On the Motion of Floating Bodies Part II," Communications in Pure and Applied Mathematics, Vol. 3, 1950, pp 45-101.

48. Karman, T. von, "Calculation of Pressure Distribution on Airship Hulls," National Advisory Committee for Aeronautics, Technical Memorandum No. 574, 1930, 30 pages.

49. Keating, T. and Webber, N.B., "The Generation of Periodic Waves in a Laboratory Channel : a Comparison between Theory and Experiment," Proceedings of the Institute of Civil Engineers, Part 2, Vol.63, Dec. 1977, pp 819-832.

50. Keulegan, G.H. and Carpenter, L.H., "Forces on Cylinders and Plates in an Oscillating Fluid," Journal of Research National Bureau Standards, Vol 60, No.5, May 1958, pp 423-440.

51. Lamb, Sir H., "Hydrodynamics," Cambridge University Press, 6th Edition, 1932.

52. Lebreton, J.C. and Cormault, P., "Wave Action on Slightly Immersed Structures, Some Theoretical and Experimental Considerations," Proceedings of the Symposium "Research on Wave Action," Delft, Netherlands. Vol.4, 1969.

53. Liggett, J.A. and Liu, P.L-F. Lecture notes for the course - Boundary Integral Equation Method Applied to Flow in Porous Media, at the School of Civil and Environmental Engineering, Cornell University, July 1979.

54. Lighthill, M.J. "Waves and Hydrodynamic Loading" Conference on the Behaviour of Offshore Structures, Imperial College, London, Aug 1979.

55. Longuet-Higgins, M.S., "A Theory of the Origin of Microseisms," Philosophical Transactions of the Royal Society of London, A243, 1950, pp1-35.

56. Longuet-Higgins, M.S. and Cokelet, E.D., "The Deformation of Steep Surface Waves on Water, I. A Numerical Method of Computation," Proceedings of the Royal Society of London, Vol. A.350, 1976, pp1-26.

57. Longuet-Higgins, M.S. and Ursell, F., "Sea Waves and Microseisms," Nature, Vol. 162, Oct. 1948, p 700.

58. MacCamy, R. and Fuchs, R.A. "Wave Forces on Piles: A Diffraction Theory", Technical Memorandum No 69, U.S. Army Corps of Engineers, Beach Erosion Board, Washington D.C., Dec, 1954.

59. Miller, B.L. and Matten, R.B., "A Technique for the Analysis of Wave-loading data Obtained from Model Tests," NPL Report Mar.Sci. R136, June 1976.

60. Monacella, V.J., "The Disturbance Due to a Slender Ship Oscillating in Waves in a Fluid of Finite Depth," Journal of Ship Research, Vol.10, No.4, 1966, pp 242-252.

61. Morison, J.R., O'Brien, M.P., Johnson, J.W. and Schaaf, S.A. "The Force Exerted by Surface Waves on Piles," Journal of Petroleum Technology. AIME, Vol 189, 1950, pp 149-154.

62. Morse, P.M. and Feshbach, H, Methods of Theoretical Physics, Vol. II, McGraw-Hill, 1953.

63. Murphy, J.E., "Integral Equation Failure in wave Calculations," Journal of the Waterways, Harbours and Coastal Engineering Division, ASCE, Vol. 104, No.WW4, Aug. 1978, pp 330-334.

64. Nath, J.H. and, Harleman, D.R.F. "Response of Vertical Cylinder to Random Waves," Proc. ASCE, Vol 96, Ww2, May 1970, pp 373-386.

65. Newman, J.N., "The Exciting Forces on Fixed Bodies in Waves," Journal of Ship Research, Vol.6, 1962, pp 10-17.

66. Oliveira, E.R.A., "Plane Stress Analysis by a General Integral Method", Journal of the Engineering Mechanics Division, A.S.C.E., Vol. 94, No. EM1, Feb. 1968, pp 79-101.

67. Oortmerssen, G.Van, "Some Aspects of Very Large Offshore Structures," 9th Symposium on Naval Hydrodynamics, Office of Naval Research, Paris, 1972.

68. Phillips, O.M., The Dynamics of the Upper Ocean, Cambridge University Press, Cambridge, England, 1966, pp 41-42.

69. Pierson, W.J. and Holmes, P. "Irregular Wave forces on a Pile", Proc. ASCE, Vol 91, WW4, Nov 1965, pp 1 - 10.

70. Rainey, R.C.T. "The Dynamics of Tethered Platforms", Journal of the Royal Institute of Naval Architects, 1977.

71. Sarpkaya, T. "The Hydrodynamic Resistance of Roughened Cylinders in Harmonic Flow", Journal of the Royal Institute of Naval Architects, 1977.

72. Sarpkaya, T. and Isaacson, M., Mechanics of Wave Forces on Offshore Structures, Van Nostrand Reinhold Co. 1981.

73. Sawaragi, T., Nakamura, T., Kita, H., "Characteristics of Lift Forces on a Circular pile in Waves", Coastal Engineering in Japan, Vol 19, 1976, pp 59-71.

74. Shaw, R.P. "Coupling Boundary Integral Equation Methods to Other Numerical Techniques," International Symposium on Recent Advances in Boundary Element Methods, Southampton, July 1978 pp 137-147.

75. Sneddon, I.N., Special Functions of Mathematical Physics and Chemistry, Oliver and Boyd, Ltd. Edinburgh, 1961.

76. Symm, G.T., "Integral Equation Methods in Potential Theory; II", Proceedings of the Royal Society of London, Series A, Vol. 275, 1963, pp 33-46.

77. Ursell, F. "On The Exterior Problems of Acoustics", Proceedings of the Cambridge Philosophical Society, Vol. 74, 1973, pp 117-125.

78. Ursell, F., Dean, R.G. and Yu, Y.S., "Forced Small-Amplitude Water Waves : A Comparison of Theory and Experiment". Journal of Fluid Mechanics, Vol. 7, 1960, pp 33-52.

79. Venkatanarasaiah, P., discussion of "Nonlinear Wave Forces on Large Offshore Structures". by M.de St. Q. Isaacson, Journal of the Waterway, Port, Coastal and Ocean Division, ASCE, Vol.104, No. WW2, May 1978, pp 245-246.

80. Verley, R.L.P. "Wave Forces on Structures - an Introduction", BHRA report No. TN 1319, Nov. 1975.

81. Walker, S. "Boundary Elements in Fluid/Structure Interaction Problems," in Proceedings of the 2nd International Seminar on Recent Advances in Boundary Elements, Southampton, 1979 pp 347-364.

82. Watson, G.N., A Treatise on the Theory of Bessel Functions, Cambridge University Press, 1944.

83. Watson, J.O., "Advanced Implementation of the Boundary Element Method for Two-and Three-dimensional Elastostatics" in Developments in Boundary Element, Methods - 1, eds P.K. Banerjee and R. Butterfield, Applied Science Publishers, London, 1979, Chapter 3.

84. Wehausen, J.V. and Laitone, E.V., "Surface Waves", Encyclopedia of Physics (ed. S. Flugge), Vol.9, Fluid Dynamics III, Springer-Verlag, Berlin, Germany, 1960, pp 446-778.

85. Whitham, G.B., "Mass, Momentum and Energy Flux in Water-Waves", Journal of Fluid Mechanics, Vol.12, 1962, pp 135-147.

86. Whitham, G.B., "Nonlinear Dispersion of Water Waves", Journal of Fluid Mechanics, Vol.27, 1967, pp 399-412.

87. Wiegel, R.L., Oceanographical Engineering, Prentice Hall, Inc., Englewood Cliffs, N.J. 1964.

88. Wilson, B.W. and Reid, R.O., "Discussion of Wave Force Coefficients" Proceedings ASCE, Vol 189, WW1, Feb 1963, pp 61-65.

89. Yuen, H.C. and Lake, B.M., "Instabilities of Waves on Deep Water", Annual Reviews of Fluid Mechanics, Vol. 12, 1980, pp 303-334.

90. Zdravkovich, M.M. and Namork, J.E., "Formation and Reversal of Vortices around Circular Cylinders Subjected to Water Waves", Proc. ASCE, Vol 103, WW3, Aug. 1977, pp 378 - 383.

91. Zienkiewicz, O.C., The Finite Element Method in Engineering Science, McGraw-Hill, London, 1971.

92. Zienkiewicz, O.C., Kelly, D.W. and Bettess, P., "The Coupling of the Finite Element Method and Boundary Solution Procedures," International Journal for Numerical Methods in Engineering, Vol.11, 1977, pp 355-375.

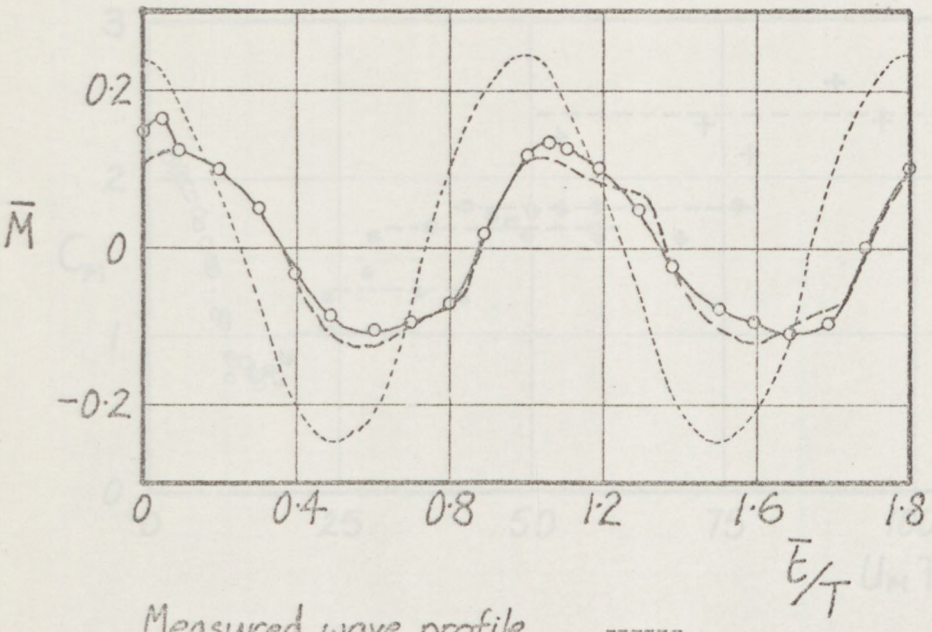

Measured wave profile -----
Theoretical moment - - -
Measured moment —o—

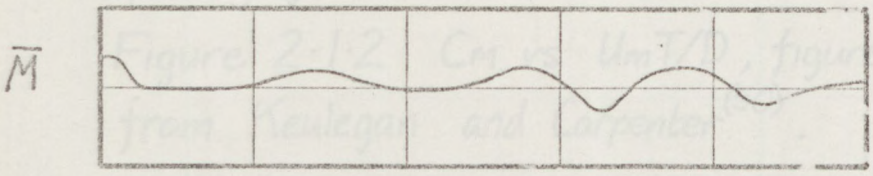

Approximate remainder function showing strong evidence of a harmonic at twice the wave frequency.

Fig. 2·1·1 Reproduced figure 5 from Morison et al[61] plus remainder function.

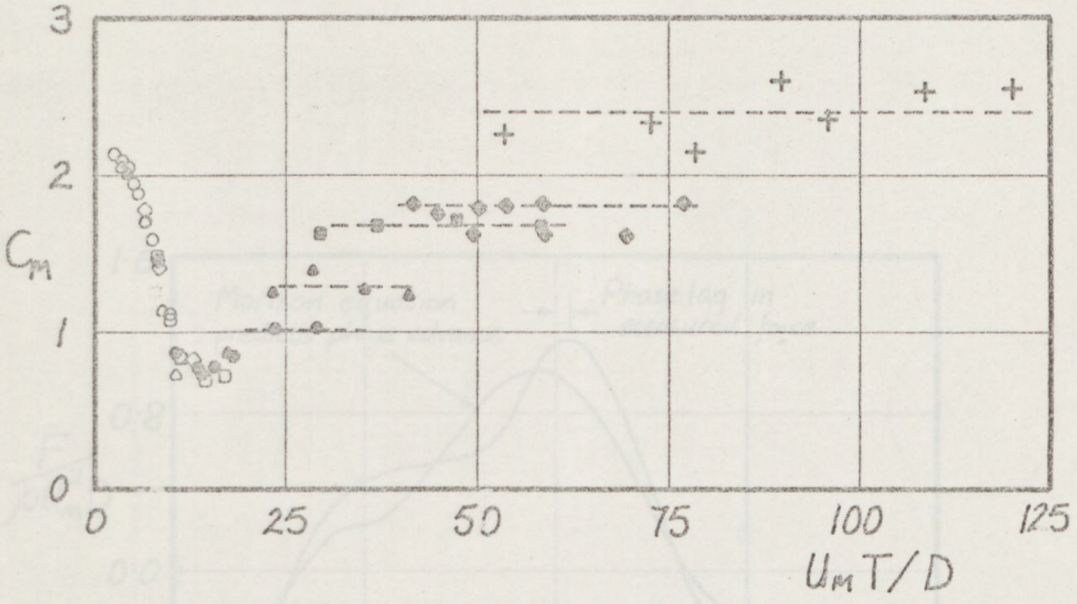

Diameter (inches):	3	2·5	2	1·75	1·5	1·25	1	0·75	0·5
Corresponding symbol:	○	△	□	◇	●	▲	■	◆	+

Figure 2·1·2 Cm vs UmT/D, figure 10 from Keulegan and Carpenter[50].

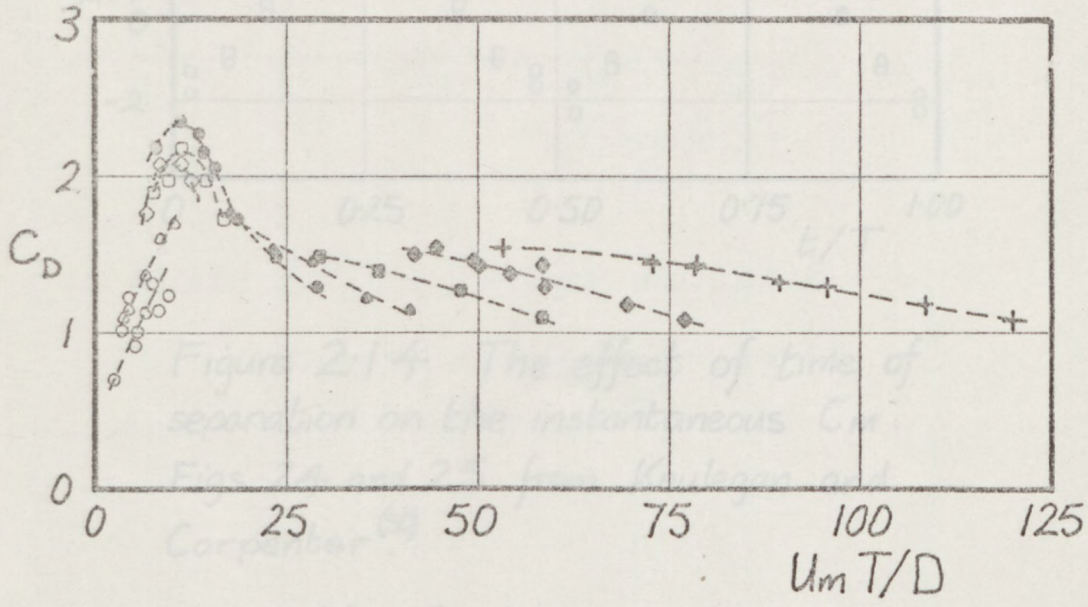

Figure 2·1·3 C_D vs $U_m T/D$, figure 11 from Keulegan and Carpenter[50].

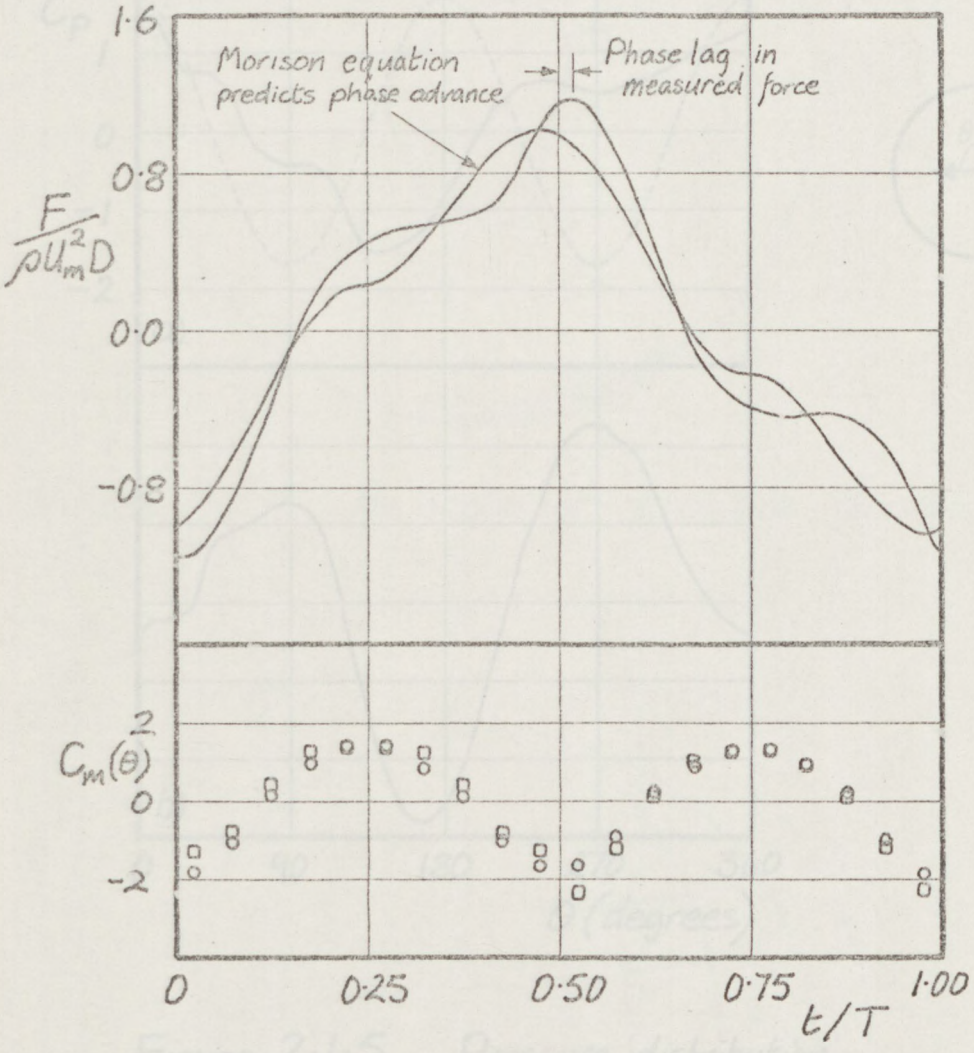

Figure 2·1·4 The effect of time of separation on the instantaneous C_m. Figs 24 and 25 from Keulegan and Carpenter.[50]

$C_m = 0·80$, $C_D = 2·05$, $U_m T/D = 15·6$

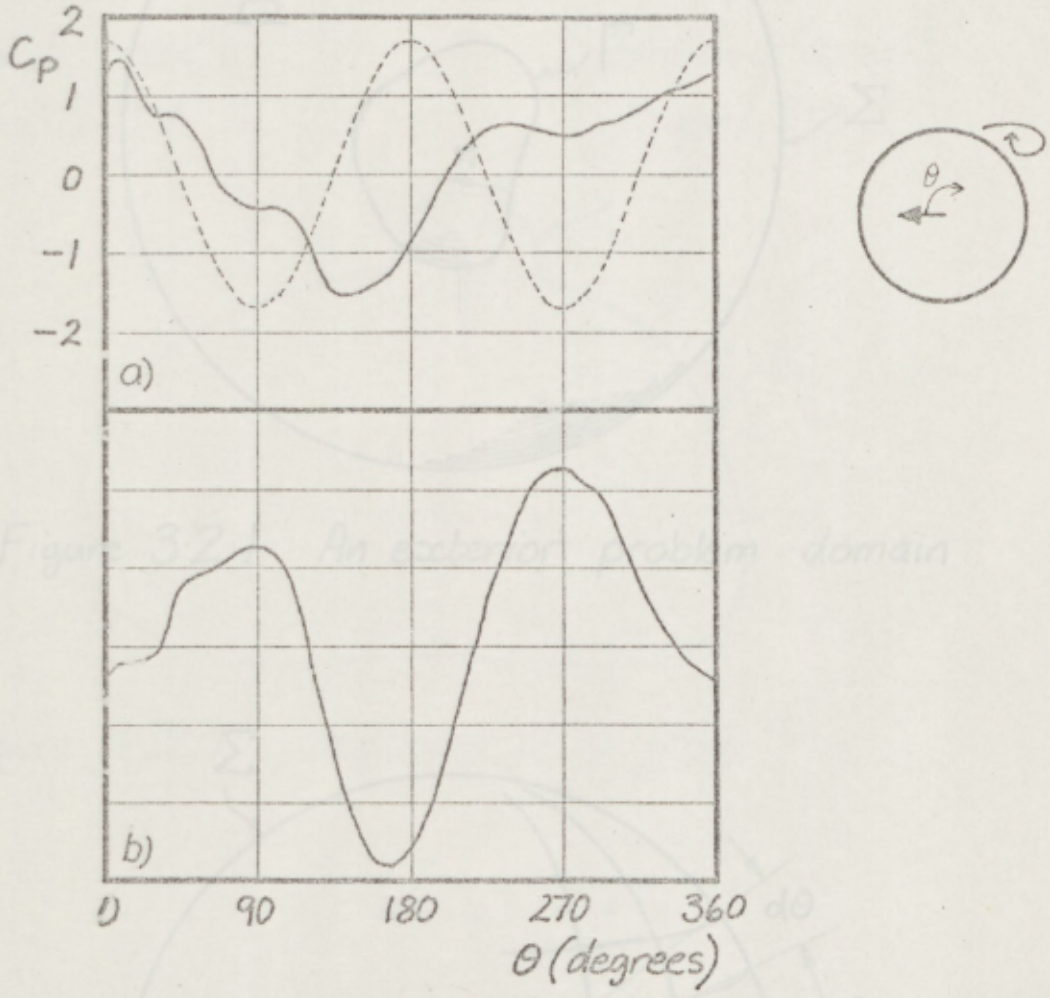

Figure 2·1·5 Pressure distribution due to observed vorticity. Figure 10 from Isaacson and Maull [42].

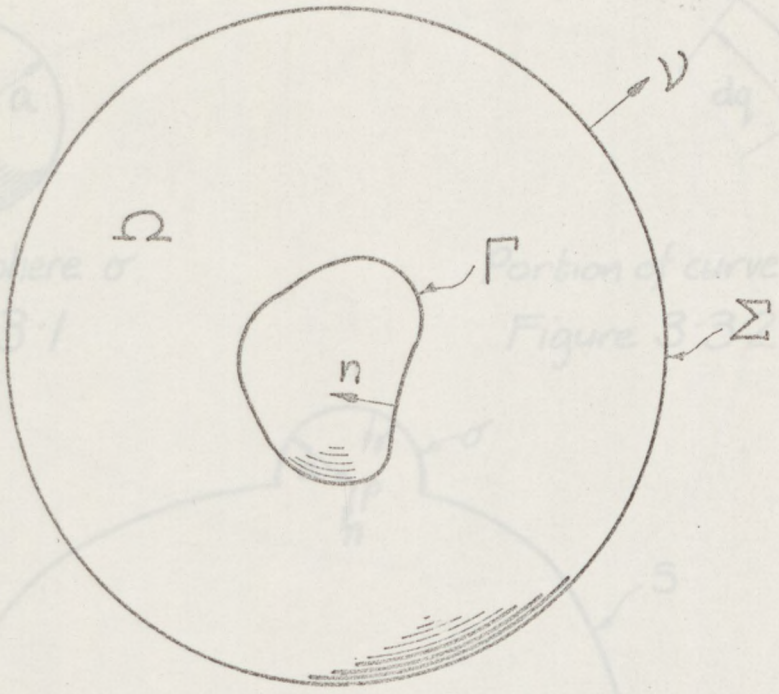

Figure 3·2·1 An exterior problem domain

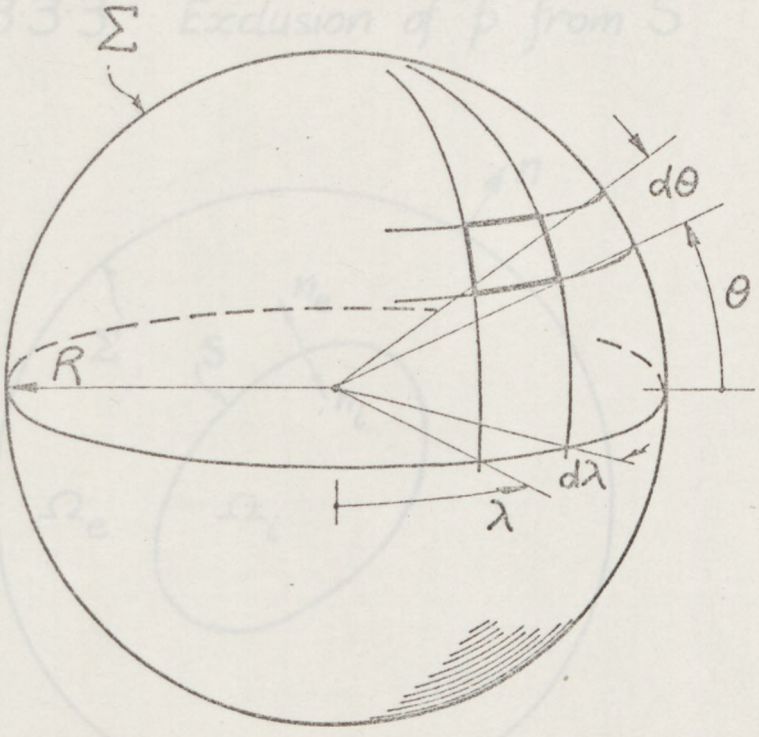

Figure 3·2·2 Coordinate system on Σ

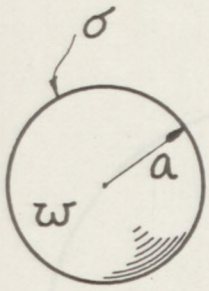

The small sphere σ
Figure 3·3·1

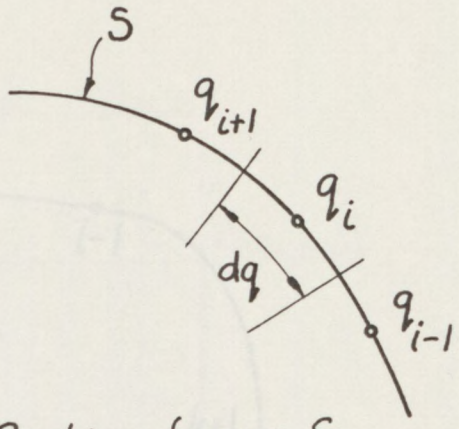

Portion of curve S
Figure 3·3·2

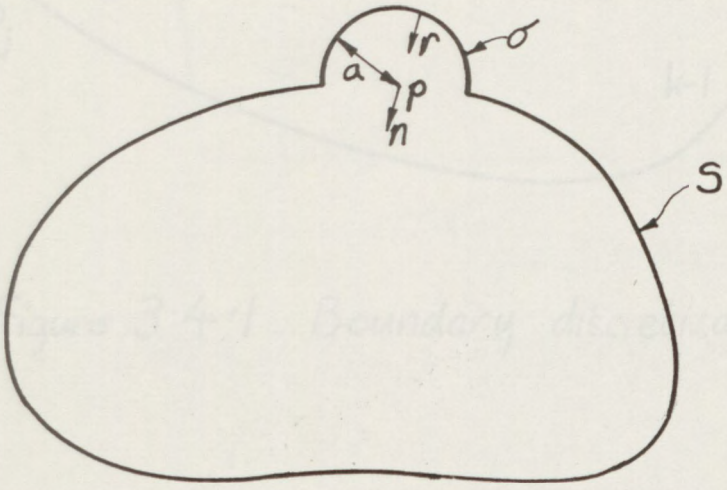

Figure 3·3·3 Exclusion of p from S

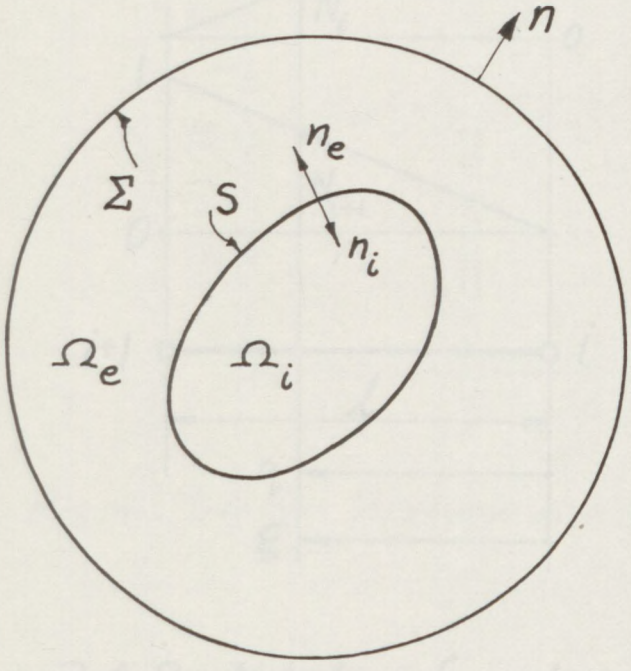

Figure 3·3·4 Exterior and Interior domains

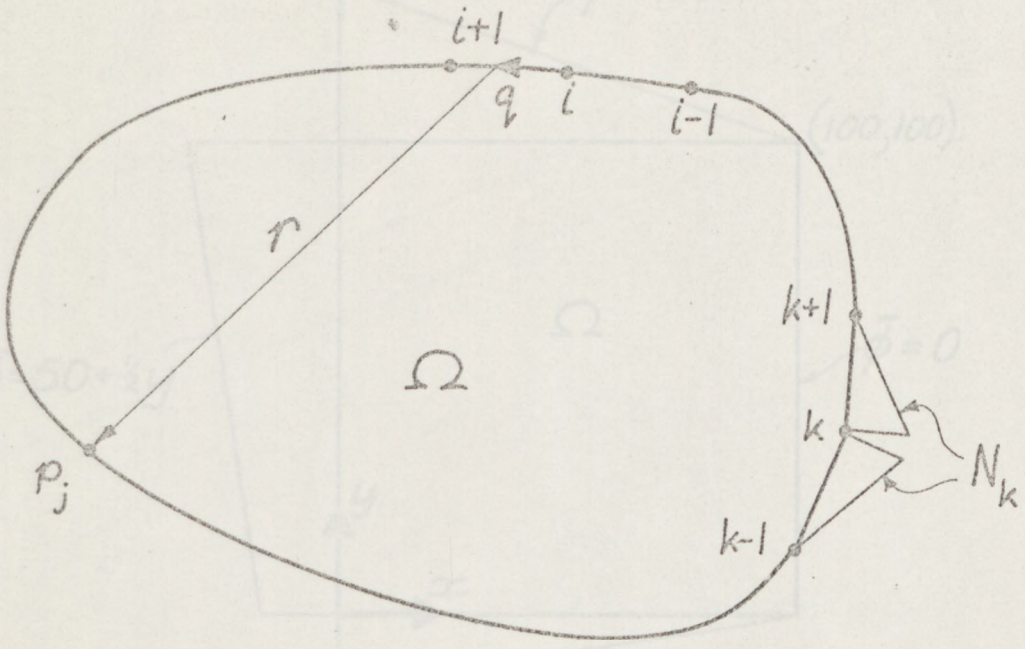

Figure 3·4·1 Boundary discretization

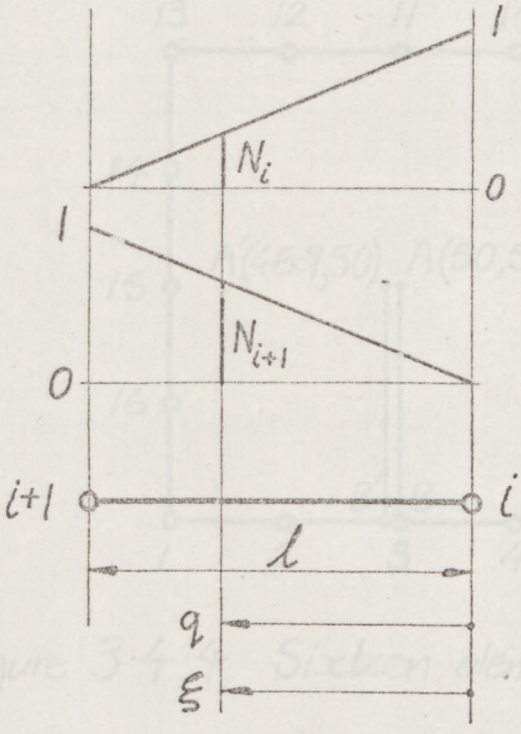

Figure 3·4·2 Notation for element i

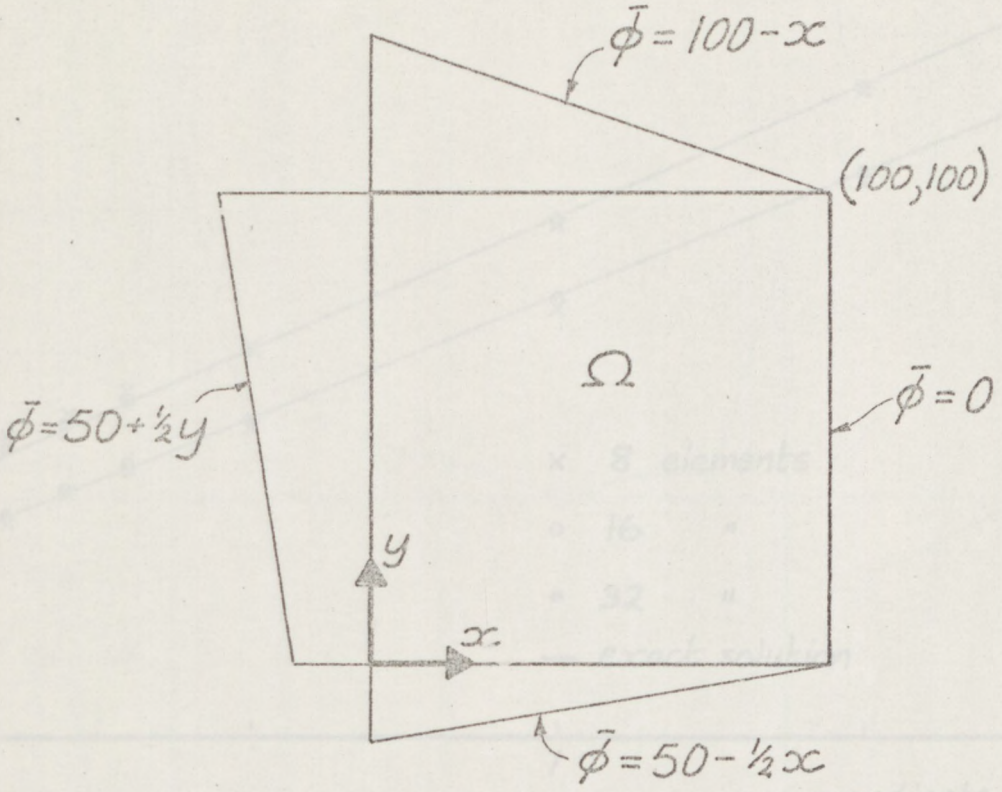

Figure 3·4·3 Boundary conditions

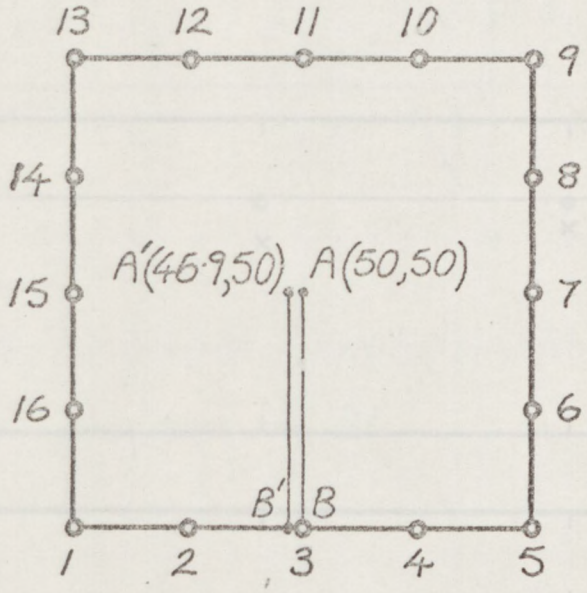

Figure 3·4·4 Sixteen element discretization

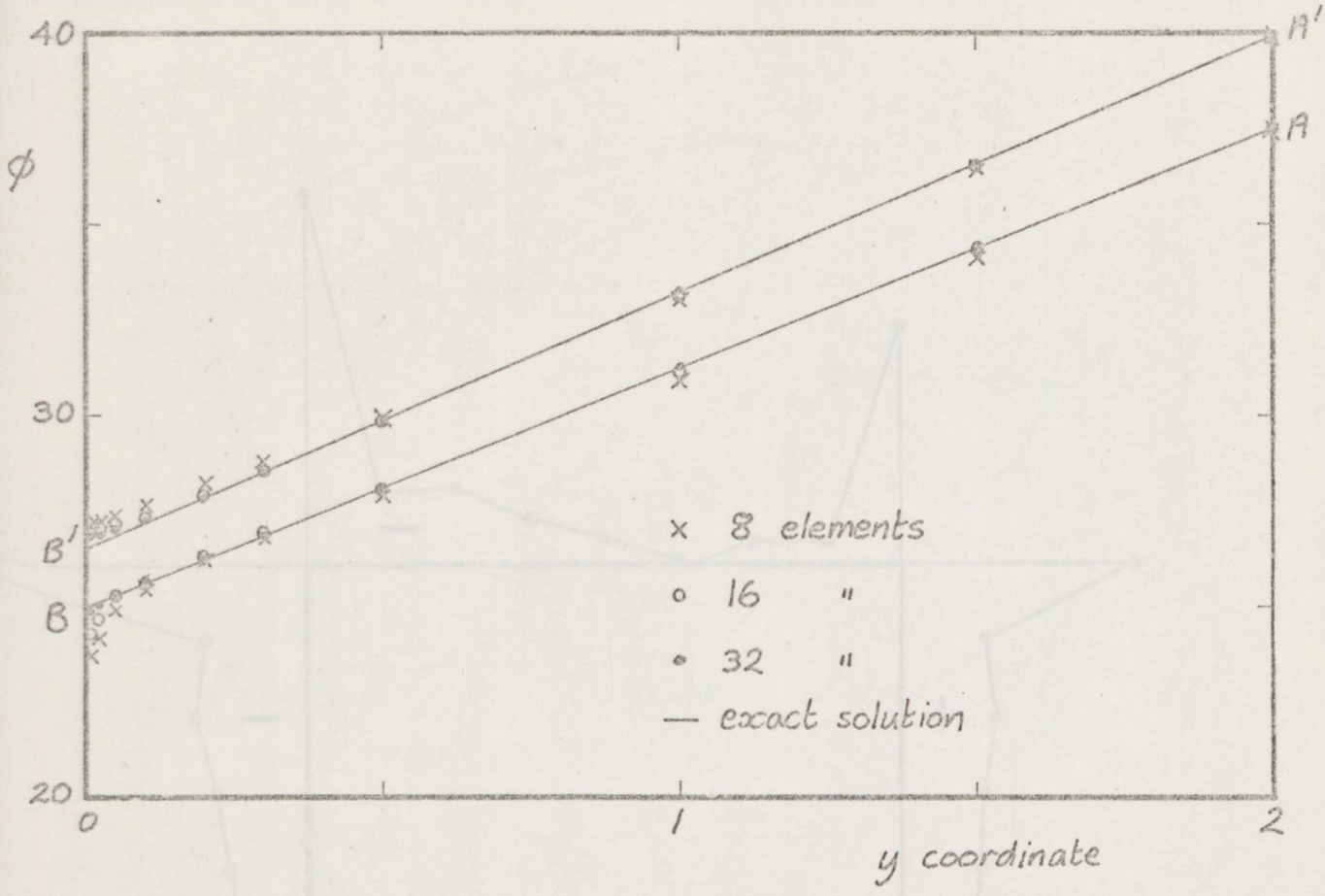

Figure 3·4·5 Numerical results from program ALB1

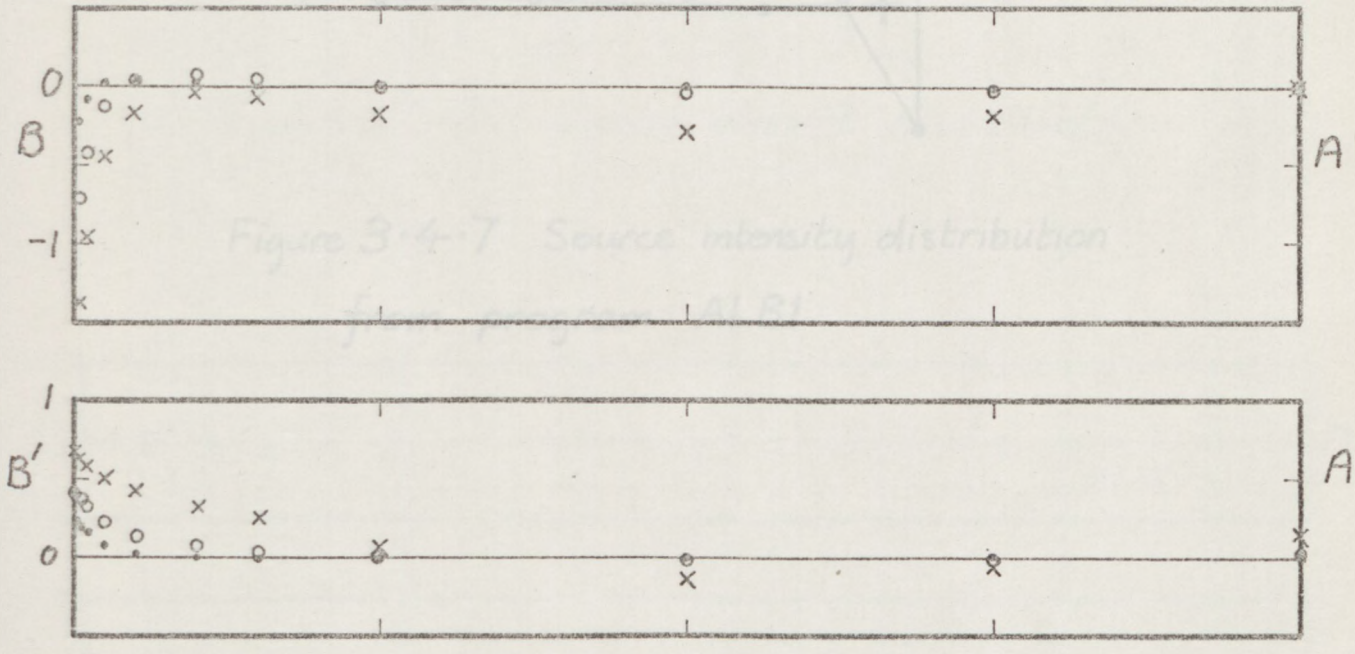

Figure 3·4·6 Difference between numerical and theoretical results

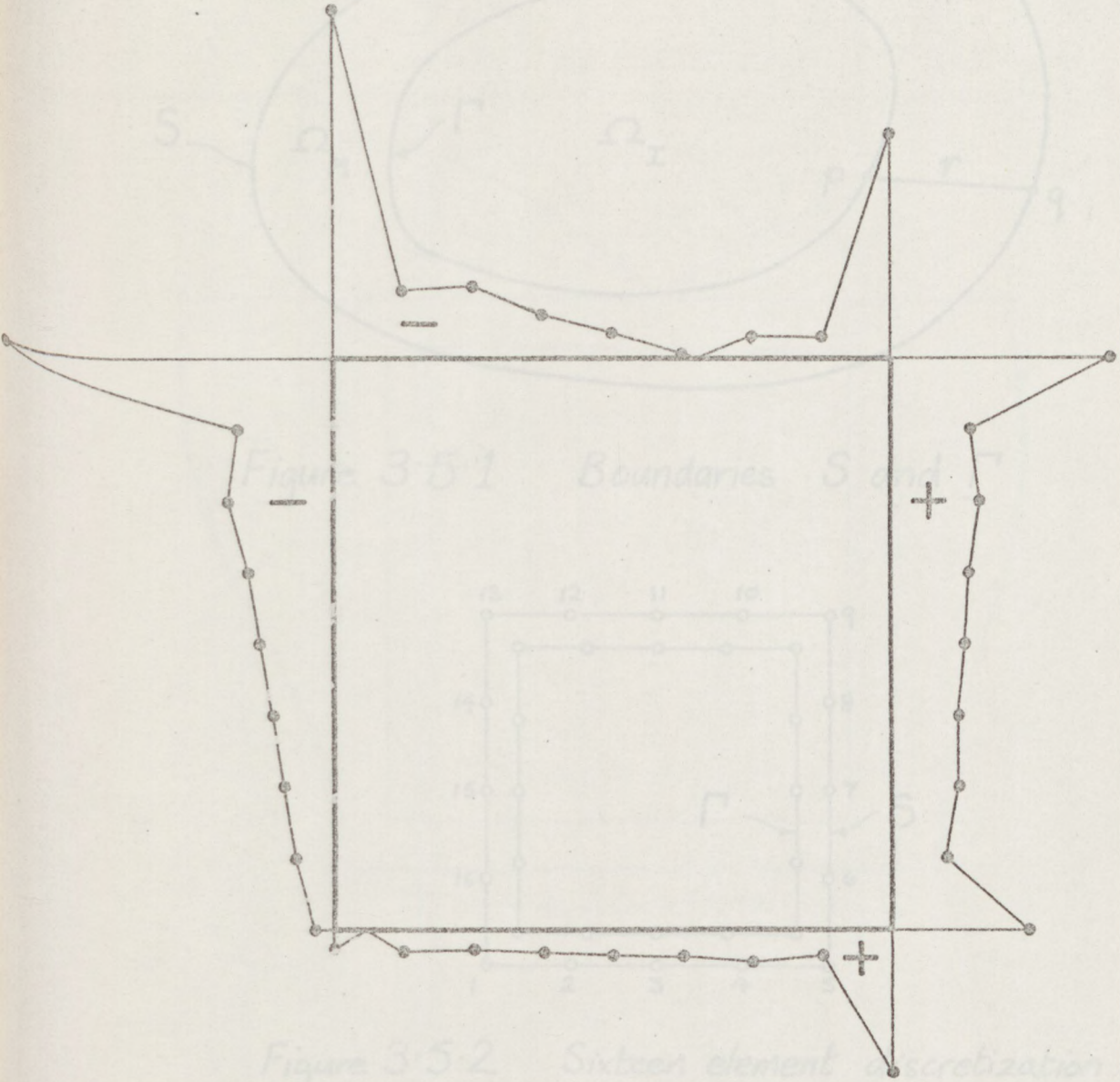

Figure 3·4·7 Source intensity distribution from program ALB1

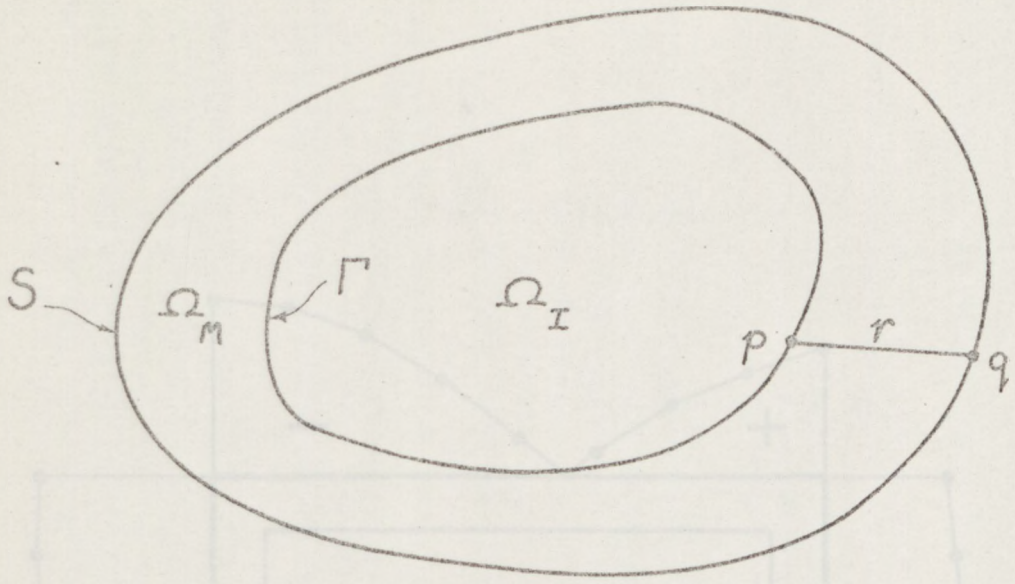

Figure 3·5·1 Boundaries S and Γ

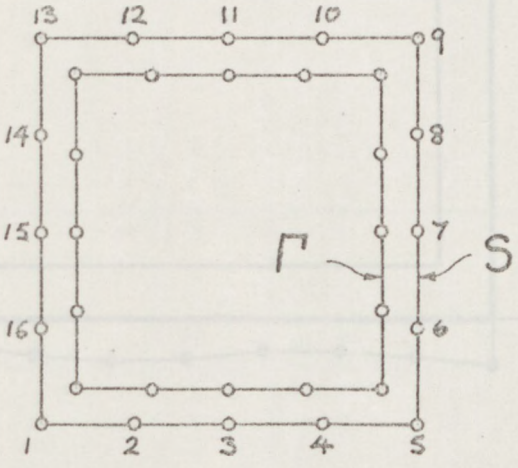

Figure 3·5·2 Sixteen element discretization

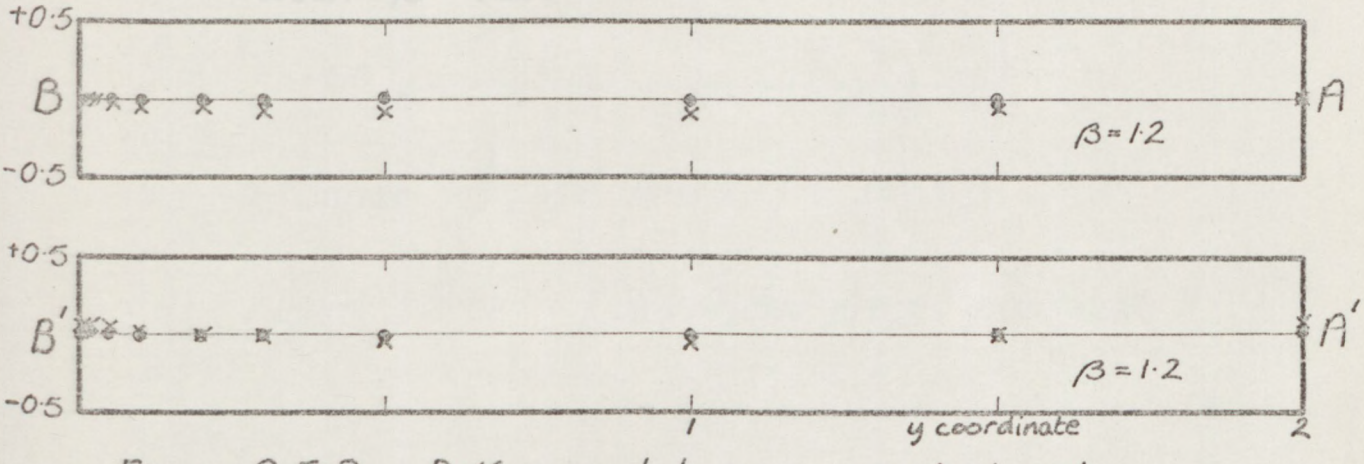

Figure 3·5·3 Difference between numerical and theoretical results (see also fig. 3·4·6)

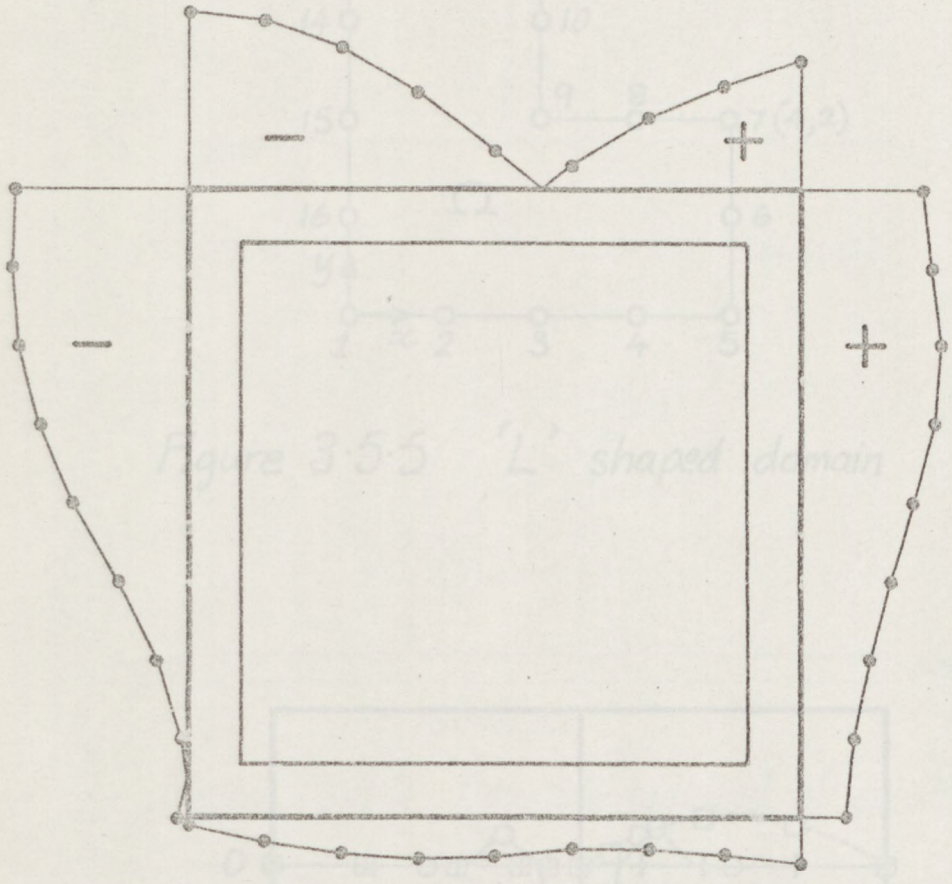

Figure 3·5·4 Source intensity distribution from program ALB2 with $\beta = 1{\cdot}2$.

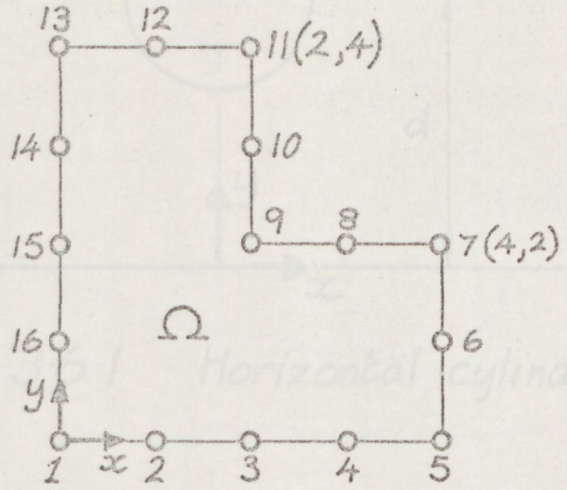

Figure 3·5·5 'L' shaped domain

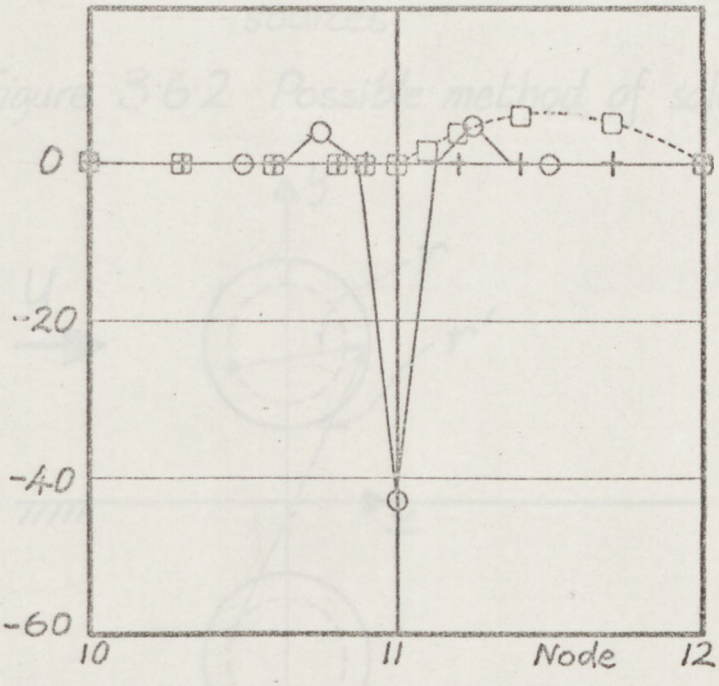

—o— Symm (76), ···□··· $\beta = 1{\cdot}2$, + $\beta = 3$.

Figure 3·5·6 Comparitive errors near node 11

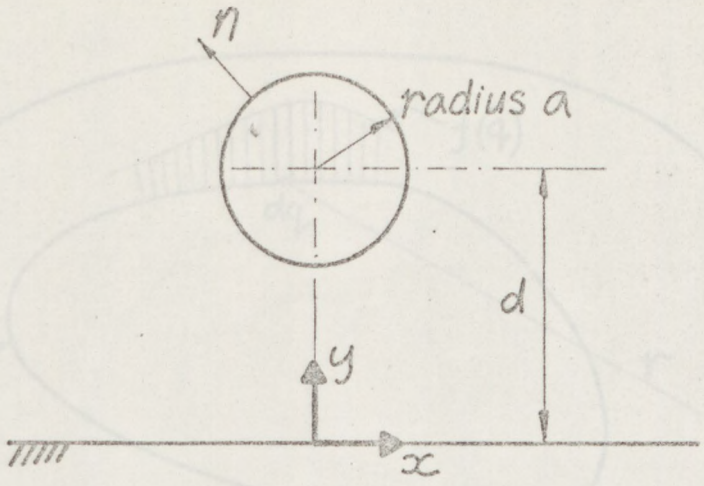

Figure 3·6·1 Horizontal cylinder.

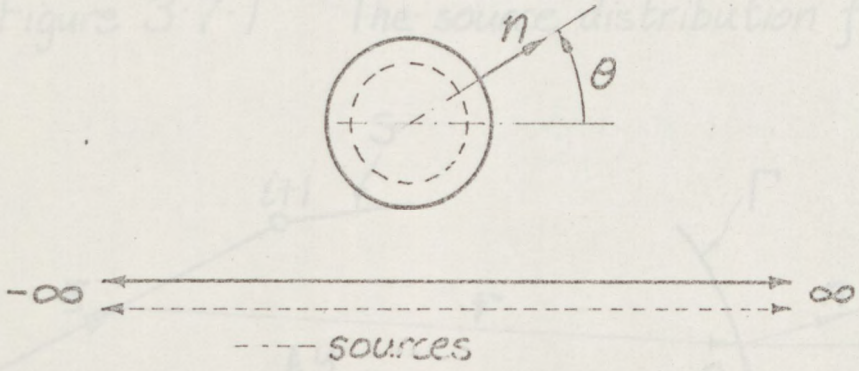

Figure 3·6·2 Possible method of solution.

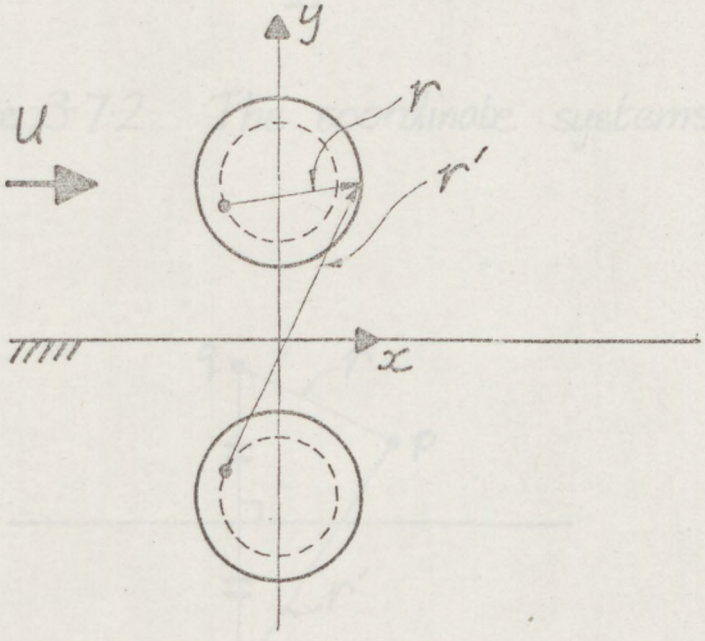

Figure 3·6·3 Method of solution utilizing the method of images.

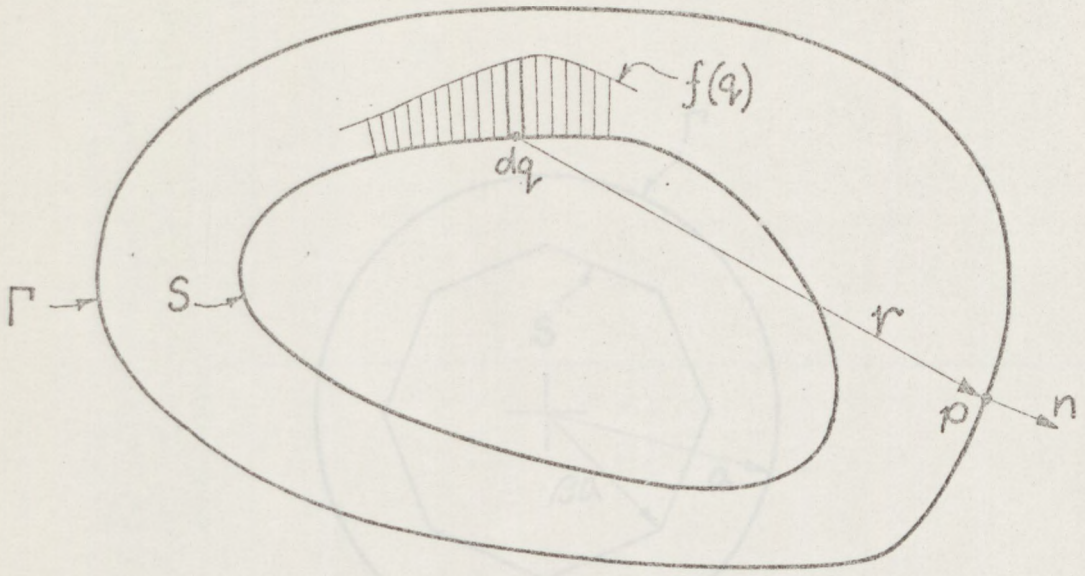

Figure 3·7·1 The source distribution f

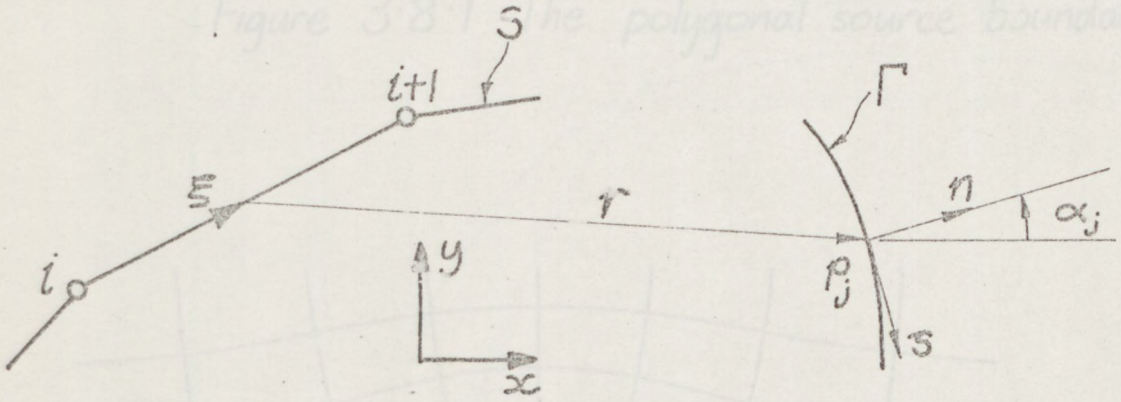

Figure 3·7·2 The coordinate systems

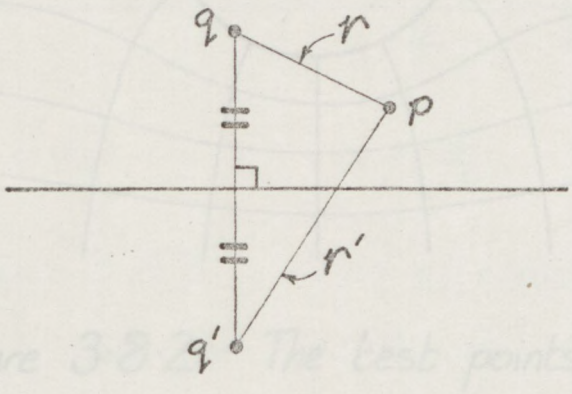

Figure 3·7·3 The image distance r'

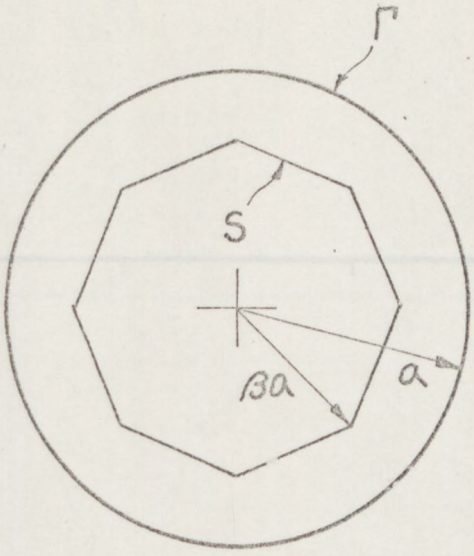

Figure 3·8·1 The polygonal source boundary

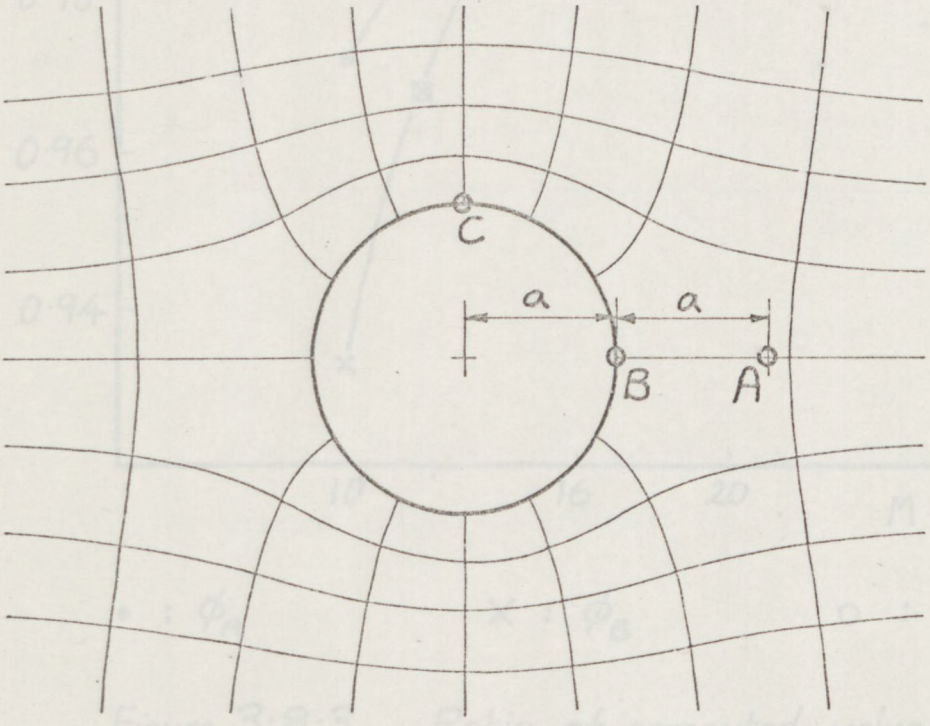

Figure 3·8·2 The test points A, B & C.

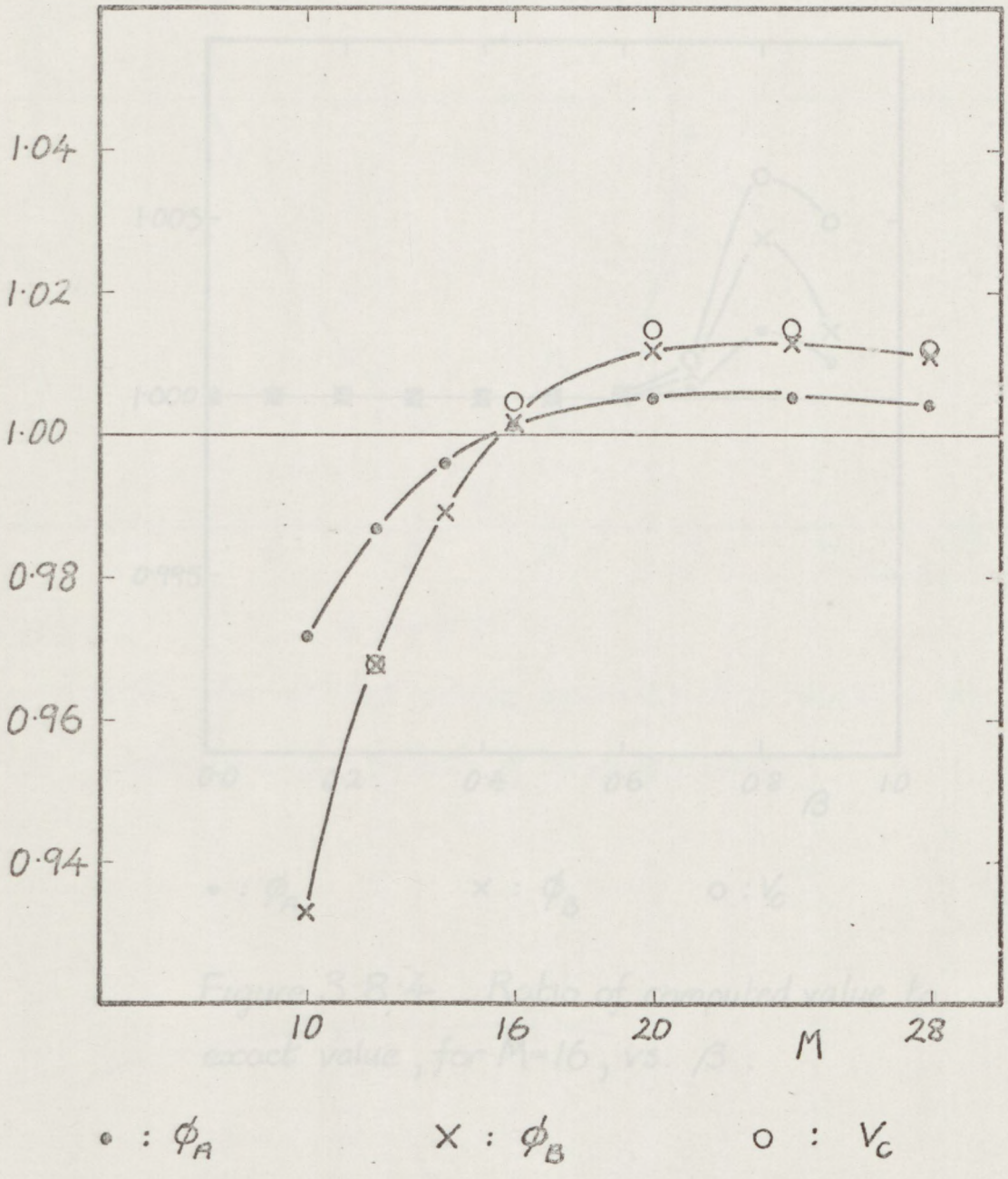

Figure 3·8·3 Ratio of computed value to exact value, for $\beta = 0{\cdot}9$, vs. M.

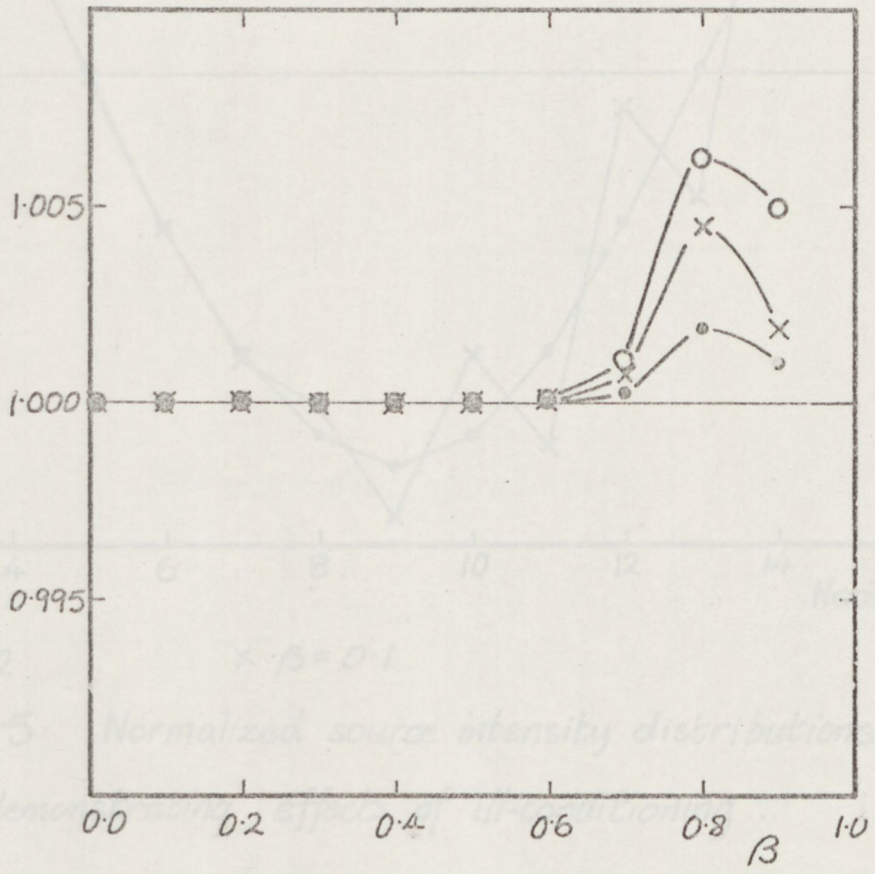

• : ϕ_A × : ϕ_B o : V_c

Figure 3·8·4 Ratio of computed value to exact value, for M=16, vs. β.

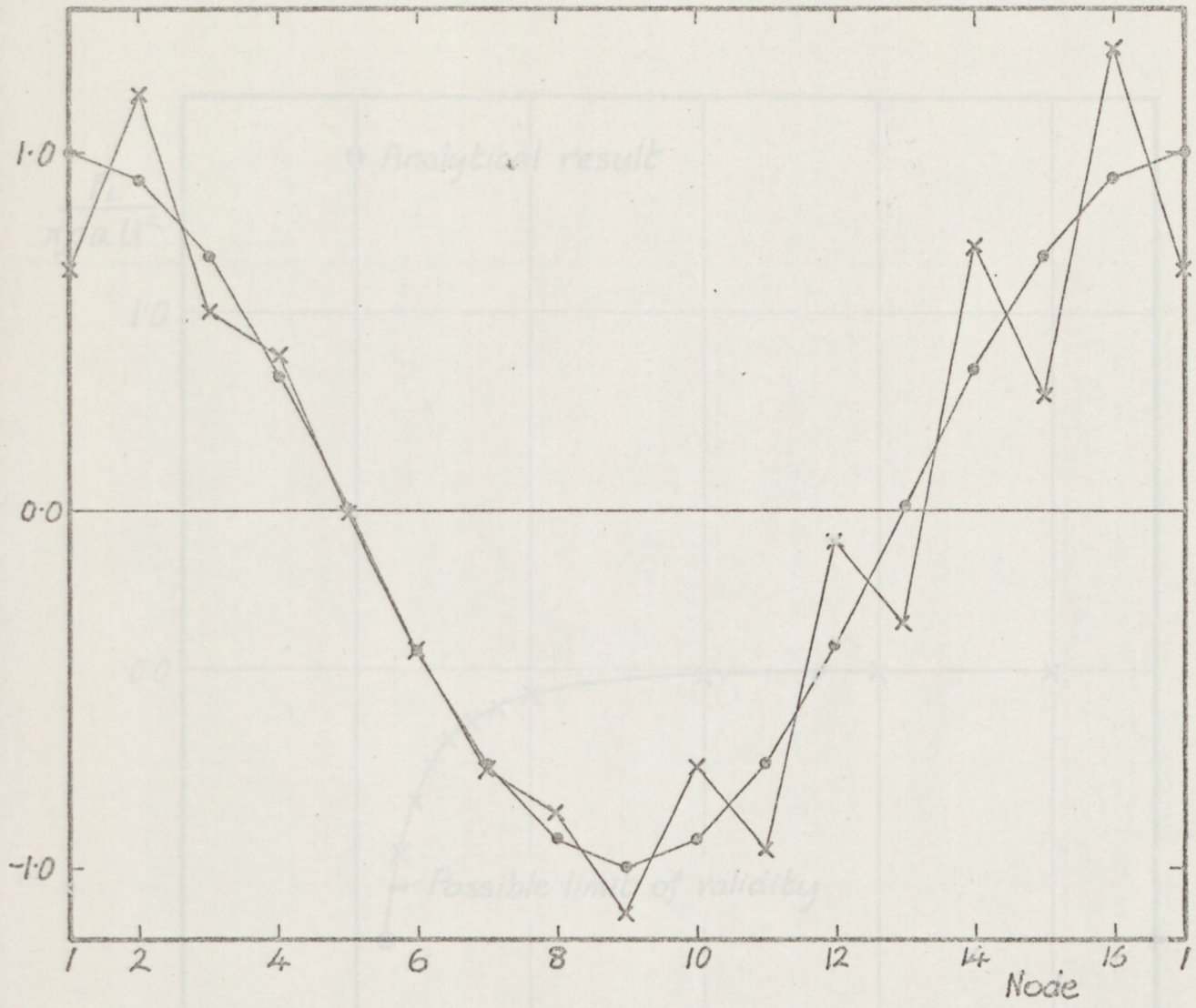

• $\beta \geq 0.2$ × $\beta = 0.1$

Figure 3·8·5 Normalized source intensity distributions for $M = 16$, demonstrating effects of ill-conditioning.

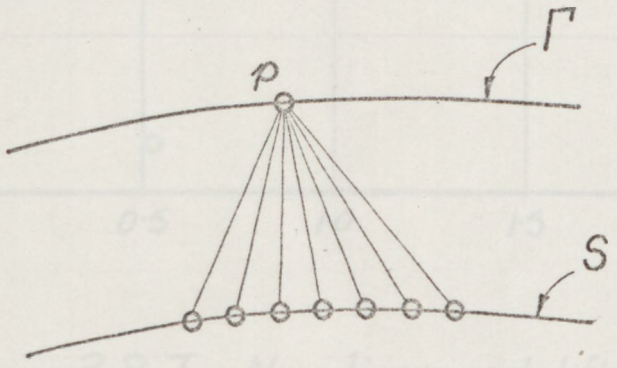

Figure 3·8·6 Ill-conditioning as M increases.

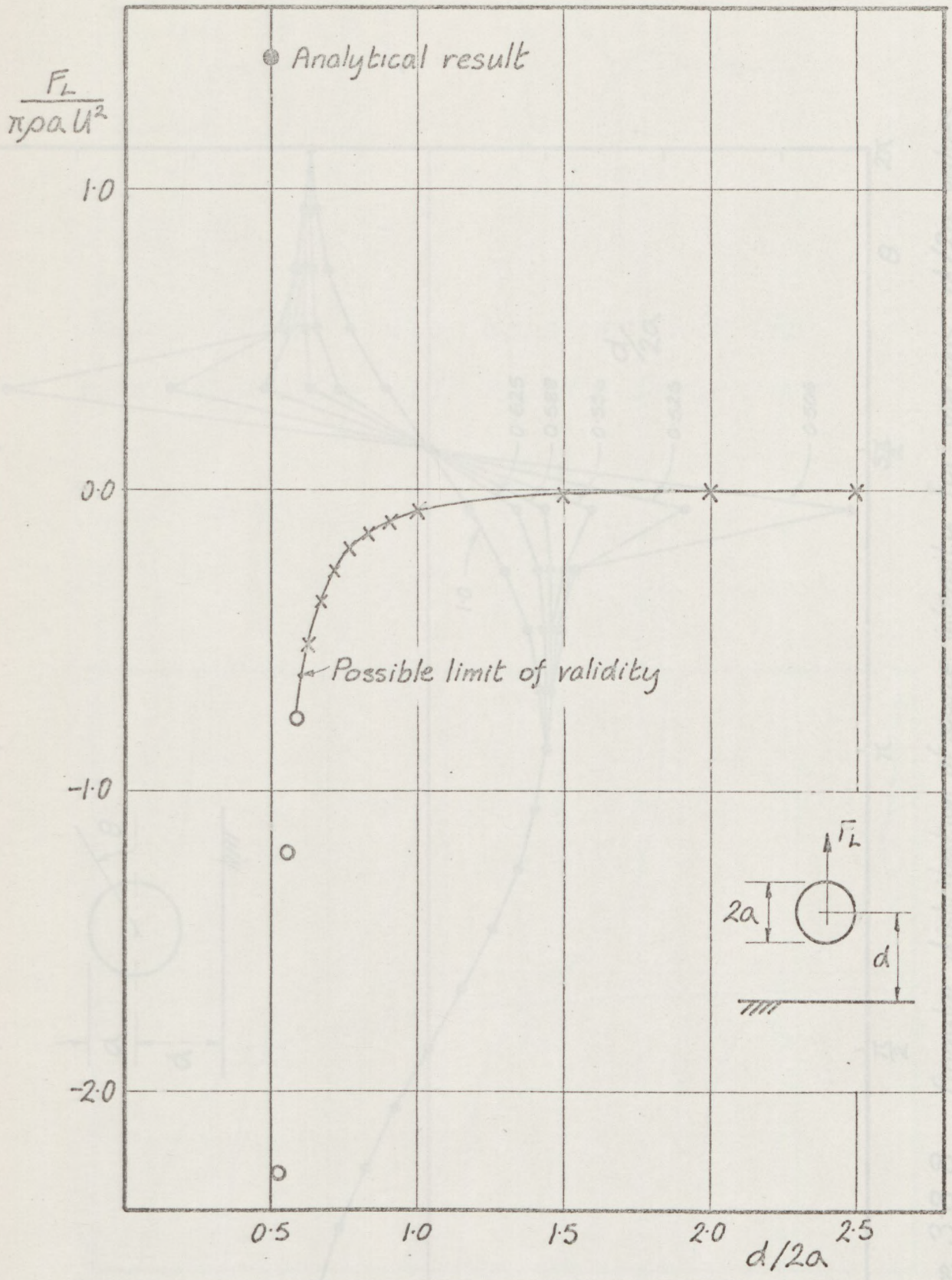

Figure 3·8·7 Non-dimensional lift force vs. d/2a

$M = 20$ $\beta = 0.9$

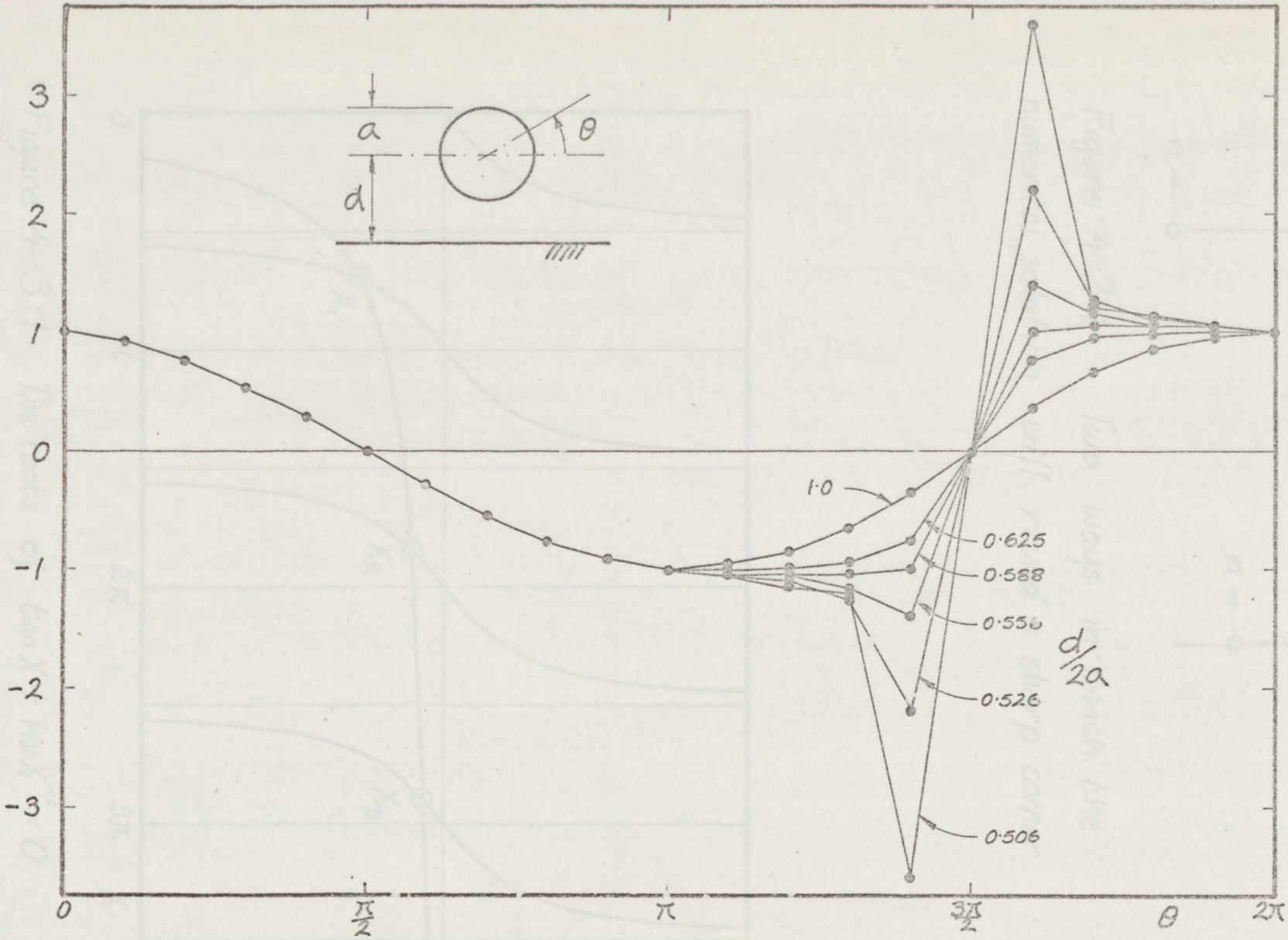

Figure 3·8·8 Angular distribution of source intensity for various d/2a values.

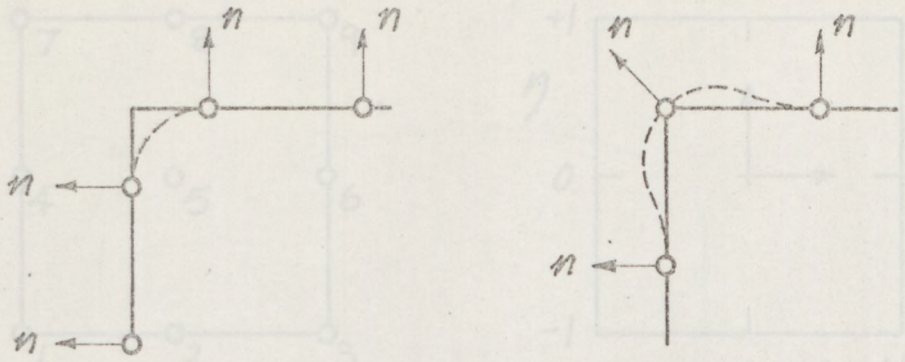

Figure 4·2·1 Two ways in which the numerical solution will round a sharp corner.

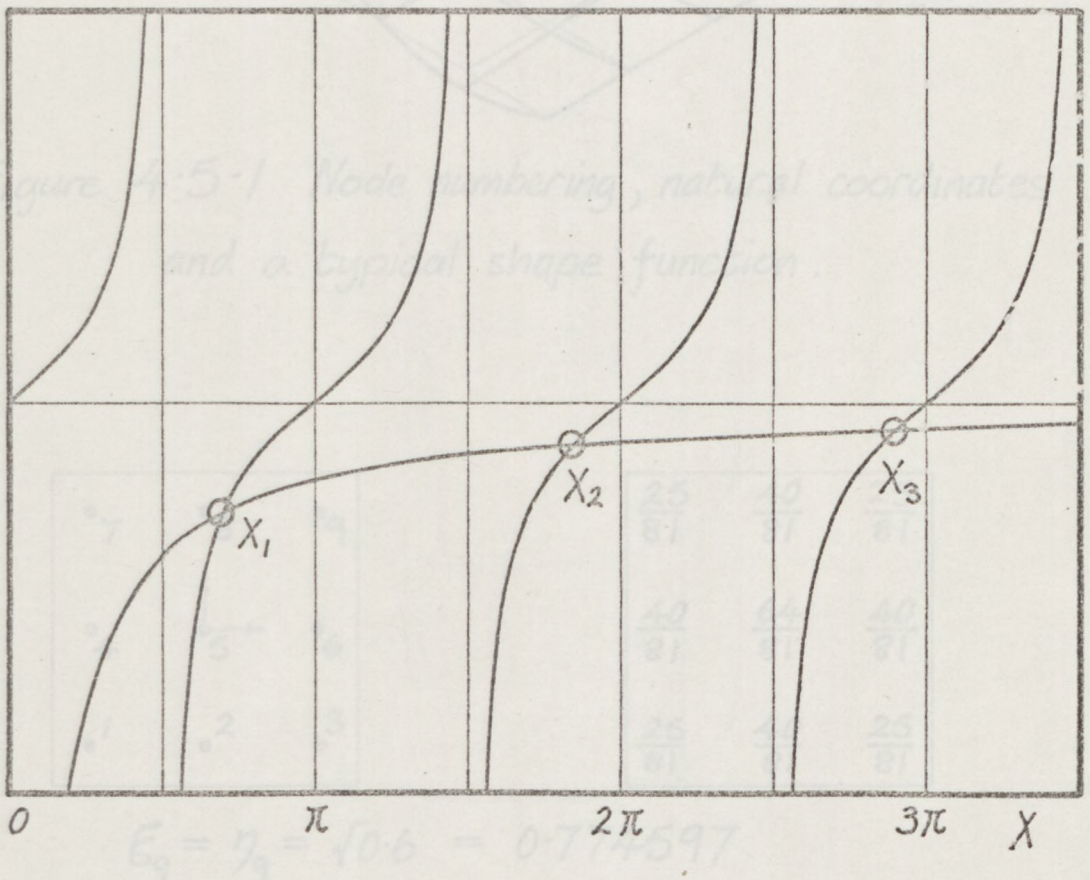

Figure 4·3·1 The roots of $\tan X + h\nu X^{-1} = 0$

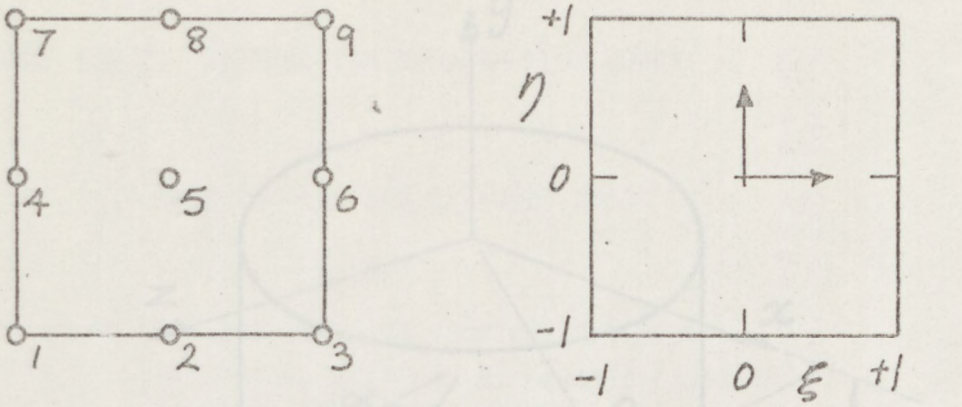

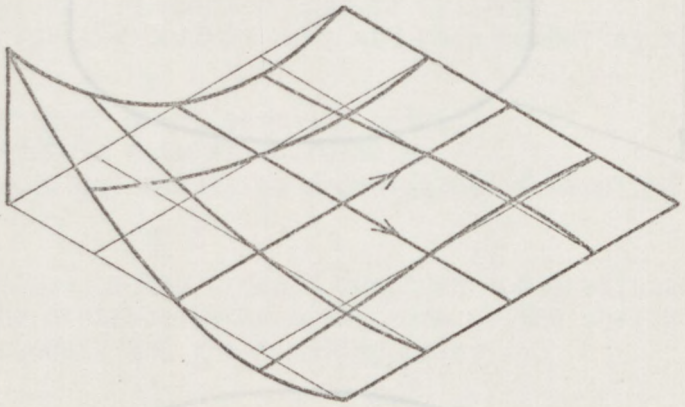

Figure 4·5·1 Node numbering, natural coordinates and a typical shape function.

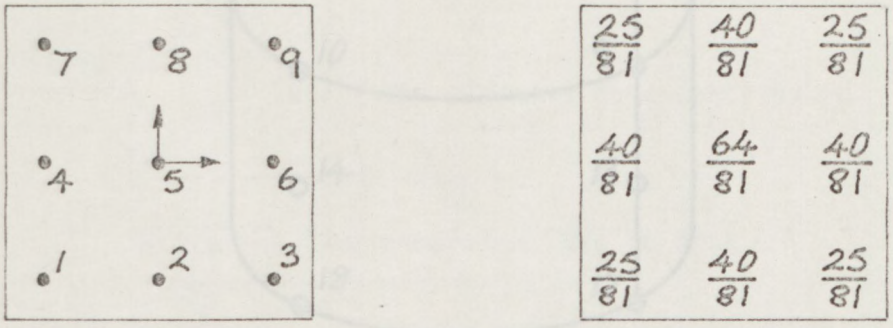

$$\xi_9 = \eta_9 = \sqrt{0.6} = 0.774597$$

Figure 4·5·2 Gauss quadrature points and weights.

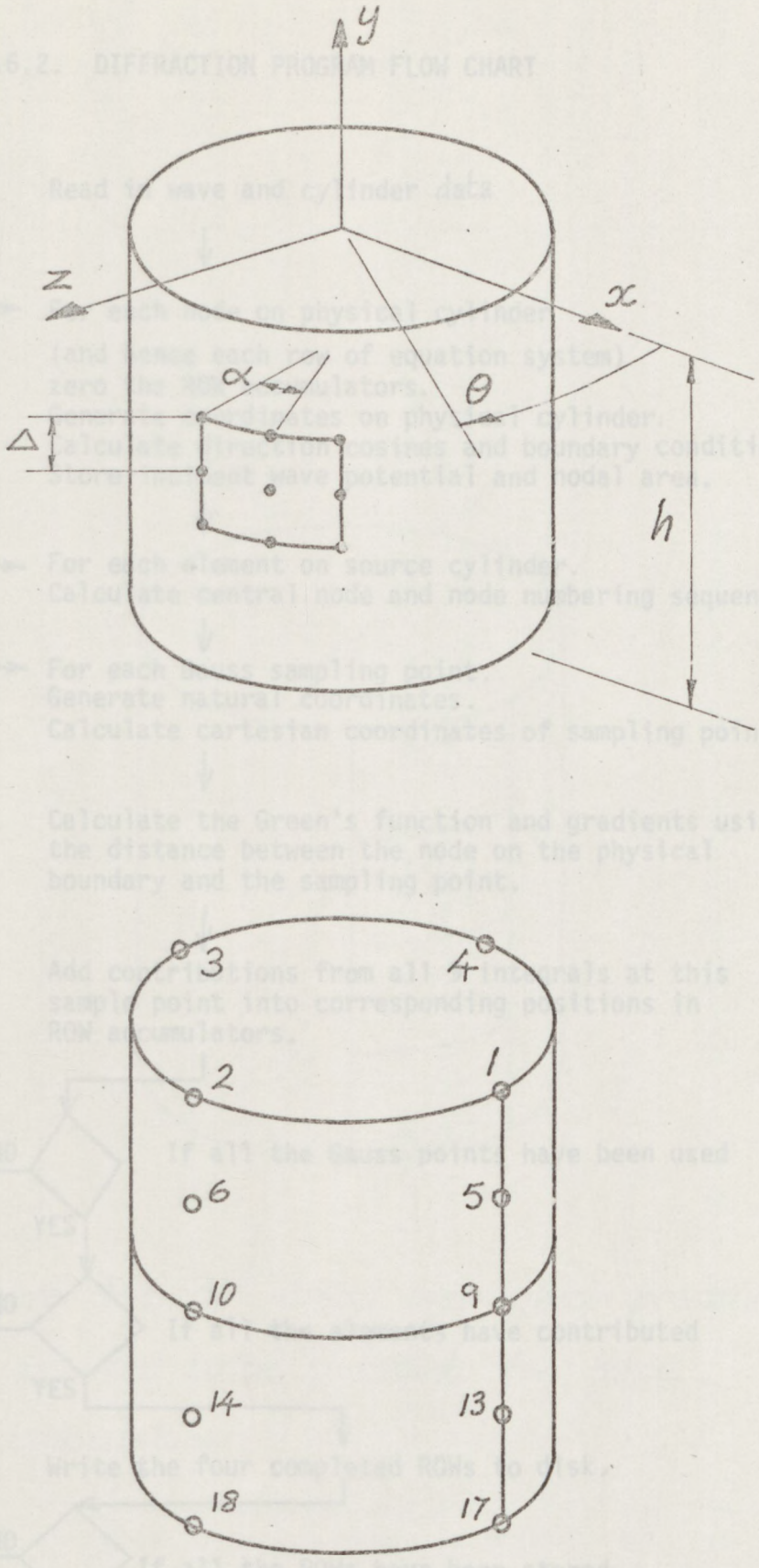

Figure 4.6.1 Coordinate systems and twenty node discretization

FIGURE 4.6.2. DIFFRACTION PROGRAM FLOW CHART

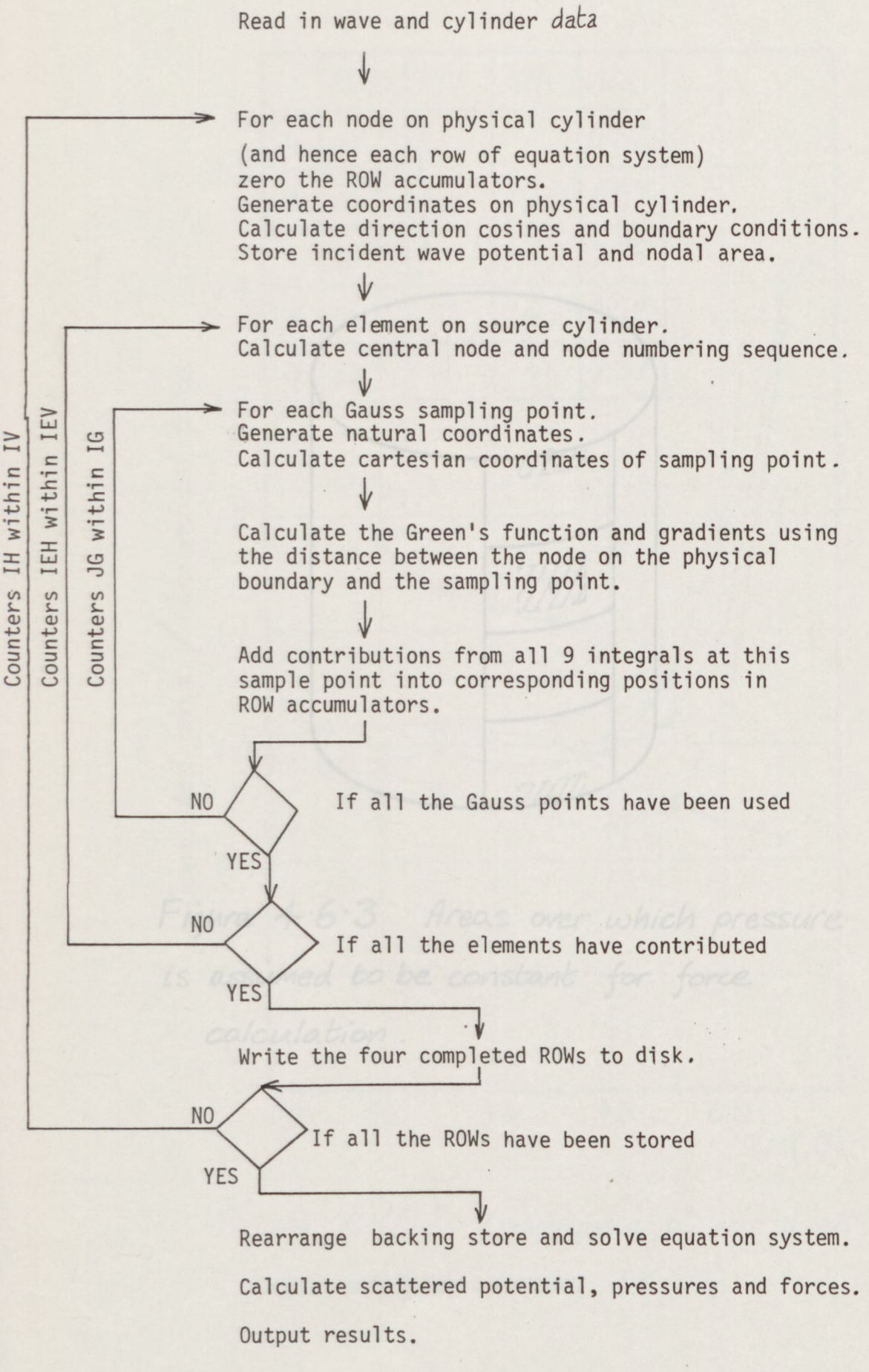

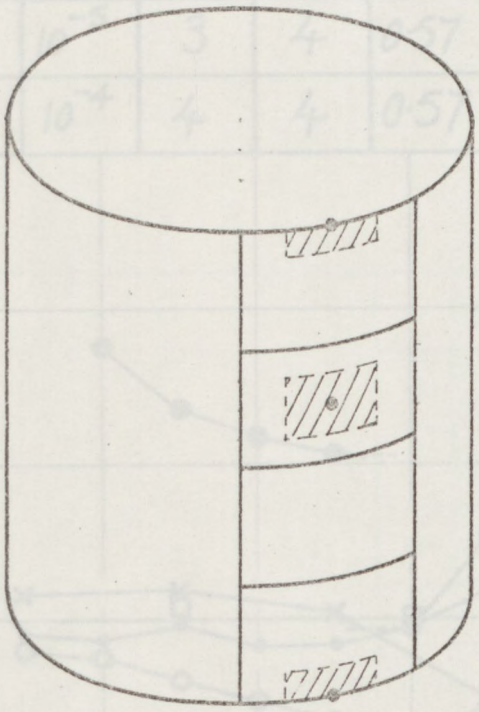

Figure 4·6·3 Areas over which pressure is assumed to be constant for force calculation.

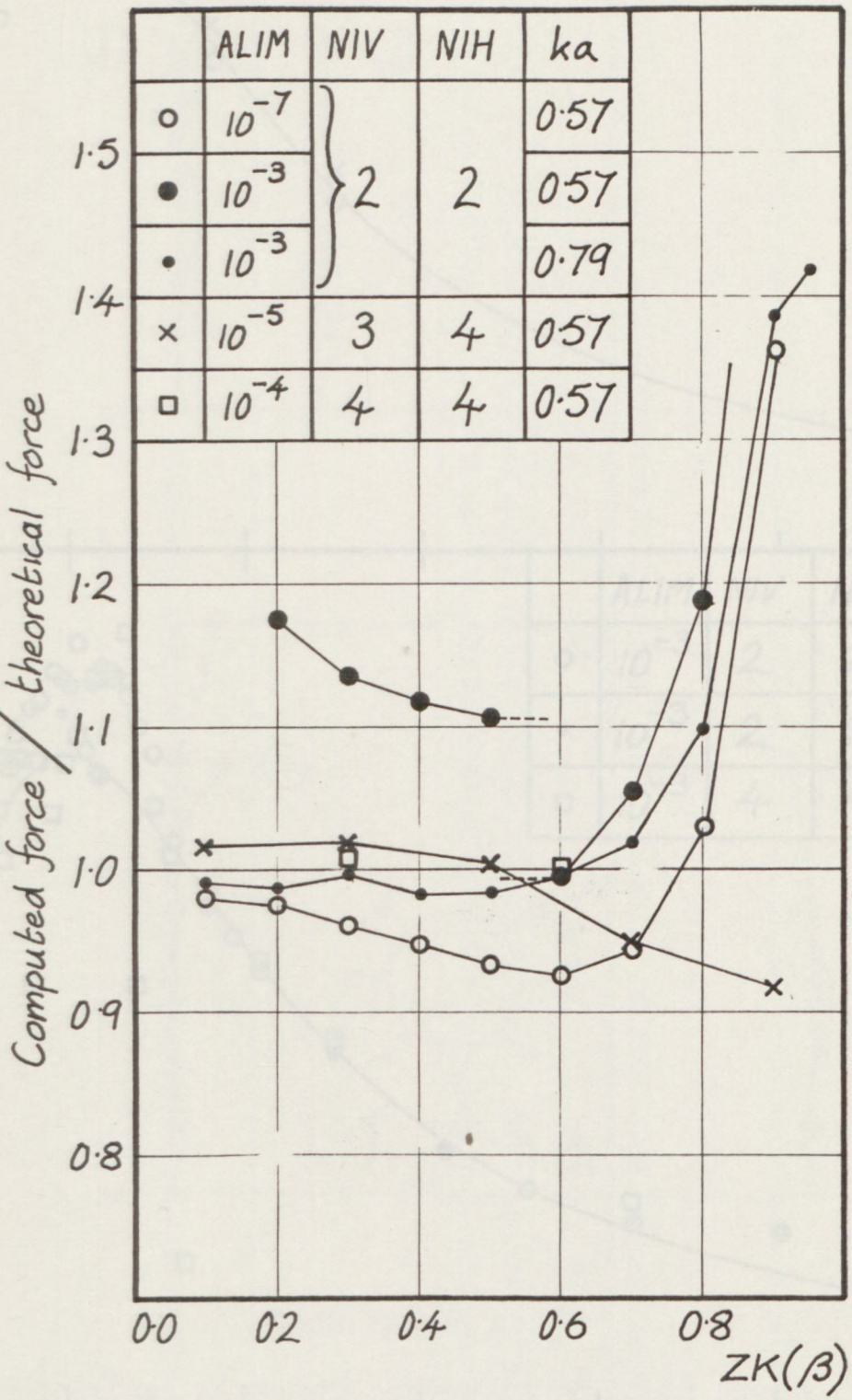

Figure 4·7·1 Convergence of normalized force with decreasing ZK(β).

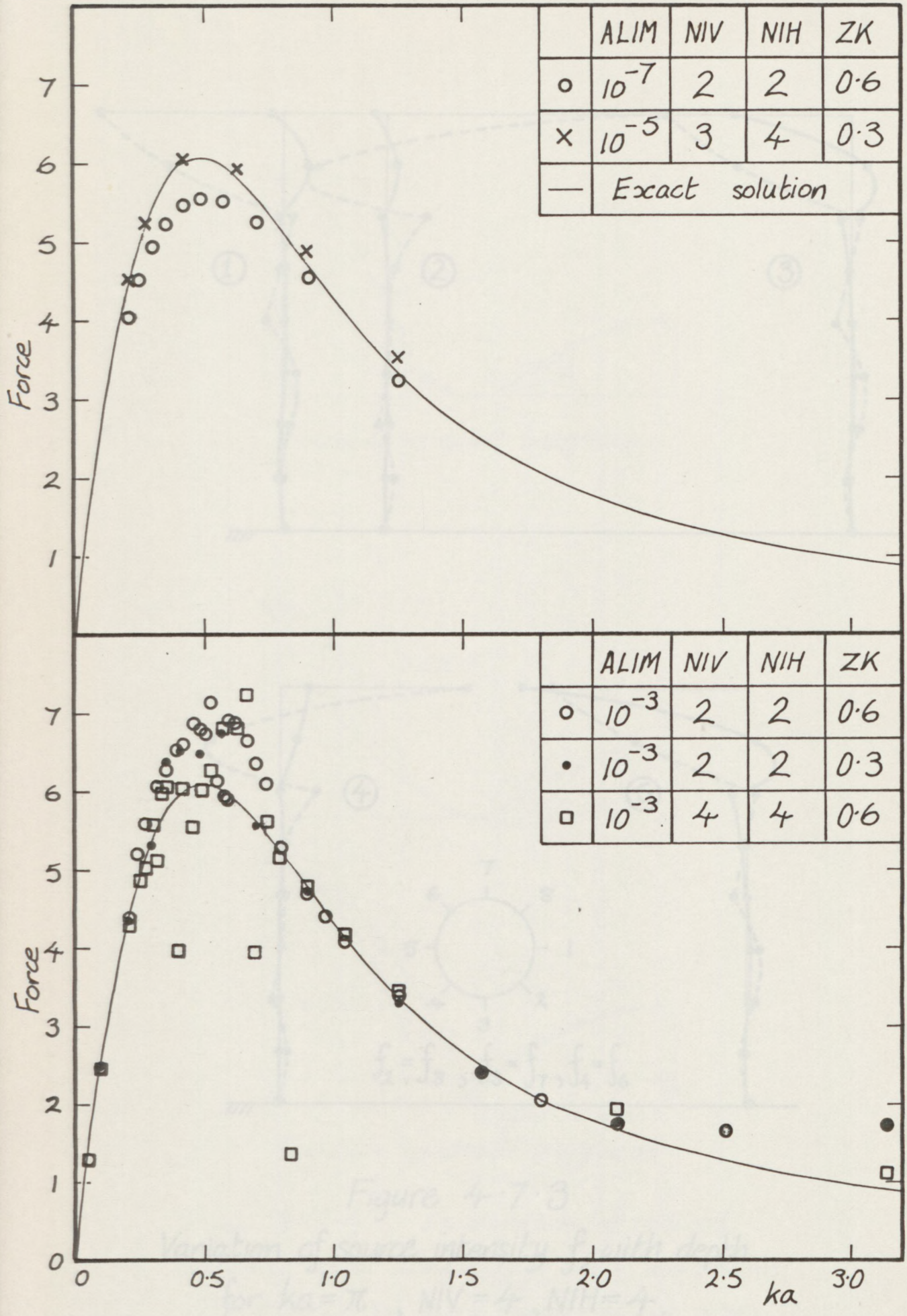

Figure 4·7·2 Computed force expressed as $\frac{F}{\rho g a^2 \frac{H}{2}}$ against ka

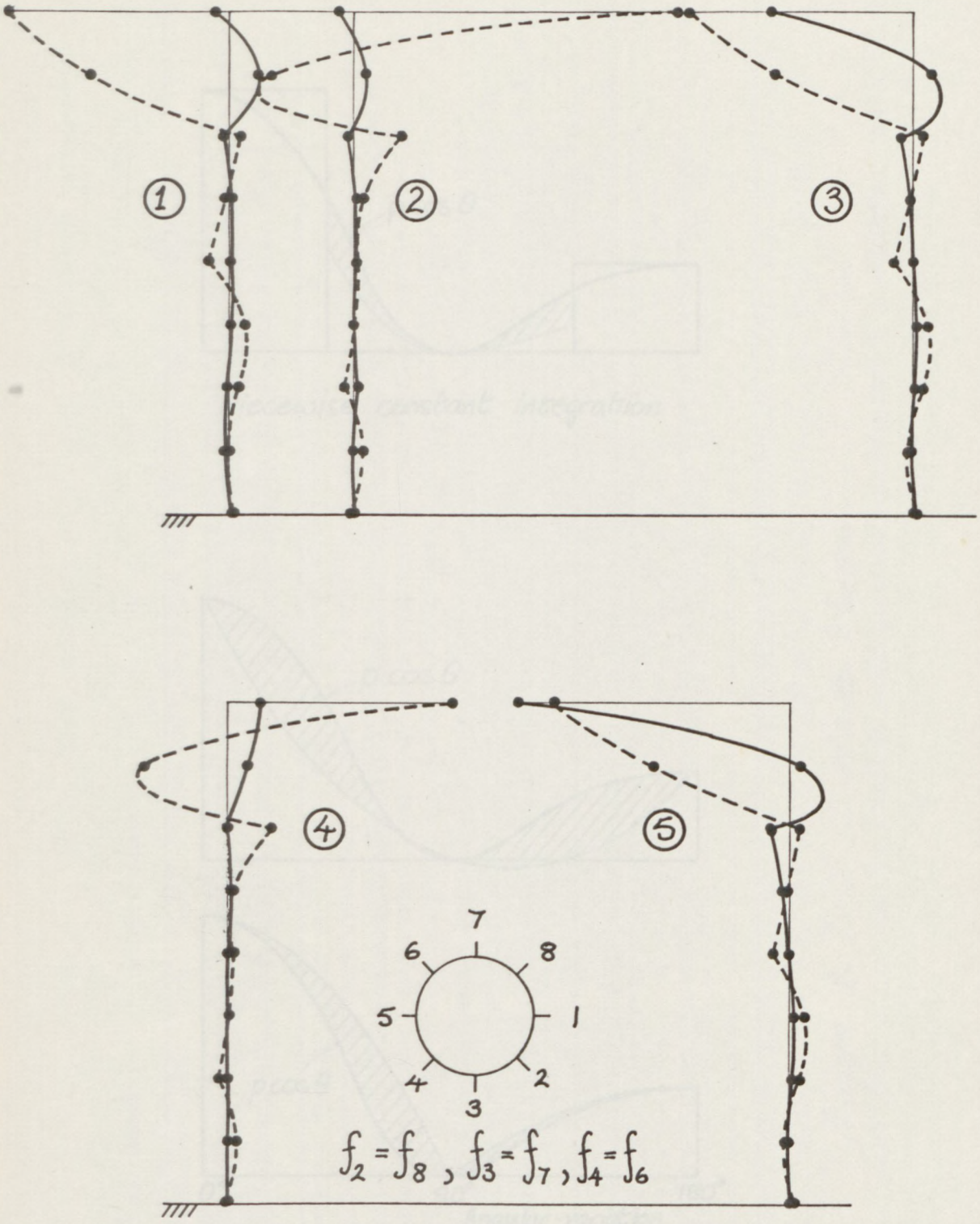

Figure 4·7·3

Variation of source intensity f, with depth for $ka = \pi$, NIV = 4 , NIH = 4.

Real ---- Imaginary ——

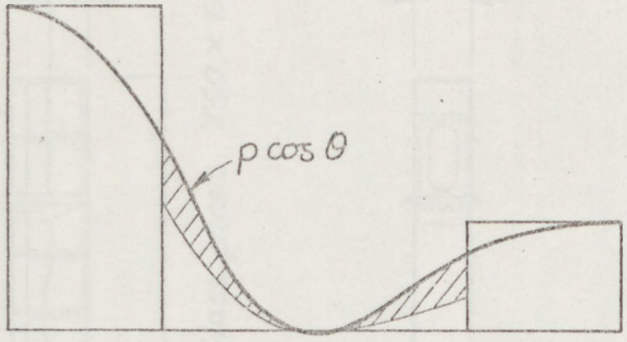

Piecewise constant integration

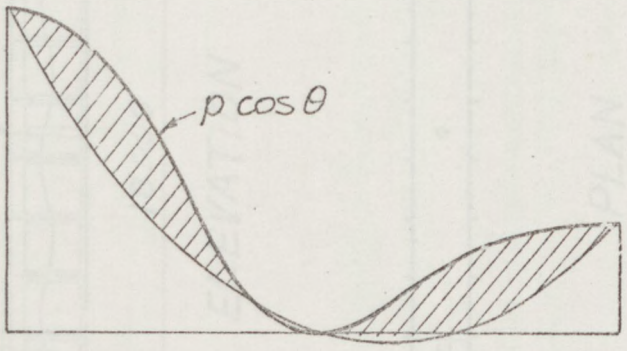

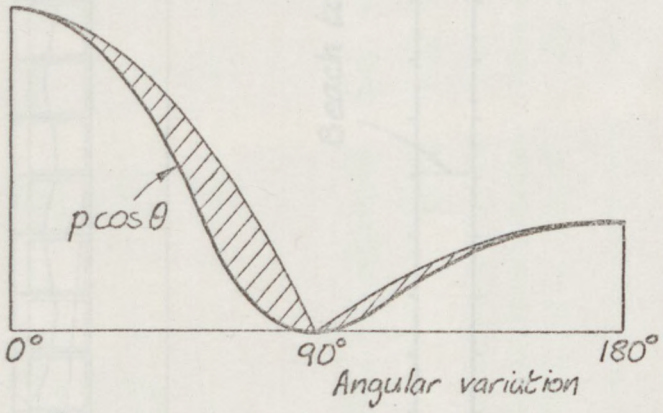

Piecewise quadratic integration

Figure 4·7·4 Explanation of reduced accuracy when using higher order integration. The shaded areas are a measure of the error.

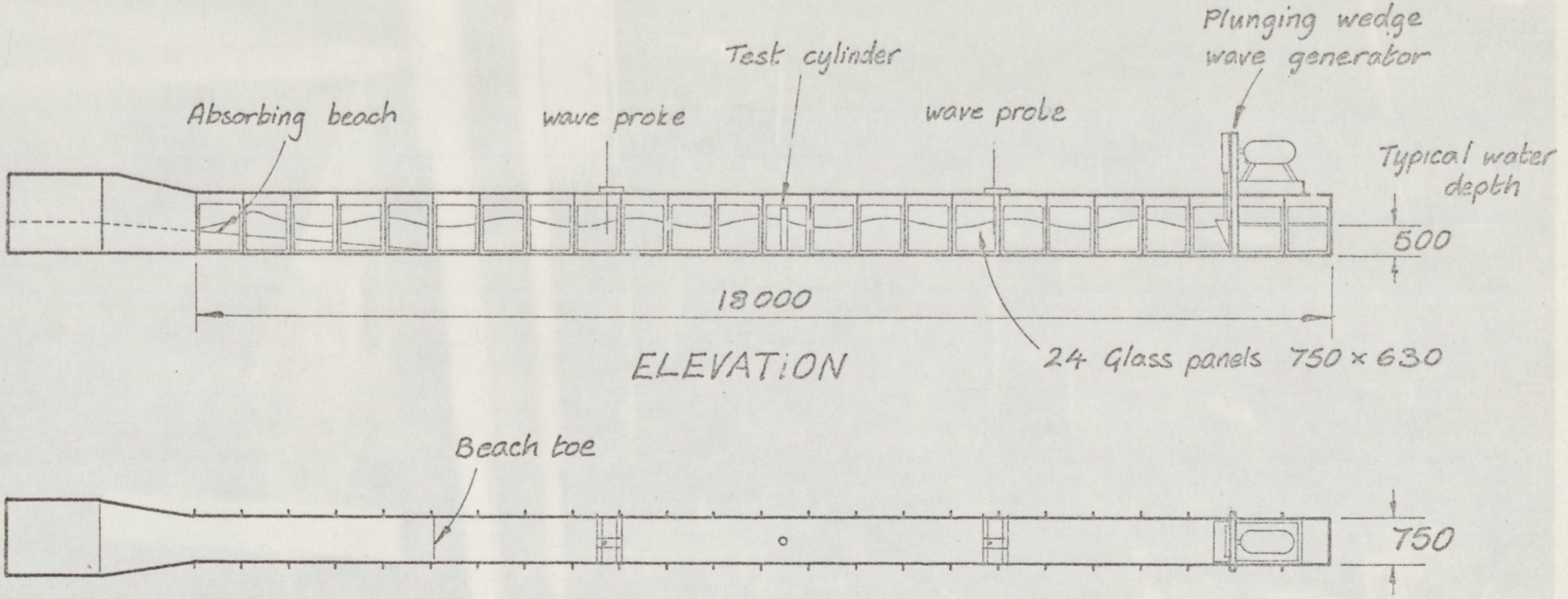

Figure 5·1·1 Wave Flume

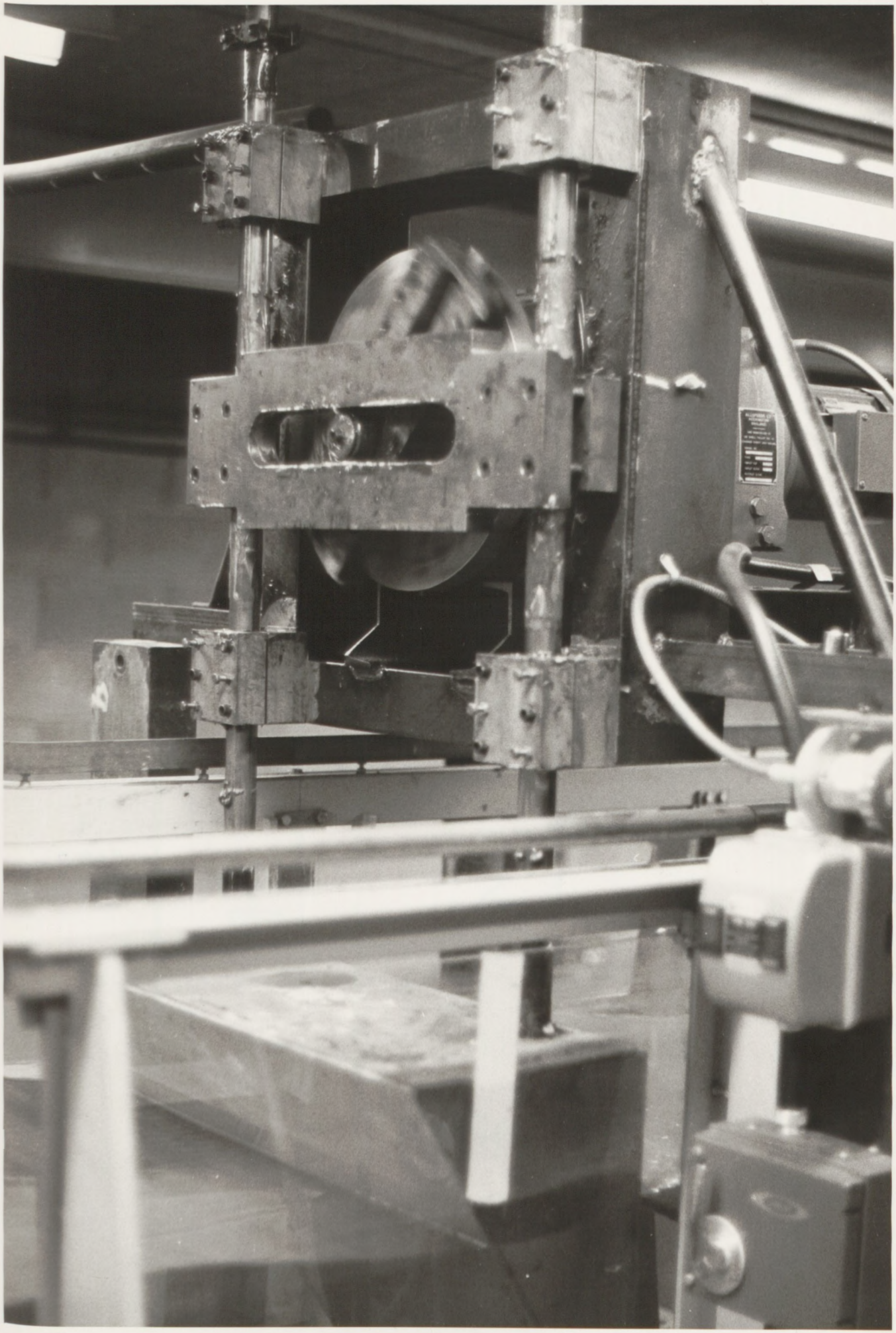

FIGURE 5·1·2 THE WAVE GENERATOR

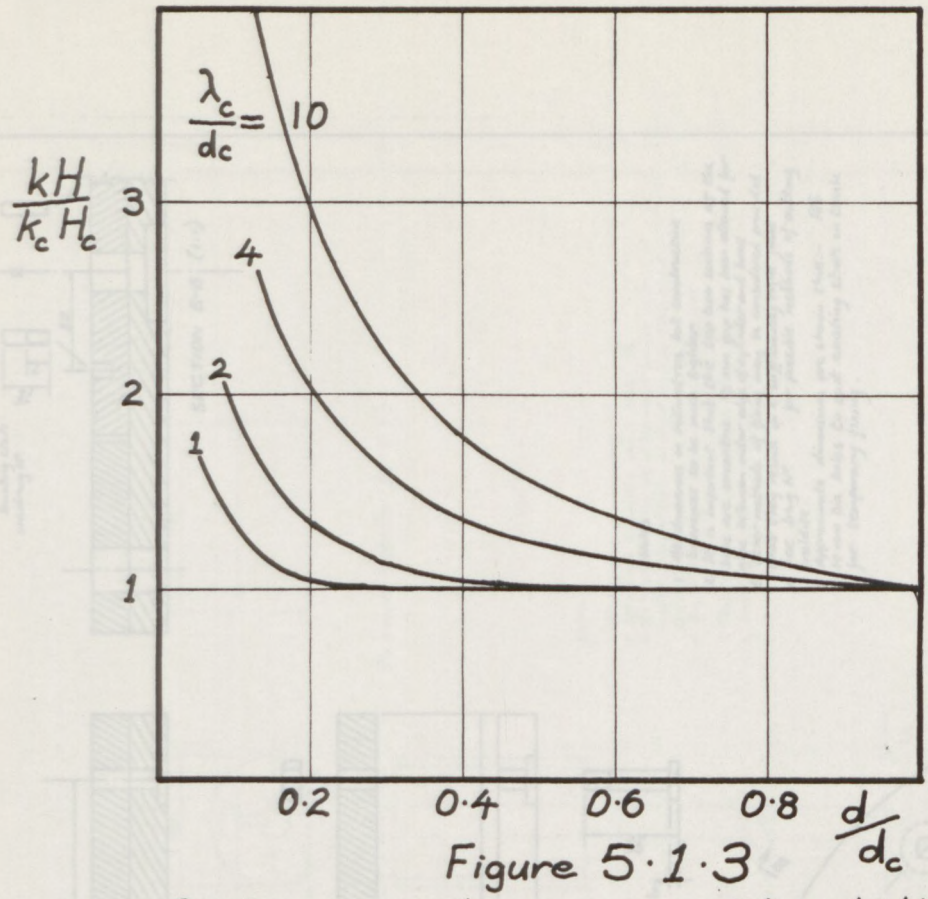

Figure 5·1·3

Relative wave steepness vs. relative depth

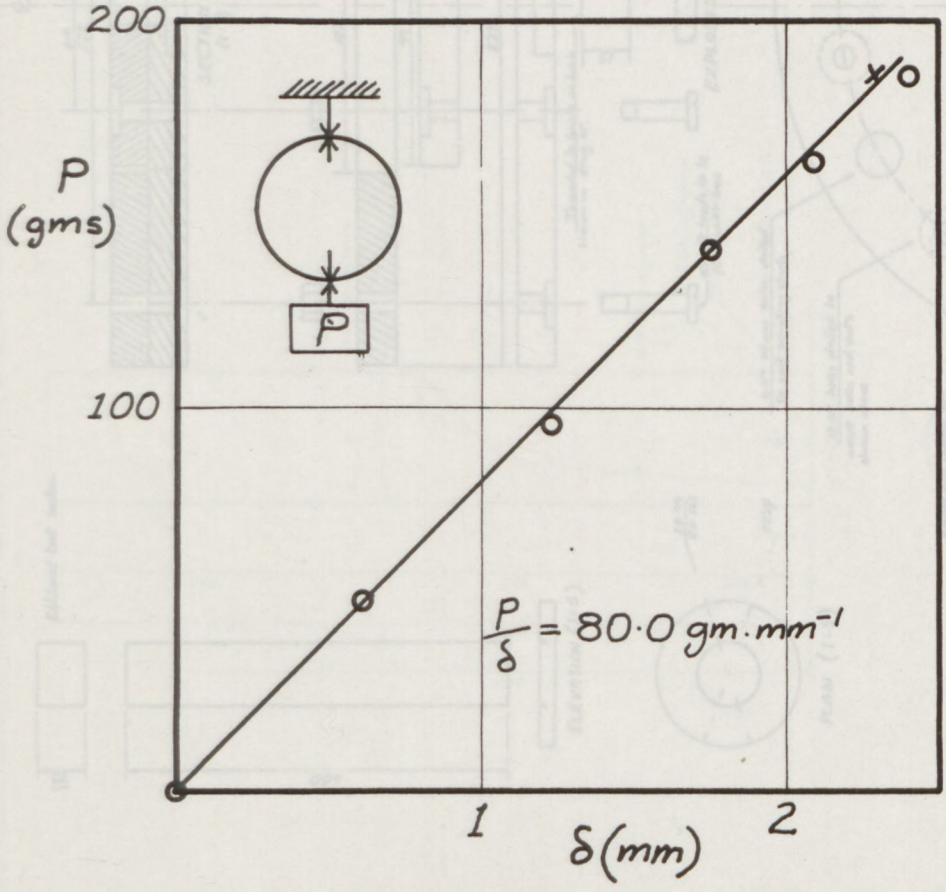

Figure 5·2·1

Araldite test specimen

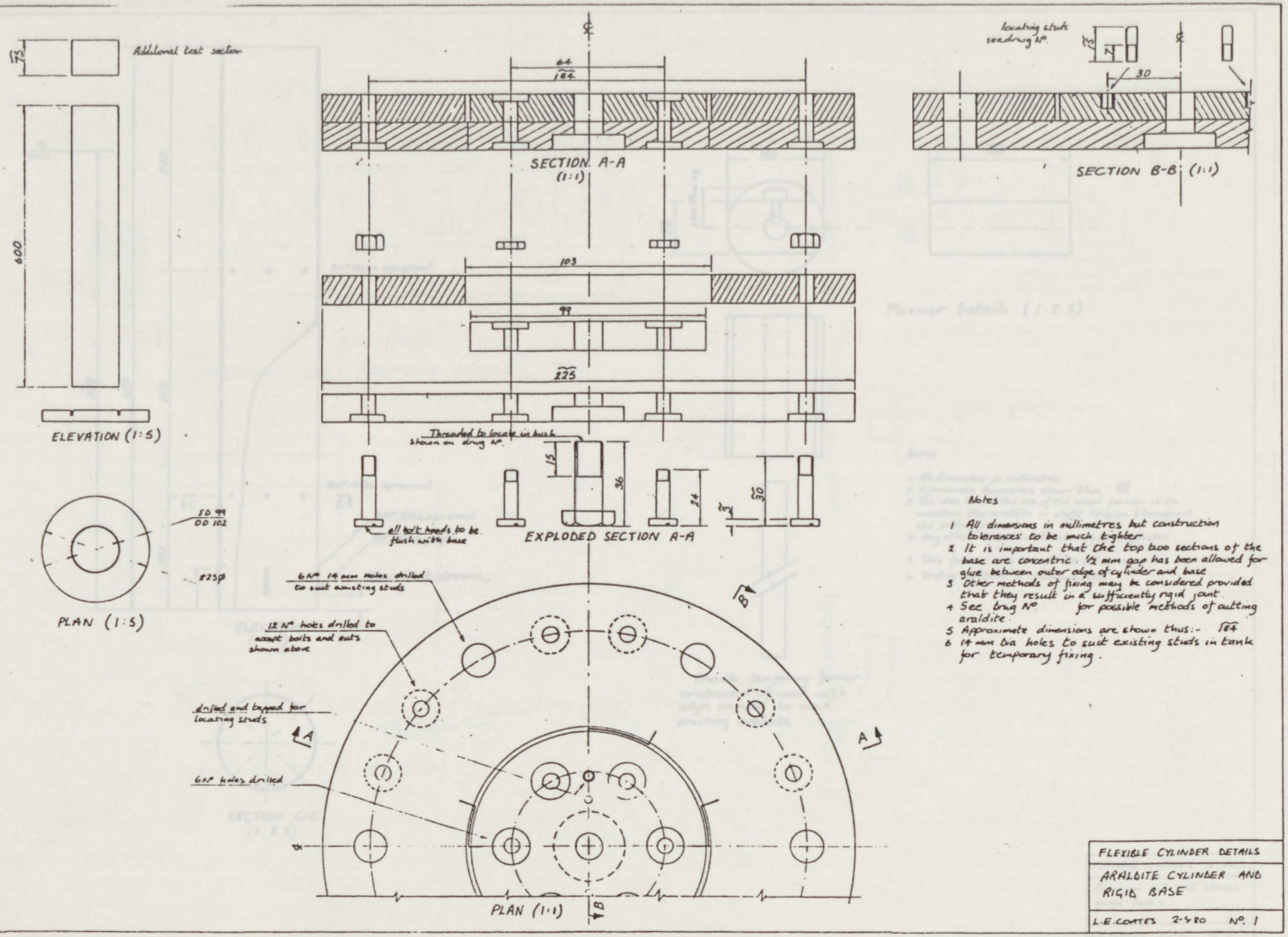
Additional test section
75
600
ELEVATION (1:5)
SECTION A-A (1:1)
64
184
103
99
225
Threaded to locate in bush shown on drwg No.
15
36
14
30
3
all bolt heads to be flush with base
EXPLODED SECTION A-A
locating studs see drwg No.
SECTION B-B (1:1)
ID 99
OD 102
225p
PLAN (1:5)
6 No 14 mm holes drilled to suit existing studs
12 No holes drilled to accept bolts and nuts shown above
drilled and tapped for locating studs
6 No holes drilled
A
B
PLAN (1:1)
Notes
1 All dimensions in millimetres but construction tolerances to be much tighter
2 It is important that the top two sections of the base are concentric. ½ mm gap has been allowed for glue between outer edge of cylinder and base
3 Other methods of fixing may be considered provided that they result in a sufficiently rigid joint.
4 See drwg No. for possible methods of cutting araldite.
5 Approximate dimensions are shown thus:- 184
6 14 mm dia holes to suit existing studs in tank for temporary fixing.
FLEXIBLE CYLINDER DETAILS
ARALDITE CYLINDER AND RIGID BASE
L.E.COATES 2-5-80 No. 1

Figure 5.2.2

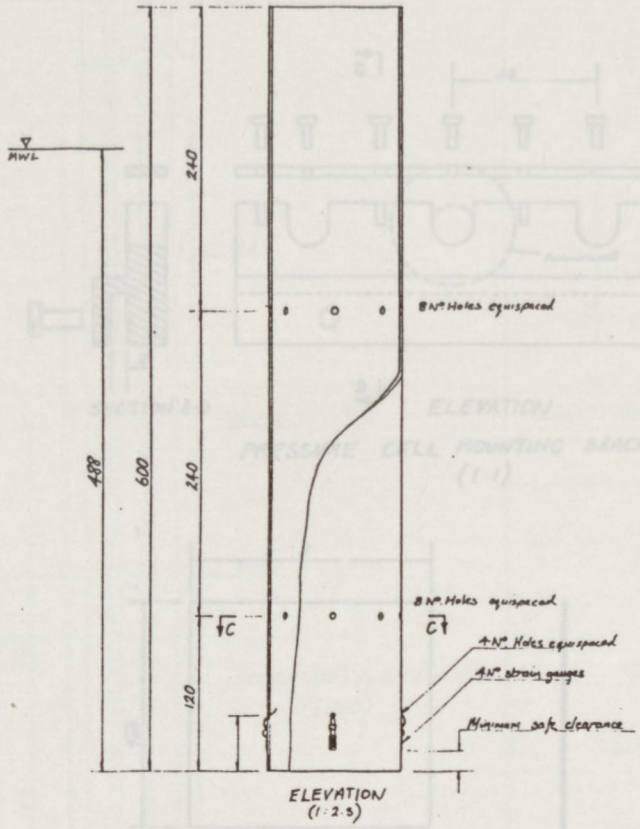

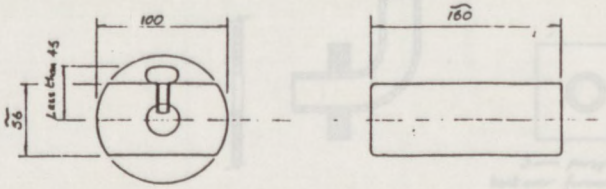

Former Details (1:2.5)

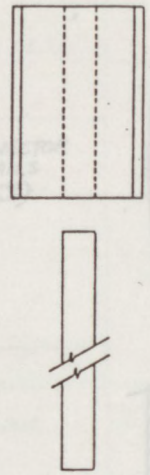

Possible temporary former constructed of wood with edges rounded to avoid cracking araldite

Notes

1. All dimensions in millimetres
2. Approximate dimensions shown thus $\widetilde{56}$
3. The idea behind the use of the wood former is to maintain the araldite in slight tension throughout the drilling process
4. Any other suitable method may be suggested
5. This former may be used to aid sawing
6. Drilling by hand is recommended

FLEXIBLE CYLINDER DETAILS
Pressure cell and strain gauge holes
L.F. COATES 3-5-80 Nº 2

Figure 5.2.3

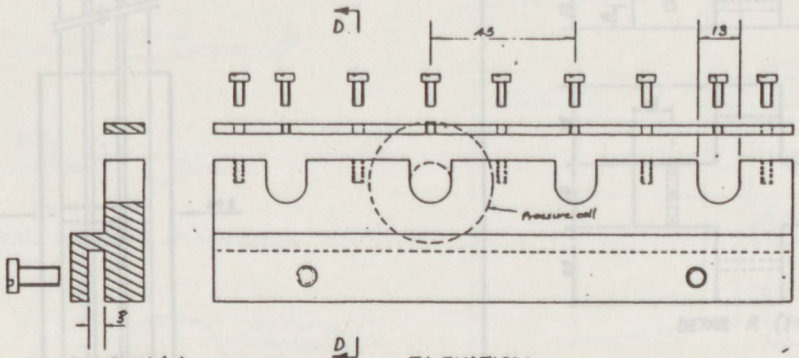

PRESSURE CELL MOUNTING BRACKETS (2 No)
(1:1)

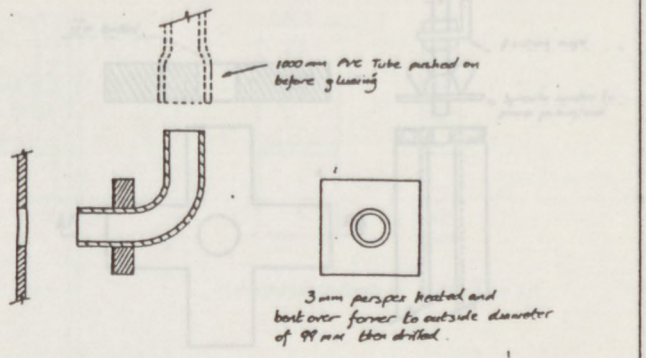

CONNECTOR DETAILS (DO NOT SCALE)

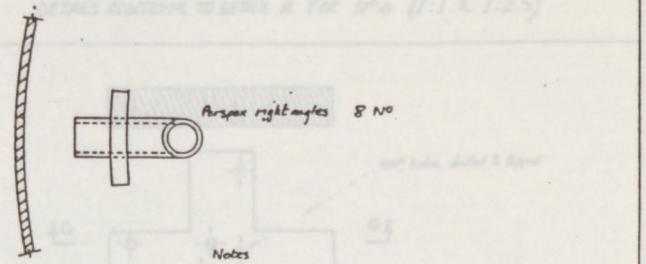

Notes

1 All dimensions in millimetres
2 Approximate dimensions shown thus ~
3 4 No connectors must be mounted at an angle of 5° to the vertical to avoid fouling transducers

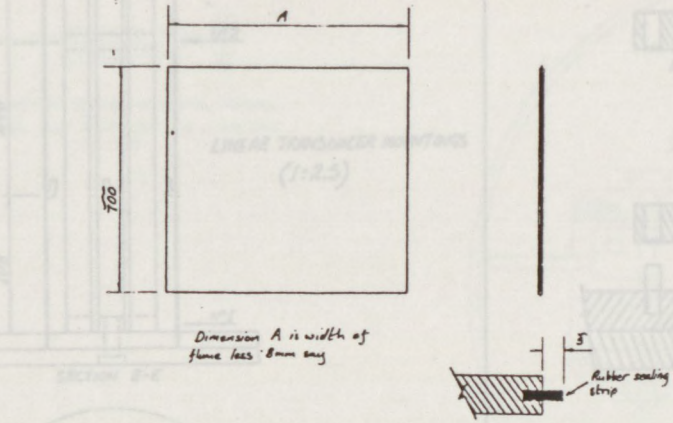

FLUME BLANKING PLATES (2 No)
(1:10)

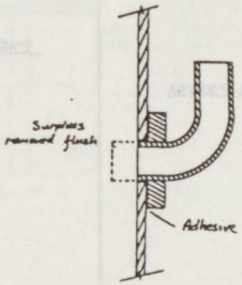

FLEXIBLE CYLINDER DETAILS
Pressure cell mounting brackets & pvc tube connectors
6-5-80 L.E. Coates No. 3

Figure 5.2.4

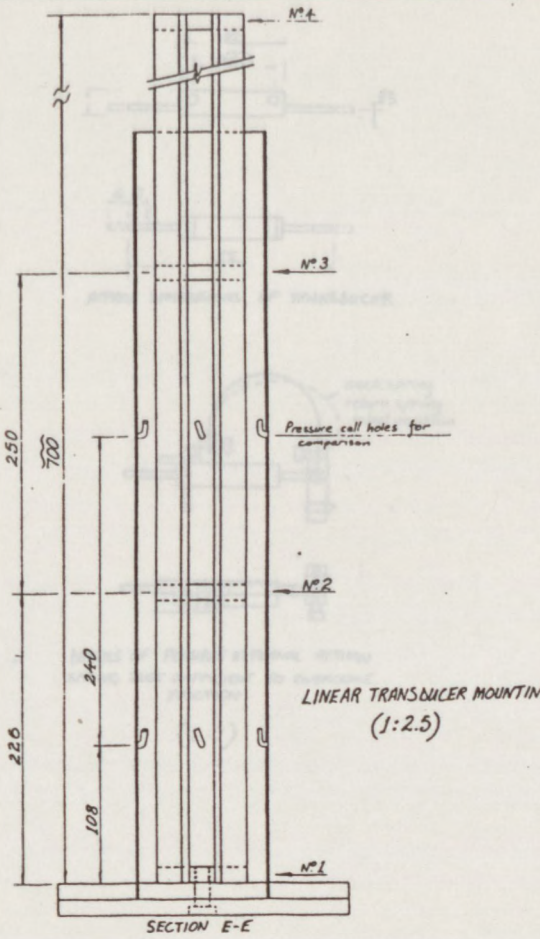

LINEAR TRANSDUCER MOUNTINGS (1:2.5)

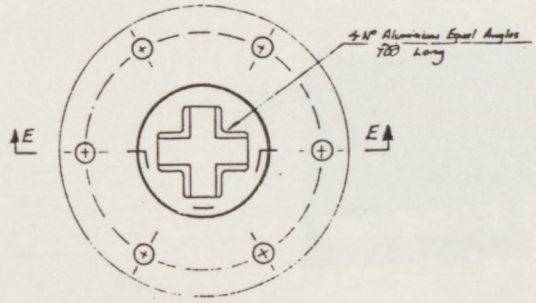

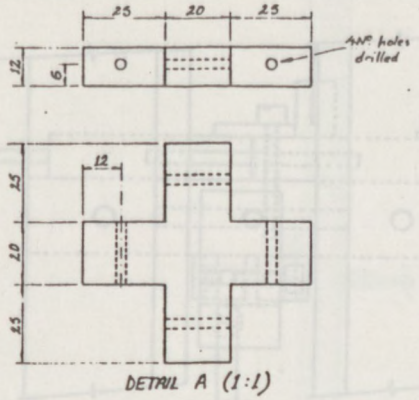

DETAIL A (1:1)

STABILITY AND MOUNTING CROSSES, GENERAL (Nos 1,2,3&4)

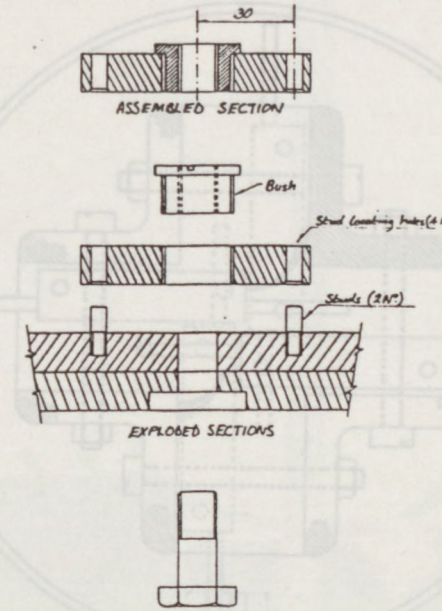

DETAILS ADDITIONAL TO DETAIL A FOR No 1 (1:1)

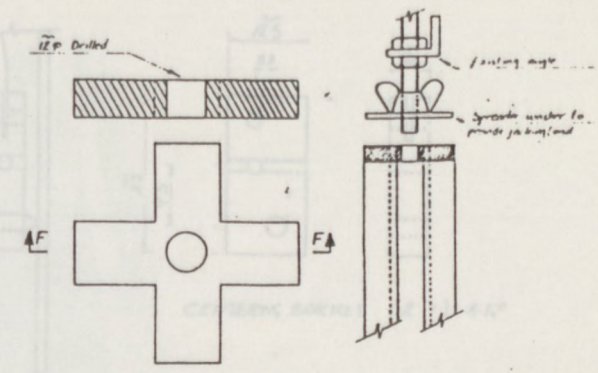

DETAILS ADDITIONAL TO DETAIL A FOR No 4 (1:1 & 1.2.5)

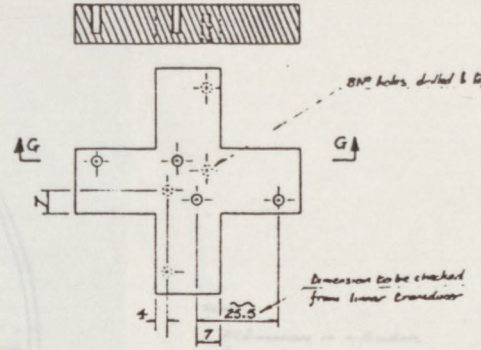

DETAILS ADDITIONAL TO DETAIL A FOR No 2 & No 3 (1:1)

Notes
1. All dimensions in millimetres
2. Approx dimensions shown thus 700
3. See also drawing No 5
4. Material for crosses unspecified (possibly perspex or PVC)
5. Various details omitted for clarity

FLEXIBLE CYLINDER DETAILS
LINEAR TRANSDUCER MOUNTINGS & JACKING LOAD ANGLES
L E COATES 16-5-80 No 4

Figure 5.2.5

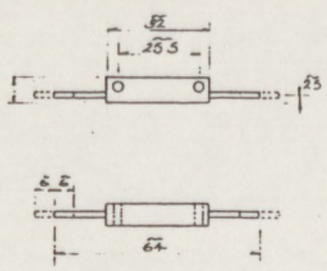

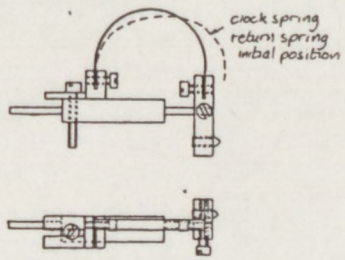

DETAILS OF POSSIBLE EXTERNAL RETURN SPRING JUST SUFFICIENT TO OVERCOME FRICTION

(1:1)

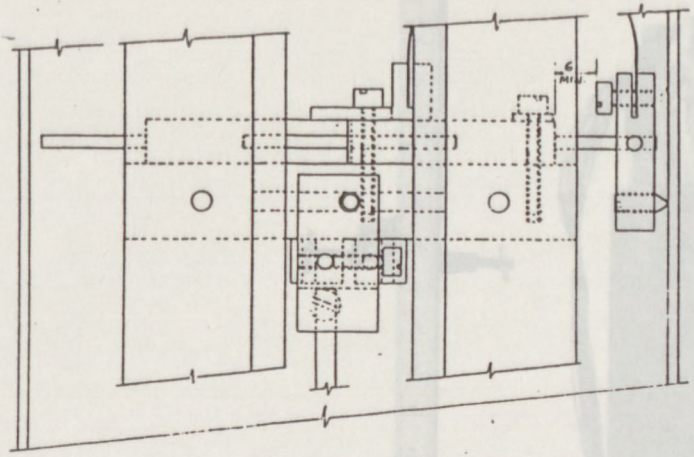

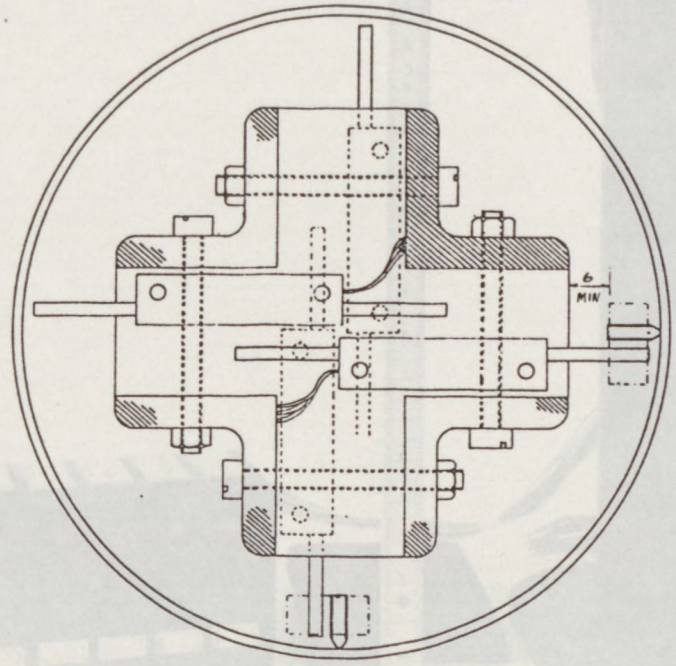

TRANSDUCER MOUNTING DETAILS

(2:1)

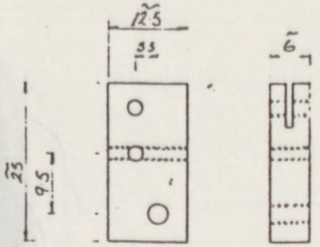

CENTERING BRACKET (2:1) 4 Nº

Notes -

1. All dimensions in millimetres
2. Approximate dimensions shown thus ~~25~~
3. NUMEROUS DETAILS OMITTED FOR CLARITY

FLEXIBLE CYLINDER DETAILS
TRANSDUCER MOUNTINGS
L.E.COATES 23-5-80 Nº 5

Figure 5.2.6

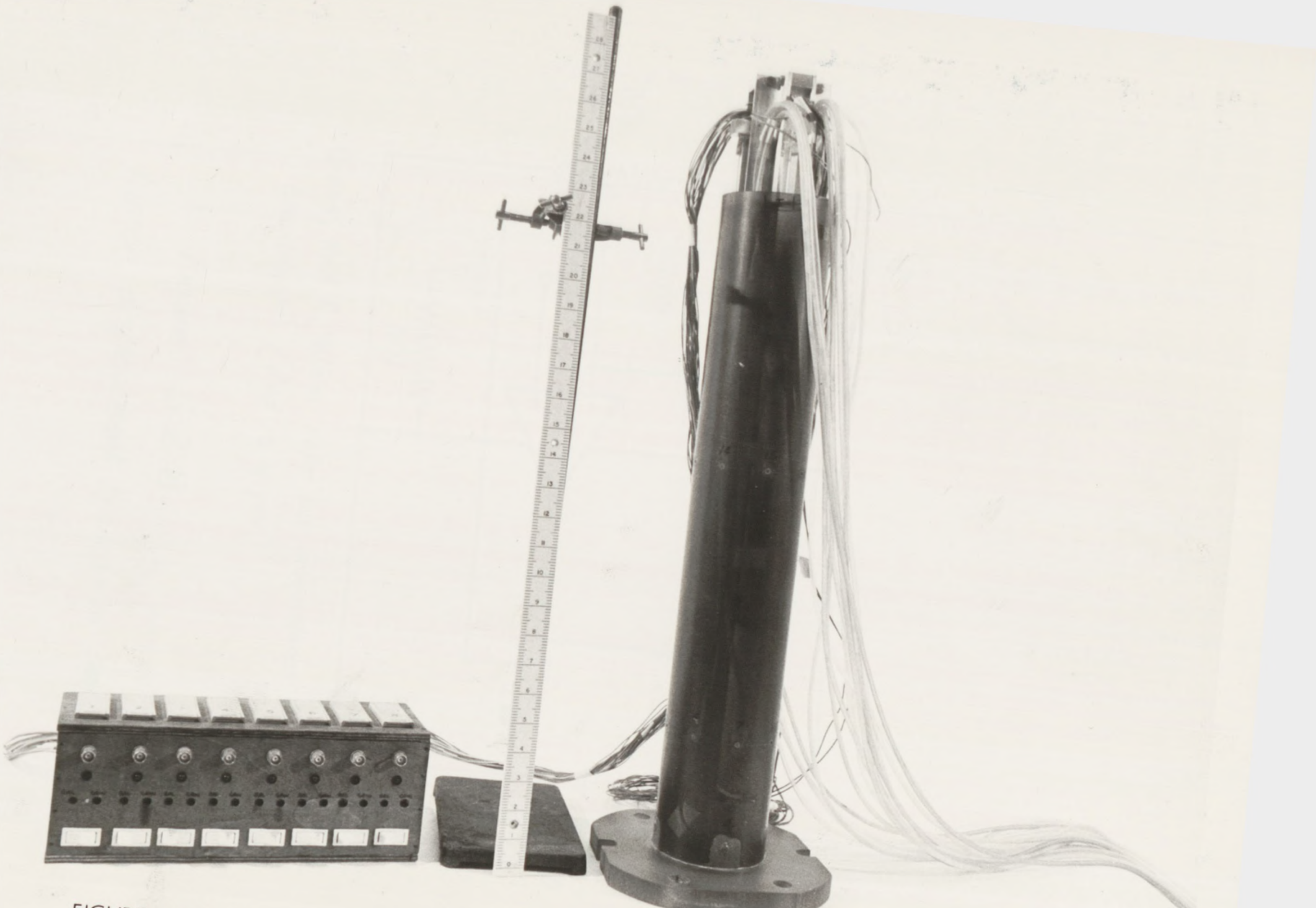

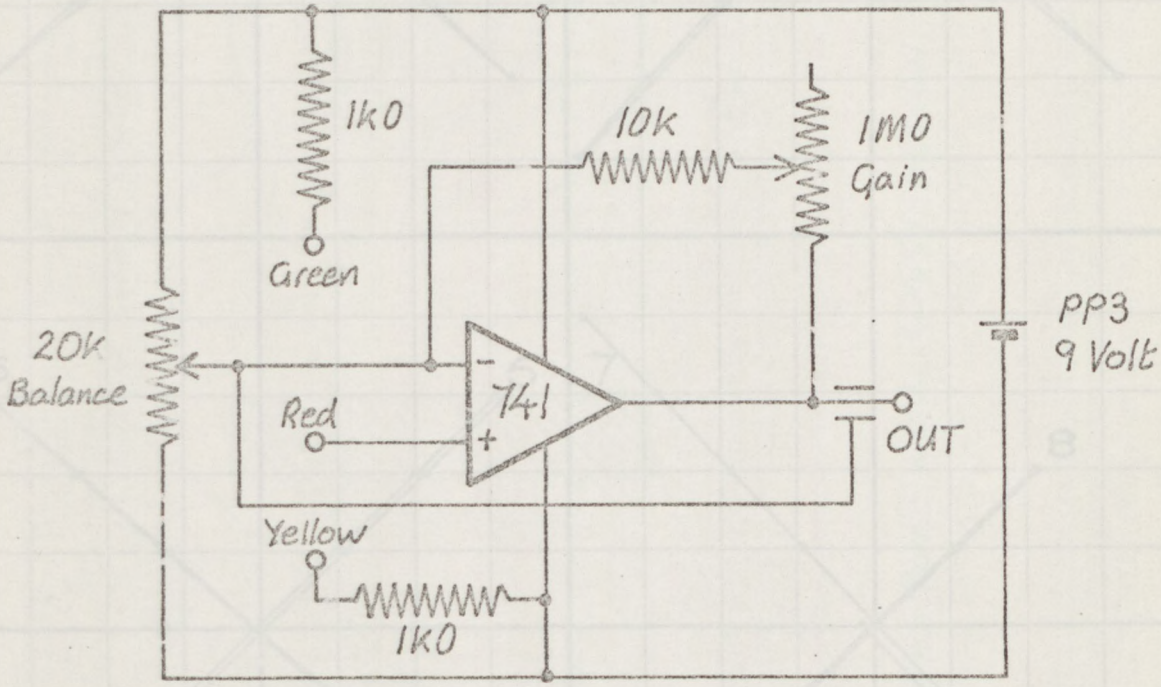

Green, Red & Yellow refer to connections to transducer (Red is wiper)

Figure 5·2·8

Linear displacement transducer amplifier

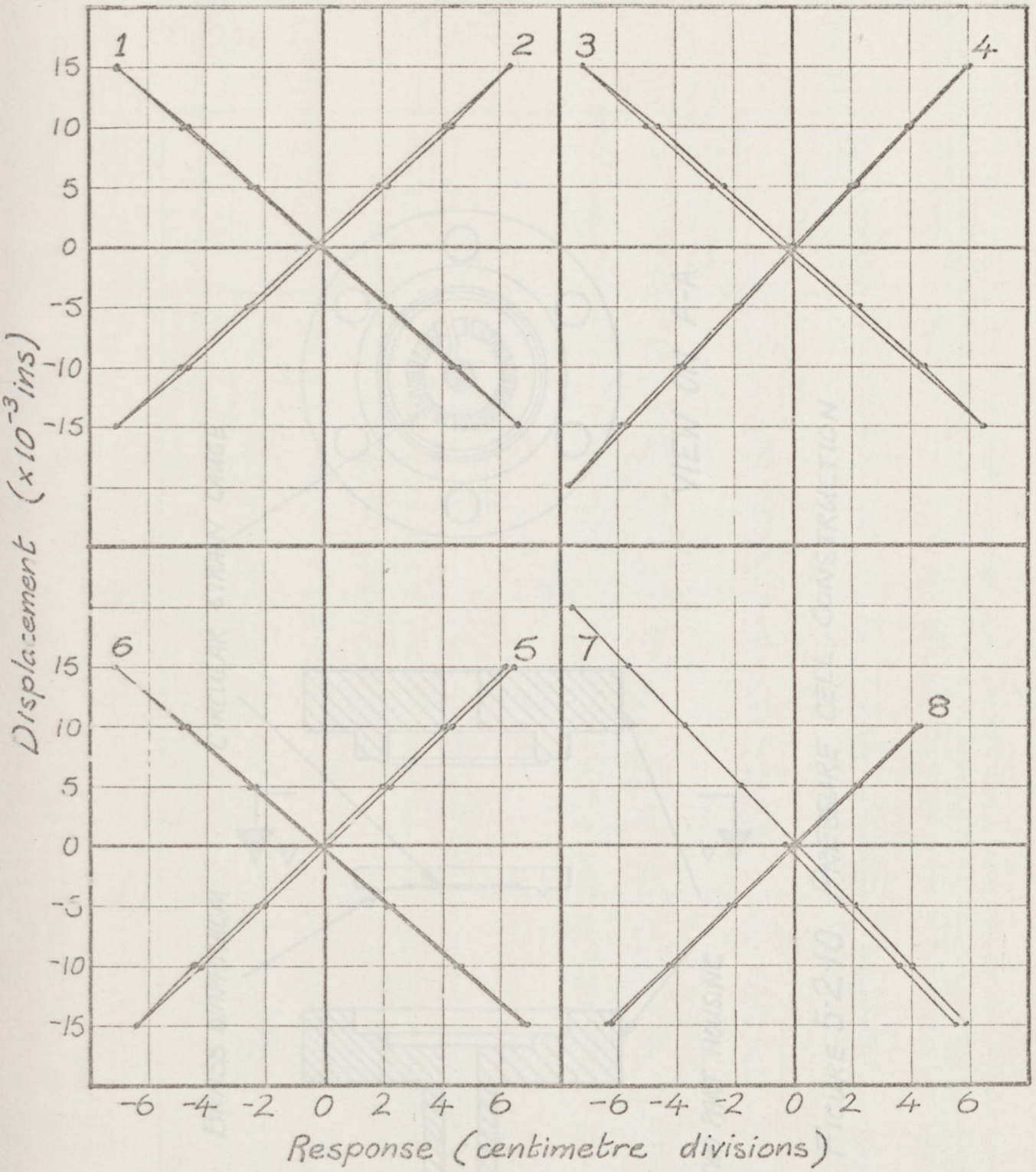

Displacement transducer calibration constants

1	1 div.	: 55·7 μm	2	1 div.	: 56·7 μm
3	1 div.	: 55·5 μm	4	1 div.	: 65·2 μm
5	1 div.	: 59·4 μm	6	1 div.	: 54·9 μm
7	1 div.	: 66·3 μm	8	1 div.	: 60·2 μm

Figure 5·2·9

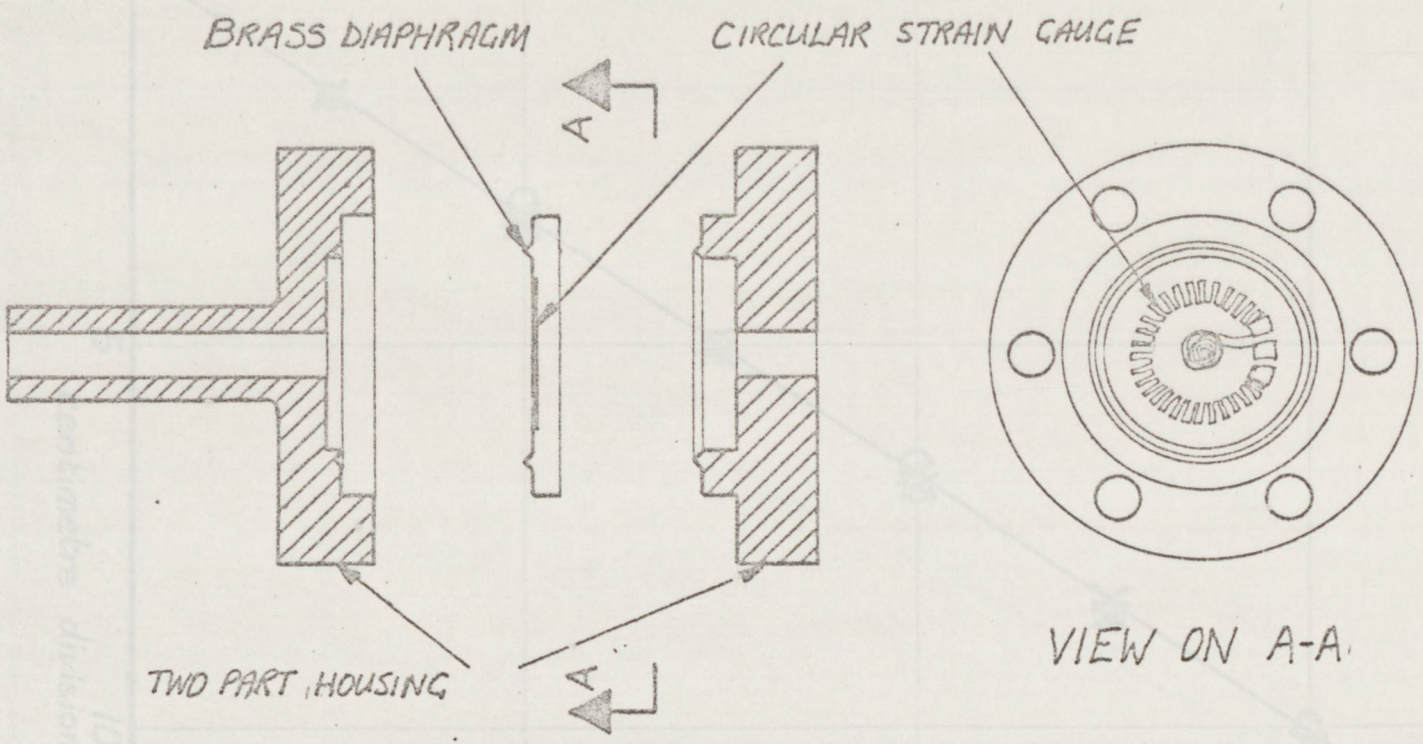

FIGURE 5·2·10 PRESSURE CELL. CONSTRUCTION

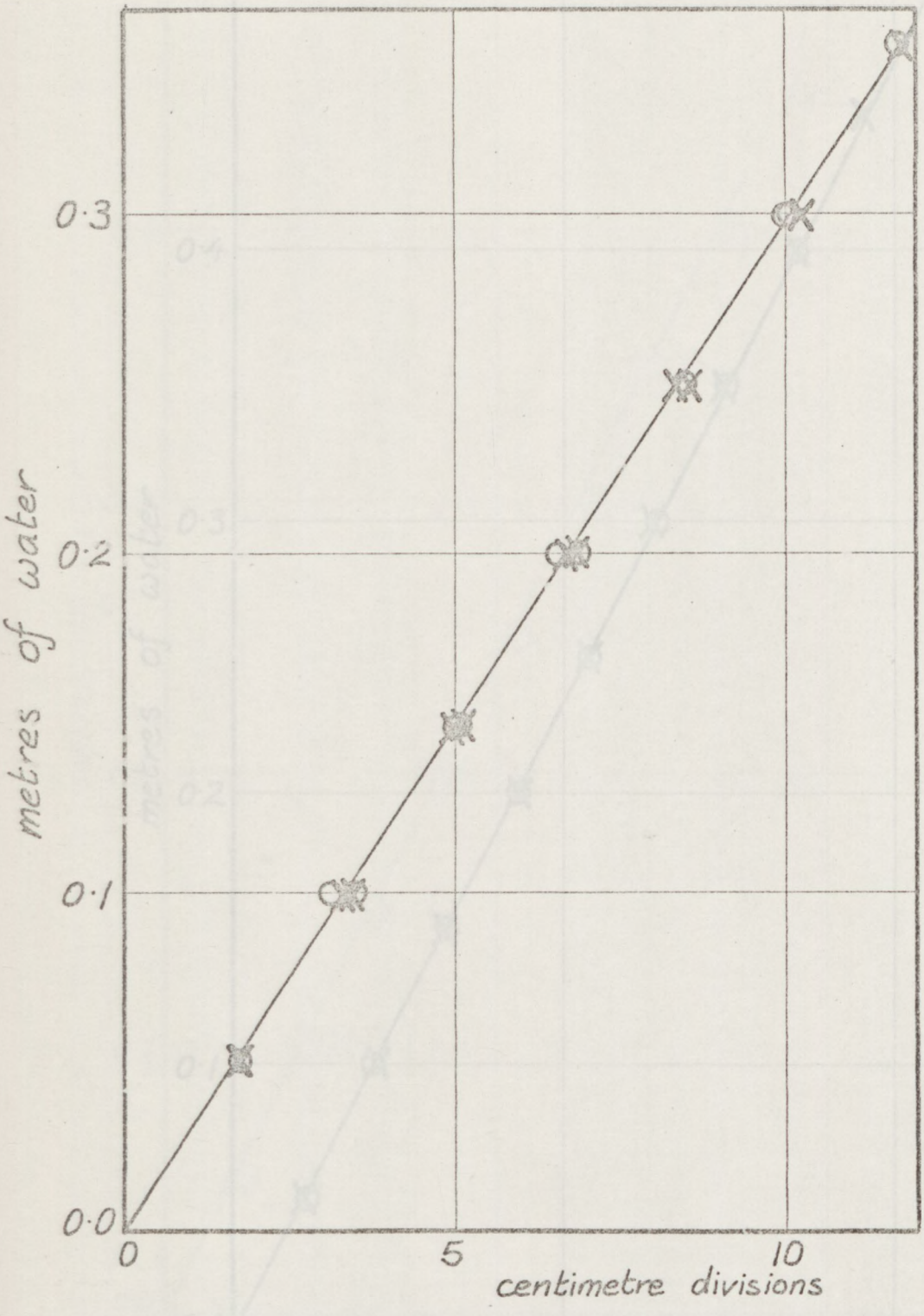

Figure 5·2·11

Calibration of pressure transducer 1

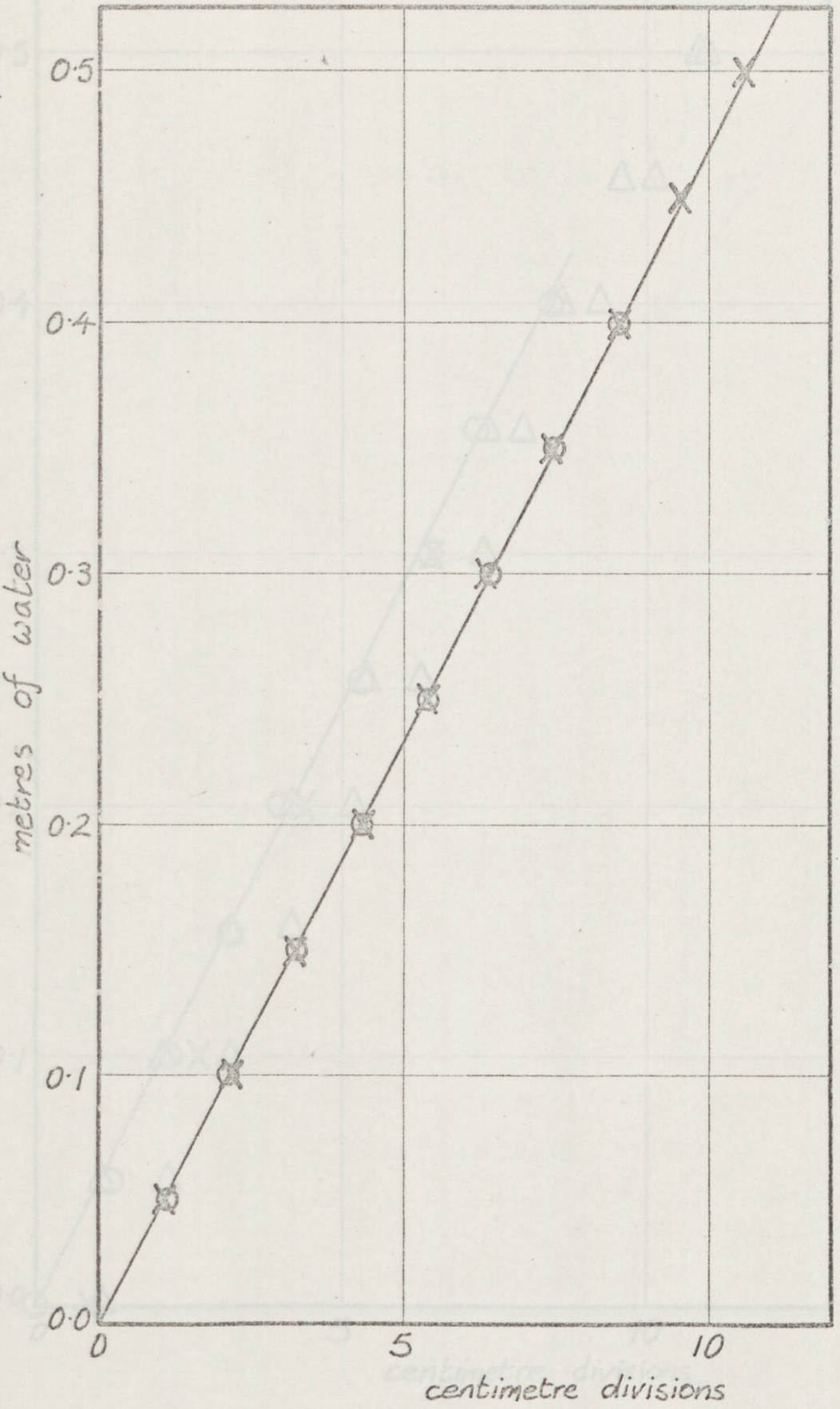

Figure 5·2·12

Calibration of pressure transducer 2

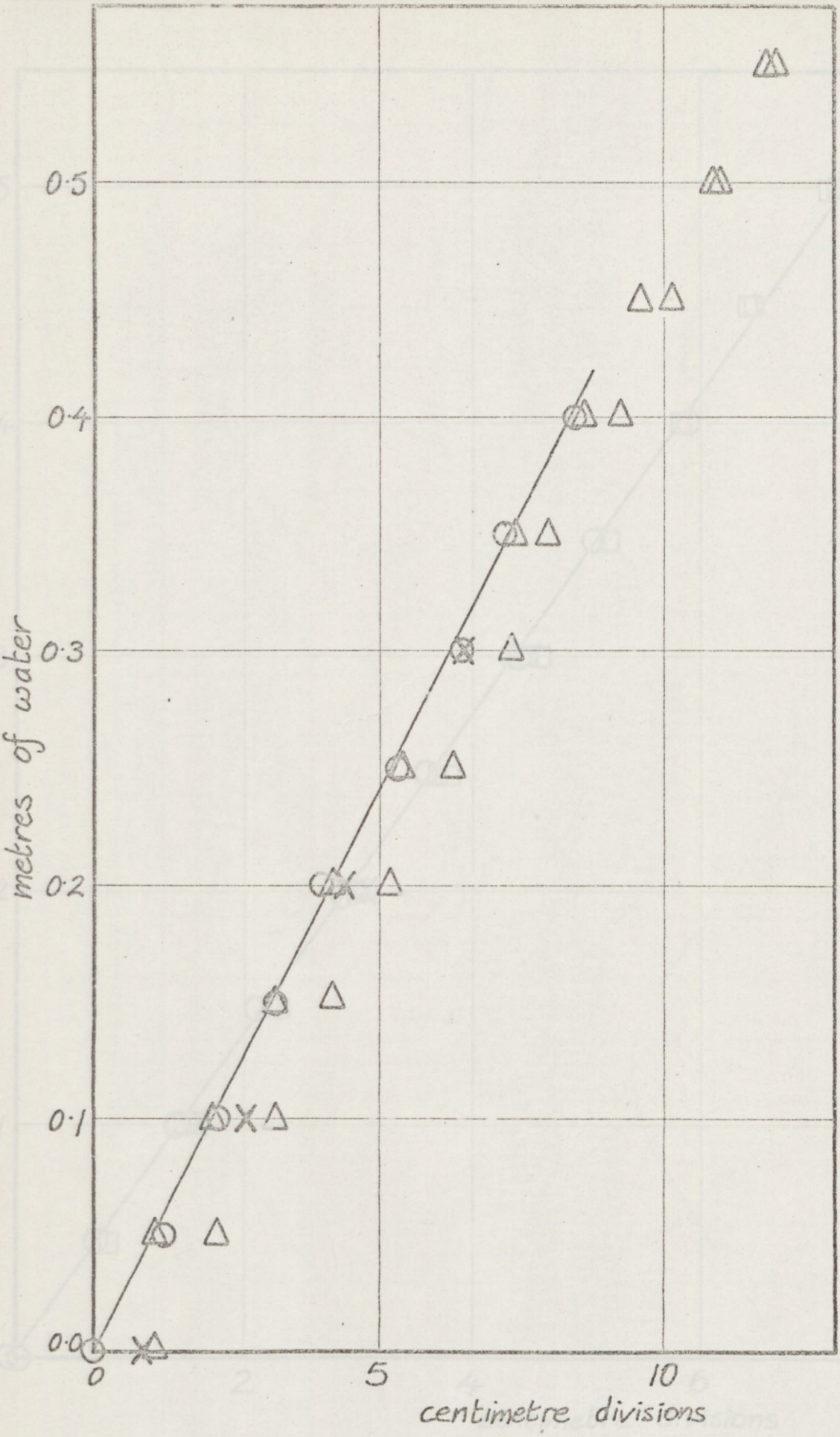

Figure 5·2·13

Calibration of pressure transducer 3

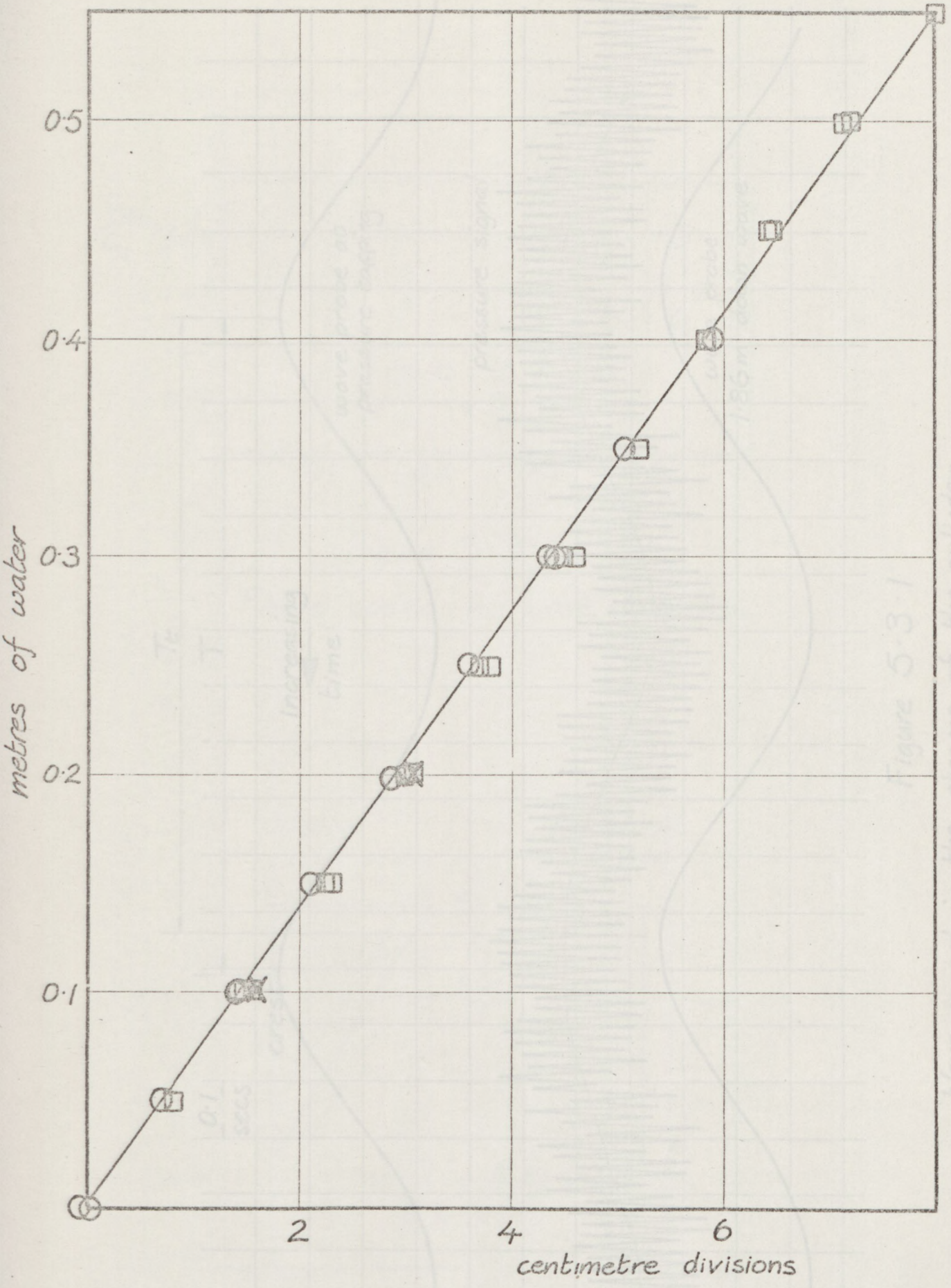

Figure 5·2·14

Calibration of pressure transducer 4

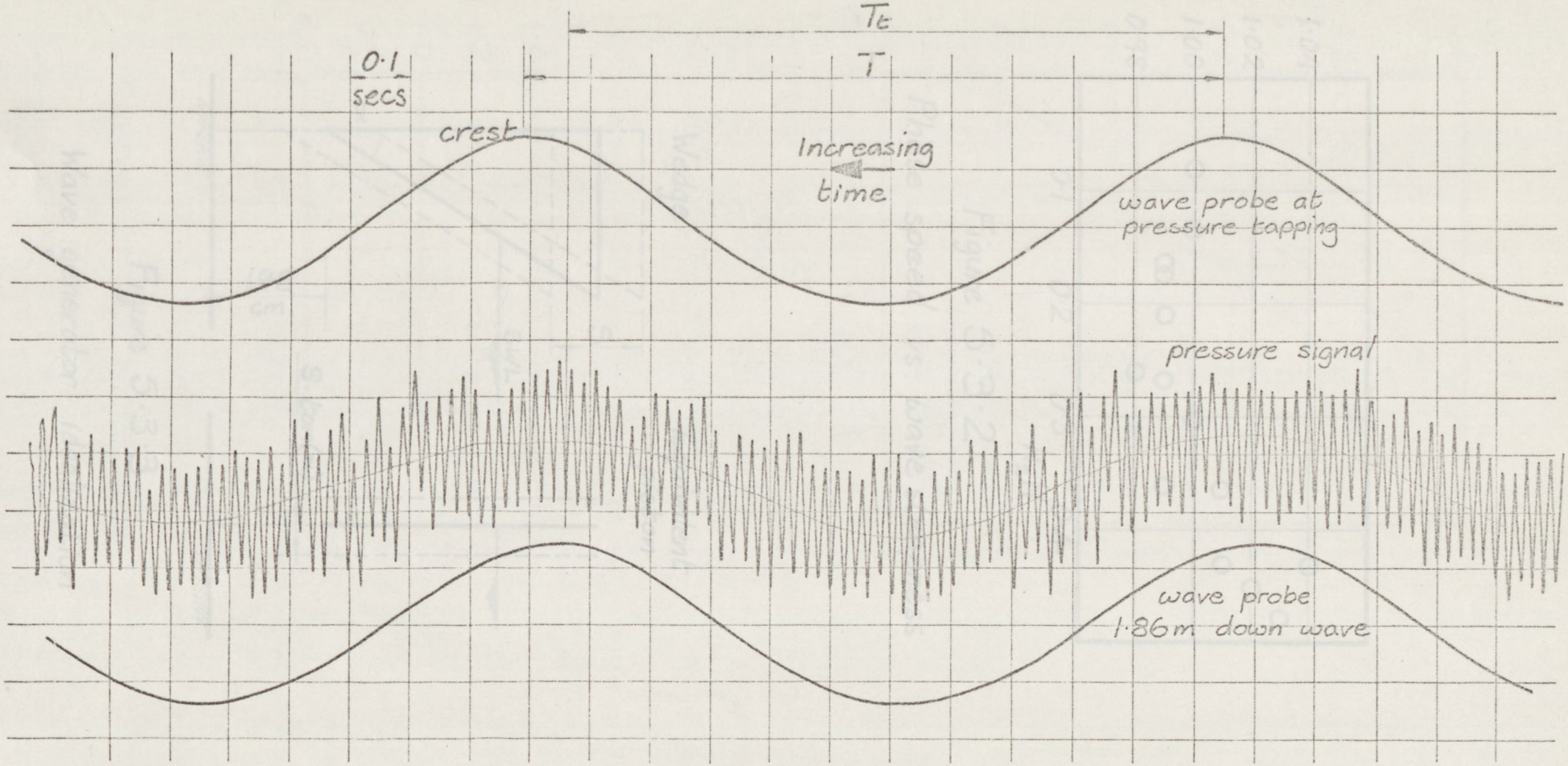

Figure 5·3·1

Wave record in the absence of the cylinder

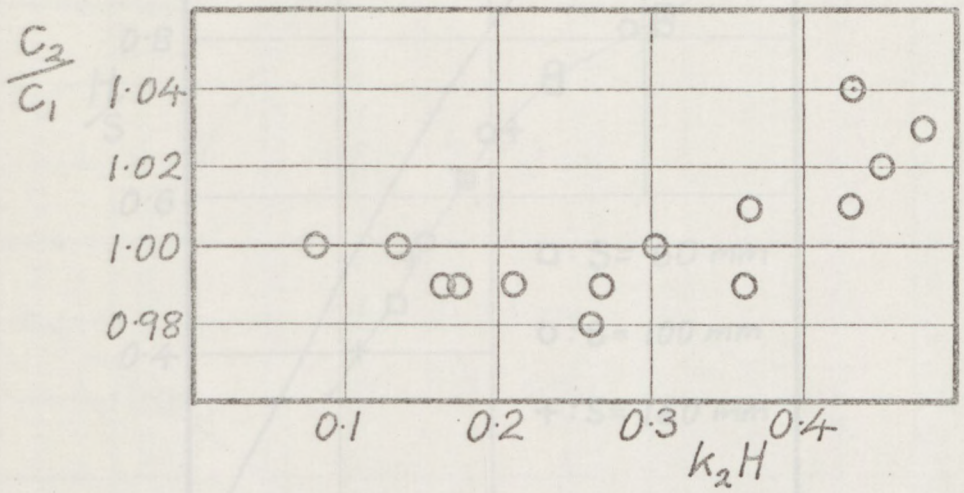

Figure 5·3·2

Phase speed vs. wave steepness

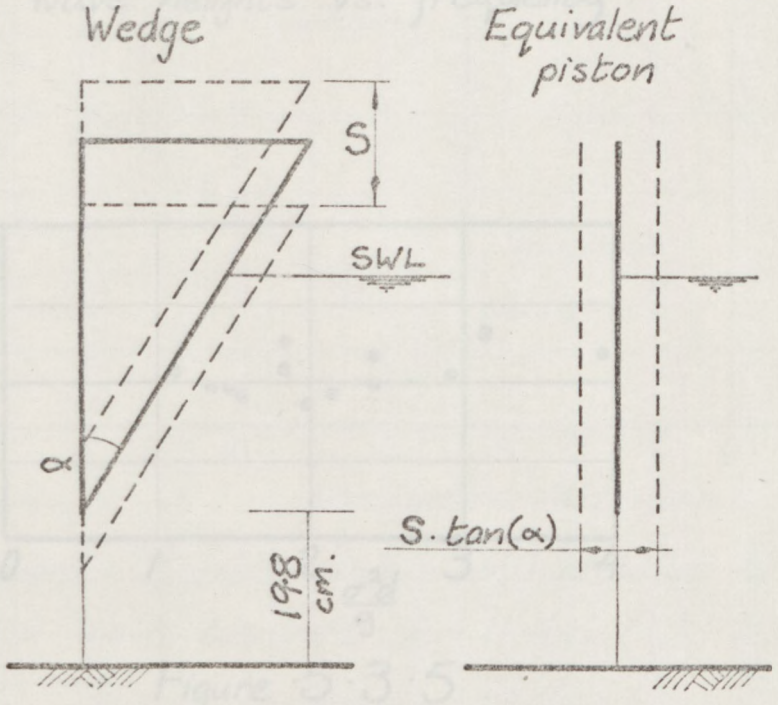

Figure 5·3·3

Wave generator idealization

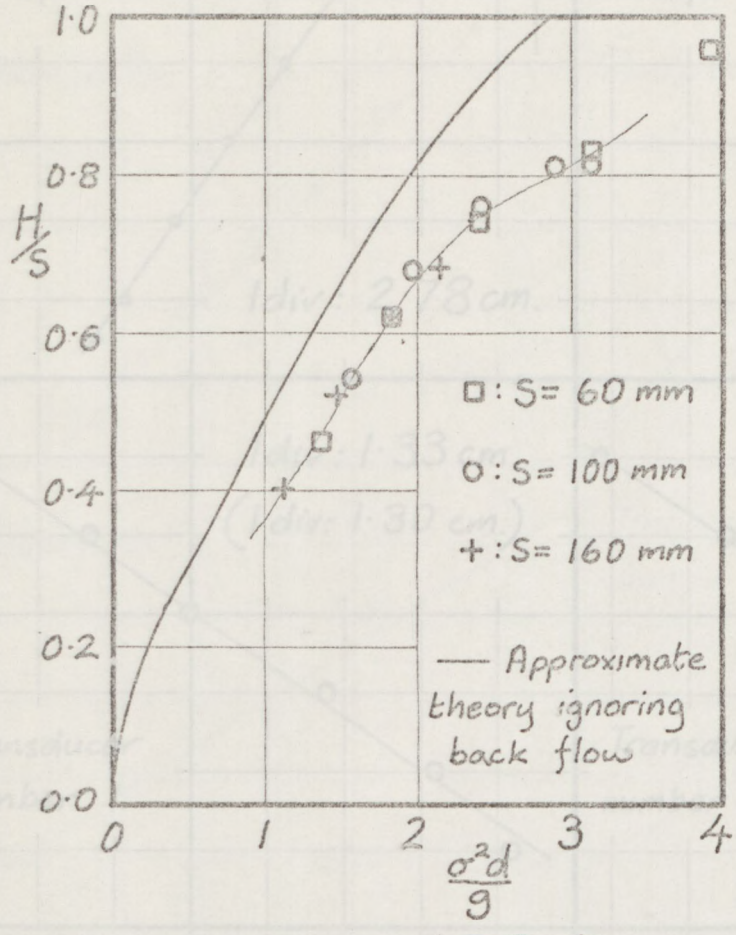

Figure 5·3·4

Wave heights vs. frequency

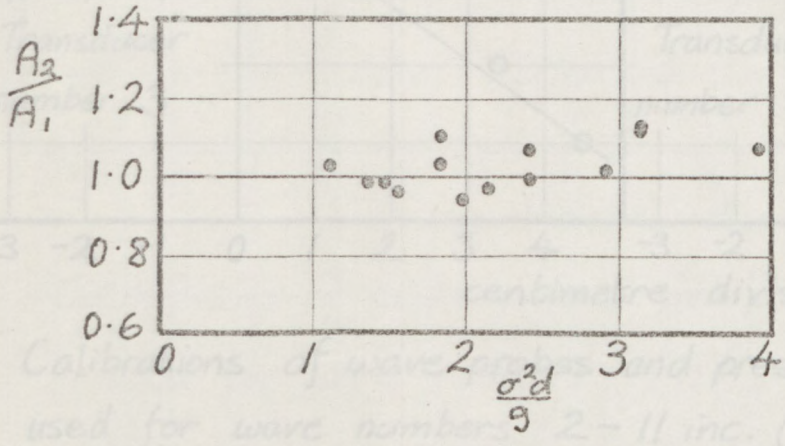

Figure 5·3·5

Pressures in wave vs. frequency

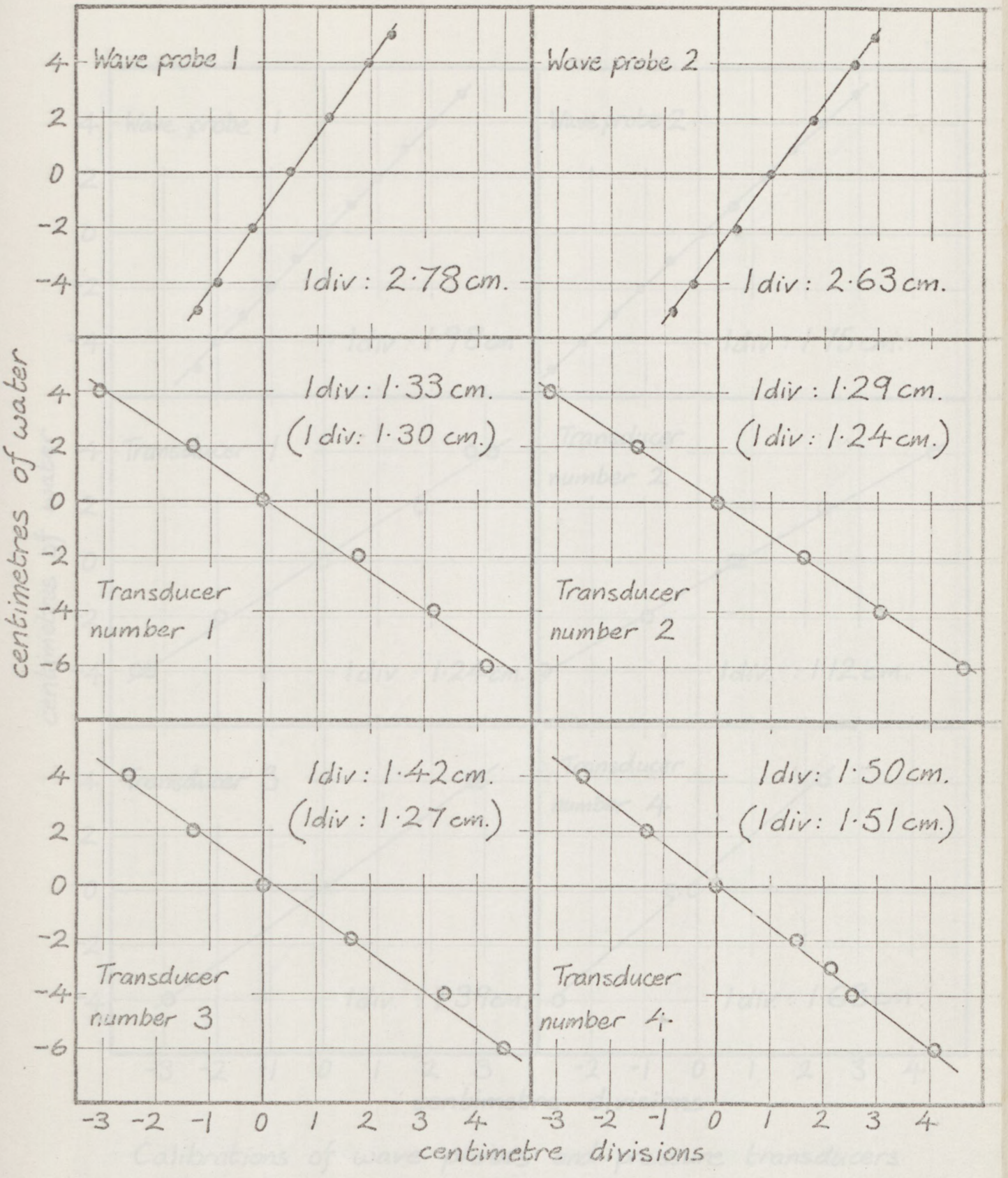

Calibrations of wave probes and pressure transducers used for wave numbers 2 – 11 inc. (13 – 22 inc.)

Figure 5·4·1

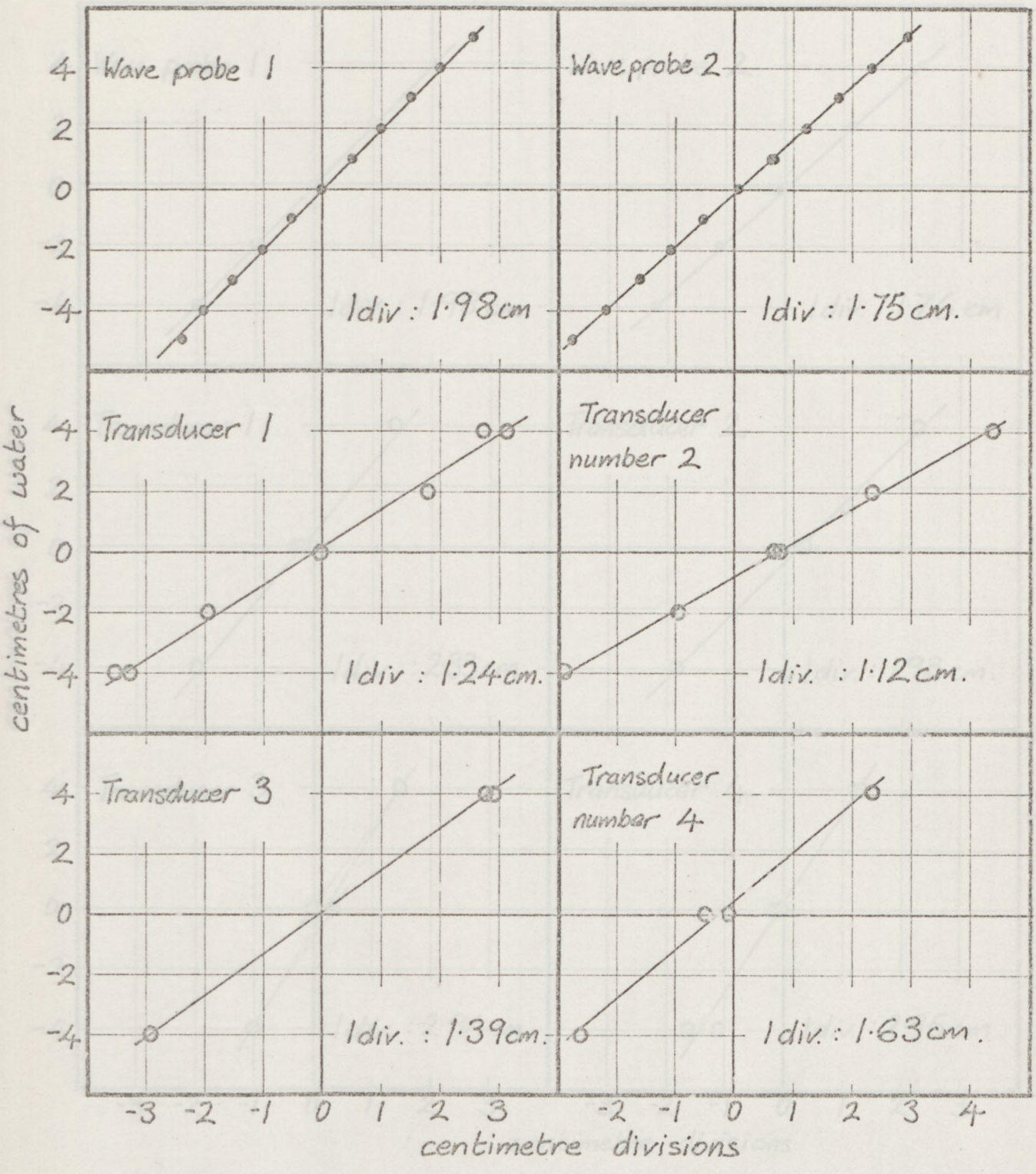

Calibrations of wave probes and pressure transducers used for wave numbers 23 - 31 inc.

Figure 5·4·2

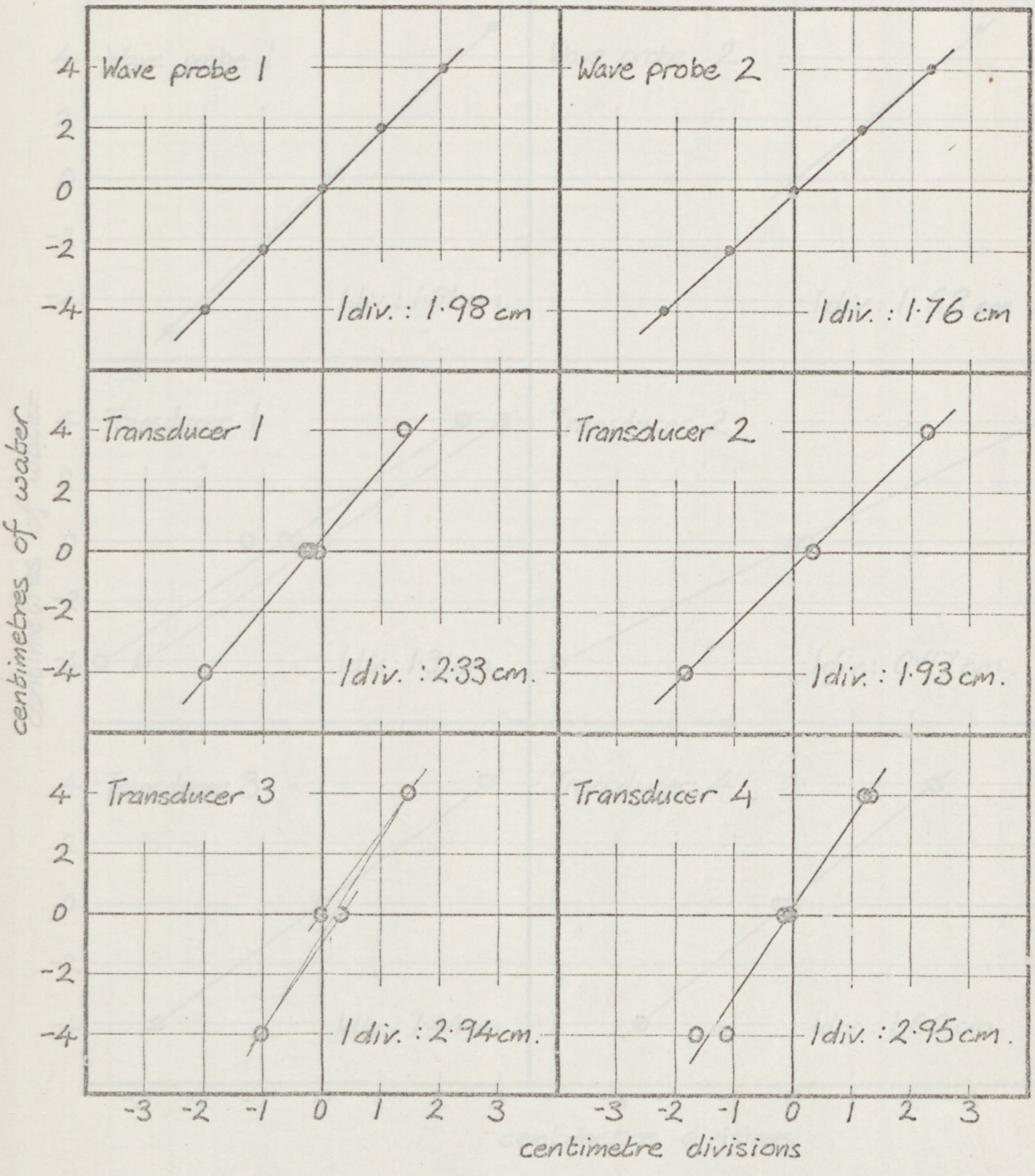

Calibrations of wave probes and pressure transducers used for wave numbers 33a - 33c inclusive.

Figure 5·4·3

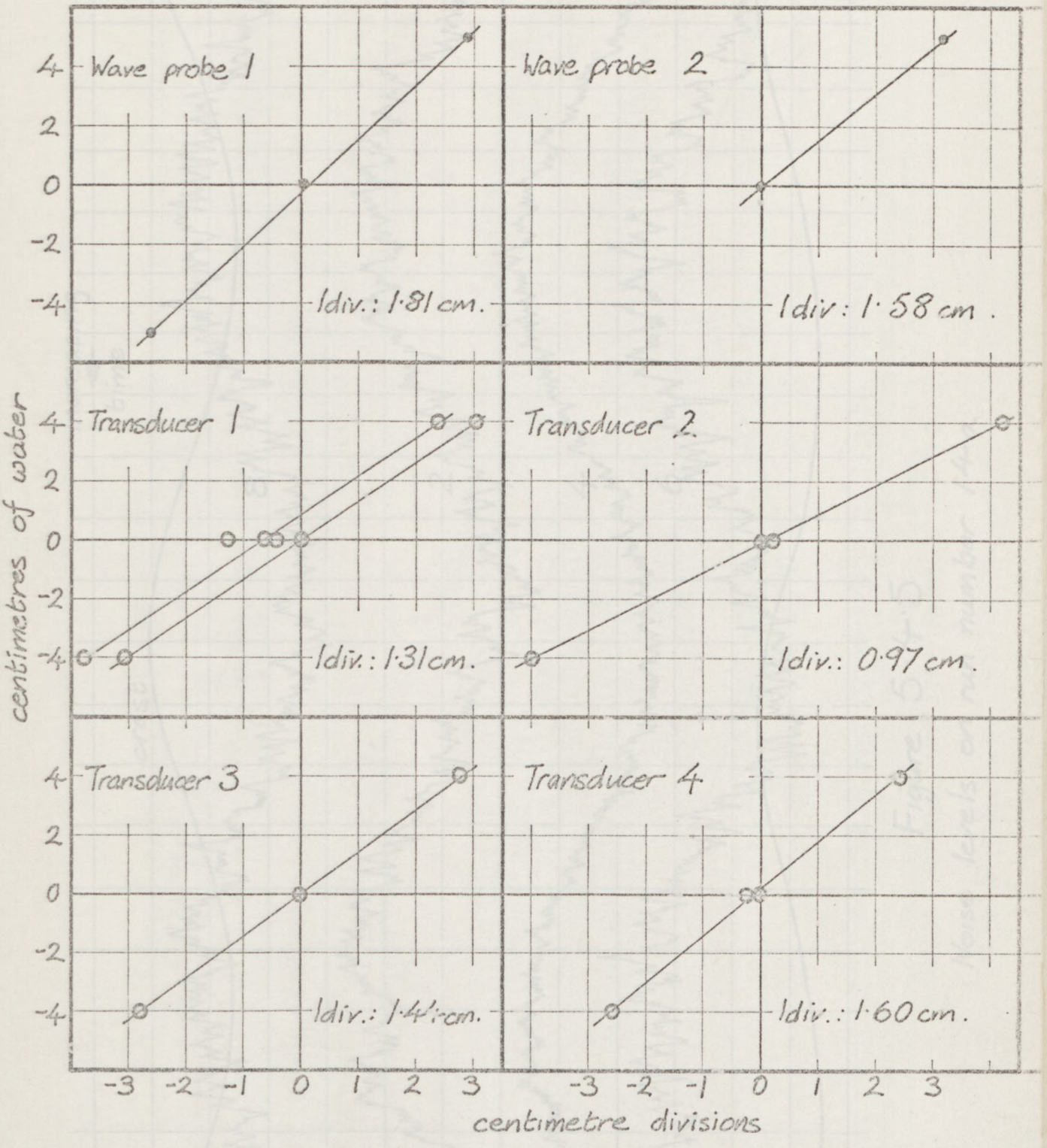

Calibrations of wave probes and pressure transducers used for wave numbers 40 – 43 inc.

Figure 5·4·4

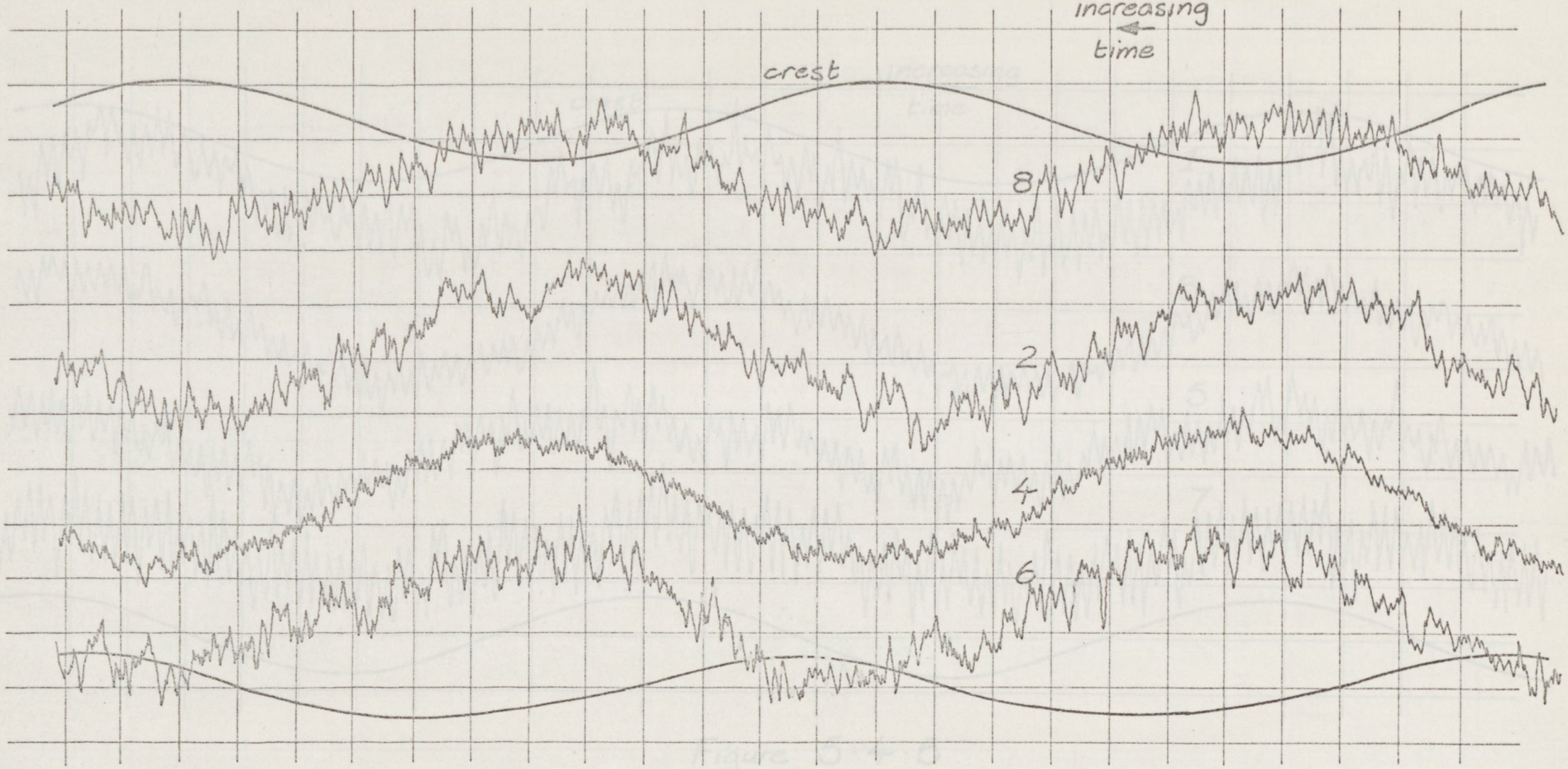

Figure 5·4·5

Noise levels on run number 14a

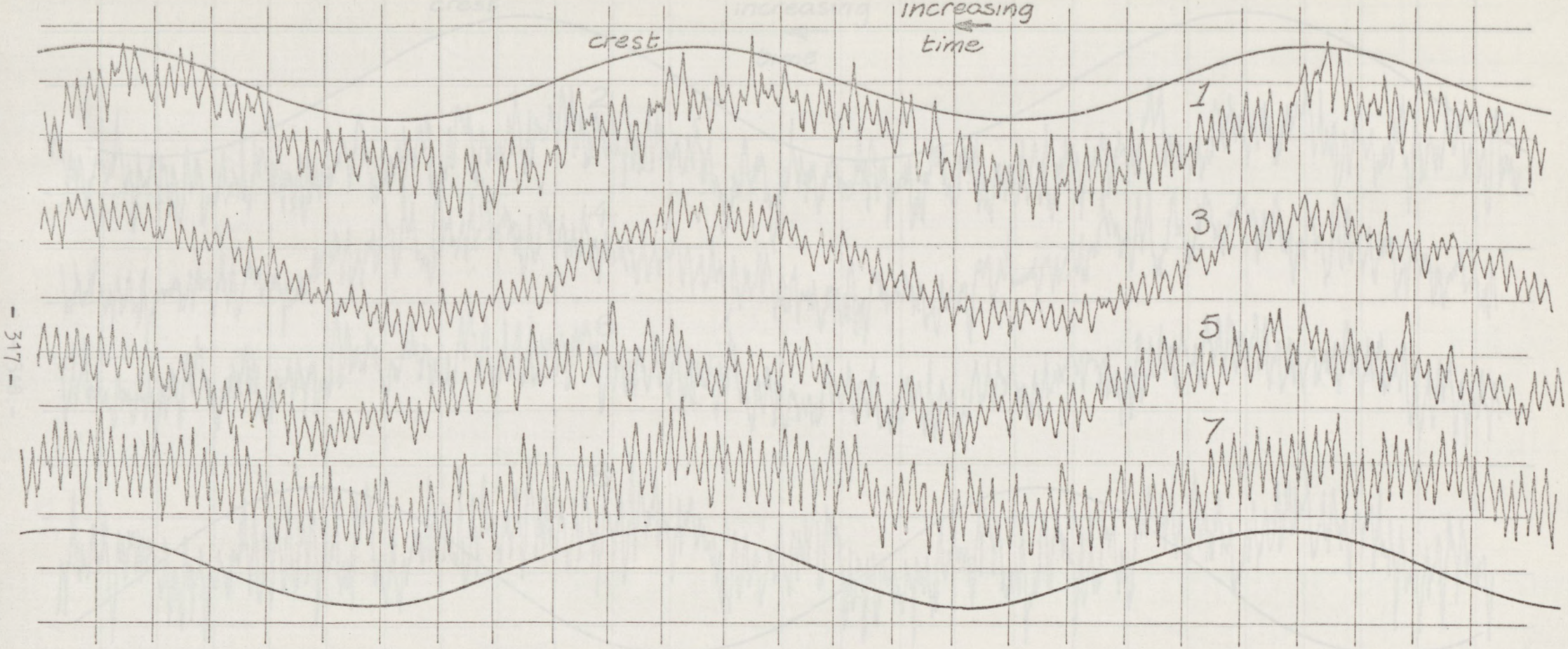

Figure 5·4·6

Noise levels on run number 24a

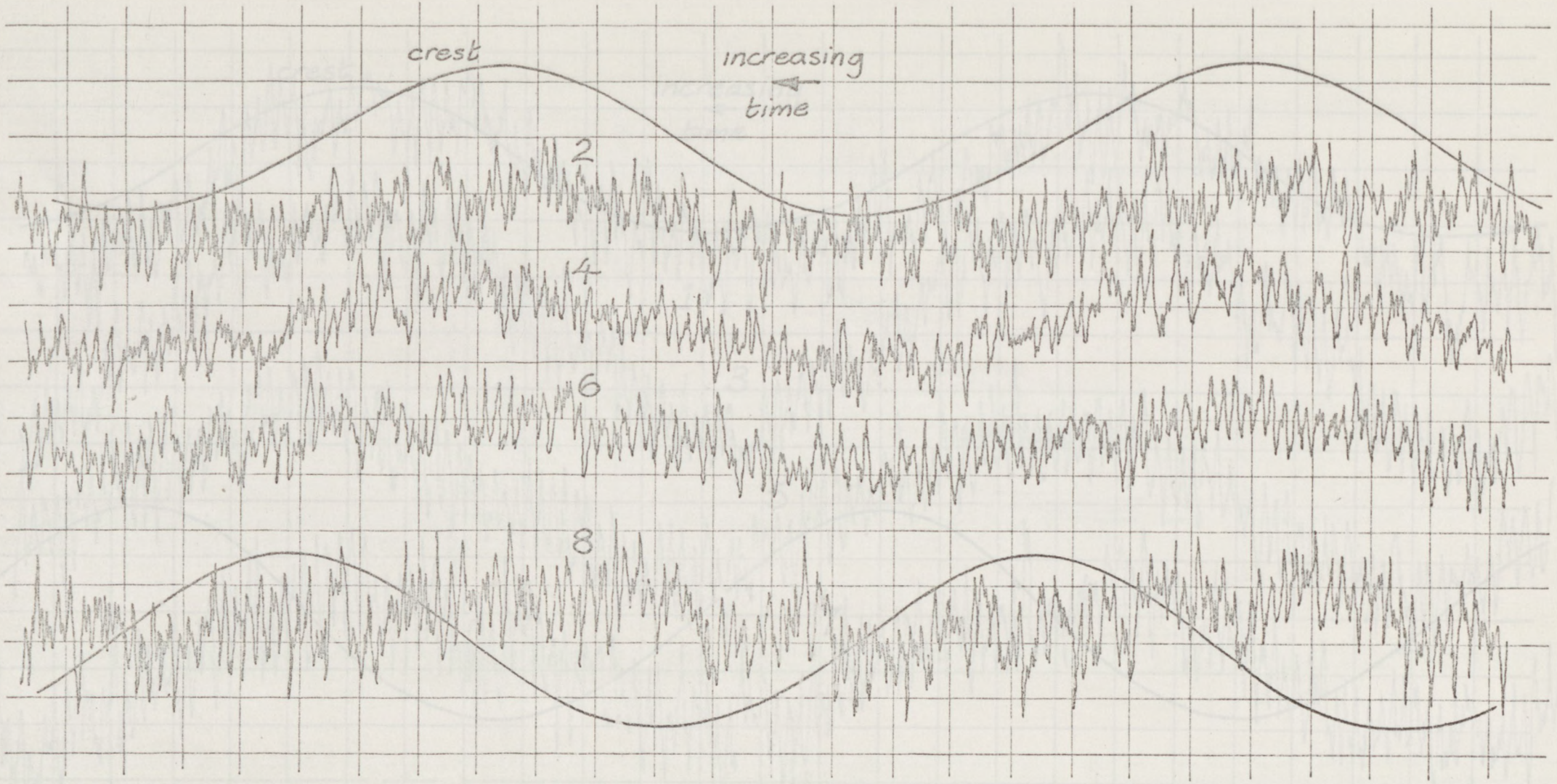

Figure 5·4·7

Noise levels on run number 33a

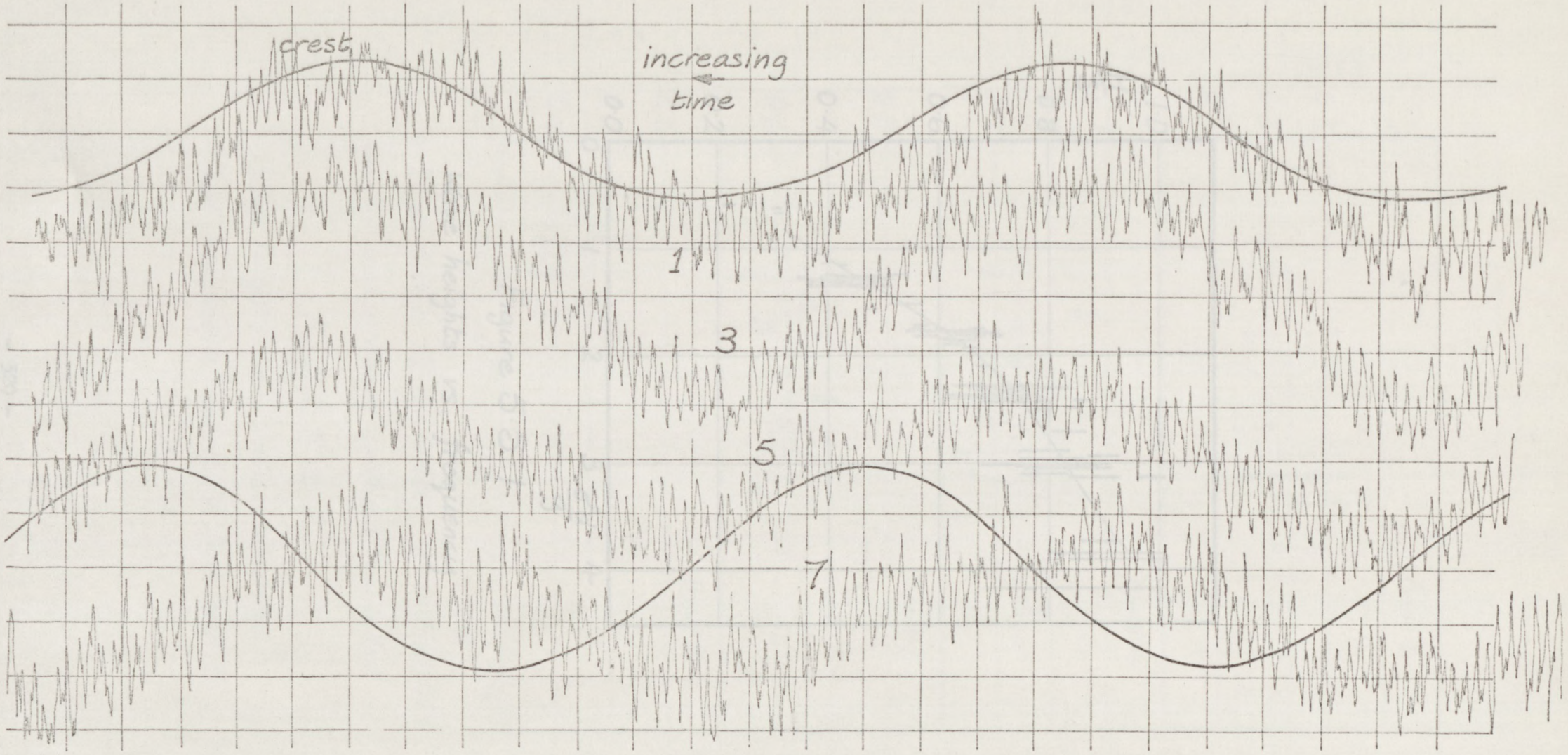

Figure 5·4·8

Noise levels on run number 40a

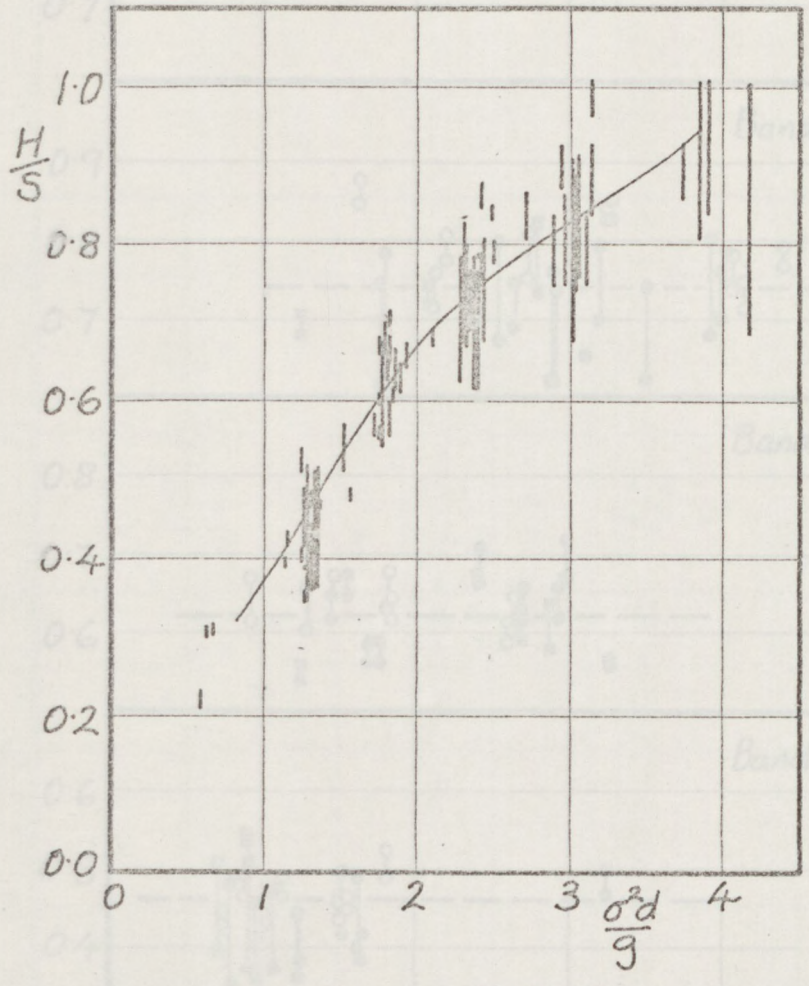

Figure 5·5·1

Wave heights vs. frequency

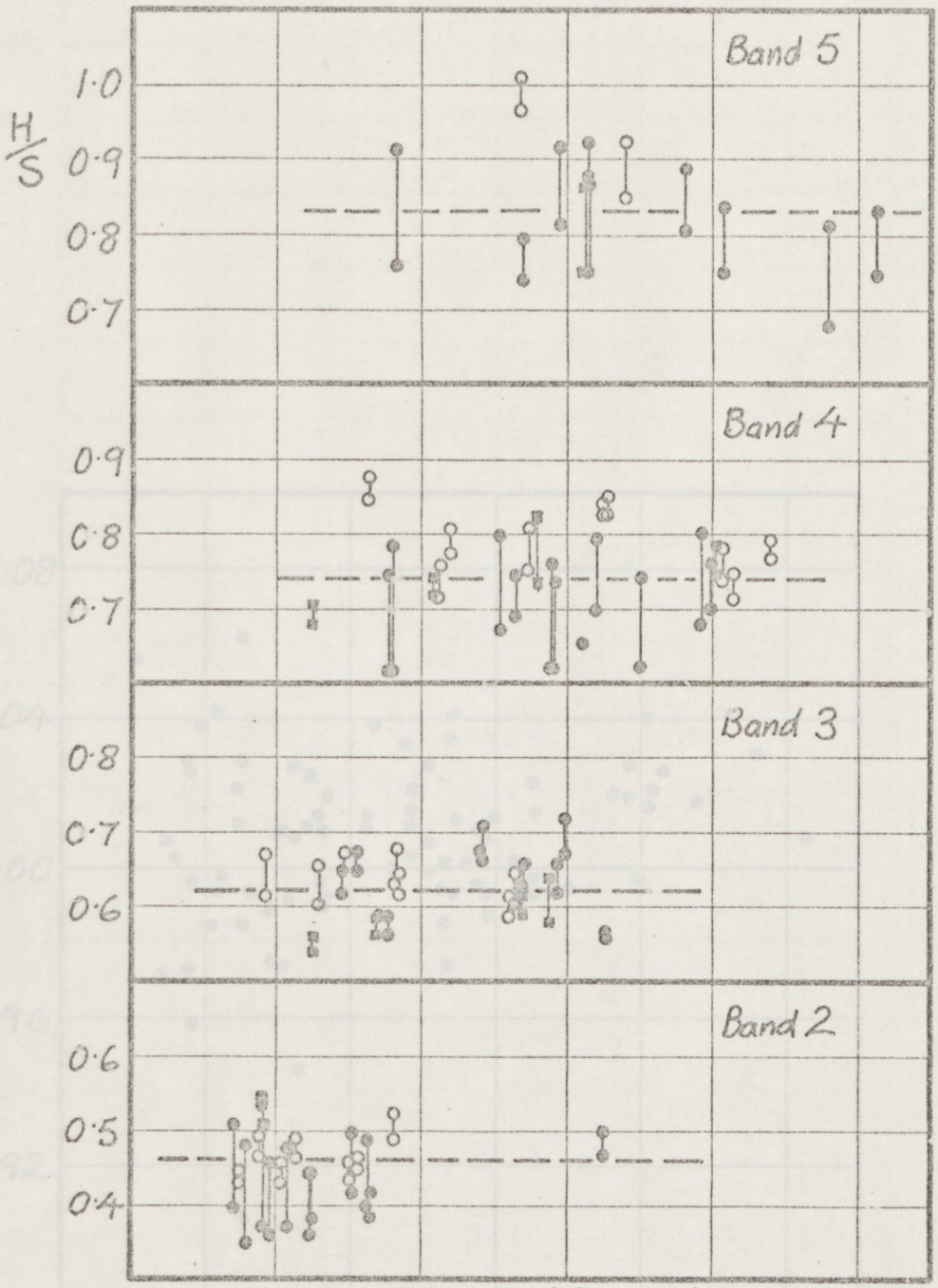

Figure 5·5·2

Wave heights vs. wave steepness for frequency bands 2, 3, 4 and 5

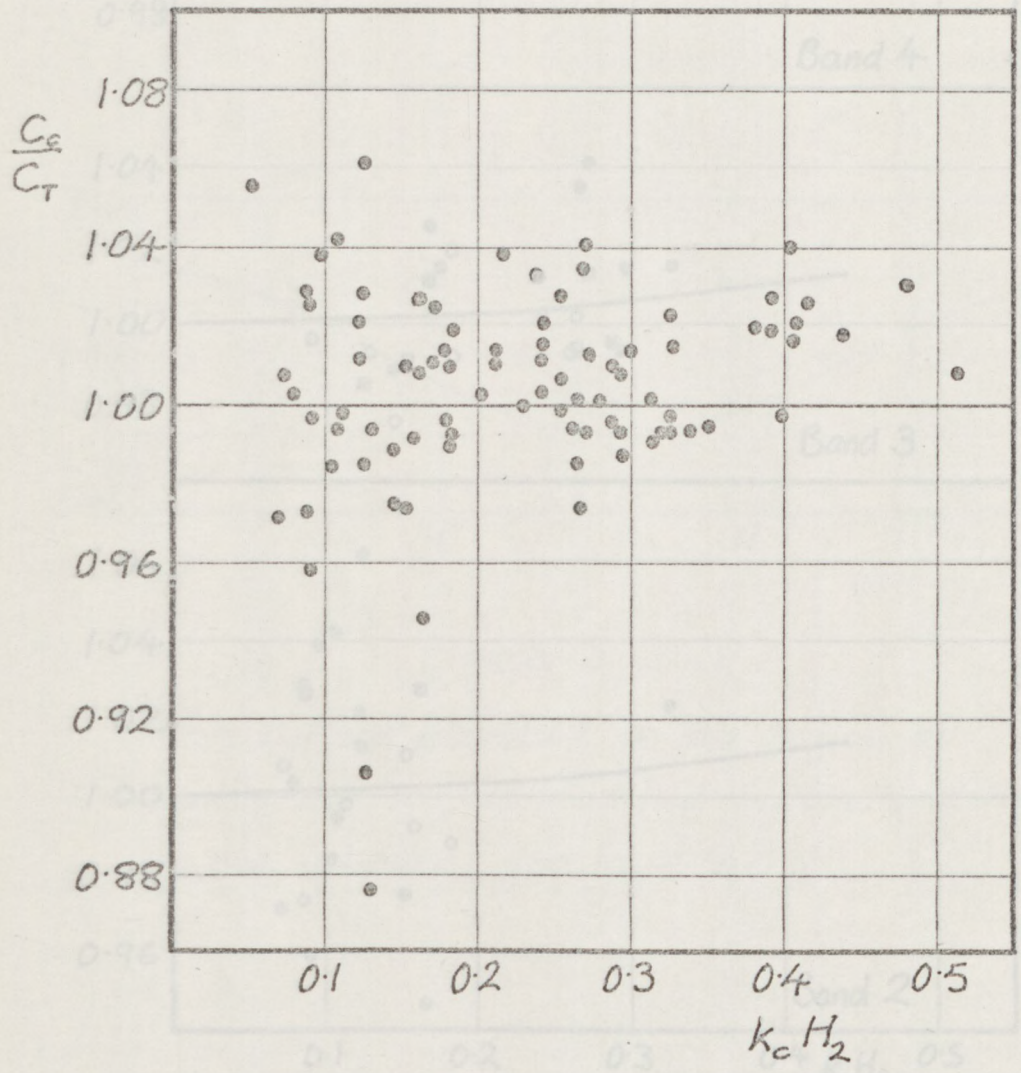

Figure 5·5·3

Phase speeds vs. wave steepness

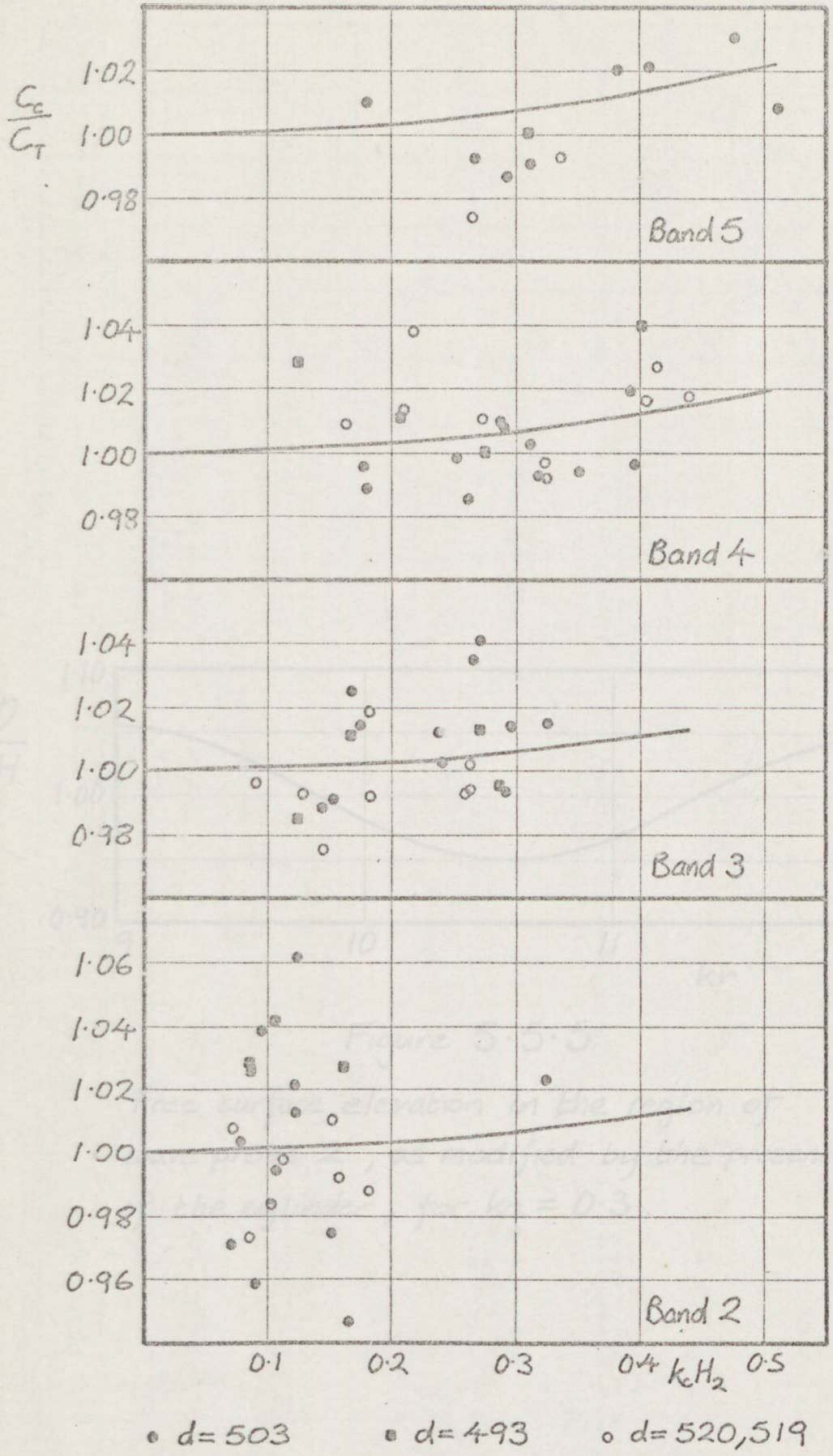

Figure 5·5·4

Phase speeds vs. wave steepness for frequency bands 2,3,4, and 5

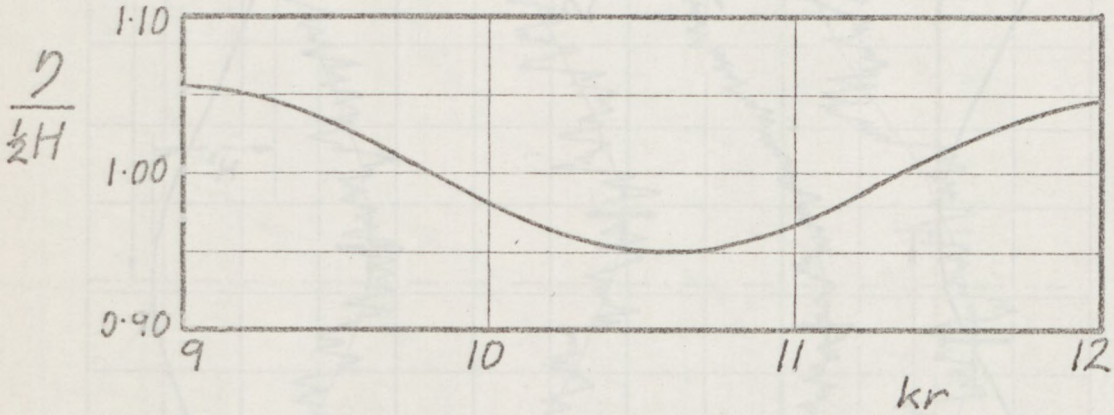

Figure 5·5·5

Free surface elevation in the region of wave probe 2, as modified by the presence of the cylinder, for $ka = 0.3$.

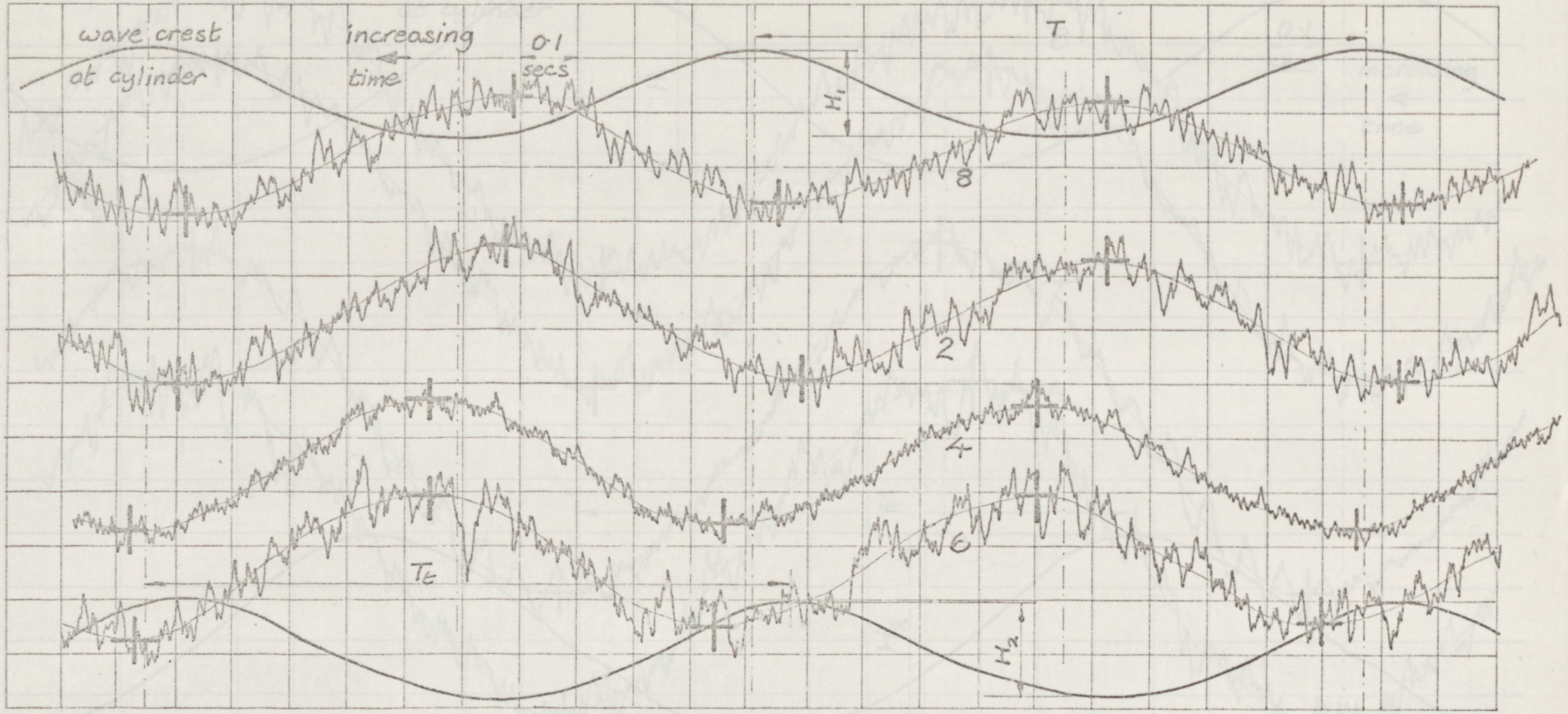

Figure 5·5·6

Measurements on wave number 146

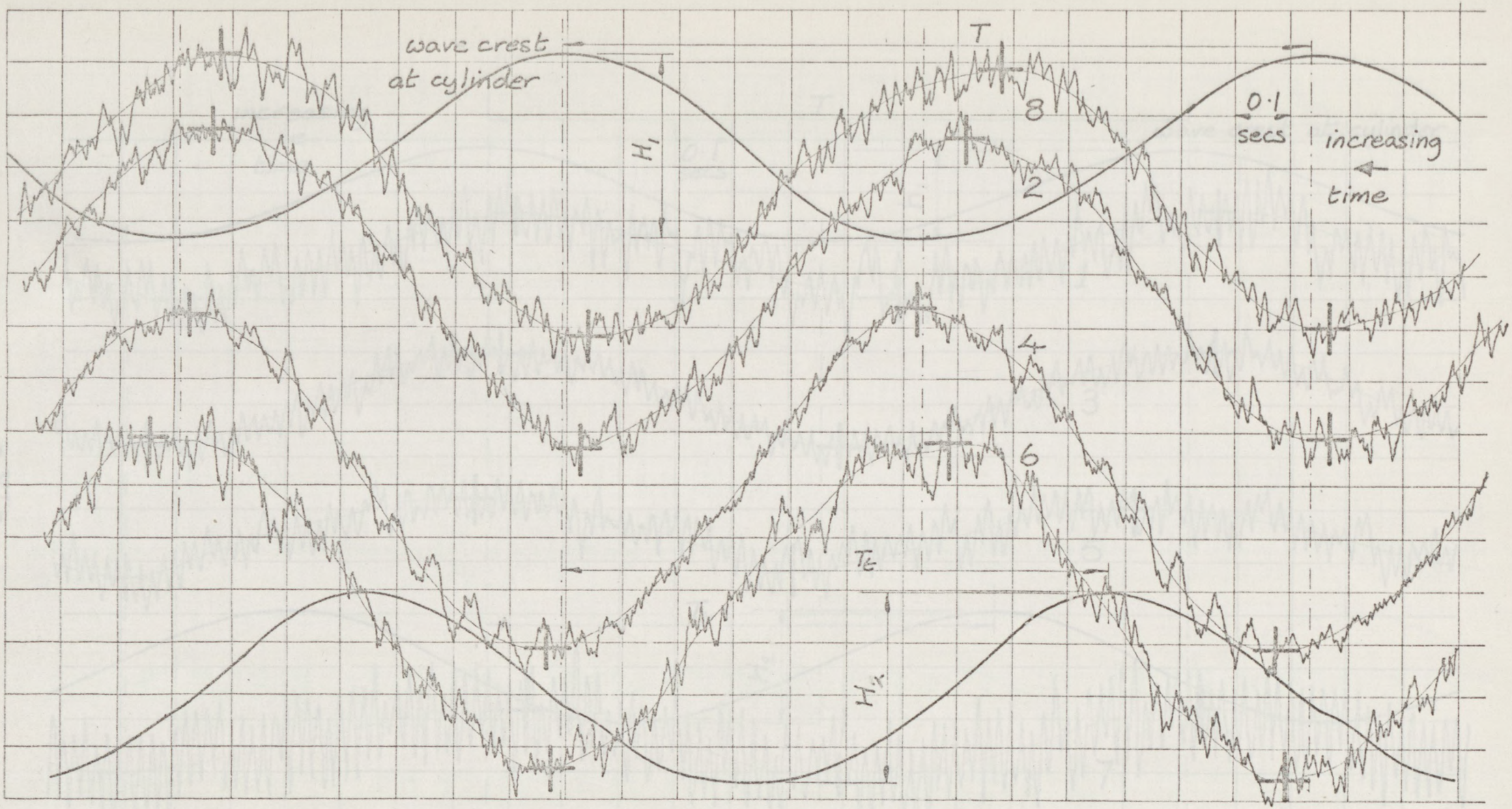

Figure 5·5·7

Measurements on wave number 18a

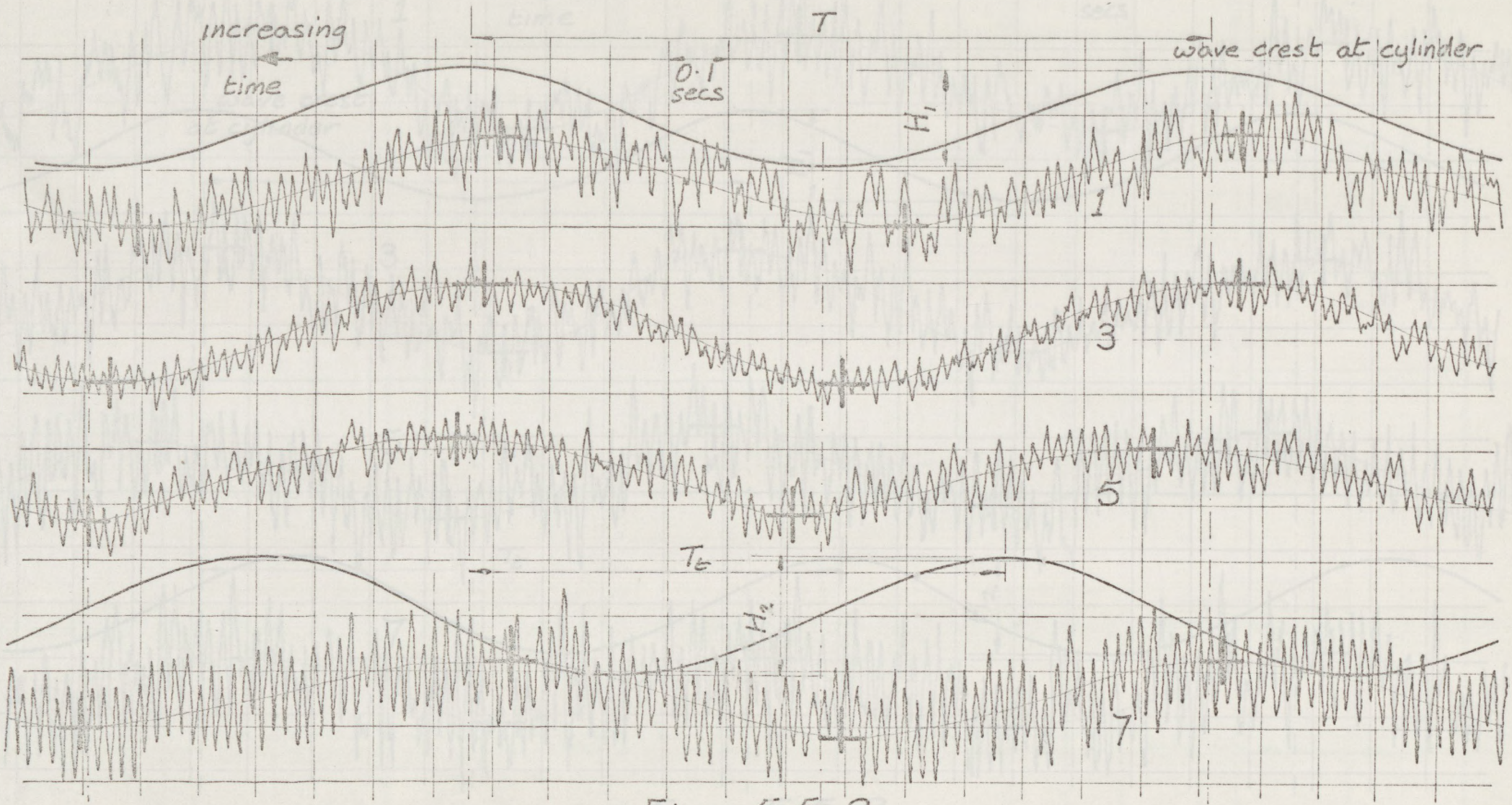

Figure 5·5·8

Meosurements on wave number 30a

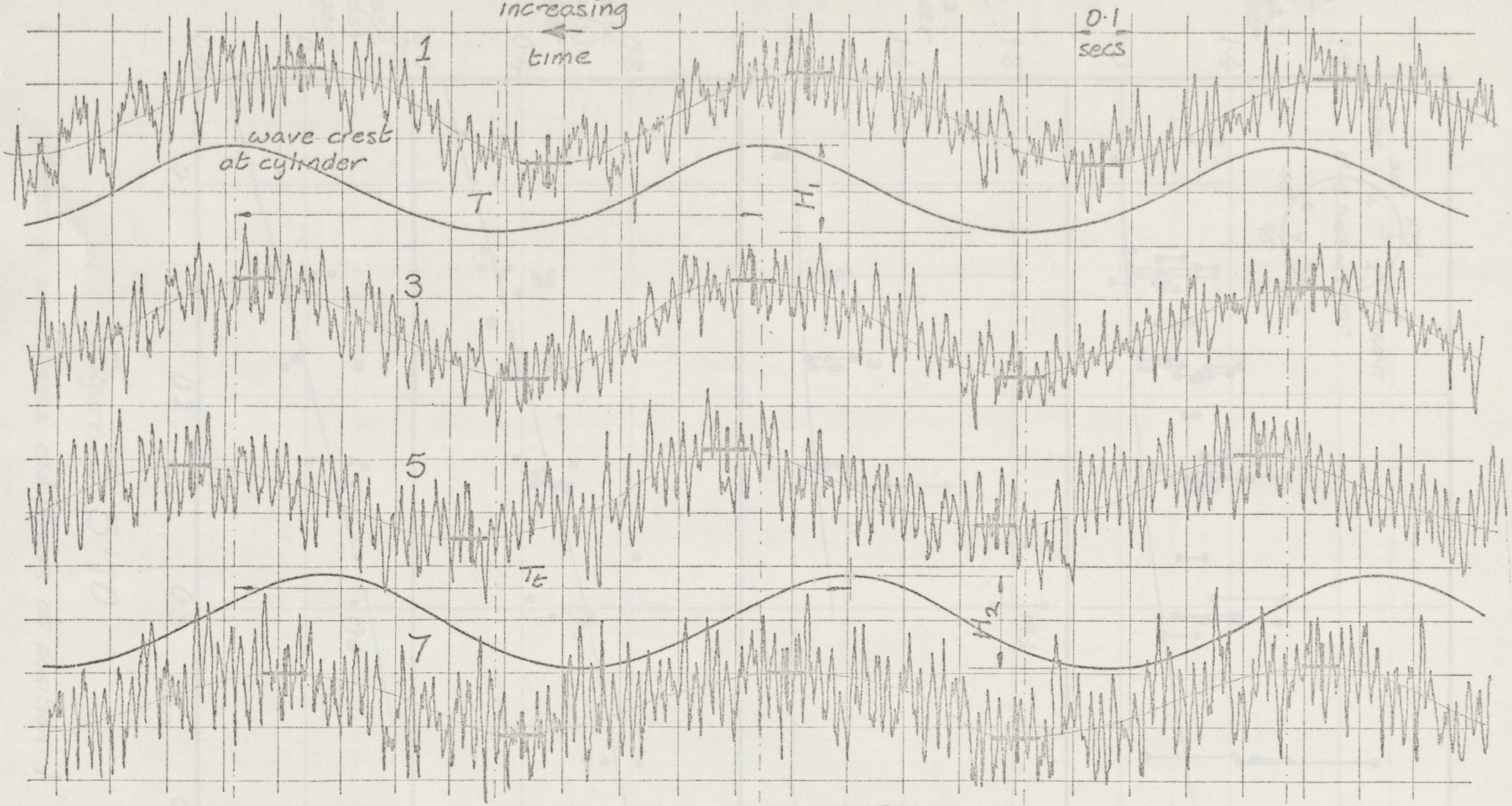

Figure 5·5·9

Measurements on wave number 43a.

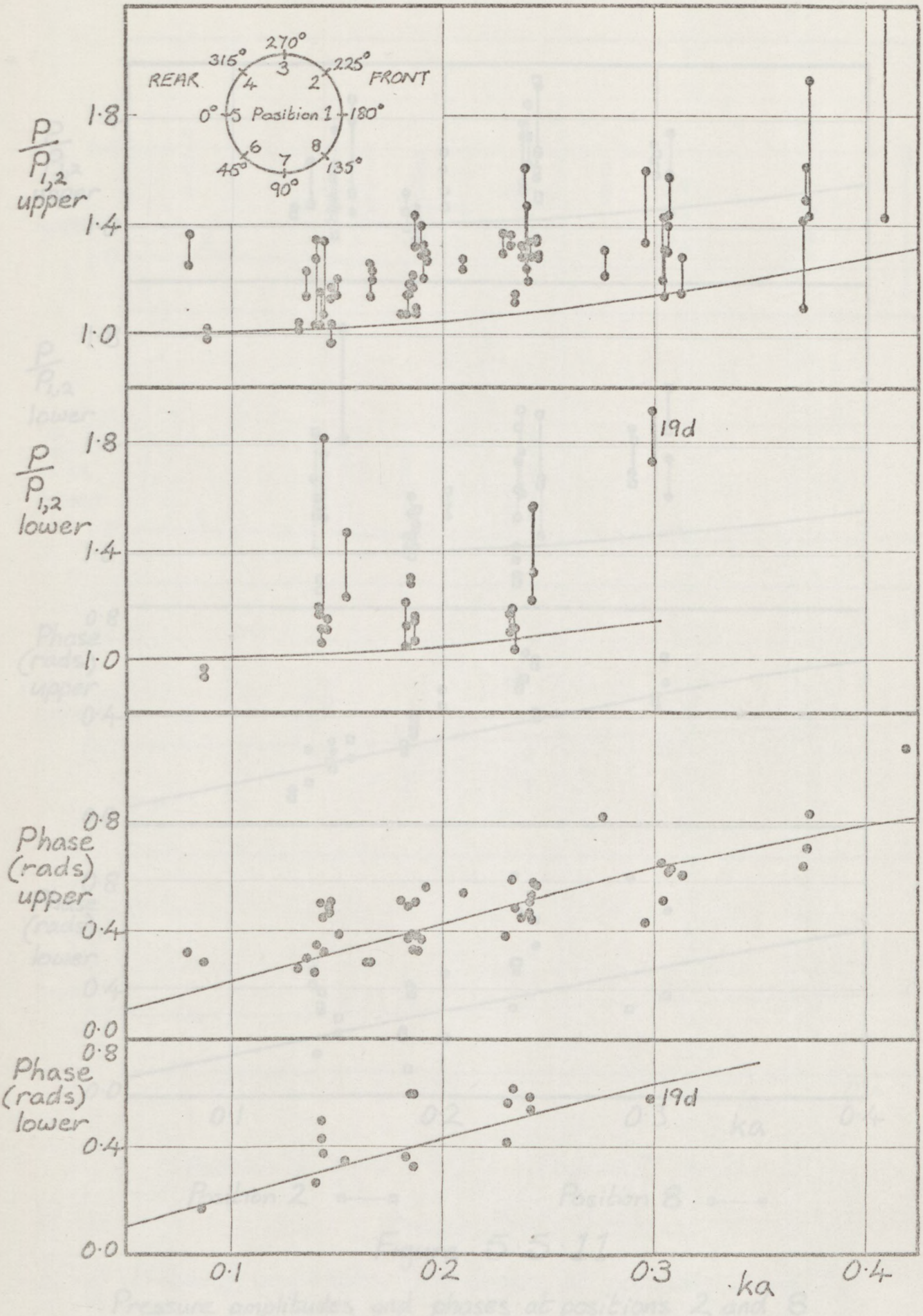

Figure 5·5·10

Pressure amplitudes and phases at position 1

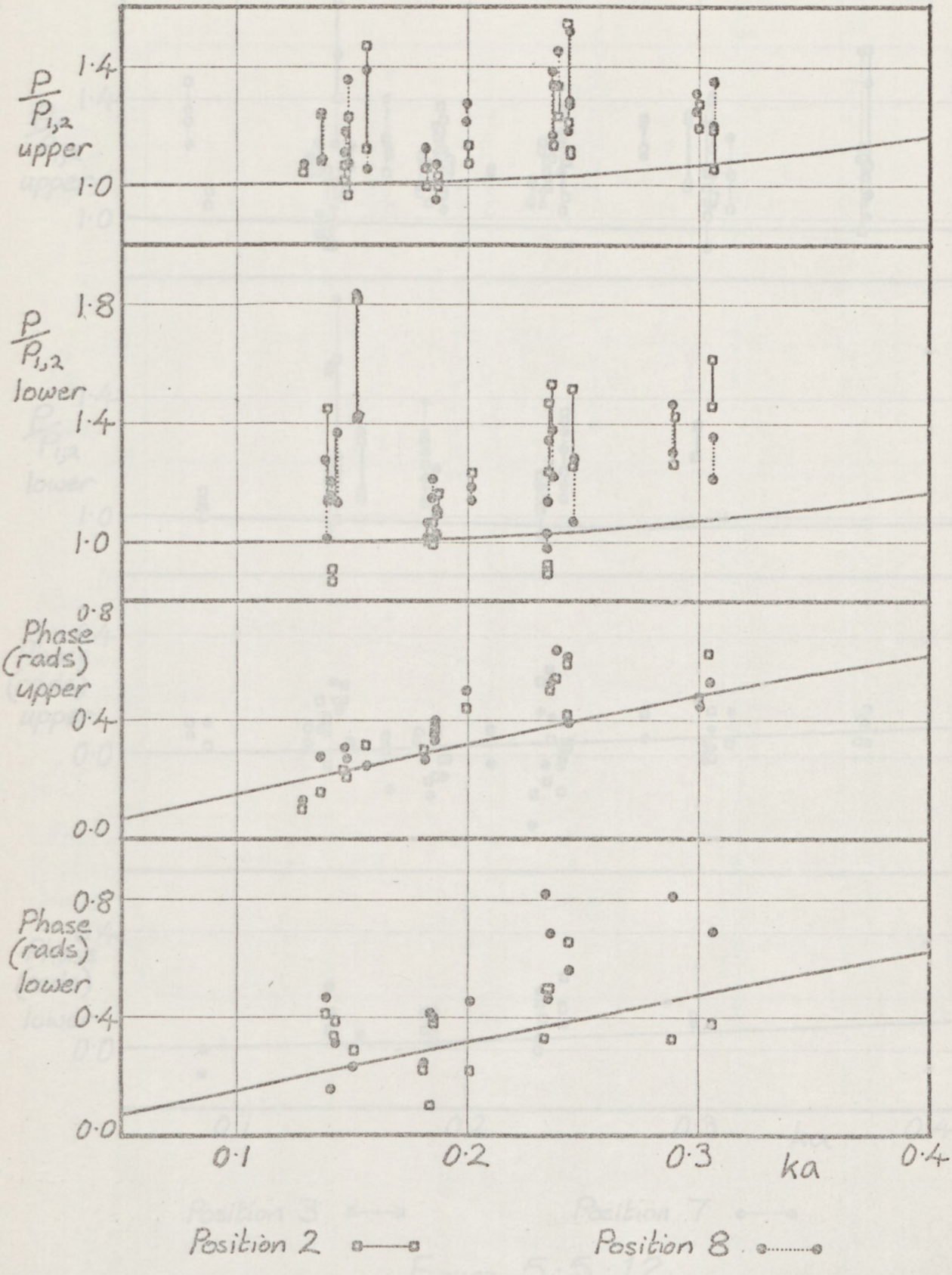

Figure 5·5·11

Pressure amplitudes and phases at positions 2 and 8

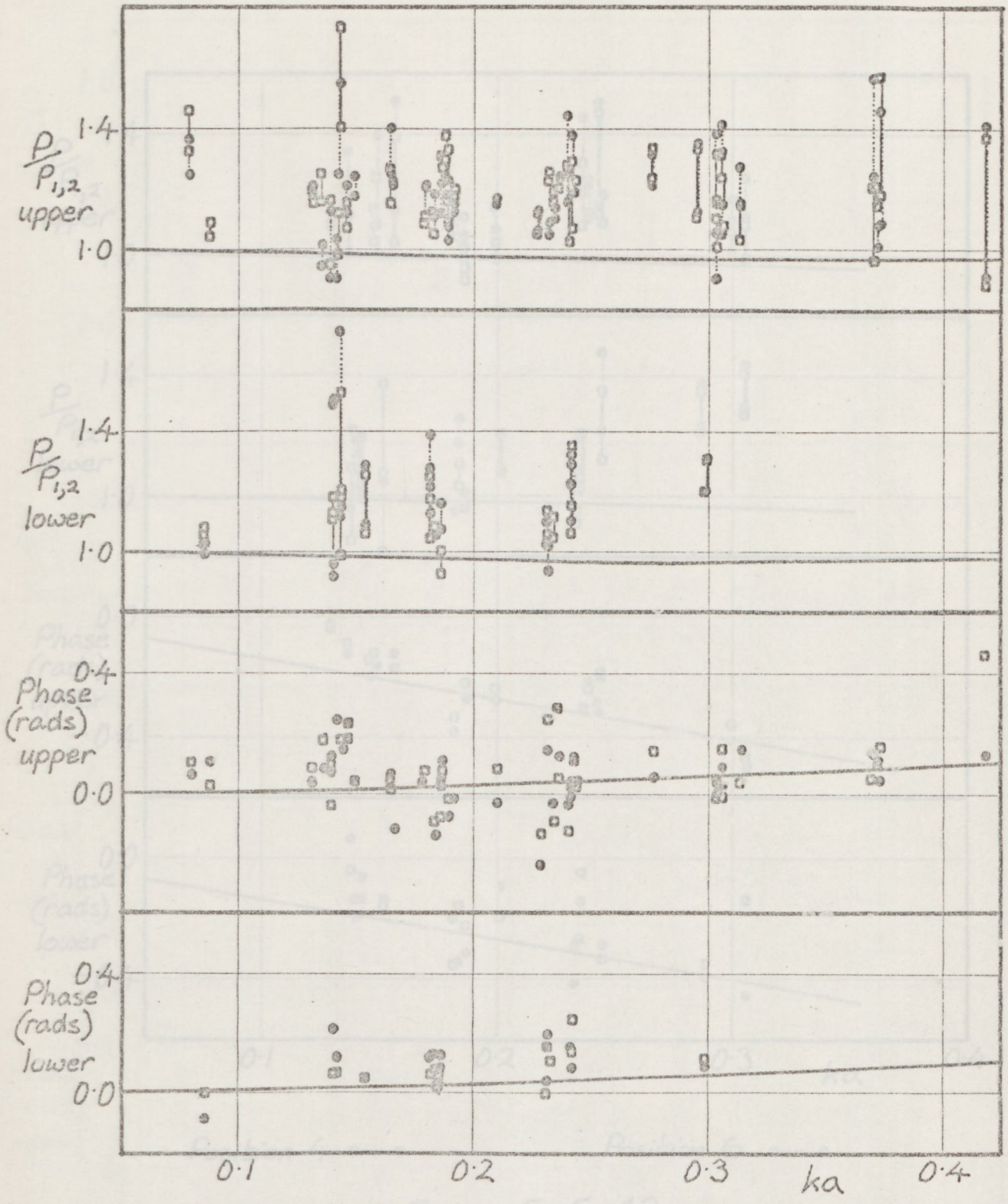

Figure 5·5·12

Pressure amplitudes and phases at positions 3 and 7

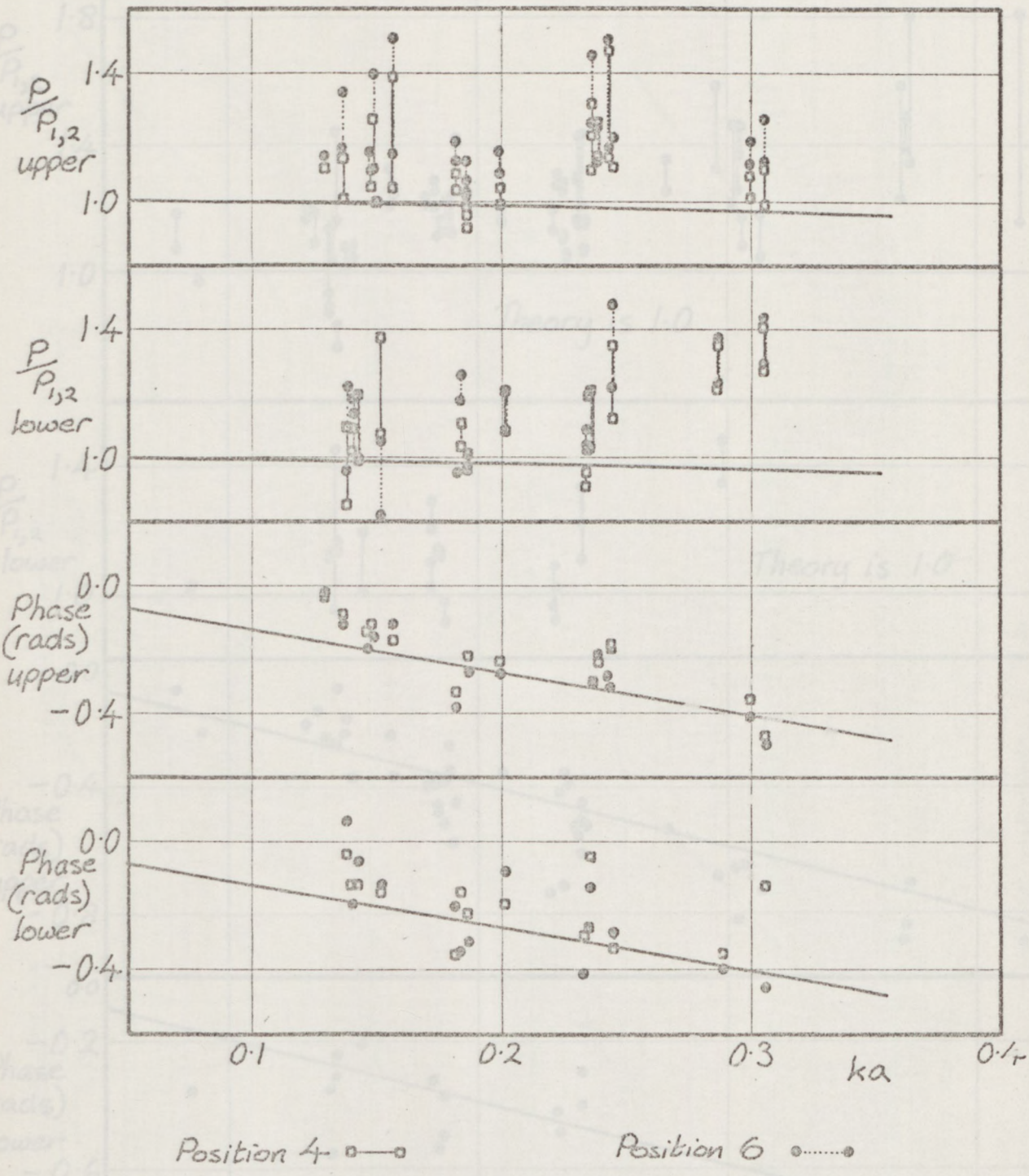

Figure 5·5·13

Pressure amplitudes and phases at positions 4 and 6

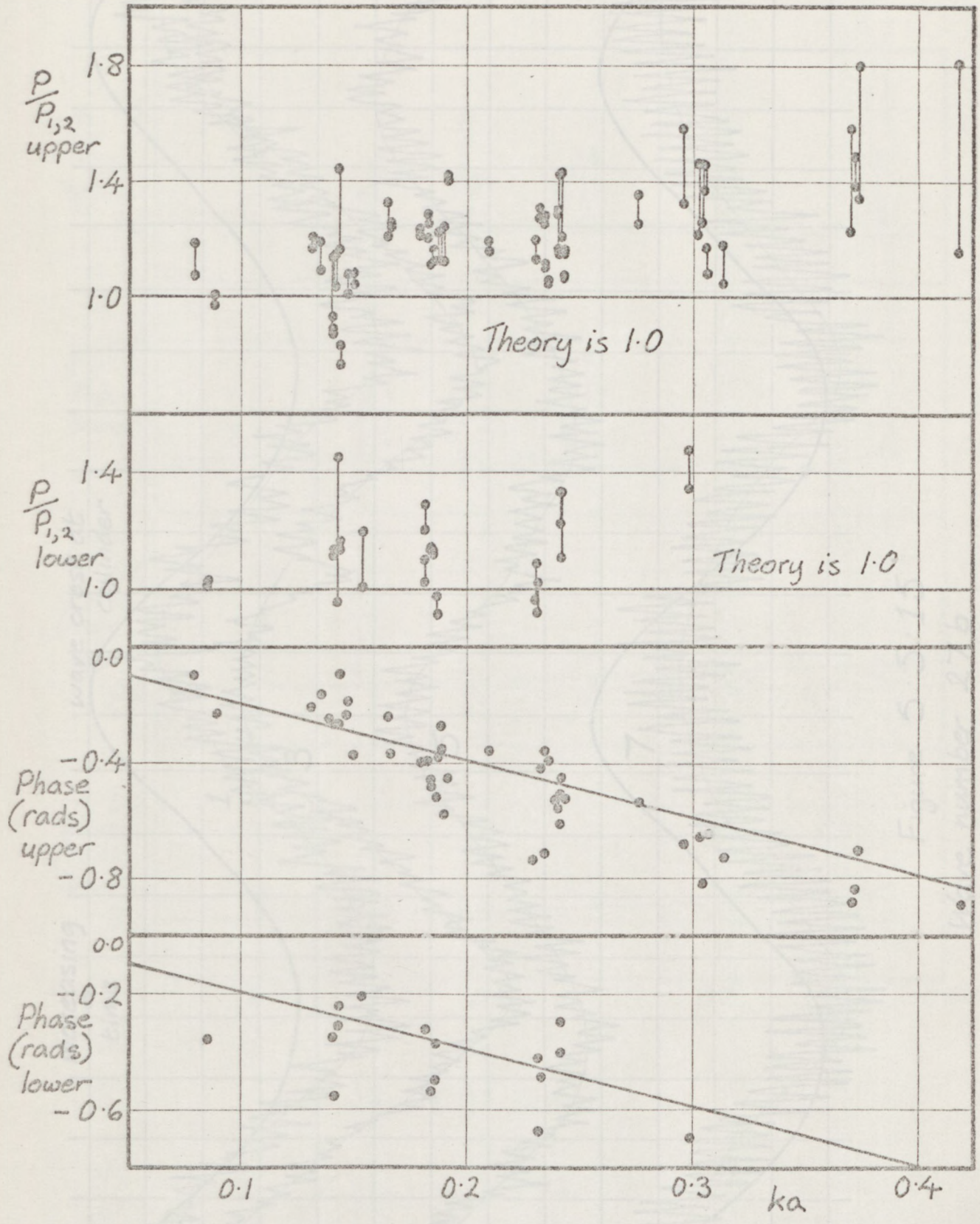

Figure 5·5·14

Pressure amplitudes and phases at position 5

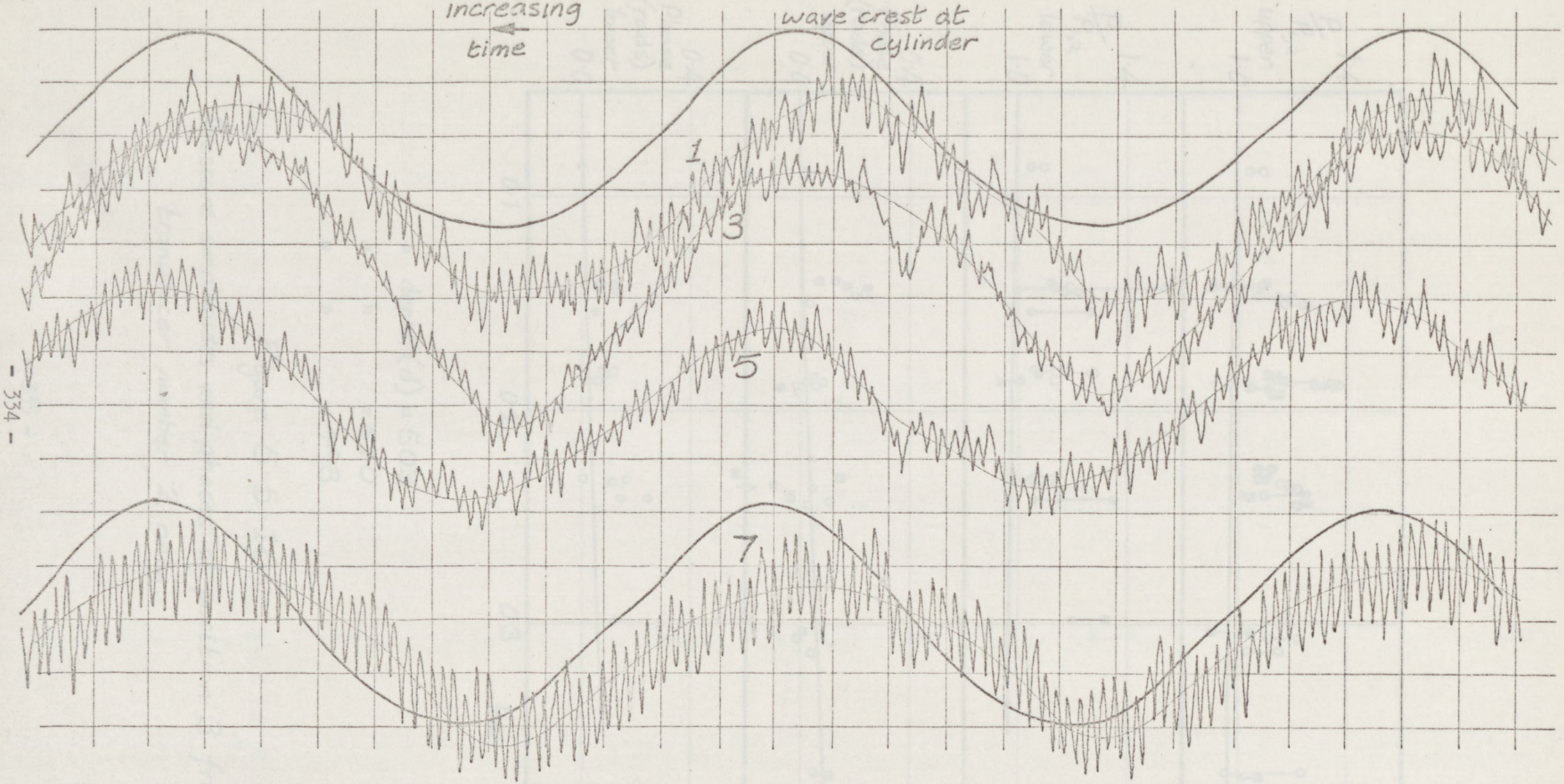

Figure 5·5·15

Wave number 27b

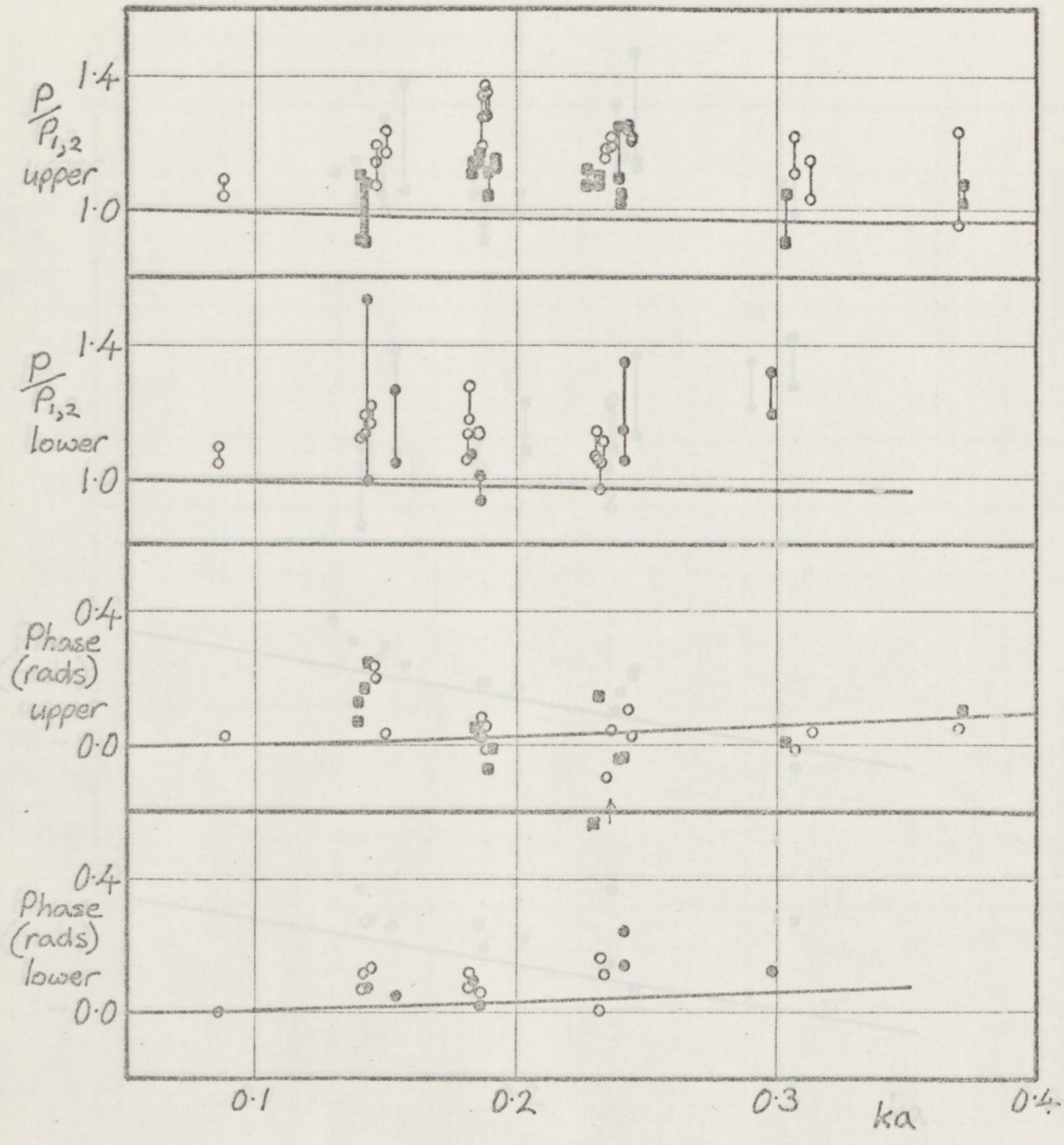

• depth (d) = 503
○ » = 520
◦ » = 493

Figure 5·5·16

Pressure amplitudes and phases at position 3 from transducer number 2 only.

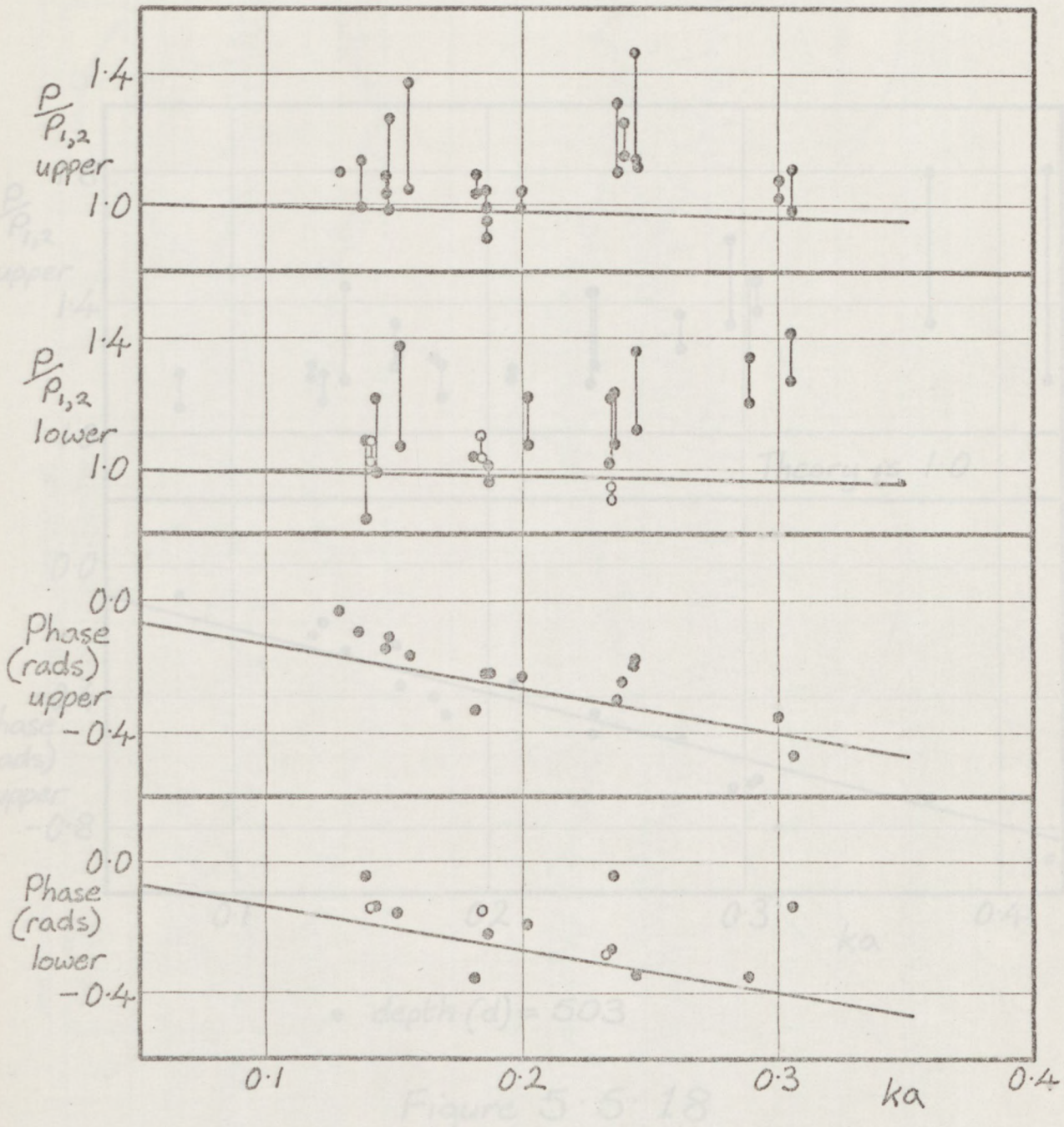

• depth (d) = 503
○ » = 520

Figure 5·5·17

Pressure amplitudes and phases at position 4 from transducer number 2 only

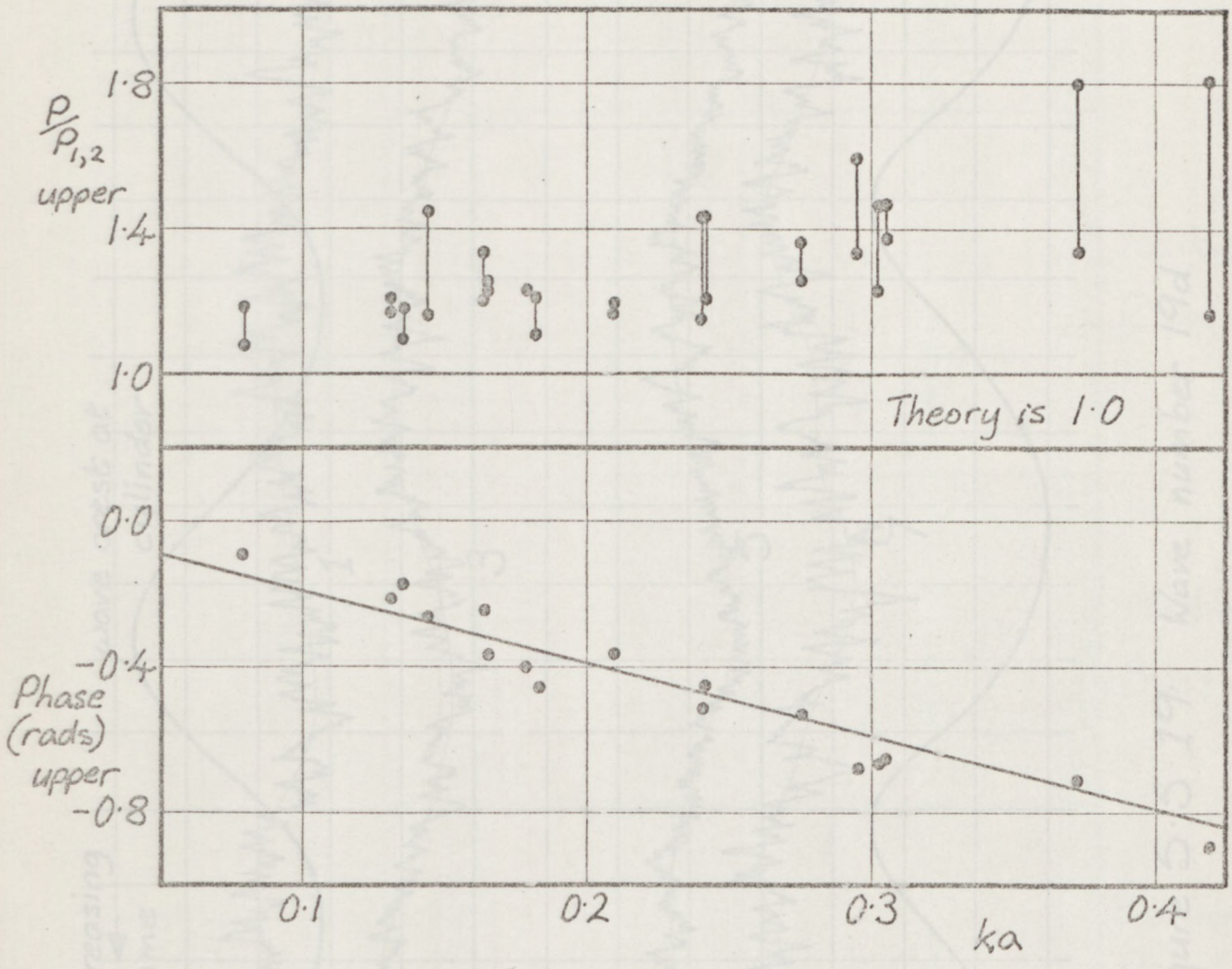

• depth (d) = 503

Figure 5·5·18

Pressure amplitudes and phases at position 5 from transducer number 2 only

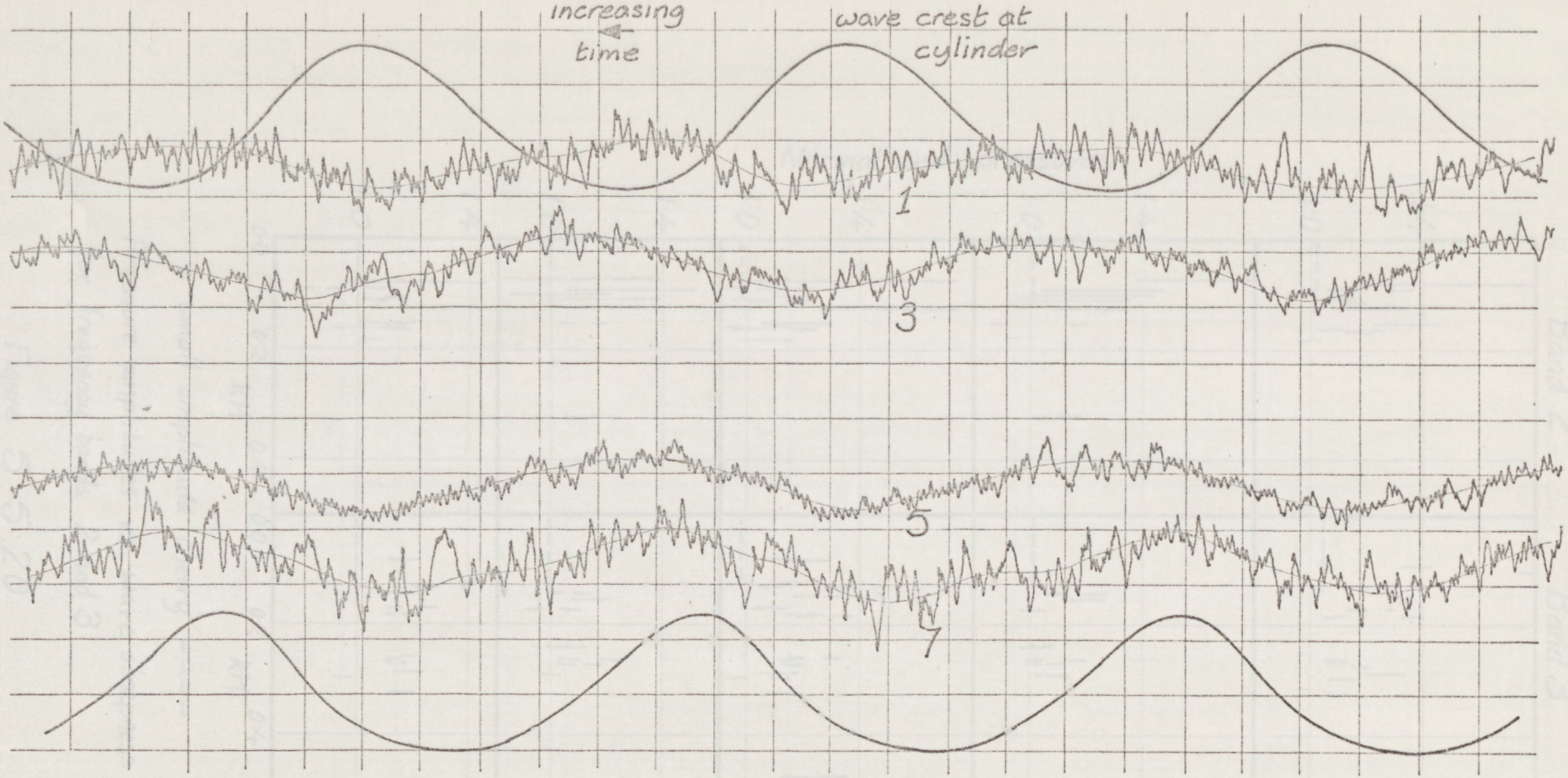

Figure 5·5·19 Wave number 19d

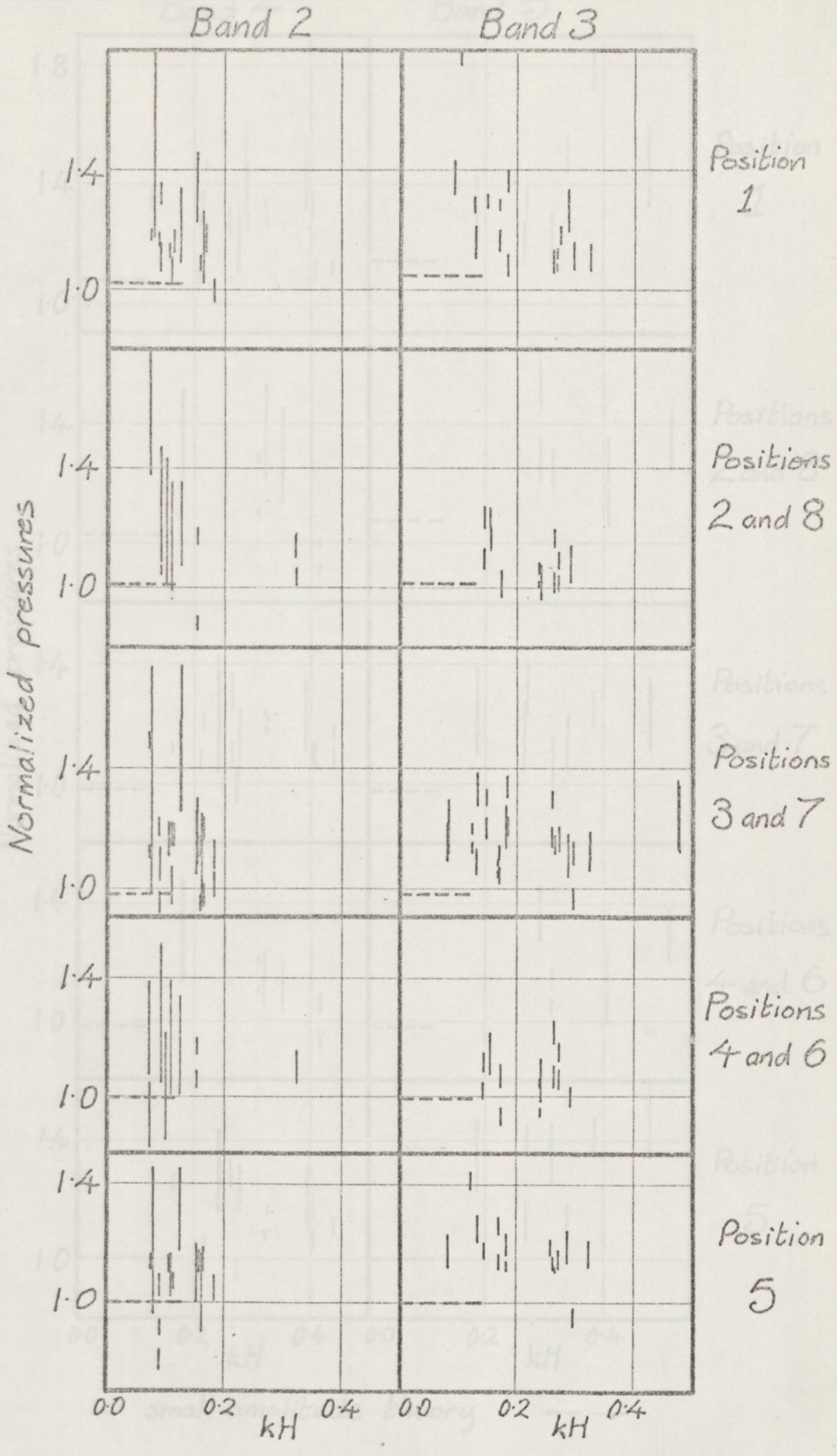

small amplitude theory - - - -

Pressure amplitudes vs. wave steepness for frequency bands 2 and 3

Figure 5·5·20

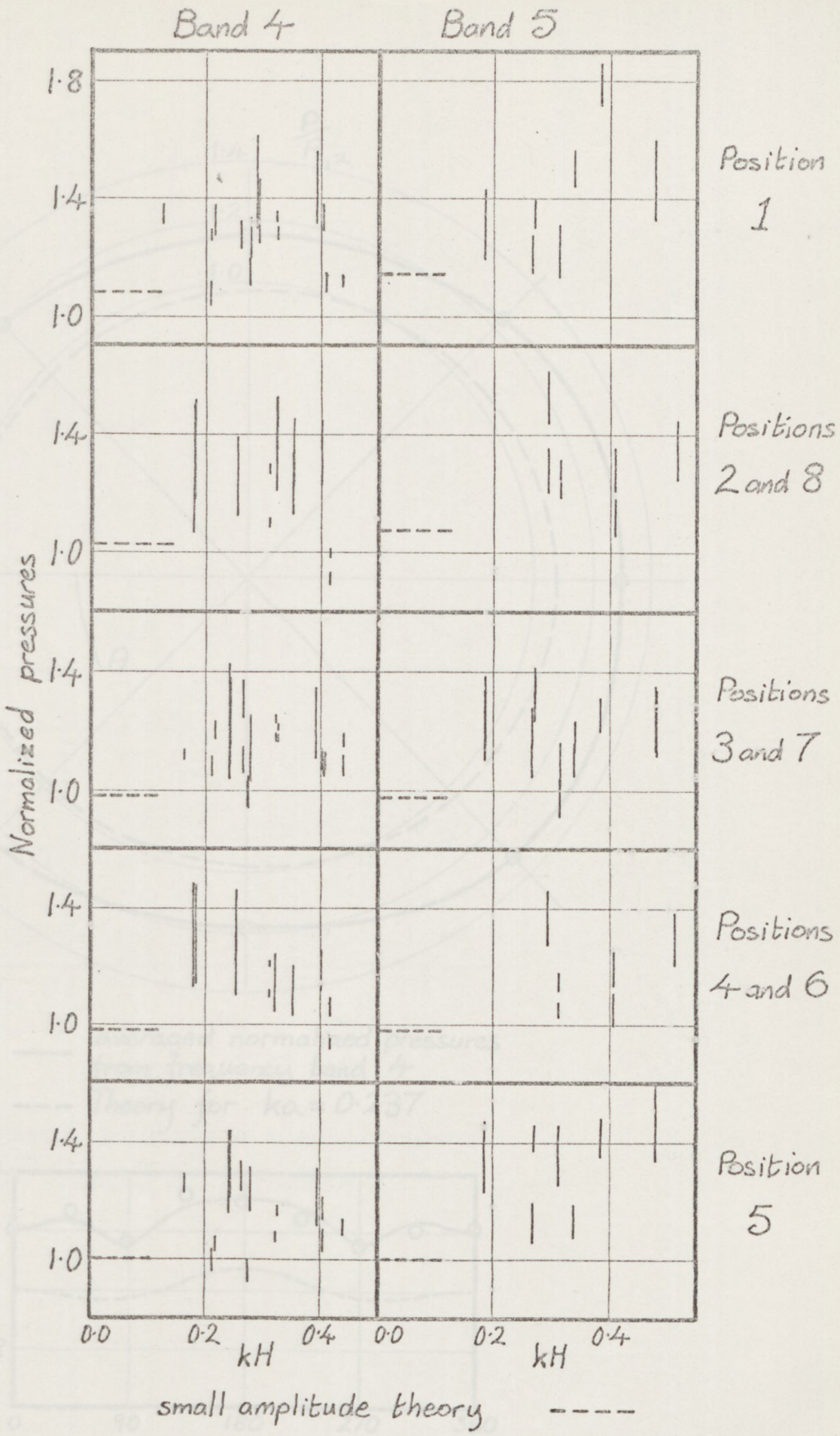

Pressure amplitudes vs. wave steepness for frequency bands 4 and 5

Figure 5·5·21

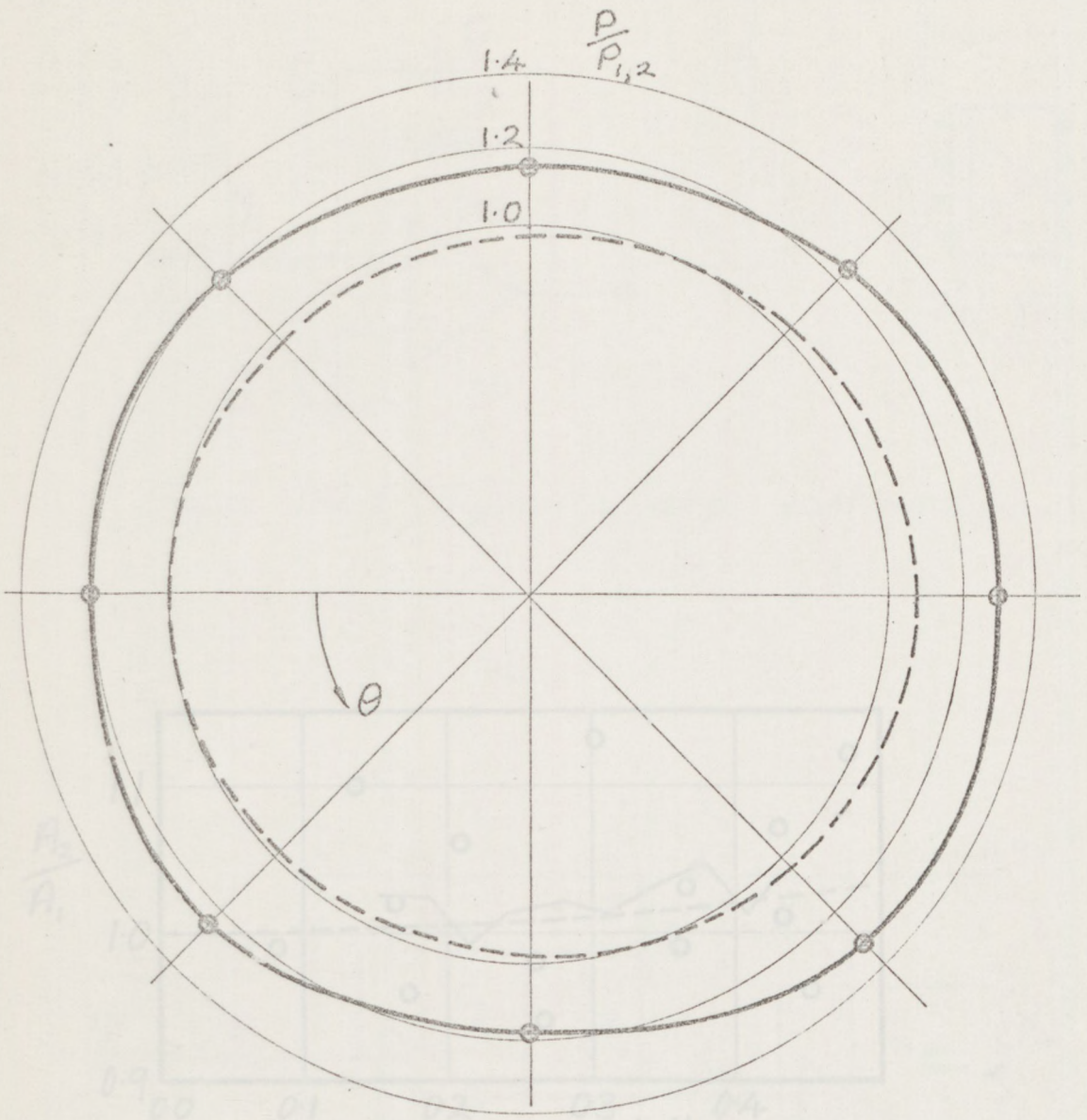

—— averaged normalized pressures from frequency band 4

--- Theory for ka = 0·237

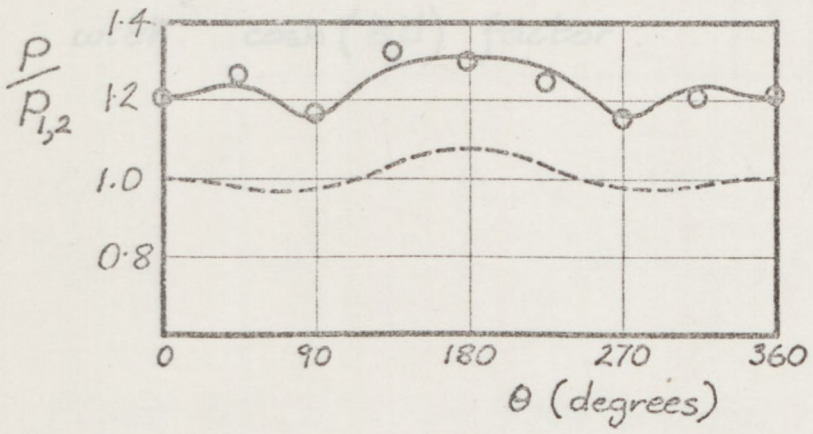

Figure 5·5·22

Angular pressure variation for upper pressure tappings, from frequency band 4.

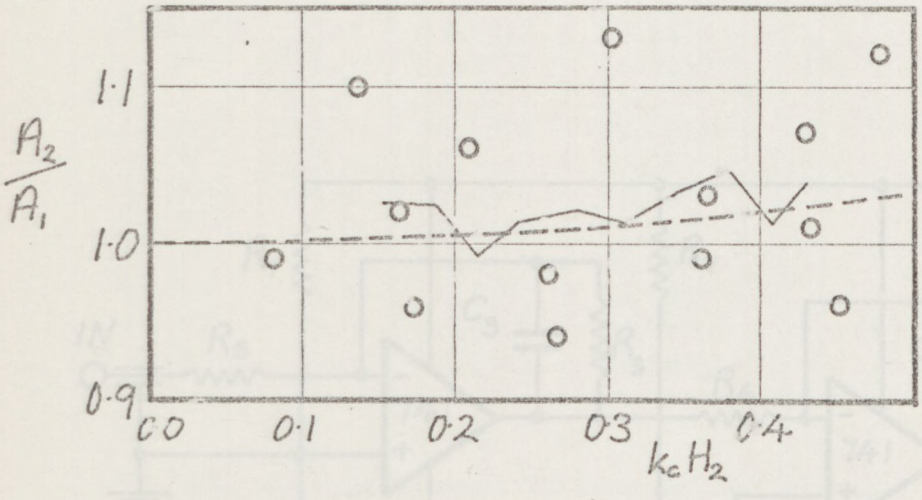

Figure 5·5·23

Averaged pressures in wave compared with $\cosh\left(\frac{kH}{2}\right)$ factor.

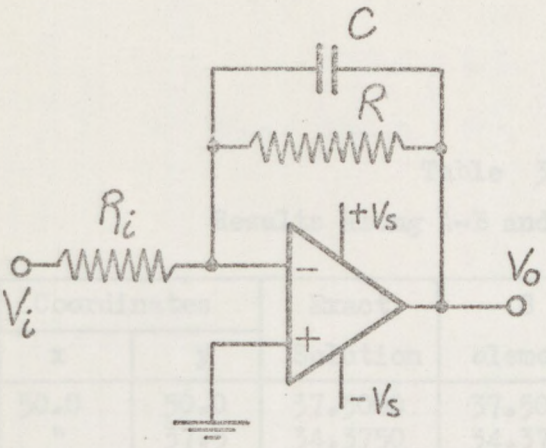

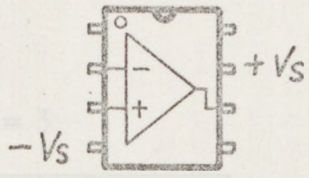

741 Pin-outs.

Figure A·2·1 Typical op.amp. configuration

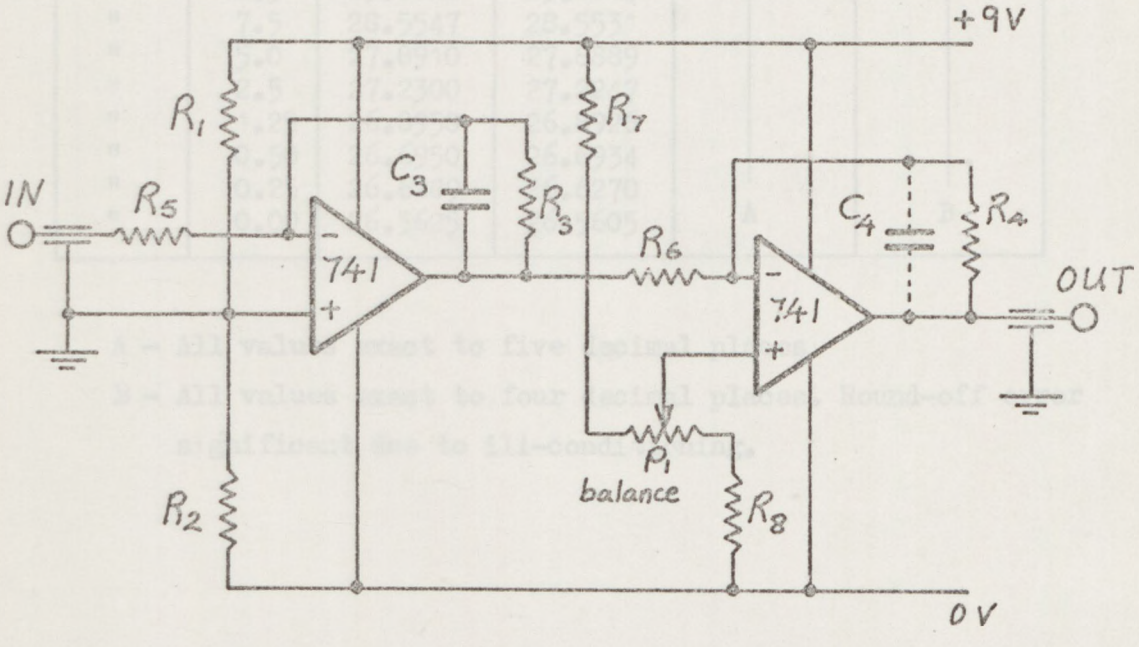

R_1, R_2 - 470K ; R_3, R_4 - 1MΩ ; R_5, R_6 - vary

R_7, R_8 - 1kΩ ; P_1 - 10k ; C_3, C_4 - 0·01μF

Figure A.2.2 Two stage amplifier / filter.

Table 3.5.1

Results along A-B and A'-B' for $\beta = 3$

Coordinates		Exact	8	16	32
x	y	Solution	elements	elements	elements
50.0	50.0	37.5000	37.5000	A	B
"	37.5	34.3750	34.3748		
"	25.0	31.2500	31.2497		
"	12.5	28.1250	28.1247		
"	7.5	26.8750	26.8747		
"	5.0	26.2500	26.2498		
"	2.5	25.6250	25.6249		
"	1.25	25.3125	25.3124		
"	0.50	25.1250	25.1250		
"	0.25	25.0625	25.0625		
46.875	50.0	39.8438	39.8439		
"	37.5	36.5234	36.5230		
"	25.0	33.2031	33.2022		
"	12.5	29.8828	29.8814		
"	7.5	28.5547	28.5531		
"	5.0	27.8910	27.8889		
"	2.5	27.2300	27.2247		
"	1.25	26.8950	26.8926		
"	0.50	26.6950	26.6934		
"	0.25	26.6289	26.6270		
"	0.00	26.5625	26.5605	A	B

A - All values exact to five decimal places

B - All values exact to four decimal places. Round-off error significant due to ill-conditioning.

TABLE 3.5.2.

'L' Shaped domain - ϕ = 1000 x

coordinates		Potential ϕ	
x	y	β = 1.2	β = 3.0
1.0	4.0	1000.0000	1000.0000
1.3	4.0	1305.1305	1300.0040
1.6	4.0	1605.7795	1600.0047
1.8	4.0	1803.5839	1800.0030
1.9	4.0	1901.9039	1900.0017
2.0	4.0	2000.0000	1999.9999
2.0	3.9	1999.9574	1999.9996
2.0	3.8	1999.9507	1999.9995
2.0	3.6	1999.9746	1999.9995
2.0	3.3	2000.0048	1999.9997
2.0	3.0	2000.0000	1999.9999

TABLE 4.7.1. Non dimensional theoretical Force $\frac{h}{a} = 4$

ka	FORCE	ka	FORCE	ka	FORCE
0.05	1.2442	1.05	4.0961	2.05	1.6997
0.10	2.4102	1.10	3.8950	2.10	1.6409
0.15	3.4313	1.15	3.7038	2.15	1.5853
0.20	4.2715	1.20	3.5229	2.20	1.5362
0.25	4.9250	1.25	3.3524	2.25	1.4828
0.30	5.4062	1.30	3.1922	2.30	1.4355
0.35	5.7386	1.35	3.0418	2.35	1.3906
0.40	5.9465	1.40	2.9009	2.40	1.3479
0.45	6.0522	1.45	2.7689	2.45	1.3073
0.50	6.0742	1.50	2.6453	2.50	1.2687
0.55	6.0281	1.55	2.5296	2.55	1.2320
0.60	5.9272	1.60	2.4212	2.60	1.1969
0.65	5.7834	1.65	2.3196	2.65	1.1634
0.70	5.6077	1.70	2.2244	2.70	1.1345
0.75	5.4078	1.75	2.1350	2.75	1.1010
0.80	5.1935	1.80	2.0510	2.80	1.0717
0.85	4.9712	1.85	1.9721	2.85	1.0438
0.90	4.7465	1.90	1.8978	2.90	1.0170
0.95	4.5238	1.95	1.8279	2.95	0.9914
1.00	4.3062	2.00	1.7619	3.00	0.9668

Table 4.7.2a Numerical results

NIH = 4	NIV = 4
ZK = 0.6	ALIM = 10^{-3}

ka	Computed Force	Exact Force
0.052	1.276	1.302
0.105	2.472	2.512
0.209	4.347	4.408
0.251	4.845	4.939
0.273	5.047	5.168
0.299	5.509	5.400
0.314	5.114	5.514
0.331	5.978	5.628
0.349	6.096	5.734
0.370	14.789	5.835
0.393	3.953	5.923
0.419	6.034	5.997
0.449	5.521	6.051
0.483	6.013	6.075
0.524	6.270	6.060
0.571	6.809	5.991
0.628	6.811	5.850
0.661	7.251	5.746
0.698	3.920	5.614
0.739	5.616	5.452
0.785	5.135	5.257
0.838	1.328	5.025
0.898	4.782	4.757
1.047	4.191	4.108
1.257	3.422	3.331
2.094	1.942	1.648
3.142	1.108	0.902

Table 4.7.2b Numerical results

NIH = 2	NIV = 2	ALIM = 10^{-3}	
ka	Exact Force	Computed Forces	
		ZK = 0.3	ZK = 0.6
0.052	1.302	-	1.272
0.105	2.512	2.477	2.454
0.209	4.408	4.345	4.382
0.242	4.828	-	5.213
0.251	4.939	4.879	-
0.273	5.168	-	5.599
0.299	5.400	5.297	-
0.314	5.514	-	6.070
0.349	5.734	6.386	6.295
0.393	5.923	-	6.538
0.419	5.997	6.563	6.575
0.449	6.051	-	6.897
0.465	6.067	-	6.824
0.483	6.075	6.646	6.755
0.503	6.073	-	6.752
0.524	6.060	-	7.178
0.546	6.033	-	6.131
0.571	5.991	6.799	5.957
0.587	5.957	-	5.919
0.598	5.931	-	6.933
0.628	5.850	-	6.903
0.661	5.746	-	6.679
0.698	5.614	5.522	6.388
0.739	5.452	-	6.122
0.785	5.257	-	5.237
0.898	4.757	4.690	4.692
0.967	4.451	-	4.374
1.047	4.108	-	4.084
1.257	3.331	3.239	3.322
1.571	2.484	2.395	2.395
1.795	2.059	-	2.025
2.094	1.648	1.743	1.741
2.513	1.259	-	1.626
3.142	0.902	1.725	1.714

Table 4.7.2c Numerical results

NIH = 2		NIV = 2	ALIM = 10^{-7}		
ka = 0.571			ZK = 0.6		
ZK	Computed Force	F_{C/F_E}	ka	Computed Force	Exact Force
0.1	5.864	0.979	0.209	4.047	4.408
0.2	5.818	0.971	0.251	4.531	4.939
0.3	5.751	0.960	0.299	4.950	5.400
0.4	5.667	0.946	0.349	5.240	5.734
0.5	5.579	0.931	0.419	5.490	5.997
0.6	5.543	0.925	0.483	5.580	6.075
0.7	5.647	0.943	0.571	5.543	5.991
0.8	6.169	1.030	0.698	5.264	5.614
0.9	8.168	1.363	0.898	4.551	4.757
0.95	11.093	1.852	1.257	3.221	3.331

Table 4.7.2d
Numerical results

NIH = 4 ZK = 0.3	NIV = 3 ALIM = 10^{-5}	
ka	Computed Force	Exact Force
0.209	4.537	4.408
0.273	5.269	5.168
0.419	6.092	5.997
0.628	5.936	5.850
0.898	4.884	4.757
1.257	3.522	3.331

Table 4.7.2e Numerical results

NIH = 2	NIV = 2		ALIM = 10^{-3}	
ZK	ka = 0.785 Exact Force = 5.257		ka = 0.571 Exact Force = 5.991	
	Computed Force	F_{C/F_E}	Computed Force	F_{C/F_E}
0.1	5.203	0.990	9.304	1.553
0.2	5.186	0.986	7.051	1.177
0.3	5.237	0.996	6.799	1.135
0.4	5.157	0.981	6.691	1.117
0.5	5.168	0.983	6.625	1.106
0.6	5.237	0.996	5.957	0.994
0.7	5.345	1.017	6.308	1.053
0.8	5.765	1.097	7.113	1.187
0.9	7.296	1.388	9.952	1.661
0.95	7.452	1.418	13.494	2.252

Table 4.7.2f Numerical results

ka	0.571			
NIH	4			
NIV ALIM	3 10^{-5}		4 10^{-4}	
ZK	Computed Force	F_{C/F_E}	Computed Force	F_{C/F_E}
0.1	6.088	1.016	-	-
0.3	6.099	1.018	6.040	1.008
0.5	6.007	1.003	-	-
0.6	-	-	6.010	1.003
0.7	5.663	0.945	-	-
0.9	5.488	0.916	-	-

y/h	θ Degrees	Normalised pressures $p/\frac{1}{2}\rho gH$			
		Computed		Theoretical	
		Real	Imaginary	Real	Imaginary
0.00	0	0.814	-0.473	0.899	-0.405
	90	-0.182	-0.968	-0.168	-0.978
	180	-1.182	-0.834	-1.241	-0.894
-0.25	0	0.464	-0.276	0.519	-0.234
	90	-0.105	-0.557	-0.097	-0.564
	180	-0.677	-0.483	-0.716	-0.516
-0.50	0	0.281	-0.165	0.313	-0.141
	90	-0.063	-0.336	-0.058	-0.340
	180	-0.409	-0.290	-0.432	-0.311
-0.75	0	0.189	-0.112	0.211	-0.095
	90	-0.043	-0.227	-0.040	-0.230
	180	-0.276	-0.197	-0.292	-0.210
-1.00	0	0.163	-0.096	0.181	-0.082
	90	-0.037	-0.195	-0.034	-0.197
	180	-0.237	-0.168	-0.250	-0.180

	Average errors %
10.0	17.2
8.3	1.1
5.1	6.6

ZK = 0.5 ALIM = 10^{-7}

NIH = 2 NIV = 2

Total computed force = 5.579

Total theoretical force = 5.991

Error = 6.9 %

Table 4.7.3

Computed pressures on circular cylinder 1

y/h	θ Degrees	Normalised pressures $p/\frac{1}{2}\rho gH$			
		Computed		Theoretical	
		Real	Imaginary	Real	Imaginary
0.00	0	0.888	-0.419	0.899	-0.405
	45	0.600	-0.646	0.609	-0.640
	90	-0.168	-0.975	-0.168	-0.978
	135	-0.938	-0.979	-0.947	-0.984
	180	-1.229	-0.890	-1.241	-0.894
-0.16	0	0.614	-0.289	0.621	-0.280
	45	0.415	-0.446	0.421	-0.442
	90	-0.116	-0.674	-0.116	-0.676
	135	-0.649	-0.676	-0.655	-0.680
	180	-0.850	-0.614	-0.858	-0.618
-0.33	0	0.432	-0.202	0.435	-0.196
	45	0.292	-0.312	0.295	-0.310
	90	-0.081	-0.472	-0.081	-0.473
	135	-0.456	-0.474	-0.459	-0.477
	180	-0.597	-0.431	-0.601	-0.433
-0.50	0	0.310	-0.144	0.313	-0.141
	45	0.210	-0.224	0.212	-0.223
	90	-0.058	-0.340	-0.058	-0.340
	135	-0.328	-0.340	-0.330	-0.343
	180	-0.429	-0.309	-0.432	-0.311
-0.66	0	0.235	-0.109	0.236	-0.107
	45	0.159	-0.169	0.160	-0.168
	90	-0.044	-0.256	-0.044	-0.257
	135	-0.248	-0.257	-0.249	-0.259
	180	-0.325	-0.233	-0.326	-0.235
-0.83	0	0.194	-0.090	0.194	-0.088
	45	0.131	-0.139	0.132	-0.138
	90	-0.036	-0.211	-0.036	-0.212
	135	-0.204	-0.212	-0.205	-0.213
	180	-0.267	-0.192	-0.268	-0.193
-1.00	0	0.181	-0.084	0.181	-0.082
	45	0.122	-0.130	0.123	-0.129
	90	-0.034	-0.196	-0.034	-0.197
	135	-0.190	-0.197	-0.191	-0.198
	180	-0.249	-0.179	-0.250	-0.180

ZK = 0.5 ALIM = 10^{-5}
NIH = 4 NIV = 3

Computed force = 6.007
Theoretical force = 5.991
Error = 0.27 %

Average errors %	
0.9	2.9
1.2	0.8
0.0	0.3
0.8	0.6
0.8	0.6

Table 4.7.4 Computed pressures on cylinder 2

Table 4.7.5 Comparitive computation times

Number of Elements	Number of Nodes	Number of operations with 9 Gauss pts.	Number of operations with 4 Gauss pts.	Number of operations using facet method
4	20	720	320	400
12	56	6048	2688	3136
16	72	10368	4608	5184

Measured data					Calculated results							
Generator amplitude a (mms)	Period T(secs)	Time of travel T_t(secs)	Wave height H(mms)	Pressure amplitude A_2(mm H_2O)	Frequency parameter $\sigma^2 d/g$	Celerity C_2 (m/s)	Ratio C_2/C_1	Ratio $H/2a$	Wave steepness k_2H	Calculated pressure A_1(mm H_2O)	Ratio A_2/A_1	Error in mm H_2O
50	1.16	1.12	53.7	17.3	1.57	1.66	0.99	0.54	0.175	18.6	0.96	-0.8
	1.03	1.21	67.5	20.0	1.99	1.54	0.99	0.68	0.269	21.2	0.94	-1.2
	0.93	1.31	75.9	21.1	2.42	1.42	0.99	0.76	0.361	21.4	0.99	-0.3
	0.85	1.36	80.5	21.1	2.91	1.37	1.04	0.81	0.433	20.8	1.01	0.3
	0.82	1.42	81.4	22.2	3.15	1.31	1.03	0.81	0.479	19.8	1.12	2.4
80	1.36	1.02	64.8	25.5	1.14	1.82	0.99	0.40	0.165	25.0	1.02	0.5
	1.19	1.11	83.3	28.9	1.48	1.68	0.98	0.52	0.261	29.4	0.98	-0.5
	1.07	1.15	99.9	33.9	1.85	1.61	1.01	0.62	0.365	32.8	1.03	1.1
	0.99	1.21	109.2	32.2	2.15	1.54	1.02	0.68	0.451	33.5	0.96	-1.3
30	1.23	1.07	27.8	10.0	1.39	1.74	1.00	0.46	0.081	10.1	0.99	-0.1
	1.07	1.16	37.0	13.3	1.85	1.60	1.00	0.62	0.136	12.1	1.10	1.2
	0.93	1.31	44.4	13.3	2.42	1.42	0.99	0.74	0.210	12.5	1.06	0.8
	0.82	1.47	50.0	13.3	3.15	1.27	1.00	0.83	0.302	11.8	1.13	1.5
	0.73	1.62	57.4	12.2	3.94	1.15	1.01	0.96	0.430	11.4	1.07	0.8

Table 5.3.1

Table 5.5.1a Experimental results

RUN No.	d* (mm)	$k_C a$	$k_C H_2$	cosh kh / cosh kd	Position/ Transducer	Amplitude* (mm H_2O)	Phase* (rads)	P/P_2	P/P_1
2a	503	0.242	0.291	0.538	1U / 4	24.0	0.53	1.47	1.24
					3U / 3	21.0	0.05	1.29	1.08
					5U / 2	23.5	-0.45	1.44	1.21
					7U / 1	23.0	0.02	1.38	1.16
2b	503	0.241	0.289	0.541	1U / 4	26.3	0.51	1.61	1.30
					3U / 3	21.0	-0.12	1.28	1.03
					5U / 2	23.4	-0.51	1.43	1.15
					7U / 1	23.6	-0.02	1.44	1.16
3a	503	0.080	0.054	0.881	1U / 4	20.3	0.32	1.37	1.25
					3U / 3	21.7	0.11	1.47	1.33
					5U / 2	17.6	-0.10	1.19	1.08
					7U / 1	20.3	0.07	1.37	1.25
3b	503	0.136	0.166	0.745	1U / 4	28.1	0.30	1.22	1.13
					3U / 3	28.7	0.18	1.25	1.16
					5U / 2	27.3	-0.17	1.19	1.10
					7U / 1	23.4	0.08	1.02	0.94
3c	503	0.166	0.252	0.677	1U / 4	31.5	0.28	1.22	1.20
					3U / 3	31.5	0.05	1.22	1.20
					5U / 2	32.5	-0.37	1.26	1.24
					7U / 1	32.5	-0.11	1.26	1.24
3d	503	0.183	0.326	0.643	1U / 4	33.0	0.49	1.07	1.15
					3U / 3	32.6	-0.09	1.06	1.14
					5U / 2	34.5	-0.46	1.12	1.21
					7U / 1	34.1	-0.13	1.10	1.19
4a	503	0.132	0.240	0.754	1U / 4	36.0	0.26	1.04	1.01
					3U / 3	41.3	0.09	1.18	1.15
					5U / 2	41.6	-0.21	1.21	1.18
					7U / 1	41.8	0.04	1.21	1.18
5a	503	0.144	0.123	0.726	1U / 4	21.0	0.32	1.34	1.08
					3U / 3	27.3	0.20	1.74	1.40
					5U / 2	22.7	-0.26	1.45	1.17
					7U / 1	24.3	0.16	1.55	1.25
5b	503	0.165	0.202	0.679	1U / 4	26.3	0.28	1.25	1.13
					3U / 3	26.6	0.01	1.27	1.15
					5U / 2	28.0	-0.24	1.33	1.21
					7U / 1	29.4	0.06	1.40	1.27
5c	503	0.179	0.269	0.650	1U / 4	26.3	0.51	1.07	1.08
					3U / 3	27.3	0.08	1.11	1.12
					5U / 2	29.9	-0.40	1.22	1.23
					7U / 1	29.7	0.04	1.21	1.22
6a	503	0.296	0.479	0.462	1U / 4	30.0	0.43	1.60	1.33
					3U / 3	25.2	—	1.34	1.12
					5U / 2	29.9	-0.68	1.59	1.33
					7U / 1	25.6	—	1.36	1.14
7c	503	0.276	0.264	0.489	1U / 4	15.4	0.82	1.31	1.21
					3U / 3	15.8	0.15	1.34	1.24
					5U / 2	16.0	-0.53	1.36	1.26
					7U / 1	15.5	0.06	1.31	1.22

Table 5.5.1b Experimental results

RUN No.	d* (mm)	$k_C a$	$k_C H_2$	cosh kh cosh kd	Position/ Transducer	Amplitude* (mm H_2O)	Phase* (rads)	P/P_2	P/P_1
7d	503	0.306	0.270	0.450	1U / 4	13.9	0.61	1.39	1.30
					3U / 3	13.3	0.15	1.33	1.24
					5U / 2	14.6	-0.65	1.46	1.37
					7U / 1	14.2	0.03	1.42	1.33
10a	503	0.303	0.182	0.453	1U / 4	9.8	0.65	1.43	1.19
					3U / 3	9.1	0.05	1.33	1.10
					5U / 2	10.1	-0.66	1.47	1.22
					7U / 1	9.5	0.04	1.39	1.15
10b	503	0.373	0.238	0.375	1U / 4	11.6	0.83	1.93	1.44
					3U / 3	9.5	0.16	1.58	1.18
					5U / 2	10.8	-0.71	1.80	1.34
					7U / 1	8.8	0.04	1.46	1.09
10c	503	0.419	0.228	0.332	1U / 4	10.0	1.07	2.20	1.42
					3U / 3	6.2	0.46	1.37	0.88
					5U / 2	8.2	-0.89	1.81	1.16
					7U / 1	6.4	0.13	1.41	0.91
11a	503	0.210	0.393	0.592	1U / 4	35.3	0.54	1.27	1.23
					3U / 3	32.7	0.09	1.17	1.14
					5U / 2	33.4	-0.36	1.20	1.17
					7U / 1	32.6	-0.03	1.17	1.14
13a	503	0.148	0.107	0.715	8U / 4	17.7	0.27	1.36	1.07
					2U / 3	15.9	0.21	1.22	0.96
					4U / 2	16.4	-0.11	1.26	0.99
					6U / 1	18.2	-0.15	1.40	1.10
13b	503	0.186	0.240	0.636	8U / 4	21.1	0.34	1.02	0.96
					2U / 3	22.5	0.35	1.09	1.02
					4U / 2	21.7	-0.22	1.05	0.98
					6U / 1	23.4	-0.27	1.13	1.06
13c	503	0.244	0.311	0.536	8U / 4	21.9	0.61	1.27	1.28
					2U / 3	19.0	0.60	1.10	1.11
					4U / 2	19.2	-0.18	1.11	1.12
					6U / 1	20.8	-0.32	1.20	1.21
14a	503	0.156	0.091	0.692	8U / 4	14.3	0.25	1.39	1.05
					2U / 3	15.2	0.32	1.47	1.12
					4U / 2	14.2	-0.17	1.38	1.04
					6U / 1	15.6	-0.11	1.51	1.15
14b	503	0.187	0.176	0.634	8U / 4	15.1	0.40	1.01	1.07
					2U / 3	14.6	0.36	0.97	1.04
					4U / 2	13.6	-0.22	0.91	0.96
					6U / 1	15.6	-0.27	1.04	1.11
14c	503	0.237	0.254	0.546	8U / 4	20.4	0.53	1.39	1.17
					2U / 3	19.7	0.50	1.34	1.13
					4U / 2	19.2	-0.30	1.31	1.10
					6U / 1	21.4	-0.30	1.46	1.23
14d	503	0.306	0.407	0.450	8U / 4	18.1	0.52	1.20	1.35
					2U / 3	15.9	0.62	1.05	1.18
					4U / 2	14.9	-0.47	0.99	1.11
					6U / 1	16.9	-0.47	1.12	1.26

Table 5.5.1c Experimental results

RUN No.	d* (mm)	$k_C a$	$k_C H_2$	cosh kh / cosh kd	Position / Transducer	Amplitude* (mm H_2O)	Phase* (rads)	P/P_2	P/P_1
15a	503	0.200	0.146	0.611	8U / 4	14.3	0.50	1.27	1.20
					2U / 3	12.7	0.44	1.13	1.07
					4U / 2	11.8	-0.23	1.05	0.99
					6U / 1	13.0	-0.27	1.16	1.09
15b	503	0.243	0.180	0.537	8U / 4	15.1	0.39	1.53	1.19
					2U / 3	15.2	0.42	1.54	1.20
					4U / 2	14.5	-0.20	1.47	1.14
					6U / 1	14.9	-0.28	1.51	1.17
15c	503	0.300	0.313	0.458	8U / 4	15.8	0.45	1.31	1.24
					2U / 3	15.2	0.46	1.26	1.19
					4U / 2	13.0	-0.35	1.08	1.02
					6U / 1	14.3	-0.41	1.19	1.12
16a	503	0.137	0.125	0.742	8U / 4	21.1	0.28	1.24	1.08
					2U / 3	21.2	0.16	1.24	1.08
					4U / 2	19.5	-0.09	1.14	1.00
					6U / 1	22.8	-0.12	1.34	1.16
16b	503	0.182	0.271	0.644	8U / 4	27.2	0.27	1.13	1.07
					2U / 3	25.4	0.30	1.05	1.00
					4U / 2	26.3	-0.33	1.09	1.03
					6U / 1	28.6	-0.38	1.18	1.12
17a	503	0.239	0.399	0.544	8U / 4	33.2	0.64	1.45	1.33
					2U / 3	30.5	0.54	1.33	1.23
					4U / 2	28.5	-0.24	1.25	1.15
					6U / 1	27.9	-0.21	1.22	1.12
18a	503	0.129	0.242	0.761	8U / 4	38.5	0.13	1.07	1.07
					2U / 3	37.4	0.10	1.04	1.04
					4U / 2	39.7	-0.03	1.10	1.10
					6U / 1	40.9	-0.02	1.14	1.14
18b	503	0.147	0.325	0.720	8U / 4	47.5	0.31	1.18	1.11
					2U / 3	43.2	0.23	1.07	1.01
					4U / 2	44.6	-0.14	1.11	1.04
					6U / 1	46.8	-0.19	1.16	1.09
19a	503	0.143	0.078	0.484	1L / 1	11.0	0.43	1.81	1.17
					3L / 2	9.3	0.07	1.53	0.99
					5L / 3	8.9	-0.31	1.46	0.95
					7L / 4	10.5	0.12	1.73	1.12
19b	503	0.184	0.170	0.347	1L / 1	10.5	0.59	1.30	1.28
					3L / 2	8.8	0.09	1.09	1.07
					5L / 3	9.3	-0.54	1.15	1.13
					7L / 4	8.6	0.14	1.06	1.05
19c	503	0.242	0.265	0.214	1L / 1	7.8	0.58	1.32	1.22
					3L / 2	6.8	0.25	1.15	1.06
					5L / 3	7.9	-0.40	1.34	1.23
					7L / 4	7.9	0.15	1.34	1.23
19d	503	0.299	0.382	0.132	1L / 1	8.1	0.57	1.91	1.73
					3L / 2	5.6	0.12	1.32	1.20
					5L / 3	6.3	-0.69	1.48	1.35
					7L / 4	5.6	0.09	1.32	1.20

Table 5.5.1d Experimental results

RUN No.	d* (mm)	$k_C a$	$k_C H_2$	cosh kh / cosh kd	Position / Transducer	Amplitude* (mm H_2O)	Phase* (rads)	P/P_2	P/P_1
20a	503	0.154	0.153	0.443	1L / 1	16.2	0.35	1.46	1.22
					3L / 2	13.9	0.05	1.26	1.05
					5L / 3	13.3	-0.21	1.20	1.00
					7L / 4	14.3	0.05	1.29	1.08
20b	503	0.187	0.298	0.338	1L / 1	15.6	0.32	1.15	1.07
					3L / 2	13.6	0.01	1.00	0.93
					5L / 3	13.3	-0.37	0.98	0.91
					7L / 4	15.8	0.09	1.17	1.08
20c	503	0.242	0.392	0.213	1L / 1	13.6	0.54	1.57	1.32
					3L / 2	11.8	0.14	1.36	1.15
					5L / 3	11.4	-0.29	1.31	1.11
					7L / 4	11.3	0.09	1.30	1.10
21a	503	0.143	0.123	0.484	2L / 1	14.3	0.33	1.36	1.12
					4L / 2	12.7	-0.14	1.21	0.99
					6L / 3	12.7	-0.06	1.21	0.99
					8L / 4	14.3	0.31	1.36	1.12
21b	503	0.187	0.293	0.337	2L / 1	14.3	0.38	1.08	1.15
					4L / 2	12.7	-0.22	0.96	1.02
					6L / 3	12.7	-0.32	0.96	1.02
					8L / 4	13.6	0.39	1.02	1.10
21c	503	0.235	0.350	0.225	2L / 1	12.3	0.50	1.46	1.23
					4L / 2	10.2	-0.27	1.21	1.02
					6L / 3	10.1	-0.26	1.20	1.01
					8L / 4	11.3	0.47	1.34	1.13
21d	503	0.289	0.513	0.144	2L / 1	9.1	0.33	1.41	1.26
					4L / 2	8.7	-0.35	1.35	1.21
					6L / 3	8.9	-0.40	1.38	1.23
					8L / 4	9.4	0.31	1.46	1.30
22a	503	0.139	0.097	0.501	2L / 1	12.7	0.41	1.44	1.13
					4L / 2	9.6	-0.04	1.09	0.85
					6L / 3	10.8	0.07	1.22	0.96
					8L / 4	11.3	0.47	1.28	1.00
22b	503	0.182	0.239	0.353	2L / 1	11.7	0.22	1.00	1.02
					4L / 2	12.1	-0.36	1.03	1.05
					6L / 3	11.1	-0.20	0.95	0.96
					8L / 4	12.2	0.24	1.04	1.06
22c	503	0.236	0.320	0.224	2L / 1	11.7	0.50	1.53	1.34
					4L / 2	9.4	-0.04	1.23	1.08
					6L / 3	9.0	-0.14	1.18	1.03
					8L / 4	10.5	0.68	1.37	1.21
22d	503	0.152	0.071	0.452	2L / 1	9.7	0.28	1.81	1.40
					4L / 2	7.4	-0.16	1.38	1.07
					6L / 3	5.7	-0.13	1.06	0.82
					8L / 4	9.8	0.23	1.83	1.42
22e	503	0.202	0.155	0.299	2L / 1	7.1	0.22	1.23	1.18
					4L / 2	6.5	-0.19	1.12	1.08
					6L / 3	7.0	-0.09	1.21	1.16
					8L / 4	6.8	0.46	1.17	1.13

Table 5.5.1e Experimental results

RUN No.	d* (mm)	$k_C a$	$k_C H_2$	cosh kh / cosh kd	Position / Transducer	Amplitude* (mm H_2O)	Phase* (rads)	P/P_2	P/P_1
22f	503	0.245	0.179	0.208	2L / 1	5.8	0.66	1.51	1.25
					4L / 2	5.2	-0.34	1.36	1.12
					6L / 3	5.7	-0.28	1.49	1.23
					8L / 4	4.9	0.57	1.28	1.06
22g	503	0.306	0.295	0.125	2L / 1	4.9	0.38	1.61	1.45
					4L / 2	4.3	-0.13	1.41	1.27
					6L / 3	4.4	-0.45	1.45	1.30
					8L / 4	4.1	0.69	1.35	1.21
24a	520	0.187	0.091	0.597	1U / 1	10.5	0.50	1.44	1.32
					3U / 2	9.5	0.02	1.30	1.19
					5U / 3	9.0	-0.52	1.23	1.13
					7U / 4	8.9	0.11	1.22	1.12
24b	520	0.235	0.163	0.509	1U / 1	No information			
					3U / 2	"	"		
					5U / 3	11.1	-0.35	1.25	1.29
					7U / 4	9.8	0.28	1.10	1.14
24c	520	0.313	0.268	0.397	1U / 1	9.8	0.60	1.15	1.28
					3U / 2	8.9	0.04	1.04	1.16
					5U / 3	9.0	-0.73	1.05	1.18
					7U / 4	9.8	0.15	1.15	1.28
24d	520	0.370	0.244	0.334	1U / 1	8.0	0.63	1.41	1.10
					3U / 2	7.0	0.05	1.24	0.96
					5U / 3	9.0	-0.88	1.59	1.23
					7U / 4	8.9	0.14	1.57	1.22
25a	520	0.150	0.088	0.679	1U / 1	11.4	0.39	1.14	1.20
					3U / 2	11.8	0.04	1.18	1.24
					5U / 3	10.4	-0.37	1.04	1.09
					7U / 4	11.8	0.05	1.18	1.24
25b	520	0.189	0.146	0.594	1U / 1	15.3	0.32	1.32	1.28
					3U / 2	15.4	-0.01	1.33	1.29
					5U / 3	13.9	-0.27	1.20	1.16
					7U / 4	14.2	0.03	1.23	1.19
25c	520	0.237	0.218	0.506	1U / 1	15.5	0.45	1.32	1.27
					3U / 2	14.3	0.05	1.22	1.18
					5U / 3	12.5	-0.39	1.07	1.03
					7U / 4	14.6	0.13	1.24	1.20
25d	520	0.307	0.338	0.405	1U / 1	16.1	0.62	1.43	1.57
					3U / 2	12.6	-0.01	1.12	1.23
					5U / 3	12.1	-0.64	1.08	1.18
					7U / 4	11.8	0.09	1.05	1.15
26a	520	0.147	0.112	0.688	1U / 1	14.9	0.50	1.13	1.17
					3U / 2	15.1	0.20	1.14	1.19
					5U / 3	13.9	-0.23	1.05	1.09
					7U / 4	15.5	0.23	1.17	1.22
26b	520	0.188	0.183	0.596	1U / 1	20.4	0.38	1.40	1.33
					3U / 2	20.1	0.06	1.38	1.31
					5U / 3	18.0	-0.35	1.23	1.17
					7U / 4	18.3	0.05	1.25	1.19

Table 5.5.1f Experimental results

RUN No.	d* (mm)	$k_C a$	$k_C H_2$	cosh kh / cosh kd	Position / Transducer	Amplitude* (mm H_2O)	Phase* (rads)	P/P_2	P/P_1
26c	520	0.244	0.325	0.494	1U / 1	21.1	0.56	1.28	1.26
					3U / 2	20.1	0.03	1.22	1.20
					5U / 3	19.4	-0.52	1.17	1.16
					7U / 4	19.5	0.04	1.18	1.17
26d	520	0.243	0.324	0.495	1U / 1	22.3	0.57	1.35	1.33
					3U / 2	20.7	0.11	1.25	1.24
					5U / 3	18.0	-0.55	1.09	1.08
					7U / 4	19.5	0.12	1.18	1.17
27a	520	0.147	0.182	0.686	1U / 1	20.4	0.47	0.96	1.03
					3U / 2	22.9	0.24	1.07	1.16
					5U / 3	21.5	-0.19	1.01	1.08
					7U / 4	20.8	0.18	0.97	1.05
27b	520	0.187	0.260	0.597	1U / 1	22.9	0.33	1.10	1.06
					3U / 2	27.6	0.08	1.32	1.28
					5U / 3	25.3	-0.38	1.21	1.17
					7U / 4	25.1	0.05	1.20	1.16
27c	520	0.234	0.439	0.510	1U / 1	26.6	0.48	1.10	1.14
					3U / 2	27.7	-0.09	1.15	1.19
					5U / 3	26.4	-0.72	1.10	1.13
					7U / 4	24.4	-0.03	1.01	1.05
28a	520	0.088	0.127	0.843	1U / 1	31.0	0.29	1.01	0.97
					3U / 2	33.3	0.03	1.09	1.05
					5U / 3	30.9	-0.23	1.01	0.97
					7U / 4	30.1	0.11	0.98	0.94
29a	520	0.086	0.129	0.659	1L / 1	23.5	0.17	0.95	0.98
					3L / 2	26.6	0.00	1.07	1.11
					5L / 3	25.5	-0.36	1.03	1.07
					7L / 4	25.2	-0.09	1.02	1.05
29b	520	0.142	0.158	0.467	1L / 1	14.5	0.50	1.11	1.16
					3L / 2	15.4	0.11	1.18	1.23
					5L / 3	15.3	-0.56	1.17	1.22
					7L / 4	12.6	0.22	0.96	1.01
29c	520	0.186	0.264	0.322	1L / 1	13.9	0.60	1.20	1.21
					3L / 2	14.0	0.06	1.21	1.22
					5L / 3	14.1	-0.50	1.22	1.23
					7L / 4	14.2	0.13	1.23	1.24
29d	520	0.231	0.405	0.216	1L / 1	12.4	0.41	1.30	1.22
					3L / 2	12.1	0.00	1.27	1.22
					5L / 3	11.7	-0.67	1.23	1.15
					7L / 4	11.8	0.04	1.24	1.16
30a	520	0.144	0.104	0.459	1L / 1	9.6	0.38	1.16	1.21
					3L / 2	10.1	0.13	1.22	1.27
					5L / 3	9.7	-0.24	1.17	1.22
					7L / 4	9.8	0.10	1.18	1.23
30b	520	0.182	0.182	0.333	1L / 1	10.1	0.36	1.20	1.11
					3L / 2	11.5	0.07	1.37	1.27
					5L / 3	10.0	-0.31	1.19	1.10
					7L / 4	11.0	0.00	1.31	1.21

Table 5.5.1g Experimental results

RUN N°.	d* (mm)	$k_C a$	$k_C H_2$	cosh kh / cosh kd	Position / Transducer	Amplitude* (mm H_2O)	Phase* (rads)	P/P_2	P/P_1
30c	520	0.232	0.274	0.215	1L / 1	8.5	0.57	1.33	1.23
					3L / 2	7.5	0.16	1.17	1.08
					5L / 3	7.1	-0.42	1.11	1.03
					7L / 4	7.3	0.20	1.14	1.05
31a	520	0.141	0.074	0.473	1L / 1	7.7	0.25	1.22	1.24
					3L / 2	7.3	0.07	1.16	1.17
					5L / 3	7.4	-0.35	1.18	1.19
					7L / 4	9.8	0.30	1.56	1.58
31b	520	0.182	0.130	0.332	1L / 1	7.7	0.36	1.29	1.19
					3L / 2	7.3	0.12	1.22	1.13
					5L / 3	8.3	-0.32	1.39	1.28
					7L / 4	8.9	0.23	1.49	1.38
31c	520	0.233	0.210	0.213	1L / 1	5.6	0.62	1.15	1.23
					3L / 2	5.6	0.11	1.15	1.23
					5L / 3	5.2	-0.48	1.07	1.15
					7L / 4	5.7	0.15	1.18	1.26
33a	519	0.141	0.152	0.475	2L / 1	11.6	0.39	0.89	0.94
					4L / 2	14.0	-0.14	1.08	1.14
					6L / 3	15.4	-0.20	1.19	1.25
					8L / 4	15.5	0.16	1.20	1.26
33b	519	0.184	0.265	0.328	2L / 1	13.6	0.10	1.14	1.07
					4L / 2	14.2	-0.15	1.19	1.12
					6L / 3	16.1	-0.35	1.35	1.27
					8L / 4	15.5	0.42	1.30	1.22
33c	519	0.234	0.414	0.212	2L / 1	9.3	0.33	0.98	1.03
					4L / 2	9.6	-0.28	1.01	1.07
					6L / 3	11.0	-0.41	1.16	1.22
					8L / 4	10.3	0.82	1.09	1.14
40a	493	0.140	0.163	0.752	1U / 1	22.5	0.25	1.02	1.27
					3U / 2	20.1	0.13	0.91	1.13
					5U / 3	19.8	-0.26	0.90	1.11
					7U / 4	20.7	0.10	0.94	1.16
40b	493	0.186	0.272	0.658	1U / 1	28.0	0.39	1.16	1.21
					3U / 2	27.4	0.03	1.13	1.18
					5U / 3	27.2	-0.48	1.13	1.17
					7U / 4	28.2	-0.07	1.17	1.22
40c	493	0.190	0.287	0.652	1U / 1	29.8	0.38	1.20	1.33
					3U / 2	25.9	-0.07	1.04	1.15
					5U / 3	28.1	-0.58	1.13	1.25
					7U / 4	26.8	-0.02	1.08	1.19
40d	493	0.228	0.402	0.586	1U / 1	35.7	0.38	1.37	1.30
					3U / 2	29.3	-0.23	1.12	1.06
					5U / 3	31.3	-0.74	1.20	1.14
					7U / 4	29.6	-0.13	1.14	1.07
41a	493	0.142	0.108	0.749	1U / 1	14.7	0.50	1.02	1.15
					3U / 2	13.7	0.17	0.95	1.07
					5U / 3	14.8	-0.26	1.03	1.16
					7U / 4	14.0	0.19	0.97	1.09

Table 5.5.1h Experimental results

RUN No.	d* (mm)	$k_C a$	$k_C H_2$	cosh kh / cosh kd	Position / Transducer	Amplitude* (mm H_2O)	Phase* (rads)	P/P_2	P/P_1
41b	493	0.183	0.169	0.664	1U / 1	17.7	0.38	1.14	1.18
					3U / 2	17.2	0.05	1.11	1.14
					5U / 3	19.4	-0.39	1.25	1.29
					7U / 4	16.0	0.06	1.03	1.06
41c	493	0.240	0.279	0.567	1U / 1	22.2	0.47	1.34	1.19
					3U / 2	20.8	-0.04	1.26	1.11
					5U / 3	21.9	-0.53	1.32	1.17
					7U / 4	19.2	0.02	1.16	1.03
41d	493	0.140	0.090	0.753	1U / 1	15.7	0.35	1.29	1.35
					3U / 2	12.6	0.07	1.03	1.09
					5U / 3	10.8	-0.25	0.89	0.93
					7U / 4	13.2	-0.04	1.08	1.14
42a	493	0.143	0.089	0.746	1U / 1	12.4	0.46	1.06	1.06
					3U / 2	10.6	0.25	0.91	0.99
					5U / 3	9.0	-0.09	0.77	0.84
					7U / 4	12.0	0.19	1.03	1.13
42b	493	0.192	0.126	0.648	1U / 1	13.7	0.56	1.27	1.30
					3U / 2	12.1	-0.01	1.13	1.15
					5U / 3	15.1	-0.45	1.40	1.43
					7U / 4	12.8	-0.01	1.19	1.21
42c	493	0.241	0.210	0.565	1U / 1	15.8	0.45	1.27	1.28
					3U / 2	12.8	-0.03	1.03	1.04
					5U / 3	16.0	-0.61	1.29	1.30
					7U / 4	14.2	0.02	1.15	1.15
42d	493	0.304	0.314	0.480	1U / 1	14.1	0.51	1.13	1.31
					3U / 2	11.4	0.01	0.91	1.06
					5U / 3	15.7	-0.82	1.26	1.46
					7U / 4	12.6	-0.01	1.01	1.17
43a	493	0.232	0.125	0.579	1U / 1	10.7	0.59	1.36	1.32
					3U / 2	8.6	0.15	1.09	1.06
					5U / 3	10.3	-0.42	1.31	1.27
					7U / 4	9.9	0.25	1.26	1.22
43b	493	0.372	0.253	0.404	1U / 1	11.1	0.70	1.60	1.49
					3U / 2	7.5	0.11	1.08	1.01
					5U / 3	10.3	-0.83	1.49	1.38
					7U / 4	8.6	0.10	1.24	1.15

Table 5.5.2a Experimental results

RUN N°.	S* (mm)	T* (secs)	L* (m)	T_t* (secs)	$\frac{\sigma^2 d}{g}$	Band	C_T ($m.s^{-1}$)	C_{C_1} ($m.s^{-1}$)	H_1* (mm)	H_2* (mm)
2a	98	0.918	1.80	1.264	2.401	4	1.413	1.424	72.3	60.5
2b	98	0.920	1.80	1.260	2.391	4	1.415	1.429	75.1	60.5
3a	160	1.865	1.80	0.851	0.582	1	2.004	2.115	37.0	33.7
3b	160	1.260	1.80	0.971	1.276	2	1.753	1.853	66.7	61.8
3c	160	1.140	1.80	1.077	1.557	-	1.659	1.671	77.8	76.3
3d	160	1.072	1.80	1.111	1.761	3	1.593	1.620	89.0	96.0
4a	220	1.324	1.80	0.990	1.155	-	1.796	1.817	94.5	92.1
5a	120	1.248	1.80	1.019	1.300	2	1.745	1.766	53.7	43.1
5b	120	1.149	1.80	1.077	1.533	-	1.667	1.671	68.4	61.8
5c	120	1.072	1.80	1.093	1.762	3	1.592	1.647	75.1	75.5
6a	120	0.817	1.80	1.376	3.033	5	1.269	1.308	97.3	81.5
7c	60	0.864	1.80	1.357	2.710	-	1.338	1.326	52.0	48.1
7d	60	0.819	1.80	1.424	3.020	5	1.272	1.264	47.5	44.4
10a	40	0.816	1.80	1.406	3.042	5	1.267	1.280	36.4	30.3
10b	40	0.725	1.80	1.539	3.848	6	1.132	1.170	43.1	32.1
10c	40	0.697	1.80	1.660	4.167	6	1.086	1.084	42.5	27.4
11a	140	0.983	1.80	1.173	2.094	-	1.494	1.534	96.6	94.3
13a	98	1.236	1.80	1.043	1.326	2	1.736	1.725	46.1	36.3
13b	98	1.067	1.80	1.130	1.777	3	1.589	1.593	69.5	65.0
13c	98	0.918	1.80	1.271	2.401	4	1.413	1.416	63.9	64.4
14a	80	1.226	1.80	1.087	1.347	2	1.729	1.657	38.9	29.5
14b	80	1.057	1.80	1.125	1.810	3	1.578	1.600	44.5	47.3
14c	80	0.934	1.80	1.260	2.321	4	1.432	1.429	63.9	53.9
14d	80	0.808	1.80	1.404	3.103	5	1.256	1.282	59.8	67.1
15a	60	1.034	1.80	1.173	1.895	3	1.552	1.534	38.9	36.8
15b	60	0.926	1.80	1.279	2.359	4	1.423	1.408	47.3	36.8
15c	60	0.829	1.80	1.412	2.943	5	1.288	1.275	55.6	52.6
16a	120	1.250	1.80	0.971	1.296	2	1.747	1.853	52.8	46.0
16b	120	1.058	1.80	1.096	1.809	3	1.578	1.642	79.2	75.0
17a	120	0.931	1.80	1.263	2.335	4	1.429	1.425	91.5	84.2
18a	240	1.341	1.80	0.981	1.125	-	1.807	1.835	94.5	94.7
18b	240	1.223	1.80	1.019	1.353	2	1.727	1.766	119.5	111.8
19a	80	1.257	1.80	1.024	1.281	2	1.752	1.758	38.9	27.6
19b	80	1.063	1.80	1.111	1.793	3	1.582	1.621	47.3	46.6
19c	80	0.931	1.80	1.279	2.335	4	1.429	1.408	59.8	55.2
19d	80	0.817	1.80	1.389	3.030	5	1.271	1.296	70.9	64.4
20a	120	1.221	1.80	1.071	1.357	2	1.726	1.681	59.8	50.0
20b	120	1.058	1.80	1.125	1.809	3	1.578	1.600	86.2	80.2
20c	120	0.913	1.80	1.256	2.426	4	1.406	1.433	96.5	81.5
21a	120	1.243	1.80	1.013	1.311	2	1.741	1.777	52.8	43.4
21b	120	1.071	1.80	1.139	1.766	3	1.591	1.580	73.7	78.9
21c	120	0.940	1.80	1.258	2.291	4	1.440	1.431	89.0	75.0
21d	120	0.837	1.80	1.375	2.893	5	1.298	1.309	100.1	89.4
22a	98	1.255	1.80	0.990	1.286	2	1.750	1.817	45.0	35.2
22b	98	1.077	1.80	1.113	1.745	3	1.598	1.617	65.3	66.3
22c	98	0.939	1.80	1.260	2.295	4	1.439	1.429	77.8	68.4
22d	60	1.236	1.80	1.067	1.326	2	1.736	1.686	30.6	23.7
22e	60	1.026	1.80	1.175	1.921	3	1.545	1.531	40.3	38.7
22f	60	0.920	1.80	1.279	2.392	4	1.414	1.408	44.5	36.8
22g	60	0.822	1.80	1.428	2.995	5	1.278	1.261	54.2	48.7

Table 5.5.2b Experimental results

RUN No.	S^* (mm)	T^* (secs)	L^* (m)	T_t^* (secs)	$\frac{\sigma^2 d}{g}$	Band	C_T ($m.s^{-1}$)	C_C ($m.s^{-1}$)	H_1^* (mm)	H_2^* (mm)
24a	40	1.065	1.60	1.008	1.845	3	1.593	1.587	26.7	24.5
24b	40	0.933	1.60	1.106	2.406	4	1.434	1.447	33.7	35.0
24c	40	0.817	1.60	1.292	3.133	5	1.272	1.239	38.6	43.1
24d	40	0.733	1.60	1.370	3.898	6	1.143	1.168	43.6	33.3
25a	60	1.237	1.60	0.939	1.367	2	1.751	1.704	28.1	29.4
25b	60	1.074	1.60	1.024	1.815	3	1.602	1.562	40.2	39.0
25c	60	0.915	1.60	1.094	2.501	4	1.410	1.463	48.1	46.4
25d	60	0.817	1.60	1.267	3.133	5	1.272	1.263	50.5	55.5
26a	80	1.236	1.60	0.917	1.371	2	1.749	1.745	37.0	38.5
26b	80	1.066	1.60	1.012	1.843	3	1.594	1.581	51.5	49.0
26c	80	0.921	1.60	1.137	2.466	4	1.419	1.408	67.7	67.0
26d	80	0.921	1.60	1.132	2.469	4	1.418	1.414	67.5	67.2
27a	120	1.240	1.60	0.923	1.360	2	1.754	1.733	57.8	62.3
27b	120	1.067	1.60	1.008	1.837	3	1.596	1.587	72.3	70.0
27c	120	0.929	1.60	1.099	2.424	4	1.430	1.456	91.5	94.5
28a	240	1.787	1.60	0.879	0.655	1	2.011	1.821	75.6	72.6
29a	240	1.814	1.60	0.905	0.636	1	2.018	1.767	72.5	75.3
29b	120	1.266	1.60	0.910	1.306	2	1.773	1.758	53.5	56.0
29c	120	1.072	1.60	1.005	1.821	3	1.601	1.592	71.3	71.8
29d	120	0.937	1.60	1.093	2.386	4	1.439	1.464	94.1	88.4
30a	80	1.260	1.60	0.920	1.319	2	1.768	1.739	34.7	36.2
30b	80	1.069	1.60	0.982	1.832	3	1.598	1.629	54.5	50.4
30c	80	0.938	1.60	1.099	2.381	4	1.440	1.456	64.4	59.5
31a	60	1.260	1.60	0.897	1.319	2	1.768	1.783	26.3	26.6
31b	60	1.085	1.60	0.999	1.778	3	1.614	1.602	39.0	35.9
31c	60	0.934	1.60	1.099	2.399	4	1.436	1.456	42.6	45.5
33a	120	1.260	1.60	0.896	1.315	2	1.768	1.786	51.9	54.6
33b	120	1.073	1.60	0.997	1.813	3	1.602	1.605	77.2	72.7
33c	120	0.926	1.60	1.093	2.434	4	1.426	1.464	84.9	89.4
40a	120	1.260	1.60	0.893	1.251	2	1.745	1.792	47.3	58.5
40b	120	1.063	1.60	1.001	1.759	3	1.578	1.598	70.4	73.5
40c	120	1.063	1.60	1.019	1.759	3	1.578	1.570	69.0	76.2
40d	120	0.934	1.60	1.076	2.276	4	1.430	1.487	94.1	89.0
41a	80	1.239	1.60	0.887	1.293	2	1.731	1.804	34.2	38.4
41b	80	1.075	1.60	0.995	1.719	3	1.590	1.608	45.3	46.6
41c	80	0.928	1.60	1.126	2.308	4	1.421	1.421	66.1	58.5
41d	60	1.264	1.60	0.892	1.242	2	1.749	1.794	30.8	32.4
42a	60	1.242	1.60	0.897	1.287	2	1.733	1.784	28.6	31.3
42b	60	1.062	1.60	1.029	1.760	3	1.578	1.555	32.6	33.2
42c	60	0.920	1.60	1.121	2.345	4	1.412	1.427	43.6	43.9
42d	60	0.819	1.60	1.258	2.963	5	1.271	1.272	44.7	52.0
43a	40	0.930	1.60	1.092	2.296	4	1.425	1.465	28.1	27.2
43b	40	0.729	1.60	1.369	3.734	6	1.137	1.169	36.9	34.3

Table 6.1.1.

Normalised computed pressures at the still water level - $P/\frac{1}{2}\rho gH$, for ka = 0.571, NIV = 3 and NIH = 4

θ degrees	Exact	ZK=0.1	ZK=0.5	ZK=0.9
0	0.9858	0.9845	0.9882	1.0836
45	0.8831	0.8751	0.8830	0.8628
90	0.9921	0.9901	0.9917	1.0452
135	1.3662	1.3561	1.3691	1.3431
180	1.5293	1.5264	1.5333	1.6263

Table A.1.1

Exact solution for pressure on cylinder

	θ \ ka	0.05	0.10	0.15	0.20	0.25	0.30	0.35	0.40	0.45	0.50
Amplitude	0	0.999	0.998	0.998	0.999	1.000	1.001	1.002	1.001	0.999	0.995
	π / 4	0.998	0.994	0.989	0.983	0.976	0.968	0.958	0.945	0.930	0.912
	π / 2	0.997	0.991	0.984	0.977	0.972	0.969	0.967	0.968	0.972	0.978
	3π / 4	0.998	0.998	1.004	1.017	1.041	1.075	1.118	1.170	1.226	1.285
	π	1.000	1.004	1.019	1.046	1.087	1.141	1.207	1.280	1.356	1.432
Phase (rads)	0	-0.099	-0.196	-0.293	-0.390	-0.489	-0.589	-0.690	-0.792	-0.895	-0.999
	π / 4	-0.069	-0.137	-0.203	-0.269	-0.335	-0.402	-0.469	-0.537	-0.604	-0.670
	π / 2	0.002	0.008	0.017	0.029	0.044	0.062	0.080	0.100	0.121	0.141
	3π / 4	0.073	0.151	0.234	0.319	0.402	0.482	0.554	0.618	0.672	0.717
	π	0.102	0.210	0.321	0.432	0.537	0.633	0.717	0.788	0.846	0.894

ka	0.05	0.10	0.15	0.20	0.25	0.30	0.35	0.40
σ	2.11	3.84	5.14	6.12	6.93	7.62	8.25	8.82
$f(H_z)$	0.34	0.61	0.82	0.97	1.10	1.21	1.31	1.40
ϕ(rads)	-0.02	-0.04	-0.05	-0.06	-0.07	-0.08	-0.08	-0.09
$\cos\phi$	1.000	0.999	0.999	0.998	0.998	0.997	0.997	0.996
2ϕ(rads)	-0.04	-0.08	-0.10	-0.12	-0.14	-0.15	-0.17	-0.18
$\cos^2\phi$	0.998	0.994	0.989	0.985	0.981	0.977	0.973	0.969

Table A.2.1.

Phase lag and amplitude reduction of 2 stage filter.

(fc $\doteq$ 16 H_z, depth d = 0.5m)

APPENDIX A.1.

THE PRESSURE ON A FIXED CIRCULAR CYLINDER IN WATER OF DEPTH h

The velocity of waves incident from the negative x direction is

$$\Phi_I = Re\left\{ \frac{gH}{2\sigma} \frac{\cosh k(y+h)}{\cosh kh} . e^{ikx} . e^{-i\sigma t} \right\}$$

$$= Re\left\{ \phi(x,y) . e^{-i\sigma t} \right\} \qquad \text{A .1.1.}$$

The wave shape is given by the linearized form of Bernoulli's equation

$$\eta = -\frac{1}{g} \frac{\partial \Phi_I}{\partial t}\bigg|_{y=0} = Re\left\{ -\frac{H}{2} e^{ikx} (-i) . e^{-i\sigma t} \right\}$$

$$= -\frac{H}{2} \sin(kx - \sigma t) \qquad \text{A.1.2.}$$

which at x = 0 becomes

$$\eta = \frac{H}{2} \sin \sigma t \qquad \text{A.1.3.}$$

If the axis of the vertical cylinder is placed at x = y = 0, then the boundary conditions may be more simple applied if the incident wave is expressed in cylindrical polar co-ordinates.

By definition the Bessel functions of integral order are the coefficients of the expansion

$$\exp \frac{x}{2}\left(\lambda - \frac{1}{\lambda}\right) = \sum_{n=-\infty}^{\infty} J_n(x)\,\lambda^n \qquad \text{A.1.4.}$$

Let $\lambda = ie^{i\theta}$, then

$$\exp \frac{x}{2}\left(\lambda - \frac{1}{\lambda}\right) = e^{ix\cos\theta} \qquad \text{A.1.5.}$$

In order to involve only Bessel functions of positive order

$$J_{-n}(x) = (-1)^n J_n(x) \qquad \text{A.1.6.}$$

is used.

$$\therefore \quad e^{ix\cos\theta} = \sum_{n=-\infty}^{\infty} J_n(x)\, i^n e^{in\theta}$$

$$= J_o(x) + \sum_{1}^{\infty} J_n(x)\, i^n e^{in\theta} + \sum_{-\infty}^{-1} J_n(x)\, i^n e^{in\theta}$$

A.1.7.

which becomes finally

$$e^{ix\cos\theta} = J_o(x) + \sum_{1}^{\infty} 2\, i^n J_n(x) \cos n\theta \qquad \text{A.1.8.}$$

The complex spatial part of the incident potential may be expressed in polar coordinates as

$$\phi_I = \frac{gH}{2\sigma} \frac{\cosh k(y+h)}{\cosh kh} . e^{ikx} = T . e^{ikr\cos\theta} \qquad \text{A.1.9.}$$

which from A.1.8. becomes

$$\phi_I = T \sum_{n=0}^{\infty} \varepsilon_n\, i^n J_n(x) \cos n\theta \qquad \text{A.1.10.}$$

where the Jacobi symbol ε_n obeys the relations

$$\varepsilon_o = 1 \; ; \; \varepsilon_n = 2 \quad \text{for} \quad n > 0 \qquad \text{A.1.11.}$$

Because of the symmetry of the problem about the x axis, and the exclusion of the origin from the fluid domain, the most general expression for the potential due to scattering by the cylinder may be expressed as

$$\phi_s = T \sum_{n=0}^{\infty} \cos n\theta \left\{ A_n . H_n^{(1)}(kr) + B_n . H_n^{(2)}(kr) \right\} \qquad \text{A.1.12.}$$

The asymptotic expansions for the Hankel functions of the first and second kinds behave for large kr as

$$H_n^{(1)}(kr) \sim \sqrt{\frac{2}{\pi kr}} \cdot e^{-\frac{\pi i}{2}(n+\frac{1}{2})} e^{ikr} \qquad \text{A.1.13.}$$

and $$H_n^{(2)}(kr) \sim \sqrt{\frac{2}{\pi kr}} \cdot e^{\frac{\pi i}{2}(n+\frac{1}{2})} . e^{-ikr} \qquad \text{A.1.14.}$$

Because of the original choice of $e^{-i\sigma t}$ for the harmonic time, then the solution representing waves travelling outwards from the cylinder is of the form

$$\phi_s = T \sum_{n=0}^{\infty} \cos n\theta . A_n . H_n^{(1)}(kr) \qquad \text{A.1.15.}$$

The total potential is therefore

$$\phi = T \sum_{n=0}^{\infty} \left\{ \varepsilon_n i^n J_n(kr) + A_n H_n^{(1)}(kr) \right\} \cos n\theta \qquad \text{A.1.16.}$$

The radial gradientof this potential at r = a must be zero to satisfy the only remaining kinematic condition (a is the cylinder radius). Therefore

$$A_n = -\varepsilon_n i^n \frac{J_n'(ka)}{H_n^{(1)'}(ka)} \qquad \text{A.1.17.}$$

The final solution is therefore

$$\Phi = Re\left\{ T e^{-i\sigma t} \sum_{n=0}^{\infty} \varepsilon_n i^n \cos n\theta \left[J_n(kr) - \frac{J_n'(ka)\, H_n^{(1)}(kr)}{H_n^{(1)\prime}(ka)} \right] \right\} \qquad \text{A.1.18.}$$

The variation of the free water surface shown in figure 5.5.5 was obtained by substituting this expression into Bernoulli's equation. The effect of the side walls of the wave flume was therefore not taken into account.

The pressure on the cylinder may similarly be found from Bernoulli's equation as

$$p = -\rho \left. \frac{\partial \Phi}{\partial t} \right|_{r=a}$$

$$= Re\left\{ \rho T \sigma e^{-i\sigma t} \sum_{n=0}^{\infty} \varepsilon_n i^{n+1} \cos n\theta \left[\frac{J_n'(ka) H_n^{(1)\prime}(ka) - J_n'(ka) H_n'(ka)}{H_n^{(1)\prime}(ka)} \right] \right\} \qquad \text{A.1.19.}$$

The Wronksian relation between $J_n(x)$ and $H_n^{(1)}(x)$ may be found from that usually quoted for $J_n(x)$ and $Y_n(x)$

$$J_n(x)\, Y_n'(x) - J_n'(x)\, Y_n(x) = \frac{2}{\pi x} \qquad \text{A.1.20.}$$

The argument x may be dropped for simplicity so that

$$J_n H_n^{(1)\prime} - J_n' H_n^{(1)} = J_n\left(J_n' + iY_n'\right) - J_n'\left(J_n + iY_n\right) = \frac{2i}{\pi x} \qquad \text{A.1.21.}$$

Equation A .1.19. simplifies to

$$p = Re\left\{ \frac{2\rho T \sigma e^{-i\sigma t}}{\pi ka} \sum_{n=0}^{\infty} -\varepsilon_n i^n \frac{\cos n\theta}{H_n^{(1)\prime}(ka)} \right\} \qquad \text{A.1.22.}$$

Although this expression for the pressure is in its most concise mathematical form, for numerical evaluation the real and imaginary parts must be readily identifiable. The experimental pressures in chapter 5 were all divided by the pressure in the wave at the same depth. For direct comparison equation A.1.22. may be expressed in this non-dimensional form as

$$p^* = -\frac{2}{\pi ka} Re\left\{\sum_{n=0}^{\infty} \frac{\varepsilon_n \cos n\theta \, i^n}{(J_n')^2 + (Y_n')^2} (J_n' - iY_n')(\cos\sigma t - i\sin\sigma t)\right\} \qquad \text{A.1.23.}$$

By separating the odd and even terms of the infinite series, the troublesome i^n term may be made wholly real by a suitable redefinition of the summing indices. Taking real parts as defined in equation A.1.1. yields

$$p^* = A\cos\sigma t + B\sin\sigma t = \sqrt{A^2+B^2}\,\sin(\sigma t + \alpha) \qquad \text{A.1.24.}$$

where $\alpha = \tan^{-1}\frac{A}{B}$

and $$A = -\frac{2}{\pi ka}\sum_{m=0}^{\infty}(-1)^m\left[\frac{J_{2m}'\varepsilon_{2m}\cos 2m\theta}{(J_{2m}')^2 + (Y_{2m}')^2} + \frac{Y_{2m+1}'\varepsilon_{2m+1}\cos(2m+1)\theta}{(J_{2m+1}')^2 + (Y_{2m+1}')^2}\right]$$

and $$B = \frac{2}{\pi ka}\sum_{m=0}^{\infty}(-1)^m\left[\frac{Y_{2m}'\varepsilon_{2m}\cos 2m\theta}{(J_{2m}')^2 + (Y_{2m}')^2} - \frac{J_{2m+1}'\varepsilon_{2m+1}\cos(2m+1)\theta}{(J_{2m+1}')^2 + (Y_{2m+1}')^2}\right]$$

The arguments of all the Bessel functions are all (ka) and have therefore been omitted for clarity. This result is distinctly different from that of Chakrabarti and Tam[15]. Because of the normalisation process it is directly comparable with a diffraction

amplification factor for wave height at the cylinder. As mentioned in chapter 5 results for the relatively small amount of diffraction at ka = 0.5 are available and agree exactly with the above expression.

The theoretical curves in figures 5.5.10 to 5.5.14 were calculated from the above expressions.

Although tables of Bessel functions are available, they were evaluated in this case by using a small programmable calculator (Casio FX601P) This was done using the same techniques as in the FORTRAN segment of the diffraction program. Convergence of the above series was quite rapid for values of ka less than 0.5, usually requiring less than four terms for reasonable accuracy.

The program listings for Bessel functions $J_n(x)$ and $Y_n(x)$ for small x are included here since they may be of general interest. Most of the currently available programmable calculators have all the necessary functions used in thse programs, but those few which still use reverse polish notation would necessitate considerable modification.

The Bessel coefficient of the first kind may be evaluated for small x by

$$J_n(x) = \frac{\left(\frac{x}{2}\right)^n}{n!} \sum_{s=1}^{\infty} \frac{(-1)^s n! \left(\frac{x}{2}\right)^{2s}}{s!(n+s)!} \qquad \text{A.1.25.}$$

Po	AC, Min0 , Min 5	Clear accumulators
	1, EXP, 7,+/-,MinF	Set accuracy limit at 10^{-7}
	MR2,÷, 2, =,Min 2,	Put $\frac{x}{2}$ in memory 2
	1, Min 3	Initialise term memory
	MR1, if x = 0 , GOTO1	Avoid evaluating $(0)^0$
	MR2, x^y, MR1, ÷ MR1, x!, =,Min 3	First term
LBL1	MR3, M + 5	Initialise accumulator
	ISZ	Increment memory 0
	+/-,X,MR2 ,x^2,÷,MR0	} Calculate next term
	÷,(MR0 + MR1),=, Min3	} Calculate next term
	÷, MR5,=,ABS,if x⩾F, GOTO 1	Convergence check
	MR5	Return with result.

The program multiplies the present term by a term dependent factor to obtain the next term and checks for convergence on the number of significant figures. This convergence check fails prematurely in the uncommon event of memory 5 becoming zero (as at the second term of $J_0(2)$). This may be overcome by using as the penultimate line

÷, MR5, if x = 0, e^x, =, ABS, if x⩾F, GOTO1

To run the program put n in memory 1 and x in memory 2.

The Bessel coefficient of the second kind may be expressed as

$$Y_n(x) = \frac{2}{\pi} \sum_{r=0}^{\infty} \frac{\left(\frac{x}{2}\right)^n}{n!} \frac{(-1)^r n! \left(\frac{x}{2}\right)^{2r}}{r!(n+r)!} \left(\gamma + \ln \frac{x}{2} - \frac{1}{2}(\phi(r) + \phi(r+n)) \right)$$

$$- \frac{2}{\pi} \sum_{r=0}^{n-1} \frac{(n-1)!}{2\left(\frac{x}{2}\right)^n} \frac{(n-r-1)!}{r!(n-1)!} \cdot \left(\frac{x}{2}\right)^{2r} \qquad \text{A.1.26.}$$

Using a rearranged form of Sneddon's notation. The program listing follows a similar pattern to that for Jn(x) and therfore comments have not been included.

```
Po    AC, Min4, Min5, 1, EXP, 7, +/-, MinF
      MR2,÷,2, =, Min 2
      1,Min3, MR1, if x = 0, GOTO1, MR2, x^y, MR1, ÷ MR1, x!, =, Min 3
LBL1  AC, Min9, MR4, GOSUB, P9, MR1, +, MR4, =, GOSUB, P9
      MR2, ln, +, MR8, -, MR9, ÷ 2, =,
      X, MR3, = M + 5, ÷, MR5, =, ABS, Min 9
      1, M+4
      MR3, +/-,X,MR2,x^2, ÷, MR4, ÷, (MR4 + MR1), =, Min 3
      MR9, if x ⩾ F, GOTO1
      MR1, Min0, if x = 0, GOTO 5
      -,1, =,x!, ÷,2,÷,MR2,x^y,MR1, =
LBL4  M-5, DSZ, GOTO6, GOTO5
LBL6  X, MR2, x^2, ÷, MR0, ÷, (MR1 - MR0), =, GOTO4
LBL5  MR5, x, 2, ÷,  , =

P9    if x = 0, GOTO3, Min 0
LBL2  MR0, 1/x, M+9
      DSZ, GOTO2
LBL3
```

The use of a convergence check based on the number of significant figures is far more important here since for small argument $Y_n(x)$ is unbounded whereas $|Jn(x)| \leqslant 1$ for all x.

To run this program put n in memory 1 and x in memory 2 as before. In addition Euler's constant = 0.577215665 must be kept in memory 8.

Table A.1.1. gives the pressure amplitudes and phases for ka = 0.05 (0.05)0.5.

APPENDIX A.2.

Filter Amplifier Details

In chapter 5 the typical noise levels on the signals from the pressure transducers were shown. The high amplification needed, to obtain a measureable signal, made the noise inevitable. The noise levels shown had already been considerably reduced by including in the intermediate amplifier stage a degree of filtering action.

These amplifiers were assembled on solderless prototyping boards to facilitate improvements. The active circuit elements were type 741 operational amplifiers.

Figure A.2.1. shows the typical configuration of a single inverting amplifier stage. V_i and V_o are the input and output voltages respectively. The only information required about the op-amp to understand how this circuit behaves is its:

a) extremely high resistance - typically 100 db,
b) high input resistance - typically 2 megohms.

The differential inputs are labelled negative (inverting) and positive (non-inverting) and the output voltage represents the difference between them multiplied by the (open loop) gain. If the output takes up its maximum value V_s (relative to earth) then the difference between the two inputs can be no more than $V_s \times 10^{-10}$. Since in many applications the non-inverting input is tied to earth, the voltage at the other input is said to be at "virtual earth".

Except for comparator action the high gain is only utilised indirectly. The use of negative feedback, although reducing considerably the overall gain, leads to a more stable configuration in which the overall gain is controlled by the external components. Since the input resistance at the negative input is so high it may be assumed that the current flowing into the amplifier is negligible.

Kirchoff's law applied to junction A (see figure A.2.1.) gives

$$\frac{V_i}{R_i} + \frac{V_o}{R} + C\frac{dV_o}{dt} = 0 \qquad \text{A.2.1.}$$

This linear differential equation may be solved by recourse to Fourier's theorem. If

$$V_i = A \sin(\sigma t) \qquad \text{A.2.2.}$$

is given, then

$$V_o = B \sin(\sigma t + \phi) \qquad \text{A.2.3.}$$

Substituting equations A.2.2. and A.2.3. into A.2.1. and equating in-phase and quadrature components yields

$$\phi = -\tan^{-1}(\sigma RC) \qquad \text{A.2.4.}$$

and

$$B = -A\frac{R}{R_i}\cos(\phi) \qquad \text{A.2.5.}$$

The cut off frequency may be defined as that which makes the phase lag 45^o, and is therefore

$$f_c = (2\pi RC)^{-1} \qquad \text{A.2.6.}$$

It may be seen that if the capacitor is removed there is no phase lag and the gain is fixed by the ratio of the feedback resistor to the input resistor. If on the other hand the feedback resistor is removed (i.e. $R \rightarrow \infty$) the output signal is always 90^{o} out of phase with the input and the circuit behaves as an integrator.

The configuration used to amplify the pressure transducer signals is shown in figure A.2.2. Two inverting amplifiers were used in series, the gain of each typically x 50. The supply was derived from a single 9 volt battery. Both input and output signals were taken relative to an artificial 'earth' fixed by a potential divider to the non-inverting input of the first amplifier. The non-inverting input of the second amplifier was connected to a potentiometer to facilitate null balancing of the final output.

The feedback resistors were usually 1 megohm and the feedback capacitors 10 nanofarads, giving a cut off frequency of about 16 Hz. For a 1 Hz input signal the phase lag would be 0.06 radians and the amplitude reduction only 0.2%, The 50Hz mains noise would be reduced by 70%.

Although the effect on the signal amplitude is small the phase lag becomes increasingly significant with frequency.

The expected phase lag and amplitude reduction (compared with d.c.) over two such amplifiers is shown in table A.2.1. There is some evidence of the effect of this on the phase results in figures 5.5.10, 5.5.14 and 5.5.18.

The input resistors were used to vary the gain as required. In some cases, only one filter capacitor was used since the noise was not significantly increased by the first amplifier.

APPENDIX A.3.

Computer Program Listings

ALB1 - Conventional two-dimensional Boundary Element method using linear source variation. Dirichlet boundary conditions only. Any shape may be specified by input co-ordinates.

ALB2 - Same as ALB1 except that the source boundary is separate.

BCYL - Two-dimensional problem of flow past a circular cylinder near a plane boundary.

DIFF - Main segment of diffraction program for a circular cylinder using separate source method. This segment must be combined with function segment BESS. List of variable names is included.

BESS - Self-contained Bessel function segment.

```
      DIMENSION B(50),F(50),A(50,50),X(50),Y(50)
     &,RX(50),RY(50)
C  READ IN PARAMETERS
      READ(1,100)NS,NRR,D
      WRITE(2,200)NS,NRR,D
      NN=NS+1;N=NS+1
C  READ IN CO-ORDINATES
      READ(1,100)(X(I),Y(I),I=1,NN)
      WRITE(2,201)(X(I),Y(I),I=1,NN)
C  READ IN BOUNDARY VALUES AT NODES
      READ(1,100)(F(I),I=1,NS)
      WRITE(2,202)(F(I),I=1,NS)
C  ZERO MATRIX
      DO 70 I=1,N
      DO 70 J=1,N
70    A(I,J)=0.
C CALCULATE EFFECT OF SOURCE I ON NODE J
      DO 1 I=1,NS
      DX=X(I)-X(I+1)
      DY=Y(I)-Y(I+1)
      B(I)=SQRT(DX*DX+DY*DY)
      DO 4 J=1,NS
      DX=X(I)-X(J)
      DY=Y(I)-Y(J)
      R1=SQRT(DX*DX+DY*DY)*D*B(I)
      DX=X(I+1)-X(J)
      DY=Y(I+1)-Y(J)
      R2=SQRT(DX*DX+DY*DY)*D*B(I)
      DX=(X(I)+X(I+1))/2.-X(J)
      DY=(Y(I)+Y(I+1))/2.-Y(J)
      R3=SQRT(DX*DX+DY*DY)*D*B(I)
      TB=D*B(I)*B(I)
      K=I+1
      IF(I.EQ.NS)K=1
      IF(I.EQ.J)GO TO 60
      IF(I+1.EQ.J)GO TO 61
      IF(I.EQ.NS.AND.J.EQ.1)GO TO 61
      A(J,I)=A(J,I)+(ALOG(R1)+2.*ALOG(R3))*B(I)/6.
      A(J,K)=A(J,K)+(ALOG(R2)+2.*ALOG(R3))*B(I)/6.
      GO TO 4
60    A(J,I)=A(J,I)+(ALOG(TB)-1.5)/2.*B(I)
      A(J,K)=A(J,K)+(ALOG(TB)-0.5)/2.*B(I)
      GO TO 4
61    A(J,I)=A(J,I)+(ALOG(TB)-0.5)/2.*B(I)
      A(J,K)=A(J,K)+(ALOG(TB)-1.5)/2.*B(I)
4     CONTINUE
      A(N,I)=A(N,I)+B(I)/2.
      K=I+1
      IF(I.EQ.NS)K=1
1     A(N,K)=A(N,K)+B(I)/2.
C FORM REST OF A()
      DO 2 I=1,NS
2     A(I,N)=1.
      A(N,N)=0.;F(N)=0.
C  SOLVER
      DO 22 I=1,N-1
      DO 22 J=I+1,N
      FAC=A(J,I)/A(I,I)
      DO 33 K=I+1,N
33    A(J,K)=A(J,K)-A(I,K)*FAC
22    F(J)=F(J)-F(I)*FAC
      F(N)=F(N)/A(N,N)
      DO 55 I=1,N-1
      M=N-I+1
      DO 66 J=1,M-1
66    F(J)=F(J)-F(M)*A(J,M)
55    F(M-1)=F(M-1)/A(M-1,M-1)
C  OUTPUT RESULTS
      WRITE(2,401)(F(I),I=1,N)
C  READ IN RESULTS POSITIONS
      READ(1,100)(RX(I),RY(I),I=1,NRR)
      WRITE(2,203)(RX(I),RY(I),I=1,NRR)
      DO 11 I=1,NRR
      OSUM=0.
      DO 12 J=1,NS
      DX=X(J)-RX(I)
      DY=Y(J)-RY(I)
      R1=SQRT(DX*DX+DY*DY)*D*B(J)
      DX=X(J+1)-RX(I)
      DY=Y(J+1)-RY(I)
      R2=SQRT(DX*DX+DY*DY)*D*B(J)
      DX=(X(J)+X(J+1))/2.-RX(I)
      DY=(Y(J)+Y(J+1))/2.-RY(I)
      R3=SQRT(DX*DX+DY*DY)*D*B(J)
      ALIM=B(J)/100000.
      TB=D*B(J)**2
      K=J+1
      IF(J.EQ.NS)K=1
      IF(R1-ALIM)64,63,63
63    IF(R2-ALIM)65,68,68
68    IF(R3-ALIM)67,69,69
69    CONTINUE
      OSUM=OSUM+(ALOG(R1)+2.*ALOG(R3))
     &*F(J)*B(J)/6.
      OSUM=OSUM+(ALOG(R2)+2.*ALOG(R3))
     &*F(K)*B(J)/6.
      GO TO 12
C CALCULATIONS FOR FIELD POINT AT SOURCE
64    OSUM=OSUM+((ALOG(TB)-1.5)*F(J)+
     &(ALOG(TB)-0.5)*F(K))*B(J)/2.
      GO TO 12
55    OSUM=OSUM+((ALOG(TB)-0.5)*F(J)+
     &(ALOG(TB)-1.5)*F(K))*B(J)/2.
      GO TO 12
67    OSUM=OSUM+(ALOG(TB/2.)-1.)
     &*(F(J)+F(K))*B(J)/2.
12    CONTINUE
      OSUM=OSUM+F(N)
      WRITE(2,204)OSUM
204   FORMAT(6H VALUE,(F15.6))
11    CONTINUE
      STOP
100   FORMAT(V)
200   FORMAT(4H NS=,I4,5H  NRR=,I4,4H  D=,F10.3)
201   FORMAT(6H      X,8X,1HY/(2F10.4))
202   FORMAT(4H PHI/(F10.4))
203   FORMAT(17H RESULT POSITIONS/(2F10.4))
401   FORMAT(8H RESULTS/(F10.4))
      END
```

ALB1

```
      DIMENSION B(50),F(50),A(50,50)
     &,PX(50),PY(50),SX(50),SY(50),
     &RX(50),RY(50)
C  READ IN PARAMETERS
      READ(1,100)NS,NRR,ZK
      NN=NS+1;N=NS+1
      PI=4.*ATAN(1.)
C READ IN P COORDS
      READ(1,100)(PX(I),PY(I),I=1,N)
C  READ IN BOUNDARY VALUES AT NODES
      READ(1,100)(F(I),I=1,NS)
      F(N)=F(1)
C  ZERO MATRIX
      DO 70 I=1,N
      DO 70 J=1,N
 70   A(I,J)=0.
CALCULATE EFFECT OF SOURCE I ON NODE J
      SUMX=0.;SUMY=0.
      DO 10 I=1,NS
      SUMX=SUMX+PX(I)
 10   SUMY=SUMY+PY(I)
      CX=SUMX/NS
      CY=SUMY/NS
      DTEM=0.
      DO 11 I=1,NS
      DIST=(PX(I)-CX)**2+(PY(I)-CY)**2
      IF(DIST-DTEM)11,12,12
 12   DTEM=DIST
 11   CONTINUE
      SRAD=ZK*SQRT(DTEM)
      DO 14 I=1,N
      PROP=SRAD/SQRT((PX(I)-CX)**2+(PY(I)-CY)**2)
      SX(I)=CX+(PX(I)-CX)*PROP
 14   SY(I)=CY+(PY(I)-CY)*PROP
      D=1./2./SRAD/SRAD/SIN(PI/NS)
      D=D*ZK/(ZK+1)
      WRITE(2,200)NS,NRR,D,ZK
      WRITE(2,310)(PX(I),PY(I),F(I),SX(I),SY(I),I=1,N)
C
      DO 1 I=1,NS
      DX=SX(I)-SX(I+1)
      DY=SY(I)-SY(I+1)
      B(I)=SQRT(DX*DX+DY*DY)
      DO 4 J=1,NS
      DX=SX(I)-PX(J)
      DY=SY(I)-PY(J)
      R1=SQRT(DX*DX+DY*DY)*D*B(I)
      DX=SX(I+1)-PX(J)
      DY=SY(I+1)-PY(J)
      R2=SQRT(DX*DX+DY*DY)*D*B(I)
      DX=(SX(I)+SX(I+1))/2.-PX(J)
      DY=(SY(I)+SY(I+1))/2.-PY(J)
      R3=SQRT(DX*DX+DY*DY)*D*B(I)
      K=I+1
      IF(I.EQ.NS)K=1
      A(J,I)=A(J,I)+(ALOG(R1)+2.*ALOG(R3))*B(I)/6.
 4    A(J,K)=A(J,K)+(ALOG(R1)+2.*ALOG(R3))*B(I)/6.
      A(N,I)=A(N,I)+B(I)/2.
      K=I+1
      IF(I.EQ.NS)K=1
      A(N,K)=A(N,K)+B(I)/2.
 1    CONTINUE
C FORM REST OF A()
      DO 2 I=1,NS
 2    A(I,N)=1.
      A(N,N)=0.
      F(N)=0.
C  SOLVER
      DO 22 I=1,N-1
      DO 22 J=I+1,N
      FAC=A(J,I)/A(I,I)
      DO 33 K=I+1,N
 33   A(J,K)=A(J,K)-A(I,K)*FAC
 22   F(J)=F(J)-F(I)*FAC
      F(N)=F(N)/A(N,N)
      DO 55 I=1,N-1
      M=N-I+1
      DO 66 J=1,M-1
 66   F(J)=F(J)-F(M)*A(J,M)
 55   F(M-1)=F(M-1)/A(M-1,M-1)
C  OUTPUT SOURCES
      WRITE(2,401)(F(I),I=1,N)
C  READ IN RESULTS POSITIONS
      READ(1,100)(RX(I),RY(I),I=1,NRR)
      WRITE(2,311)
      DO 15 I=1,NRR
      OSUM=0.
      DO 16 J=1,NS
      DX=SX(J)-RX(I)
      DY=SY(J)-RY(I)
      R1=SQRT(DX*DX+DY*DY)*D*B(J)
      DX=SX(J+1)-RX(I)
      DY=SY(J+1)-RY(I)
      R2=SQRT(DX*DX+DY*DY)*D*B(J)
      DX=(SX(J)+SX(J+1))/2.-RX(I)
      DY=(SY(J)+SY(J+1))/2.-RY(I)
      R3=SQRT(DX*DX+DY*DY)*D*B(J)
      K=J+1
      IF(J.EQ.NS)K=1
       OSUM=OSUM+(ALOG(R1)+2.*ALOG(R3))
     &*F(J)*B(J)/6.
       OSUM=OSUM+(ALOG(R2)+2.*ALOG(R3))
     &*F(K)*B(J)/6.
 16   CONTINUE
      OSUM=OSUM+F(N)
      WRITE(2,312)(RX(I),RY(I),OSUM)
 15   CONTINUE
      STOP
100   FORMAT(V)
200   FORMAT(4H NS=,I4,6H  NRR=,I4,4H  D=,
     &E13.10,6H  ZK=,F12.5)
203   FORMAT(8H RESULTS/(2F10.4))
204   FORMAT(6H VALUE,(F15.6))
401   FORMAT(8H SOURCES/(F30.8))
310   FORMAT(6X,2HPX,8X,2HPY,8X,3HPHI,
     &7X,2HSX,8X,2HSY/(5F10.4))
311   FORMAT(6H RESULTS/5X,2HRX,8X,
     &2HRY,8X,5HVALUE)
312   FORMAT(2F10.4,F12.6)
      END
```

ALB2

```
      DIMENSION B(50),F(50),A(50,50),T(50),VT(50),VTOT(50),
     1PX(50),PY(50),SX(50),SY(50),RX(50),RY(50),C(50,50)
      PI=ATAN(1.)*4.
      RO=1000.
COMMENTS TO BE INSERTED
      READ(1,100)DBED,CRAD,NDIV,ZK,NRR
      WRITE(2,200)DBED,CRAD,NDIV,ZK,NRR
      U=10.
      N=NDIV+1
      ALPHA=2.*PI/FLOAT(NDIV)
      SRAD=CRAD*ZK
C  INITIALIZE THETA -ANGLE ON CYL
      THETA=0.
CALCULATE COORDS
      DO 14 I=1,N
      PX(I)=CRAD*COS(THETA)
      PY(I)=DBED+CRAD*SIN(THETA)
      SX(I)=SRAD*COS(THETA)
      SY(I)=DBED+SRAD*SIN(THETA)
      F(I)=-1.*U*COS(THETA)
C  ALPHA IN TEXT IS T(I)
      T(I)=THETA+PI
  14  THETA=THETA+ALPHA
C INCREMENT THETA AND LOOP
C OUTPUT GENERATED DATA

     WRITE(2,310)(I,PX(I),PY(I),F(I),SX(I),SY(I),I,I=1,NDIV)
C       ZERO MATRIX A() & C() & VT()
      DO 70 I=1,N
      VT(I)=0.
      DO 70 J=1,N
      C(I,J)=0.
  70  A(I,J)=0.
CALCULATION OF MATRICES A & C TOGETHER
C  A IS SOLUTION MATRIX   C IS TANGENT VEL. MATRIX
C  I IS ELEM NUMB  J IS POINT NUMBER
      DO 1 I=1,NDIV
      K=I+1
      IF(I.EQ.NDIV)K=1
      DX=SX(I)-SX(K)
      DY=SY(I)-SY(K)
C ELEMENT LENGTH
      B(I)=SQRT(DX*DX+DY*DY)
C LOOP ON POINTS ON CYL
      DO 4 J=1,NDIV
C SET END 2 OF ELEMENT I
C DIRECTION COSINES
      ST=SIN(T(J))
      CT=COS(T(J))
C  ADDITION OF D STANDS FOR DASH OR PRIME IE IMAGE SINK
C  R1
      DX=SX(I)-PX(J)
      DY=SY(I)-PY(J)
      DYD=-SY(I)-PY(J)
      R1=SQRT(DX*DX+DY*DY)
      R1D=SQRT(DX*DX+DYD*DYD)
C  E IS NORMAL COMP , F IS TANGENTIAL COMP
      E1=(DX*CT+DY*ST)/R1/R1+(DX*CT+DYD*ST)/R1D/R1D
      F1=(DX*(-ST)+DY*CT)/R1/R1+(DX*(-ST)+DYD*CT)/R1D/R1D
C  R2
      DX=SX(K)-PX(J)
      DY=SY(K)-PY(J)
      DYD=-SY(K)-PY(J)
      R2=SQRT(DX*DX+DY*DY)
      R2D=SQRT(DX*DX+DYD*DYD)
      E2=(DX*CT+DY*ST)/R2/R2+(DX*CT+DYD*ST)/R2D/R2D
      F2=(DX*(-ST)+DY*CT)/R2/R2+(DX*(-ST)+DYD*CT)/R2D/R2D
C  R3
      DX=(SX(I)+SX(K))/2.-PX(J)
      DY=(SY(I)+SY(K))/2.-PY(J)
      DYD=-(SY(I)+SY(K))/2.-PY(J)
      R3=SQRT(DX*DX+DY*DY)
      R3D=SQRT(DX*DX+DYD*DYD)
      E3=(DX*CT+DY*ST)/R3/R3+(DX*CT+DYD*ST)/R3D/R3D
      F3=(DX*(-ST)+DY*CT)/R3/R3+(DX*(-ST)+DYD*CT)/R3D/R3D
C USING SIMPSON'S RULE
      A(J,I)=A(J,I)-B(I)/6.*(E1+2.*E3)
      A(J,K)=A(J,K)-B(I)/6.*(E2+2.*E3)
      C(J,I)=C(J,I)-B(I)/6.*(F1+2.*F3)
   4  C(J,K)=C(J,K)-B(I)/6.*(F2+2.*F3)
      A(N,I)=A(N,I)+B(I)/2.
   1  A(N,K)=A(N,K)+B(I)/2.
C FORM REST OF A()
      DO 2 I=1,NDIV
      A(I,N)=1.
   2  CONTINUE
      A(N,N)=0.
      F(N)=0.
C  SOLVE EQUATIONS
      DO 22 I=1,N-1
      DO 22 J=I+1,N
      FAC=A(J,I)/A(I,I)
      DO 33 K=I+1,N
  33  A(J,K)=A(J,K)-A(I,K)*FAC
  22  F(J)=F(J)-F(I)*FAC
      F(N)=F(N)/A(N,N)
      DO 55 I=1,N-1
      M=N-I+1
      DO 66 J=1,M-1
  66  F(J)=F(J)-F(M)*A(J,M)
  55  F(M-1)=F(M-1)/A(M-1,M-1)
C . OUTPUT VALUES OF SINKS AND CONSTANT C
      WRITE(2,401)(F(I),I=1,N)
      FX=0.
      FY=0.
CALCULATE TANGENTIAL VELOCITY
      DO 16 J=1,NDIV
      DO 17 I=1,NDIV
      VT(J)=VT(J)-C(J,I)*F(I)
  17  CONTINUE
      VTOT(J)=VT(J)-U*SIN(T(J))
      P=-RO*VTOT(J)**2/2.
      FX=FX+(3.+(-1)**J)*P*(-COS(T(J)))
      FY=FY+(3.+(-1)**J)*P*(-SIN(T(J)))
  16  CONTINUE
      FACT=2.*PI*CRAD/3./FLOAT(NDIV)/PI/RO/CRAD/U/U
      FX=FX*FACT
      FY=FY*FACT
C OUTPUT TANGENTIAL VELS
      WRITE(2,403)(VTOT(J),J=1,NDIV)
```

BCYL

```
C OUTPUT LIFT AND DRAG FORCES
      WRITE(2,402)FY,FX
CHECK SOLUTION FOR PHI
      IF(NRR.EQ.0)GO TO 71
      READ(1,101)(RX(I),RY(I),I=1,NRR)
      WRITE(2,311)
      DO 25 J=1,NRR
      OSUM=0.
      DO 26 I=1,NDIV
      K=I+1
      IF(I.EQ.NDIV)K=1
      DX=SX(I)-RX(J)
      DY=SY(I)-RY(J)
      DYD=-SY(I)-RY(J)
      R1=SQRT(DX*DX+DY*DY)
      R1D=SQRT(DX*DX+DYD*DYD)
      DX=SX(K)-RX(J)
      DY=SY(K)-RY(J)
      DYD=-SY(K)-RY(J)
      R2=SQRT(DX*DX+DY*DY)
      R2D=SQRT(DX*DX+DYD*DYD)
      DX=(SX(I)+SX(K))/2.-RX(J)
      DY=(SY(I)+SY(K))/2.-RY(J)
      DYD=-(SY(I)+SY(K))/2.-RY(J)
      R3=SQRT(DX*DX+DY*DY)
      R3D=SQRT(DX*DX+DYD*DYD)
      OSUM=OSUM+(ALOG(R1*R1D)+2.*ALOG(R3*R3D))*F(I)*B(I)/6.
   26 OSUM=OSUM+(ALOG(R2*R2D)+2.*ALOG(R3*R3D))*F(K)*B(I)/6.
      PHI=OSUM-U*RX(J)
      XCAP=2.*PI*CRAD*RX(J)/(RX(J)**2+RY(J)**2)
      YCAP=XCAP*RY(J)/RX(J)
C THEORETICAL PHI
      PHIC=-PI*CRAD*U*SINH(XCAP)/(COSH(XCAP)-COS(YCAP))
   25 WRITE(2,312)(J,RX(J),RY(J),PHI,PHIC)
   71 CONTINUE
      STOP
  100 FORMAT(2F0.0,I0,F0.0,I4)
  101 FORMAT(100F0.0)
  200 FORMAT(11H INPUT DATA/21HDBED,CRAD,NDIV,ZK,NRR/
     12F10.4,I4,F10.4,I4)
  310 FORMAT(3X,1HI,6X,2HPX,8X,2HPY,8X,3HV-N,10X,2HSX,2X,
     18X,2HSY,4X,1HI//(I4,3F10.4,2F12.3,I4))
  401 FORMAT(8H SINKS  /(8F10.4))
  402 FORMAT(1H ,'LIFT FORCE - ',F10.4,5X,'DRAG FORCE - ',
     1F10.4)
  403 FORMAT(1H ,'TANGENTIAL VELS'/(10F11.5))
  311 FORMAT(1H ,'CHECK SOLUTION ON BED CRAD = DBED')
  312 FORMAT(1H ,5X,2HRX,8X,2HRY,8X,3HPHI,8X,4HPHIC/
     1(I4,2F10.4,2F12.6))
      END
      FUNCTION SINH(X)
      SINH=0.5*(EXP(X)-EXP(-X))
      RETURN
      END
      FUNCTION COSH(X)
      COSH=0.5*(EXP(X)+EXP(-X))
      RETURN
      END
```

BCYL

```
      DIMENSION NNS(9),A(200)
      DOUBLE PRECISION XYZ(3),ABC(3),DC(200,3),CN(2),
     &FL(3,2),PHI(9),DG(3,2),DGDN(2),B(2),F(2,200),
     &G(2),ROW1(400),ROW2(400),PHIW(2,200),
     &PHIS(2,,200),SFX(2),SFZ(2),SMX(2),P(2,200),
     &ROW3(400),ROW4(400),PI,GAUSS,ZERO,SRAD,WK,V,
     &SIGMA,ALPHA,DEL,FF(400),THETA,FAC,GAMA,YMID,
     &GWT,T1,T2,T3,R1,R2,R3,AC,X,TRM1,TRM2,TRM3,
     &TOT1,TOT2,TOT3,SUM,SUMD,DX,UK,C,ARG,BESS,
     &D,E,LEVER
C
CYLRC4
      PI=4.*ATAN(1.)
      GAUSS=DSQRT(0.6)
      ALIM=0.001
      WRITE(2,894)ALIM,GAUSS
894   FORMAT(1H ,5HALIM=,E10.3,6HGAUSS=,D24.16)
      GRAV=9.81
      RO=1000.
      ZERO=0.
C
      READ(1,101)NIV,NIH
      WRITE(2,201)NIV,NIH
      N=2*NIH*(1+2*NIV)
      LSTP=N
      MREC=4*N
      CALL RANSIZ(03,MREC)
      DO 44 K=1,4.*LSTP
44    WRITE(3'K)(ZERO,I=1,N)
      DO 451 J=1,N
      DO 451 I=1,2
451   F(I,J)=0.
      READ(1,102)PRAD,ZK,DEPTH,WL,WH
      WRITE(2,202)PRAD,ZK,DEPTH,WL,WH
      SRAD=PRAD*ZK
      WK=2.*PI/WL
      V=WK*DTANH(WK*DEPTH)
      SIGMA=DSQRT(V*GRAV)
      ALPHA=PI/FLOAT(NIH)
      DEL=DEPTH/2./FLOAT(NIV)
      NE=NIV*NIH
C
      DO 20 IV=1,2*NIV+1
      WRITE(2,220)IV
220   FORMAT(4H IV=,I4)
      DO 20 IH=1,NIH*2
      DO 452 J=1,2*N
      ROW1(J)=ZERO
      ROW2(J)=ZERO
      ROW3(J)=ZERO
452   ROW4(J)=ZERO
      NOW=IH+2*NIH*(IV-1)
      THETA=ALPHA*FLOAT(IH-1)
CO ORDS ON P BOUNDARY
      XYZ(1)=PRAD*DCOS(THETA)
      XYZ(3)=PRAD*DSIN(THETA)
      XYZ(2)=-FLOAT(IV-1)*DEL
      B(1)=DCOS(WK*XYZ(1))
      B(2)=DSIN(WK*XYZ(1))
      DC(NOW,1)=DCOS(THETA)
      DC(NOW,2)=0.
      DC(NOW,3)=DSIN(THETA)
      DO 45 JJ=1,2
      F(JJ,NOW)=(DC(NOW,2)*DSINH(WK*(XYZ(2)+
     &DEPTH))*B(JJ)-FLOAT(3-2*JJ)*DC(NOW,1)*
     &DCOSH(WK*(XYZ(2)+DEPTH))*B(3-JJ))/
     &DCOSH(WK*DEPTH)/2./SIGMA*GRAV*WH*WK
45    CONTINUE
      FAC=-GRAV*WH/2./SIGMA*DCOSH(WK*(XYZ(2)+
     &DEPTH))/DCOSH(WK*DEPTH)
      PHIW(1,NOW)=FAC*B(1)
      PHIW(2,NOW)=FAC*B(2)
      A(NOW)=PRAD*ALPHA*DEL
      IF(IV.EQ.1.OR.IV.EQ.2*NIV+1) A(NOW)=A(NOW)/2.
CO-ORDS ON SOURCE BOUNDARY
      DO 19 IEV=1,NIV
      DO 19 IEH=1,NIH
      GAMA=ALPHA*(2.*FLOAT(IEH)-1.)
      YMID=-DEL*(2.*FLOAT(IEV)-1.)
COMMENT-CENTRAL NODE AND NODE NUMBERING SEQUENCE
      NC=2*IEH+(2*IEV-1)*NIH*2
      KC=0
      IF(IEH.EQ.NIH)KC=2*NIH
      NNS(1)=NC+2*NIH+1-KC;NNS(2)=NC+2*NIH
      NNS(3)=NC+2*NIH-1
      NNS(4)=NC+1-KC;NNS(5)=NC;NNS(6)=NC-1
      NNS(7)=NC-2*NIH+1-KC;NNS(8)=NC-2*NIH
      NNS(9)=NC-2*NIH-1
      DO 10 IG=1,3
      DO 10 JG=1,3
      CN(1)=GAUSS*FLOAT(JG-2)
      CN(2)=GAUSS*FLOAT(IG-2)
CALC SHAPE FNCTNS
      DO 11 IL=1,2
      FL(1,IL)=CN(IL)*(CN(IL)-1.)/2.
      FL(2,IL)=1.-CN(IL)**2
11    FL(3,IL)=CN(IL)*(CN(IL)+1.)/2.
      DO 12 IP=1,3
      DO 12 JP=1,3
12    PHI(3*IP+JP-3)=FL(JP,1)*FL(IP,2)
      GWT=(8.-3.*FLOAT(IABS(IG-2)))
      GWT=GWT*(8.-3.*FLOAT(IABS(JG-2)))/81.
CONVERT LOCAL TO GLOBAL
      ABC(2)=YMID+CN(2)*DEL
      THETA=GAMA-CN(1)*ALPHA
      ABC(1)=SRAD*DCOS(THETA)
      ABC(3)=SRAD*DSIN(THETA)
C  PREP FOR G
      T1=(XYZ(1)-ABC(1))**2
      T2=(XYZ(2)-ABC(2))**2
      T3=(XYZ(3)-ABC(3))**2
      R1=DSQRT(T1+T2+T3)
      R2=DSQRT(T1+(XYZ(2)+2.*DEPTH+ABC(2))**2+T3)
      R3=DSQRT(T1+T3)
      AC=(V*V-WK*WK)*DCOSH(WK*ABC(2)+WK*DEPTH)
      AC=AC/((WK*WK-V*V)*DEPTH+V)*2.*PI
CHOOSE G1 OR G2 BASED ON WK*R3
      TEST=WK*R3
      IF(TEST-0.1)39,38,38
C  G1
```

DIFF

```
      35  CONTINUE
          X=PI
          TOT1=0.;TOT2=0.;TOT3=0.
       2  X=(PI/2.+X)/2.
          SUM=V/X*DEPTH+DTAN(X)
          IF(SUM)1,2,2
       1  SUM=V/X*DEPTH+DTAN(X)
          SUMD=1./(DCOS(X))**2-V*DEPTH/X/X
          DX=-SUM/SUMD
          X=X+DX
          IF(DX-ALIM)4,1,1
       4  UK=X/DEPTH
          C=4.*(UK*UK+V*V)*DCOS(UK*(ABC(2)+DEPTH))
          C=C/((UK*UK+V*V)*DEPTH-V)
          ARG=UK*R3
          TRM1=C*DCOS(UK*(XYZ(2)+DEPTH))*UK**-1
          TRM1=TRM1*BESS(4,1,ARG)
          TOT1=TOT1+TRM1
          TRM2=-C*UK*DSIN(UK*(XYZ(2)+DEPTH))
          TRM2=TRM2*BESS(4,0,ARG)
          TOT2=TOT2+TRM2
          TRM3=C*DCOS(UK*(XYZ(2)+DEPTH))
          TRM3=TRM3*BESS(4,0,ARG)
          TOT3=TOT3+TRM3
C  ONLY TEST TRM1
          TEST=DSQRT(TRM1*TRM1)
          X=X+PI
          IF(TEST-ALIM)6,1,1
C  31
       6  ARG=WK*R3
          G(1)=AC*DCOSH(WK*(XYZ(2)+DEPTH))
         &*BESS(5,0,ARG)+TOT3
          G(2)=-AC*DCOSH(WK*(XYZ(2)+DEPTH))
         &*BESS(3,0,ARG)
          DG(1,1)=TOT1*(XYZ(1)-ABC(1))/R3
          D=-AC*DCOSH(WK*(XYZ(2)+DEPTH))*WK/R3
          DG(1,1)=DG(1,1)+D*BESS(5,1,ARG)
         &*(XYZ(1)-ABC(1))
          DG(1,2)=-D*BESS(3,1,ARG)*(XYZ(1)-ABC(1))
          E=AC*WK*DSINH(WK*(XYZ(2)+DEPTH))
          DG(2,1)=TOT2+E*BESS(5,0,ARG)
          DG(2,2)=-E*BESS(3,0,ARG)
          DG(3,1)=TOT1*(XYZ(3)-ABC(3)))/R3
         &+D*BESS(5,1,ARG)*(XYZ(3)-ABC(3))
          DG(3,2)=-D*BESS(3,1,ARG)*(XYZ(3)-ABC(3))
          GO TO 40
C  32
      39  CONTINUE
C     G2  NOT WRITTEN YET   USED FOR  WK*R3<0.1
          GO TO 33
C COMBINE COMPONENTS OF DGDN AND BS
      40  DGDN(1)=0.;DGDN(2)=0.
          DO 41 I=1,2
          DO 41 J=1,3
      41  DGDN(I)=DGDN(I)+DC(NON,J)*DG(J,I)
          DO 43 I=1,2
          FAC=GWT*PHI(I)*SRAD*DEL*ALPHA
          ROW1(NNS(I))=ROW1(NNS(I))+FAC*DGDN(1)
          ROW2(NNS(I))=ROW2(NNS(I))+FAC*DGDN(2)
          ROW3(NNS(I))=ROW3(NNS(I))+FAC*G(1)
      43  ROW4(NNS(I))=ROW4(NNS(I))+FAC*G(2)
      10  CONTINUE
      19  CONTINUE
C
          WRITE(3'NON)(ROW1(I1),I1=1,N)
          WRITE(3'NON+LSTP)(ROW2(I1),I1=1,N)
          WRITE(3'NON+2*LSTP)(ROW3(I1),I1=1,N)
          WRITE(3'NON+3*LSTP)(ROW4(I1),I1=1,N)
      20  CONTINUE
C REARRANGE MATRICES FOR COMPLEX ARITH.
          DO 80 I=1,N
C  ROW FROM MAT. A
          READ(3'I)(ROW1(I1),I1=1,N)
C  ROW FROM MAT.B
          READ(3'I+N)(ROW2(I1),I1=1,N)
          DO 81 J=1,N
C  ADD TERMS AT END OF EA ROW
          ROW1(J+N)=-ROW2(J)
      81  ROW2(J+N)=ROW1(J)
C  WRITE BACK
          WRITE(3'I)(ROW1(I1),I1=1,2*N)
      80  WRITE(3'I+N)(ROW2(I1),I1=1,2*N)
C
          DO 82 I=1,N
          DO 82 K=1,2
      82  FF(I+(K-1)*N)=F(K,I)
C
          DO 52 I=1,2*N-1
          READ(3'I)(ROW1(I1),I1=1,2*N)
          DO 52 J=I+1,2*N
          READ(3'J)(ROW2(I1),I1=1,2*N)
          FAC=ROW2(I)/ROW1(I)
          DO 53 K=I+1,2*N
      53  ROW2(K)=ROW2(K)-ROW1(K)*FAC
          WRITE(3'J)(ROW2(I1),I1=1,2*N)
      52  FF(J)=FF(J)-FF(I)*FAC
          FF(2*N)=FF(2*N)/ROW2(2*N)
          DO 55 I=1,2*N-1
          M=2*N-I+1
          READ(3'M-1)(ROW1(I1),I1=1,2*N)
          DO 56 J=1,M-1
          READ(3'J)(ROW2(I1),I1=1,2*N)
      56  FF(J)=FF(J)-FF(M)*ROW2(M)
      55  FF(M-1)=FF(M-1)/ROW1(M-1)
          SMX(1)=0.;SMX(2)=0.;SFX(1)=0.
          SFX(2)=0.;SFZ(1)=0.;SFZ(2)=0.
          DO 67 IV=1,2*NIV+1
          LEVER=DEPTH-FLOAT(IV-1)*DEL
          DO 67 IH=1,NIH*2
          NON=IH+2*NIH*(IV-1)
          READ(3'NON+2*N)(ROW1(I1),I1=1,N)
          READ(3'NON+3*N)(ROW2(I1),I1=1,N)
C  REAL AND IMAG. LOOP
          DO 65 L=1,2
          SUM=0.
C  SUM PRODS OF INTEGRALS AND SOURCES
          DO 66 J=1,N
          SUM=SUM+ROW1(J)*FF(J+(L-1)*N)
         &+ROW2(J)*FF(J+(2-L)*N)*FLOAT(2*L-3)
      66  CONTINUE
```

DIFF

```
      PHIS(L,NON)=SUM
      DO 68 L=1,2
      P(L,NON)=RO*SIGMA*FLOAT(2*L-3)
     &*(PHIW(3-L,NON)+PHIS(3-L,NON))
      FX=P(L,NON)*A(NON)*DC(NON,1)
      FZ=P(L,NON)*A(NON)*DC(NON,3)
      SFX(L)=SFX(L)+FX
      SFZ(L)=SFZ(L)+FZ
   68 SMX(L)=SMX(L)+FX*LEVER
   67 CONTINUE
C
      WRITE(2,211)
      DO 70 I=1,N
      XYZ(1)=PRAD*DC(I,1)
      XYZ(2)=-FLOAT((I-1)/(2*NIH))*DEL
      XYZ(3)=PRAD*DC(I,3)
      POT1=PHIW(1,I)+PHIS(1,I)
      POT2=PHIW(2,I)+PHIS(2,I)
      WRITE(2,212)I,XYZ(1),XYZ(2),XYZ(3),F(1,I),
     &F(2,I),P(1,I),P(2,I),POT1,POT2,I
      M=I-10*(I/10)-9
      IF(M.EQ.0) WRITE(2,213)
   70 CONTINUE
C
      WRITE(2,214)SFX(1),SFX(2),SFZ(1),SFZ(2)
      WRITE(2,215)SMX(1),SMX(2)
      RMAXF=DSQRT(SFX(1)**2+SFX(2)**2)
      RMAXM=DSQRT(SMX(1)**2+SMX(2)**2)
      WRITE(2,216)RMAXF,RMAXM
      AKA=WK*PRAD
      FORCE=RMAXF/RO/PRAD/PRAD/GRAV/WH*2.
      WRITE(2,224)AKA,FORCE
  224 FORMAT(5H KA=,F10.4,8H FORCE= ,F13.6)
      STOP
C
C
C
  101 FORMAT(V)
  102 FORMAT(V)
  201 FORMAT(5H NIV=,I4,6H  NIH=,I4)
  202 FORMAT(6H PRAD=,F10.4,5H  ZK=,F10.4,
     &8H  DEPTH=,F10.4,14H  WAVE LENGTH=,
     &F10.4,14H  WAVE HEIGHT=,F10.4)
  203 FORMAT(4F20.4)
  211 FORMAT(40X,15HSOURCE STRENGTH,13X,
     &8HPRESSURE,16X,9HPOTENTIAL/5H NODE,
     &6X,1HX,9X,1HY,9X,1HZ,3X,
     &3(5X,4HREAL,6X,9HIMAGINARY),2X,
     &4HNODE)
  212 FORMAT(1H ,I2,3X,3E10.3,5E12.4,I4)
  213 FORMAT(2X)
  214 FORMAT(29H TOTAL FORCE IN X DIRECTION =,
     &E10.4,13H COS(SIGMA*T),3H + ,E10.4,
     &13H SIN(SIGMA*T)/13H TOTAL FORCE ,
     &16HIN Z DIRECTION =,E10.4,
     &16H COS(SIGMA*T) + ,E10.4,
     &13H SIN(SIGMA*T))
  215 FORMAT(28H TOTAL MOMENT ABOUT BED IN X,
     &12H DIRECTION =,E10.3,13H COS(SIGMA*T),
     &3H + ,E10.3,13H SIN(SIGMA*T))
  216 FORMAT(31H MAXIMUM FORCE IN X DIRECTION =,
     &E12.5/30H MAXIMUM MOMENT ABOUT BED IN X,
     &12H DIRECTION =,E12.5)
      END
```

DIFF

```
      FUNCTION BESS(K,N,X)
C K IS KIND,N IS ORDER,X IS ARGUMENT
C HN(X),K=1;IN(X),K=2;JN(X),K=3;KN(X),K=4
C YN(X),K=5  ;HN(X) IS INOPERATIVE
C IN(X)>10. IS INOPERATIVE
C     WRITE(2,403)K,N
403   FORMAT(5H BESS,2I4)
      ALIM=0.000000000001
      PI=4.*ATAN(1.)
       GAMA=0.577215665
       ASYM=9.
       IF(X.GT.ASYM)GO TO 25
       GO TO(400,10,10,40,40),K
C  FUNCTIONS IN(X) & JN(X) FOR SMALL ARGUMENT
10    A=X/2.
      FAC=1.
      IF(N.EQ.0)GO TO 4
      DO 1 I=1,N
1     FAC=A/FLOAT(I)*FAC
C
4     TOTAL=0.
      S=0.
      TERM=FAC
2     TOTAL=TOTAL+TERM
      S=S+1.
      TERM=TERM*((-1.)**K*X*X/4.)/((FLOAT(N)+S)*S)
      TEMP=TERM**2
      IF(TEMP-ALIM)3,2,2
3     BESS=TOTAL
C     WRITE(2,201)S
201   FORMAT(3H S=,F10.4)
      RETURN
C  MOD BESS KN(X) AND YN(X)  FOR SMALL X
40    IR=0
      ACCM=0.
      TOTAL=0.
      TERM=1.
      IF(N.EQ.0)GO TO 42
      DO 53 I=1,N
53    TERM=TERM*X/2./FLOAT(I)
42    SUM=0.
      IF(IR.EQ.0)GO TO 41
      DO 43 I=1,IR
43    SUM=SUM+1./FLOAT(I)
      ACCM=-SUM/2.
41    SUM=0.
      IF(IR.EQ.0.AND.N.EQ.0)GO TO 49
      DO 44 I=1,IR+N
44    SUM=SUM+1./FLOAT(I)
49    ACCM=ACCM-SUM/2.+ALOG(X/2.)+GAMA
C
C     WRITE(2,203)ACCM,TERM
203   FORMAT(6H ACCM=,F20.10,5HTERM=,F20.10)
      TEMP=TERM*ACCM
      CHEK=SQRT(TEMP**2)
      IF(CHEK.LT.ALIM)GO TO 46
      TOTAL=TOTAL+FLOAT(2*K-9)**(N+1)*TEMP
      IR=IR+1
      TERM=TERM*X*X/4./FLOAT(IR)/FLOAT(N+IR)
     &*FLOAT(9-2*K)
      GO TO 42
46    IF(N.EQ.0)GO TO 47
      WRITE(2,206)TOTAL
206   FORMAT(14H TOTAL SO FAR=,F20.10)
      MM=0
      TERM=1./((X/2.)**N)/2.
51    PROD=1.
      IF(MM.EQ.N-1)GO TO 52
      DO 50 I=1,N-1-MM
50    PROD=PROD*FLOAT(I)
52    TEMP=TERM*PROD
C     WRITE(2,207)TEMP
207   FORMAT(6H TEMP=,F20.10)
      TOTAL=TOTAL+TEMP*FLOAT(9-2*K)
      MM=MM+1
      IF(MM.EQ.N)GO TO 47
      TERM=TERM*FLOAT(2*K-9)*(X*X/4.)/FLOAT(MM)
C     WRITE(2,208)TERM
208   FORMAT(6H TERM=,F20.10)
      GO TO 51
47    CONTINUE
C     WRITE(2,202)IR
      BESS=TOTAL*(1.+(2./PI-1.)*FLOAT(K-4))
      RETURN
25    GO TO(400,400,26,30,25),K
C  ASYMPTOTIC EXPS FOR J & Y
26    THETA=X-PI*(FLOAT(N)+0.5)/2.
      RTPT=SQRT(2./PI/X)
      A=COS(THETA)*RTPT
      B=SIN(THETA)*RTPT
      GO TO(400,400,27,400,28),K
28    C=A
      A=B
      B=-C
27    TOT1=0.;TOT2=0.
      IR=0
      TRM1=1.
      TRM2=(FLOAT(N)**2-0.25)/2./X
      TOT1=TRM1*A
       TOT2=TRM2*B
24     IR=IR+1
       DO 21 I=IR*2-2,2*IR-1
21     TRM1=TRM1*(0.5-FLOAT(N-I))*(0.5+FLOAT(N+I))
      &/FLOAT(I+1)/2./X
       TEMP=-TRM1*A
       CHEK=SQRT(TEMP**2)
       IF(CHEK.LT.ALIM)GO TO 23
       TOT1=TOT1+TEMP
       DO 22 I=2*IR-1,2*IR
22     TRM2=TRM2*(0.5-FLOAT(N-I))*(0.5+FLOAT(N+I))
      &/FLOAT(I+1)/2./X
       TEMP=-TRM2*B
       CHEK=SQRT(TEMP**2)
       IF(CHEK.LT.ALIM)GO TO 23
       TOT2=TOT2+TEMP
       GO TO 24
23     BESS=TOT1-TOT2
C      WRITE(2,202)IR
202   FORMAT(4H IR=,I4)
      RETURN
```

BESS

```
1210C  MOD BESS FCN 2ND KIND KN(X) ASYMP
1220   30  TERM=1.
1230       RTPT=SQRT(PI/2./x)/EXP(X)
1240C      WRITE(2,209)RTPT
1250  209  FORMAT(5H RTPT=,F20.10)
1260       IR=0
1270       TOTAL=TERM*RTPT
1280   31  IR=IR+1
1290       TERM=TERM*(-1.)*(0.5-FLOAT(N-IR)-1.)
1300      &*(0.5+FLOAT(N+IR)-1.)/2./X/FLOAT(IR)
1310      &/2./X/FLOAT(IR)
1320C      WRITE(2,208)TERM
1330       TEMP=RTPT*TERM
1340       CHEK=SQRT(TEMP**2)
1350       IF(CHEK.LT.ALIM)GO TO 33
1360       TOTAL=TOTAL+TEMP
1370       GO TO 31
1380   33  BESS=TOTAL
1390C      WRITE(2,202)IR
1400       RETURN
1410  400  WRITE(2,401)
1420  401  FORMAT(12H INOPERATIVE)
1430       RETURN
1440       END
```

BESS

Variable names used in diffraction computer program DIFF.

a) Real Variables.

AC	-	Constant in Green's function.
AKA	-	Nondimensional parameter, ka.
ALIM	-	Accuracy limit for series convergence.
ALPHA	-	Incremental angle, α.
ARG	-	Argument of Bessel functions.
C	-	Term dependent constant in Green's function series.
D	-	Constant in Green's function.
DEL	-	Vertical incremental distance, Δ.
DEPTH	-	Water depth, d or h.
E	-	Constant in Green's function.
FAC	-	Temporary store for multiplying factor.
FORCE	-	Non-dimensional total in line force.
GAMA	-	Angle, γ.
GAUSS	-	Constant used to define coordinates of Gauss points.
GRAV	-	Acceleration due to gravity, g.
GWT	-	Gauss Weighting factor.
PI	-	$\pi = 4 \times \tan^{-1}(1)$.
POT.I	-	Real and Imaginary parts of total potential, ϕ.
PRAD	-	Radius of physical circular cylinder, a.
R.J.	-	Three distances used in Green's function.
RMAXF	-	Maximum in line force.
RMAXM	-	Maximum in line moment.
RO	-	Density of water, ρ.
SIGMA	-	Radian frequency $\sigma = 2\pi/T$.
SRAD	-	Radius of fictitious source cylinder, r_s.
SUM	-	Temporary accumulator

T.J. - Three temporary variables.

TEMP - Temporary variable.

TEST - Temporary variable in conditional branch.

TOT.J - Three accumulators for infinite series.

TRM.J. - Three term variables for infinite series.

UK - Corresponds to m_k in text.

V - $\nu = \sigma^2/g$.

WH - Wave height, H

WK - Wave number, k.

WL - Wave length, λ.

X - Non-dimensional variable in Newton-Raphson iteration.

YMID - Vertical coordinate of element mid-point.

ZERO - Double precision zero.

ZK - Radius factor, r_s/a.

b) Real Vectors

A(NON) - Area associated with node NON.

ABC(J) - Cartesian coordinates on source cylinder, (a,b,c).

B(I) - Terms required for calculating ϕ_w.

CN(I) - Natural coordinates on transformed element, (ξ,η).

DGDN(I) - Real and imaginary parts of $\partial G/\partial n$.

FF(NON) - Right hand side vector of equations.

G(I) - Real and imaginary parts of Green's function.

PHI(K) - Interpolation fuction, ϕ_{IJ}.

ROW.L(NON) - ROW accumulators.

SFX(I) - Real and imaginary parts of in-line force.

SFZ(I) - " " " " " transverse force.

SMX(I) - " " " " " in-line moment.

XYZ(J) - Cartesian coordinates on physical cylinder, (x, y, z).

where I = 1 or 2, J = 1, 2 or 3

K = 1 to 9, L = 1 to 4

NON = 1 to N.

c) Real Arrays

DC(NON,J) - Direction cosines at node number NON.

DG(J,I) - Cartesian components of $\partial G/\partial n$.

F(I,NON) - Real and Imaginary parts of R.H.S. vector.

FL(J,I) - Lagrange interpolation functions.

P(I,NON) - Real and Imaginary parts of pressure at node NON.

PHIS(I,NON)- " " " " " ϕ_s " " "

PHIW(I,NON)- " " " " " ϕ_w " " "

where I = 1 or 2, J = 1 to 3, NON = 1 to N.

d) Integers

IEH - Horizontal plane, element counter.

IEV - Vertical plane, element counter.

IH - Horizontal plane, node counter.

IV - Vertical plane, node counter.

KC - Jump in element number per row.

LSTP - Steplength of random access memory blocks.

MREC - Total number of records in disk store.

N - Total number of nodes..

NC - Global central node number in each element.

NE - Total number of elements.

NIH - Number of equal divisions in horizontal plane.

NIV - " " " " " vertical plane.

NNS(K) - Node numbering sequence.

NON - Number of node under current consideration.

Where k = 1 to 9.

Appendix A.4.

Bessel function notation.

Several different forms of notation are used in the literature for Bessel functions. The notation used in chapters 3 and 4 is that due to Watson[82]. Reference was made to the concise presentation by Sneddon[75] (subsequently referred to as S). For some of the proofs of equations in the work of John[47] reference was made to Jeffreys and Jeffreys[46] (subsequently referred to as JJ) who use a slightly different notation.

It seems to be generally accepted that the Bessel function of the first kind is given by

$$J_n(x) = \sum_{r=0}^{\infty} \frac{(-1)^r}{r!(n+r)!} \left(\frac{x}{2}\right)^{n+2r} \qquad \text{A.4.1.}$$

The companion function, Weber's Bessel function of the second kind is given by S as

$$Y_n(x) = \frac{2}{\pi}\left\{\log\left(\frac{x}{2}\right) + \gamma\right\} J_n(x) - \frac{1}{\pi}\sum_{r=0}^{n-1} \frac{(n-r-1)!}{r!}\left(\frac{x}{2}\right)^{2r-n}$$

$$-\frac{1}{\pi}\sum_{r=0}^{\infty} \frac{(-1)^r}{r!(n+r)!}\left(\frac{x}{2}\right)^{n+2r}\left\{\phi(r+n)+\phi(r)\right\} \qquad \text{A.4.2.}$$

whereas JJ give

$$Y_n(x) = \frac{2}{\pi}\left\{\log\left(\frac{x}{2}\right)\right\} J_n(x) - \frac{1}{\pi}\sum_{r=0}^{n-1} \frac{(n-r-1)!}{r!}\left(\frac{x}{2}\right)^{2r-n}$$

$$-\frac{1}{\pi}\sum_{r=0}^{\infty} \frac{(-1)^r}{r!(n+r)!}\left(\frac{x}{2}\right)^{n+2r}\left\{F(r)+F(n+r)\right\}. \qquad \text{A.4.3.}$$

The diagamma function is defined by JJ as

$$F(z)=\frac{d}{dz}\log z! = \lim_{n\to\infty}\left(\log n - \frac{1}{z+1} - \ldots - \frac{1}{z+n}\right) \qquad \text{A.4.4.}$$

from which

$$F(0) = \lim_{n\to\infty}\left(\log n - 1 - \tfrac{1}{2} - \ldots - \tfrac{1}{n}\right) = -\gamma \qquad \text{A.4.5.}$$

where γ is Euler's constant. In a way analogous to the factorial function this function is sometimes expressed as

$$\psi(z+1) = F(z) \qquad \text{A.4.6.}$$

In equation A.4.2., ϕ is derined by S as

$$\phi(r) = \sum_{s=1}^{r}\frac{1}{s} = 1+\frac{1}{2}+\frac{1}{3}+\ldots+\frac{1}{r} \qquad \text{A.4.7.}$$

From equations A.4.5. and A.4.7. it is clear that

$$\begin{aligned}\phi(r)-\gamma &= \lim_{n\to\infty}\left(\log n - \frac{1}{r+1} - \frac{1}{r+2} - \ldots - \frac{1}{n}\right) \qquad \text{A.4.8.}\\ &= F(r)\end{aligned}$$

which, together with equation A.4.1. shows the equivalence between equations A.4.2. and A.4.3. John[47] refers to the Bessel function of the second kind as $N_n(x)$.

The asymptotic expansions for the Bessel functions are often expressed in a series form for which thereis an obvious pattern but no general term is quoted. For programming purposes such a general term must be found. For example JJ give for the modified Bessel function of the second kind

$$Kh_n(x) \sim \sqrt{\frac{2}{\pi x}}\, e^{-x}\left\{1 - \frac{1-4n^2}{1!\,8x} + \frac{(1-4n^2)(9-4n^2)}{2!\,(8x)^2} + \ldots\right\} \qquad \text{A.4.9.}$$

By defining the following notation, apparently attributable to Hankel,

$$(\alpha)_r = \alpha(\alpha+1)(\alpha+2)\times\ldots\times(\alpha+r-1) \qquad \text{A.4.10.}$$

and

$$(n,r) = \frac{(-1)^r}{r!}\left(\tfrac{1}{2}-n\right)_r \cdot \left(\tfrac{1}{2}+n\right)_r \qquad \text{A.4.11.}$$

S is able to express this function as

$$K_n(x) \sim \sqrt{\frac{\pi}{2x}}\, e^{-x} \sum_{r=0}^{\infty} \frac{(n,r)}{(2x)^r} \qquad \text{A.4.12.}$$

The equivalence between these two definitions may be straightforwardly established, but it must be noted that

$$Kh_n(x) \cdot \frac{\pi}{2} = K_n(x) \qquad \text{A.4.13.}$$

and

$$(\alpha)_0 = 1 \qquad \text{A.4.14.}$$

For small argument this function is given by S as

$$K_n(x) = (-1)^{n+1} \cdot I_n(x)\left\{\log\left(\frac{x}{2}\right) + \gamma\right\} + \frac{1}{2}\sum_{r=0}^{n-1} \frac{(-1)^r (n-r-1)!}{r!}\left(\frac{x}{2}\right)^{2r-n}$$

$$+ \frac{1}{2}(-1)^n \sum_{r=1}^{\infty} \frac{1}{r!\,(n+r)!}\left(\frac{x}{2}\right)^{2r+n}\left\{\phi(r) + \phi(n+r)\right\} \qquad \text{A.4.15.}$$

It is again generally accepted that the modified function of the first kind is given by

$$I_n(x) = \sum_{r=0}^{\infty} \frac{1}{r!(n+r)!} \left(\frac{x}{2}\right)^{n+2r} \qquad \text{A.4.16.}$$

which should be compared with equation A.4.1. The definition of $Kh_n(x)$ by JJ makes equations A.4.15. and A.4.2. just as closely related. This definition attributable to Heaviside, makes several other relations to the Hankel functions much simpler as well.

Appendix A.5. Wave radiation and quadratic correction

In chapter 3 it was shown how the problems of floating bodies in waves may be split into two parts by defining a scattered potential ϕ_S and a radiated potential ϕ_R. For the simple case of forced oscillations of a rigid body the existing program is easily utilised. The integral equation governing this problem becomes

$$\int f \frac{\partial G}{\partial n} dS = V_n \qquad \text{A.5.1.}$$

where V_n is the velocity of the body in a direction normal to the boundary. Once f is found then the radiated potential is obtained as before from

$$\phi_R = \int f G \, dS \qquad \text{A.5.2.}$$

These two equations should be compared with equations 4.2.1. and 4.3.6. The only change required by the program to evaluate the radiated potential from a swaying cylinder is in the right hand side vector of the equation system. Since Gaussian elimination is particularly efficient at solving any number of right hand side vectors it would take very little additional computation time to solve both problems in parallel.

The method of calculating the quadratic correction to the total force suggested by Lighthill[54] may therefore be simply programmed by making V_n correspond to a unit oscillation in the direction of the force. If no other changes are made then the correction obtained will relate to a primary wave of half the frequency σ given by the dispersion relation.

It appears that the analogy with the virtual work principle may be carried one stage further by only prescribing the boundary conditions on a small element of the structure. The resulting vertical velocity of the free surface when integrated with the quadratic pressure will give the quadratic correction to the force on this small element. A series of such calculations could be made to yield the variation of this force with depth.

Appendix A.6.

Equivalent forms of the Green's function

Parts of the proof of the equivalence of the two forms of the Green's function were left out of section 3. They are included here for completeness.

Most of the derivation relies on the integral relation

$$I = \int_0^\infty e^{-bk} J_0(ak)\, dk = (a^2+b^2)^{-\frac{1}{2}} \qquad \text{A.6.1.}$$

where a and b are real, which may be proved as follows.

The decay of the Bessel function with large x is not enough to counter the exponential term if b is negative. The integrand being unbounded the integral would therefore not exist. The Bessel function is not usually defined for negative argument. Accordingly it is assumed that a, $b > 0$.

The Bessel coefficients may be defined as

$$\sum_{n=-\infty}^{\infty} \lambda^n . J_n(x) = \exp\left\{\tfrac{1}{2}x\left(\lambda - \frac{1}{\lambda}\right)\right\} \qquad \text{A.6.2.}$$

Let $\lambda = e^{i\theta}$, then

$$\sum_{n=-\infty}^{\infty} J_n(x) . e^{in\theta} = \exp\left\{ix \sin\theta\right\} \qquad \text{A.6.3.}$$

The coefficient of zero order may now be isolated by recognising the periodicity of all the other terms on the left hand side, Integrating both sides from $-\pi$ to π,

$$\sum_{n=-\infty}^{\infty} J_n(x) \int_{-\pi}^{\pi} e^{in\theta}\, d\theta = \int_{-\pi}^{\pi} \exp(ix \sin\theta)\, d\theta$$

$$\therefore \qquad J_o(x) = \frac{1}{2\pi} \int_{-\pi}^{\pi} \exp(ix \sin\theta)\, d\theta \qquad \text{A.6.4.}$$

The integral in equation A.6.1. may now be expressed as

$$I = \frac{1}{2\pi} \int_{o}^{\infty} \int_{-\pi}^{\pi} e^{-bk} \cdot \exp(iak \sin\theta)\, d\theta\, dk \qquad \text{A.6.5.}$$

Since the integrand is bounded, it exists and therefore the order of integration may be changed.

$$\therefore \qquad I = \frac{1}{2\pi} \int_{-\pi}^{\pi} \int_{o}^{\infty} e^{(ia\sin\theta - b)k}\, dk\, d\theta$$

$$= \frac{1}{2\pi} \int_{-\pi}^{\pi} \frac{d\theta}{(b - ia\sin\theta)} \qquad \text{A.6.6.}$$

The range of integration may be interpreted as a passage once round the unit circle in the complex plane. The periodicity of the integrand ensures continuity at the end points. Defining the complex variable as

$$z = e^{i\theta} \qquad \text{A.6.7.}$$

whence $dz = ie^{i\theta} d\theta$ A.6.8.

and recalling that

$$i \sin\theta = \sinh i\theta = \tfrac{1}{2}\left(e^{i\theta} - e^{-i\theta}\right) \quad \text{A.6.9.}$$

the integral becomes

$$I = \frac{1}{2\pi} \int_{-\pi}^{\pi} \frac{d\theta}{b - \tfrac{1}{2}ae^{i\theta} + \tfrac{1}{2}ae^{-i\theta}}$$

$$= \frac{-1}{i\pi} \oint \frac{dz}{az^2 - 2bz - a} \quad \text{A.6.10.}$$

The value of this integral may be obtained from Cauchy's theorem once all the poles within the unit circle have been identified. The roots of the denominator are given by

$$az = b \pm \sqrt{b^2 + a^2} \quad \text{A.6.11.}$$

In this particular case these two real roots may be written as α and $-1/\alpha$. Therefore

$$I = \frac{-1}{i\pi a} \oint \frac{dz}{(z-\alpha)\left(z + \frac{1}{\alpha}\right)} \quad \text{A.6.12.}$$

where $a\alpha = b - \sqrt{a^2 + b^2}$ A.6.13.

and $-\frac{a}{\alpha} = b + \sqrt{a^2 + b^2}$ A.6.14.

The two simple poles of the integrand may be separated by the method of partial fractions thus,

$$I = \frac{-1}{i\pi a} \oint \frac{1}{\left(\alpha + \frac{1}{\alpha}\right)} \left\{ \frac{1}{(z-\alpha)} - \frac{1}{\left(z + \frac{1}{\alpha}\right)} \right\} dz \quad \text{A.6.15.}$$

Since a and b are both positive then from equation A.6.13. α is within $|z| = 1$ and therefore $-1/\alpha$ is outside it. The function $(z-\frac{1}{\alpha})^{-1}$ is therefore analytic throughout the unit circle. The residue of the integrand is therefore $(\alpha + 1/\alpha)^{-1}$, being the coefficient of $(z-\alpha)^{-1}$. The integral is then given by Cauchy's theorem as

$$I = \frac{-1}{i\pi a} \cdot 2\pi i \cdot \frac{1}{(\alpha + \frac{1}{\alpha})} \qquad \text{A.6.16.}$$

$$= (a^2+b^2)^{-\frac{1}{2}}$$

thus proving equation A.6.1.

It is now possible to show the derivation of the series form of the Green's function G, from the integral form derived for example by Wehausen and Laitone[84]. This derivation follows the line of John[47] but includes many intermediate steps.

The integral form of the Green's function may be expressed as

$$G = \frac{1}{R} + \frac{1}{R'} + \int_0^\infty \frac{2(\mu+\nu)e^{-\mu h}\cosh\mu(b+h)\cosh\mu(y+h)J_0(\mu r)d\mu}{\mu\sinh\mu h - \nu\cosh\mu h} \qquad \text{A.6.17.}$$

where

$$R = \left[(x-a)^2+(y-b)^2+(z-c)^2\right]^{\frac{1}{2}} = \left[r^2+(y-b)^2\right]^{\frac{1}{2}}$$

$$R' = \left[(x-a)^2+(y+2h+b)^2+(z-c)^2\right]^{\frac{1}{2}} = \left[r^2+(y+2h+b)^2\right]^{\frac{1}{2}}$$

$$r = \left[(x-a)^2+(z-c)^2\right]^{\frac{1}{2}}$$

'The path of integration is along the real axis except for an arc in the lower half plane, which avoids the positive real root $\mu = m_o$ of the denominator'. It is no coincidence that the complex plane chosen is that defined by the simple harmonic time. If any other plane were used the function G would not satisfy the radiation condition.

From equation A.6.1., R and R' may be expressed in integral form as

$$\frac{1}{R} = \left[r^2+(y-b)^2\right]^{-\frac{1}{2}} = \int_o^\infty e^{-\mu(y-b)} . J_o(\mu r) . d\mu \qquad \text{A.6.18.}$$

$$\frac{1}{R'} = \left[r^2+(y+2h+b)^2\right]^{-\frac{1}{2}} = \int_o^\infty e^{-\mu(y+2h+b)} . J_o(\mu r) . d\mu \qquad \text{A.6.19.}$$

which restricts the values of y and b to

$$-h < b < y \leq 0 \qquad \text{A.6.20.}$$

to ensure that the exponential terms represent a decay.

Combining equations A.6.18 and 19,

$$\frac{1}{R} + \frac{1}{R'} = \int_o^\infty e^{-\mu(y+h)} \left\{ e^{\mu(b+h)} + e^{-\mu(b+h)} \right\} J_o(\mu r)\, d\mu$$

$$= \int_0^\infty 2 . e^{-\mu(y+h)} . \cosh \mu(b+h) . J_o(\mu r)\, d\mu \qquad \text{A.6.21.}$$

The Green's function now becomes

$$G = \int_0^\infty \frac{2\cosh\mu(b+h)\,J_0(\mu r)}{\mu\sinh\mu h - \nu\cosh\mu h}\Big[(\mu\sinh\mu h - \nu\cosh\mu h).e^{-\mu(y+h)} + \\ + (\mu+\nu).e^{-\mu h}.\cosh\mu(y+h)\Big]\,d\mu \qquad \text{A.6.22.}$$

The identity

$$e^{-x} = \cosh x - \sinh x \qquad \text{A.6.23.}$$

may be used to simplify this to

$$G = \int_0^\infty p(\mu).J_0(\mu r).d\mu \qquad \text{A.6.24.}$$

where

$$p(\mu) = \frac{2\cosh\mu(b+h)(\mu\cosh\mu y + \nu\sinh\mu y)}{\mu\sinh\mu h - \nu\cosh\mu h} \qquad \text{A.6.25.}$$

John calls $p(\mu)$ a meromorphic function of μ. This is understood to mean that it is only singular at distinct points (rather than at a finite number) and may be put in the form (morphic) of partial (mero) fractions. A simple aside helps to explain how this is achieved. Consider the function

$$g(x) = \frac{f(x)}{(x^3 - 6x^2 + 11x - 6)} \qquad \text{A.6.26.}$$

The roots of the denominator are x = 1, 2 and 3 so that its partial fraction expansion may be expressed as

$$g(x) = \frac{A_1}{(x-1)} + \frac{A_2}{(x-2)} + \frac{A_3}{(x-3)} \qquad \text{A.6.27.}$$

Equating these two forms and multiplying by the denominator gives

$$f(x) = (x-2)(x-3)A_1 + (x-1)(x-3)A_2 + (x-1)(x-2)A_3 \qquad \text{A.6.28.}$$

One common alternative to equating coefficients of like powers of x, is to set x equal to each root in turn. For example

$$f(x)\Big|_{x=2} = (x-1)(x-3)\Big|_{x=2} . A_2 \qquad \text{A.6.29.}$$

from which A_2 may be found. This form is obviously unuseable when the denominator has an infinite number of roots. However, the coefficient of A_2 is clearly the denominator divided by (x-2), i.e.

$$f(x)\Big|_{x=2} = \frac{(x^3-6x^2+11x-6)}{(x-2)}\Bigg|_{x=2} . A_2 \qquad \text{A.6.30.}$$

The fraction is obviously indeterminate but its value may be established by L'Hôpital's rules. Comparing equations A.6.25. and A.6.26. it will be seen that the denominator is

$$\mu \sinh \mu h - \nu \cosh \mu h \qquad \text{A.6.31.}$$

which has the roots

$$\mu = m_k$$

and $$\mu = m_{-k} = -m_k \qquad k = 0, 1, 2 \ldots \qquad \text{A.6.32.}$$

where

$$m_k \sinh m_k h = \nu \cosh m_k h \qquad \text{A.6.33.}$$

The real roots correspond to k = 0. The expansion for $p(\mu)$ may be sought in the form

$$p(\mu) = \frac{2\cosh\mu(b+h)(\mu\cosh\mu y + \nu\sinh\mu y)}{(\mu\sinh\mu h - \nu\cosh\mu h)} = \sum_{k=0}^{\infty} \frac{A_k}{(\mu - m_k)} + \frac{A_{-k}}{(\mu + m_k)} \qquad \text{A.6.34.}$$

The coefficient of $(\mu - m_k)^{-1}$ is given by

$$2\cosh\mu(b+h)(\mu\cosh\mu y + \nu\sinh\mu y)\Big|_{\mu=m_k} = \frac{\mu\sinh\mu h - \nu\cosh\mu h}{\mu - m_k}\Big|_{\mu=m_k} \qquad \text{A.6.35.}$$

The indeterminancy of the fraction on the right hand side may be removed by applying L'Hopital's rules, thus

$$\frac{\mu\sinh\mu h - \nu\cosh\mu h}{\mu - m_k}\Big|_{\mu=m_k} = \frac{\mu h\cosh\mu h - \nu h\sinh\mu h + \sinh\mu h}{1}\Big|_{\mu=m_k} \qquad \text{A.6.36.}$$

Therefore

$$A_k = \frac{2\cosh m_k(b+h)(m_k\cosh m_k y + \nu\sinh m_k y)}{h(m_k\cosh m_k h - \nu\sinh m_k h) + \sinh m_k h} \qquad \text{A.6.37.}$$

This may be rearranged using equation A.6.33. into the form used by John,

$$A_k = 2\,\frac{m_k^2 - \nu^2}{h(m_k^2 - \nu^2) + \nu} \cdot \cosh m_k(b+h)\cdot\cosh m_k(y+h) \qquad \text{A.6.38.}$$

Since $m_{-k} = -m_k$ then $A_{-k} = A_k$, therefore equation A.6.34. becomes

$$p(\mu) = \sum_{k=0}^{\infty} \frac{\mu}{\mu^2 - m_k^2} \cdot 2A_k \qquad \text{A.6.39.}$$

The Green's function is therefore, from equation A.6.24.

$$G = \int_0^\infty 2\, J_0(\mu r) \left\{ \sum_{k=0}^{\infty} A_k \frac{\mu}{\mu^2 - m_k^2} \right\} d\mu$$

$$= \sum_{k=0}^{\infty} 2 A_k \int_0^\infty \frac{\mu\, J_0(\mu r)}{\mu^2 - m_k^2}\, d\mu \qquad \text{A.6.40.}$$

John makes use of the identity given by Watson[82] as

$$\int_0^\infty \frac{\mu\, J_0(\mu r)}{\mu^2 + t^2}\, d\mu = \frac{\pi i}{2} H_0^{(1)}(itr) \qquad \text{A.6.41.}$$

If $t = - i m_k$ this becomes

$$\int_0^\infty \frac{\mu\, J_0(\mu r)}{\mu^2 - m_k^2}\, d\mu = \frac{\pi i}{2} H_0^{(1)}(m_k r) \qquad \text{A.6.42.}$$

For $k = 1, 2, \ldots\ldots$ the m_k are all imaginary so that the path of integration does not encounter these roots. However, the positive root m_0 lies on the real axis. The path of integration in equation A.6.40 has already been specified so as to avoid this root. It so happens that this choice preserves the identity in equation A.6.42.

The Green's function is therefore

$$G = \sum_{k=0}^{\infty} 2 A_k \cdot \frac{\pi i}{2} H_0^{(1)}(m_k r)$$

$$= 2\pi i \sum_{k=0}^{\infty} \frac{m_k^2 - \nu^2}{h(m_k^2 - \nu^2) + \nu} \cdot H_0^{(1)}(m_k r) \cosh m_k(b+h) \cosh m_k(y+h) \qquad \text{A.6.43.}$$

John now lifts the restriction given by A.6.20 on the grounds that for positive r this function satisfies all the requirements of the Green's function and by the uniqueness principle must therefore be the correct expression.

LIST OF SYMBOLS

a i) Wave amplitude as used By Lighthill[54].

ii) Radius of small sphere, surface σ.

iii) Horizontal coordinate of pulsating source point.

a_{ji} A typical element of matrix [A].

a_{max} Maximum wave amplitude as used by Ursell, Dean and Yu[78].

a_{min} Minimum wave amplitude as used by Ursell, Dean and Yu[78].

A i) Projected area of structural element as used by Isaacson and Maull[42].

ii) Arbitrary two-sided surface within the fluid.

iii) Fixed point in the flow domain.

iv) Dimensionless constant in velocity due to incident wave.

v) Constant in appendix A.1.

vi) Amplitude of input voltage V_i in appendix A.2.

[A] Matrix of coefficients.

A_1, A_2 Amplitudes of pressure fluctuations in waves.

A(ka) Function of Bessel functions defined by MacCamy and Fuchs[58].

AC, ALIM & ALPHA see Appendix A.3.

b i) Radius of circular cylinder as used by Lighthill[54].

ii) Vertical coordinate of pulsating source point.

iii) Depth of immersion of wave generator wedge.

B i) Fixed point in the flow domain.

ii) Constant in appendix A.1.

iii) Amplitude of output voltage V_o in appendix A.2.

[B] Sub-matrix of equation system.

c i) Horizontal coordinate of pulsating source point.

ii) Subscript referring to constant depth section of wave flume.

C i) An unknown constant.

ii) Fixed point in the flow domain.

iii) See also Appendix A.3.

iv) Wave celerity or phase speed.

v) Feedback capacitor in amplifier.

[C] Sub-matrix of equation system.

C_1,C_2 Theoretical, experimental phase speeds.

C_h Diffraction coefficient defined by Chakrabarti and Tam[15].

C_D,C_M&C_L Drag, inertia and lift force coefficients.

d i) Water depth e.g. Isaacson[40].

ii) Distance between horizontal cylinder and the bed, Jeffreys[45].

d_c Constant water depth as used by Wiegel[87].

d_s Differential element of cylinder surface, Lighthill[54].

D i) Diameter of circular cylinder e.g. Verley[80], of sphere—Rainey[70].

ii) See also Appendix A.3.

[D] Submatrix of equation system.

DEL See Appendix A.3.

e Refers to an element length or area.

E i) Fluctuating extension as defined by Lighthill[54].

ii) See also Appendix A.3.

iii) Energy associated with a wave.

iv) Young's Modulus for Araldite.

E_k Element number k.

f	i)	An arbitrary function on the large sphere Σ.
	ii)	Frequency as used by e.g. Borgman[11].
$f(x)$		Function of x used in appendix A.6.
$f(q)$		Continuous distribution of source intensity on S.
$f'(q)$		Approximation to the distribution f(q).
f_c		Filter cut-off frequency.
f_i	i)	Source strengths of a finite number of point sources.
	ii)	Finite number of values of continuous distribution of source intensity.
F		Force on circular cylinder.
$\Gamma(t)$		Arbitrary function of time in the generalised Bernoulli equation.
F_d, F_q, F_w		Quadratic corrections to the in line force, Lighthill[54].
F_L		Lift or transverse force, Isaacson and Maull[42], Jeffreys[45].
F_y		Lift force in the positive y direction.
g		Acceleration due to gravity - 9.81 ms^{-2}.
$g(x)$		Function of x used in appendix A.6.
G		The Green's function for linear waves.
$[G]$		Matrix in direct boundary element statement.
C_o		The Green's function used by Ursell[77].
h		Water depth.
H		Wave height from crest to trough.
$[H]$		Matrix in direct boundary element statement.
$\dot{H}$		Horizontal flow velocity used by Rainey[70].
$H_n^{(1)}(x), H_n^{(2)}(x)$		Hankel functions of the first and second kinds, order n.
i	i)	Complex index, $\sqrt{-1}$.
	ii)	General index, if repeated implies summation.
$I, I_1 \& I_2$		Integrals.
$I_n(x)$		Modified Bessel function of the first kind, order n.
j		General index, if repeated implies summation.
$J_n(x)$		Bessel function of the first kind, order n.

k i) Radian wave number, $2\pi/\lambda$.

ii) Summation index.

k_1, k_2 Theoretical, experimental wave numbers.

K i) Keulegan and Carpenter number used by Sarpkaya[71].

ii) Operator in dissipative boundary conditon used by Ursell[77].

$K(f)$ Kernel function of frequency as used by Borgman[11].

$K_n(x)$ Modified Bessel function of the second kind, order n.

KC Keulegan and Carpenter number used by Isaacson and Maull[42].

ℓ i) Length of tether cable, Rainey[70].

ii) Typical boundary element length.

L i) Wave length as used by Verley[80].

ii) Exponential decay length used by Bettess[5].

$L_{I\eta}, L_{J\xi}$ Quadratic Lagrangian interpolation functions.

m Strength of singular function f, Jaswon and Symm[44].

m_o Real root of the dispersion relation, corresponds to wave number k.

m_k Imaginary roots of the dispersion relation.

M i) Mass of sphere used by Rainey[70].

ii) Number of boundary elements.

iii) Number of point sources.

n i) Ratio of group velocity to phase velocity.

ii) Order of Bessel functions.

iii) Normal direction to surface.

$\underline{n}$ Normal direction vector, components n_i.

n_i Normal directed into the interior domain.

n_e Normal directed into the exterior domain.

n_x Direction cosine used by Lighthill[54].

N Number of dimensions.

N_i Interpolation or shape functions.

N_{KC} Keulegan and Carpenter number used by Verley[80].

NE, NIH, NIV see Appendix A.3.

p i) Fluid pressure.

ii) Point on the boundary Γ.

$p(\mu)$ Meromorphic function defined by John[47].

p Vector of unknown pressures on a structure.

p* Normalised fluid pressure.

p_1, p_2 Real and Imaginary parts of the complex fluid pressure.

P i) Fluid pressure.

ii) A fixed point in the fluid.

iii) Physical boundary, corresponds to Γ.

PRAD See Appendix A.3.

q i) Position on source boundary S.

ii) Magnitude of fluid particle velocity, Lighthill[54].

$\{q\}$ Vector of normal velocity components.

$\bar{q}$ Prescribed normal fluid velocity.

Q Fixed point in the fluid domain.

r i) Cylindrical polar radial coordinate.

ii) Projection of R iii) onto the horizontal plane.

r' Distance measured from an image source.

r_s Radius of source cylinder S.

R i) Radius of the large sphere Σ.

ii) Subscript indicating radiated component.

iii) Distance from (a,b,c) to (x,y,z).

iv) Feedback resistor in filter amplifier.

R' Distance from the image of (a,b,c) to (x,y,z).

R(r) Radial variation of potential function.

R_i Input resistor see appendix A.2.

Re Reynolds number.

s i) Integer in Fourier series.

ii) Dummy root of dispersion relation.

S i) Boundary on which source distribution is placed.

ii) Subscript indicating scattered component.

iii) Vertical stroke of wave generator.

S_1, S_2 & S_3 Infinite series in Green's function.

S_{xx}, S_{yy} Spectral densities defined by Borgman[10].

SRAD See Appendix A.3.

t i) Variable time.

ii) Variable used by Jeffreys and Jeffreys[46].

iii) Dummy root of dispersion relation.

T i) Wave period.

ii) Non dimensional constant used in appendix A.1.

iii) Subscript indicating total.

T_s Time of separation of shed vorticity.

T_t Time of travel of wave crest.

u Component of fluid velocity in x direction.

$\underline{u}$ Fluid velocity vector, components u_i.

U i) Velocity of uniform stream used by Jeffreys[45].

ii) Group velocity.

$U, \dot{U}$ Velocity and acceleration used by Pierson and Holmes[69].

U_m, U_{max} Maximum velocity in x direction.

v Component of fluid velocity in y direction.

$V, \dot{V}, v_{rms}$ Velocity, acceleration and root mean square velocity, Borgman[10].

$\dot{V}$ Vertical flow velocity used by Rainey[70].

V_i Input voltage used in appendix A.2.

V_o Output voltage used in appendix A.2.

V_n Velocity component in a normal direction.

V_r Velocity component in a radial direction.

Vol Volume of tethered body used by Rainey[70].

w Component of fluid velocity in z direction.

W Subscript indicating incident wave component.

W_k Gaussian quadrature weighting factor.

x i) Horizontal cartesian coordinate.

ii) Horizontal displacement of centroid of sphere, Rainey[70].

iii) Argument of Bessel functions.

x_i Cartesian coordinate components.

X Non dimensional coordinate used by Jeffreys[45].

X_k^r rth approximation to the kth root of the dispersion relation.

X_j Body force components.

y i) Vertical cartesian coordinate.

ii) Horizontal cartesian coordinate used by some authors e.g. Lighthill[54].

Y Non dimensional coordinate used by Jeffreys[45].

Y(y) Separable y variation of potential function.

$Y_n(x)$ Bessel function of the second kind, order n.

z i) Horizontal cartesian coordinate component.

ii) Vertical cartesian coordinate as used e.g. by Havelock[29].

iii) General complex variable i.e. x + iy.

ZK see Appendix A.3.

α i) Separation constant for Laplace's equation.

ii) Semi-angle subtended by a cylindrical element.

iii) Phase lag of total wave force on cylinder, Chakrabarti and Tam[15].

iv) Amplitude of primary wave, Ursell, Dean and Yu[78].

v) Angle of wave generator wedge.

vi) Reflection coefficient used by Longuet -Higgins[55].

vii) Symbol for roots in Appendix A.6., as used by Jeffreys and Jeffreys[46].

viii) Angle of tangent at the point where a cut is made in Si).

ix) Small distance along element from singular point.

α_j j Set of angles indicated in figure 3.7.2.

β i) Frequency parameter as used by Sarpkaya[71].

ii) Ratio of source boundary size to physical boundary size.

γ i) Singular function of known form as used by Jaswon and Symm[44].

ii) Euler's constant = 0.577215665...

Γ i) Arbitrary closed surface within the fluid.

ii) Boundary on which values are prescribed.

iii) Wave function (i.e. $\nabla^2\Gamma = 0$) used by Ursell[77]

δ i) Phase angle between incident and reflected waves[78].

ii) Deflection of Araldite test piece.

$\delta(r)$ Dirac delta function centred ar $r = 0$.

δx_i Cartesian components of a small change in x_i.

Δ Half the vertical dimension of a cylindrical element.

ε Small distance defining the neighbourhood of a point.

ε_n Jacobi symbol.

ε_r Reflection coefficient, Ursell, Dean and Yu[78].

η i) Vertical coordinate of a point on the free surface.

ii) Natural coordinate corresponding to the y direction.

η_I, η_R Incident and reflected wave profiles, Ursell, Dean and Yu[78].

θ Angular coordinate, either spherical or cylindrical polar.

$\Theta(\theta)$ Separable angular variation of potential function.

λ i) Spherical polar coordinate.

ii) Wavelength.

iii) Variable in power series expansion for Bessel coefficients[46].

λ_1, λ_2 Theoretical, experimental wavelengths.

μ Integration variable in the wave number domain.

ν i) Kinematic viscosity of water.

ii) Normal direction on large sphere Σ.

iii) σ^2/g, as defined e.g. by Garrison and Chow[25].

iv) Exponent used by Liggett and Liu[53].

ξ Natural coordinate corresponding to x direction.

π = 3.14159...

ρ Density of water.

ρ_A Density of Araldite.

σ i) Surface of a small sphere.

ii) Radian frequency.

Σ i) Surface of a large sphere.

ii) Summation symbol.

ϕ i) Potential function of space, sometimes complex i.e. $\phi_1 + i\phi_2$.

ii) Force per unit length used by Borgman[10].

iii) Unknown phase angle.

iv) Phase angle of V_o with respect to V_i.

$\phi(r)$ Function defined by Sneddon[75], used in Appendix A.6.

ϕ^* Fundamental potential solution of Laplace's equation.

$\bar{\phi}$ Prescribed values of ϕ, usually on Γ.

ϕ_{IJ} Bi-quadratic Lagrangian interpolation function.

Φ Potential function of space and time.

Ψ i) Potential function in Green's theorem.

ii) Stream function.

$\Psi(x)$ Residual function.

ω i) Region within σi).

ii) Complex potential as used by Jeffreys[45].

Ω i) Body force potential.

ii) Region enclosed by Γ.

Ω_i, Ω_e Interior, exterior domain bounded by Γ.

Ω_I Interior domain bounded by Si).

Ω_M Middle domain between Si) and Γ.

∇^2 Laplacian operator.

F Diagamma function[46].

* Indicates results obtained by direct measurement.